

Coherent Population Trapping and Optical Ramsey Interference for Compact Rubidium Clock Development

Zachary Aron Warren

A DISSERTATION

Submitted in partial fulfillment of the requirements
for the degree of Doctor of Philosophy
in the Optics Graduate Program of
Delaware State University

DOVER, DELAWARE
May 2017

This dissertation is approved by the following members of the review committee:

Dr. Gour Pati, Committee Chair, Dept. of Physics & Eng., Delaware State University
Dr. Renu Tripathi, Committee Co-Chair, Dept. of Physics & Eng., Delaware State University
Dr. Mukti Rana, Committee Member, Dept. of Physics & Eng., Delaware State University
Dr. Deborah Santamore, Committee Member, Dept. of Physics & Eng., Delaware State University
Dr. Nan Yu, External Committee Member, Quantum Sciences and Technology, Jet Propulsion
Laboratory

ACKNOWLEDGMENTS

I would like to first sincerely thank my advisors, Dr. Gour Pati and Dr. Renu Tripathi, for their guidance, insight, and support throughout my graduate studies. Thank you for providing the opportunity and resources for these scientific investigations as well as academic discussions, explanations, and sharing your experience. This dissertation would not have been possible without you.

Thank you to my committee members for their time and effort in reviewing this work: Dr. Mukti Rana, Dr. Deborah Santamore, and Dr. Nan Yu.

My gratitude is extended to the department faculty and staff who provided administrative support, including Jacquelyn Jones, Shonda Poe, and Amal Juracka. I am indebted to Nick Quigley for his immeasurable help in machining parts I needed for the experiments.

I also acknowledge the financial support received from the NASA and DoD grants allowing me to conduct this research.

A special thanks goes to Dr. Aaron Pung for his time, conversation, and advice on graduate school and programming I could not have survived without. Further thanks to Josh Bascom for his perspective and engineering advice.

Finally, I would like to thank my family for all the support they have given me over the years, as well as friends who listened to and supported me along the way.

ABSTRACT

Coherent Population Trapping and Optical Ramsey Interference for Compact Rubidium Clock Development

Zachary Aron Warren

Faculty Advisor: Dr. Gour Pati
Faculty Co-Advisor: Dr. Renu Tripathi

Coherent population trapping (CPT) and optical Ramsey interference provide new avenues for developing compact, high-performance atomic clocks. In this work, I have studied the fundamental aspects of CPT and optical Ramsey interference for Raman clock development. This thesis research is composed of two parts: theoretical and experimental studies. The theoretical component of the research was initially based on pre-existing atomic models of a three-level Λ -type system in which the phenomena of CPT and Ramsey interference are formed. This model served as a starting point for studying basic characteristics of CPT and Ramsey interference such as power dependence of CPT, effects of average detuning, and ground-state decoherence on linewidth, which directly impact the performance of the Raman clock. The basic three-level model was also used to model pulsed CPT excitation and measure light shift in Ramsey interference which imposes a fundamental limit on the long-term frequency stability of the Raman clock. The theoretical calculations illustrate reduction (or suppression) of light shift in Ramsey interference as an important advantage over CPT for Raman clock development. To make the model more accurate than an ideal three-level system, I developed a comprehensive atomic model using density-matrix equations including all sixteen Zeeman sublevels in the D1 manifold of ^{87}Rb atoms in a vapor medium. The multi-level atomic model has been used for investigating characteristics of CPT and Ramsey interference under different optical excitation schemes pertaining to the

polarization states of the frequency-modulated CPT beam in a Raman clock. It is also used to study the effects of axial and traverse magnetic fields on the contrast of CPT and Ramsey interference. More importantly, the multi-level atomic model is also used to accurately calculate light shift in Ramsey interference in the D1 manifold of ^{87}Rb atoms by taking into account all possible off-resonant excitations and the ground-state decoherence among the Zeeman sublevels. Light shift suppression in Ramsey interference with pulse saturation is also found to be evident in this comprehensive model.

In the experimental component of the research, I designed a prototype of the Raman clock using a small (2 cm in length), buffer-gas filled, and isotopically pure ^{87}Rb cell. A fiber-coupled waveguide electro-optic modulator was used to generate the frequency-modulated CPT beam for the experiments. The experimental setup was operated either by continuous excitation or pulsed excitation for experimentally characterizing CPT and Ramsey interference under different experimental conditions and for testing different optical excitation schemes which were investigated theoretically. Several iterations of the clock physics package were developed in order to attain better frequency stability performance in the Raman clock. The experimental work also provided a basis to develop a new repeated-query technique for producing an ultra-narrow linewidth central fringe with a high S/N ratio, and suppressing the side fringes in Ramsey interference.

The above described research was carried out keeping in mind compact, high-performance clock development, which relies on technologies that can be miniaturized. Vapor cell based atomic clocks are ideal candidates for compact clock technology. The CPT phenomenon, observed by Raman excitation in a vapor medium, is a promising candidate for compact, high-performance Raman clock development. However, atom-field interaction involved in a vapor medium is often

more complex than other media such as cold atom or atomic beam. It is difficult to model this interaction in order to predict its influence on CPT characteristics and, hence, the performance of the Raman clock. This dissertation addresses one such problem by developing a comprehensive atomic model to investigate light shift and modification of light shift in the Raman clock, particularly with pulsed excitation. It demonstrates a clear possibility of reducing (or suppressing) the light shift associated with Ramsey interference in a vapor medium for achieving higher frequency stability in the Raman clock. Additionally, theoretical comparisons of various optical excitation techniques have been calculated to demonstrate the relative strengths and weaknesses of different schemes for Raman clock development.

Chapter 1 outlines a brief history of atomic clock technologies related to this current work. Principles of common types of atomic beam and vapor cell clocks are described, along with their applications. Determining precision of the clock requires measurement of the output frequency over time, so the clock stability is also discussed, addressing sources of noise and errors in the measured frequency. The requirements and challenges for developing portable, miniature clocks are discussed.

Chapter 2 describes an idealized three-level Λ -system, which is used to model CPT and Ramsey interference. A fundamental basis for theoretical modeling is developed in this chapter by formulating density-matrix equations. The simulations are performed with numerical solvers in both steady-state and time-dependent regimes for studying CPT phenomenon in continuous excitation and Ramsey interference in pulsed excitation. The general behaviors concerning the lineshapes and resonance properties of CPT and Ramsey interference were established. Characteristics of CPT have also been studied in density-matrix elements relating to the coherence between the ground-states and excited state. Ramsey interference is modeled to investigate how

the phenomenon responds to different pulse parameters. The three-level model serves as a simple basis for investigating CPT and Ramsey interference for these Raman clock studies.

Chapter 3 expands on the three-level model by developing a comprehensive sixteen-level atomic model by incorporating all Zeeman sublevels in the D1 manifold of ^{87}Rb atoms. Raman excitation in this multi-level model enables modeling of different polarization states for the CPT beam which in effect forms multiple three-level Λ -transitions depending on the polarization and the state selection. The model was also extended to include the effect of transverse magnetic field when calculating the resonances. Optical excitation schemes simulating different possibilities for Raman excitation were considered for the frequency-modulated beam in a Raman clock, and the drawbacks and benefits of each are discussed.

Chapter 4 specifically addresses light shift, a fundamental source of error in atomic clocks, which limits the long-term frequency stability. The slope of light shift as a function of laser intensity or laser detuning affects the long-term stability of the clock. Using the three-level model, described in Chapter 2, I calculated the light shift in Ramsey interference by modeling the interaction of the three-level atoms with bichromatic laser pulse sequence. The result obtained from this calculation revealed that light shift properties of Ramsey interference are different from CPT because of pulsed excitation. It showed an important property of light shift in Ramsey interference, that it can be reduced by strong interaction with the first pulse. Such an aspect of Ramsey interference constitutes a practically competitive scheme for compact, high-performance Raman clock development. Light shifts associated with coherent density-matrix terms are studied as they are relevant to the detection of Ramsey interference in transmission (or absorption) through the medium. For the single-velocity case, the numerically computed results from the three-level model were compared with the analytical results obtained using the adiabatic approximation.

Later, light shift is more accurately calculated in the D1 manifold of ^{87}Rb atoms by using the multi-level atomic model described in Chapter 3. Although, the light shift was found to be modified due to the presence of additional off-resonant excitations and decoherence introduced in the ground-state magnetic sublevels, the general characteristics of light suppression with pulse saturation remained valid. Effect of velocity averaging on Ramsey interference was also investigated, and shown to create a systematic frequency error which is not real in the atomic system under study.

Chapter 5 describes the design, development, and construction of the experimental atomic clock prototype. The iterations and versions of the experiment are described, leading to the most recent version. Experimental studies have been performed using a laboratory scale Raman clock employing a 2-cm long, isotopically pure rubidium cell, loaded with a buffer gas. Components involved in the experiment are chosen as to be suitable for compact clock development. A fiber-coupled waveguide EOM driven by an RF oscillator is used to produce a frequency-modulated laser beam for the experiments. The phase-locked-loops (PLL) are used as the RF frequency synthesizer for driving the EOM. Several laser lock techniques were explored for the tunable diode laser for finding one which is suitable for compact Raman clock development. Additionally, towards the end of this chapter, a brief discussion on vertical cavity surface emitting lasers (VCSELs) is presented, as they are a primary candidate for compact clock development. VCSELs can be directly modulated and thus do not require an external beam generation device such as an EOM. Methodology for generating CPT resonance and Ramsey interference fringes using the experimental setup are described. Chapter 5 reports on the experimental results obtained for CPT and Ramsey interference. These include results using various optical excitation schemes based on polarization states of the contributing CPT beams, light shift measurements, and contrast and linewidth measurements for CPT and Ramsey interference.

Chapter 6 reports on the clock frequency stability measurements using the phenomena of CPT and Ramsey interference. Conditions and parameters for achieving best clock stability are determined. Different clock schemes are compared to demonstrate short- and long-term stability improvements with CPT and Ramsey interference. A promising new interrogation method, known as repeated query technique, for acquiring Ramsey fringes is also discussed in this chapter. This technique enhances the contrast and the S/N ratio of the central fringe in Ramsey interference and significantly suppresses the side fringes by interference of multiple query signals. The frequency stability (or Allan deviation) of the clock is measured by employing the repeated query technique.

Chapter 7 concludes the dissertation with a summary of the results and methods, and addresses future avenues for improvement in the research. The future work described in this chapter pushes the experimental techniques and components closer to compact clock technologies. The future theoretical work incorporates more of the physical effects which occur in the real atomic system, leading to more accurate simulations, which will provide deeper insight into the requirements and limitations of vapor cell based compact clocks.

Appendices are provided to supplement the chapters. They present computer codes for simulation, and derivations showing magnetic field effects and equivalence of polarization schemes for the multi-level atomic model. The appendices also include supplements to the experiment section such as Helmholtz coil design simulation (COMSOL) and data collection methods (LabVIEW).

TABLE OF CONTENTS

List of Tables	xi
List of Figures	xii
List of Abbreviations	xx
Chapter 1: Introduction	1
1.1 Atomic clock technology	3
1.1.1 Atomic beam and separated field Ramsey interference	4
1.1.2 Atomic vapor and optically-pumped atomic clocks	6
1.1.3 Atomic clock stability	8
1.2 Miniature atomic clocks	10
Chapter 2: Three-level Λ-system Modeling	14
2.1 CPT in a three-level Λ -system	15
2.1.1 Dark state formation	15
2.1.2 CPT phenomenon	18
2.2 Density matrix	18
2.3 CPT simulation results	24
2.4 Pulsed CPT and Ramsey interference simulation results.....	29
2.4.1 Ramsey interference simulation results	31
2.4.2 Time domain Ramsey interference	35
Chapter 3: Multi-level Atomic Modeling	37
3.1 Multi-level atomic model for ^{87}Rb D1 manifold.....	39
3.2 Optical excitation schemes in CPT	47
3.3 Transverse magnetic field effect	51
3.4 Raman-Ramsey interference	54
Chapter 4: Light Shift in Raman-Ramsey Interference	57
4.1 Three-level model for Raman-Ramsey interference	59
4.2 Computational light shift results and discussions	62
4.3 Light shift in multi-level atomic model.....	69
4.4 Velocity averaging	72
Chapter 5: Experimental Methods and Results	80
5.1 Raman beam generation with EOM	80
5.2 Clock frequency synthesis.....	85
5.3 Laser frequency lock techniques	87
5.3.1 Dichroic atomic vapor laser lock	88
5.3.2 Single detector laser lock.....	89

5.4 Implementation of push-pull optical pumping scheme	89
5.5 Small cell physics package.....	93
5.5.1 Magnetic shield revisions	100
5.6 Ramsey pulse switching with AOM.....	102
5.7 Experimental results	104
5.7.1 CPT results.....	106
5.7.2 Ramsey results	115
5.7.3 Light shift measurements.....	117
5.7.4 VCSEL characterization	120
5.8 Repeated query technique	121
Chapter 6: Clock Stability Results	134
6.1 Shot-noise limited stability estimation.....	134
6.2 Clock servo.....	135
6.3 CPT clock stability results	137
6.3.1 Preliminary (large cell) ^{85}Rb CPT clock results	137
6.3.2 Clock results using integer PLL and large ^{87}Rb cell.....	138
6.3.3 Stability dependence on modulation amplitude.....	140
6.3.4 Clock stability with CPT in small ^{87}Rb cell.....	141
6.4 Clock stability results using Ramsey interference	143
Chapter 7: Conclusion and Future Work	146
References	150
Appendix A: MATLAB codes.....	157
A.1 Three-level CPT solver – steady state solution.....	157
A.2 Three-level CPT/Ramsey solver – time-dependent method.....	159
A.3 16-level CPT solver – steady state solution	162
Appendix B: Multi-Level Hamiltonian and Source Matrix.....	168
Appendix C: Transverse Magnetic Field Interactions.....	171
Appendix D: Energy Level Shift Calculation Using Breit-Rabi Equation.....	177
Appendix E: Push-Pull and $\text{lin}\perp\text{lin}$ Equivalence.....	179
Appendix F: COMSOL Helmholtz Coil Simulation	183
Appendix G: LabVIEW Code	185
Publications	188

LIST OF TABLES

Table 5.1: Experimentally measured CPT characteristics for different polarization schemes ...	111
Table B.1: 16-level non-Hermitian Hamiltonian	169
Table C.1: Landé g-factors for the ground and excited states of D1 line of ^{87}Rb	171

LIST OF FIGURES

Figure 1.1: Block diagram of the atomic clock	4
Figure 1.2: Cs atomic beam frequency standard using separated field Ramsey interference.	5
Figure 1.3: Schematic of an optically-pumped ^{87}Rb vapor cell atomic clock.	7
Figure 1.4: Allan deviation plotted as function of time average, τ for different types of frequency standards.	9
Figure 1.5: Microsemi (Symmetricom) chip scale atomic clock (CSAC) model SA.31m, employing a VCSEL and CPT, using <120 mW @ 25C. The Rb vapor cell is microfabricated. The CSAC has an Allan deviation of $<5 \times 10^{-11}$ at $\tau=1\text{s}$	11
Figure 2.1: Three-level atomic system with two laser fields (a) on resonance and (b) detuned from resonance.	16
Figure 2.2: Diagram illustrating Raman excitation in a three-level Λ -type atomic system using two laser fields with frequencies, ω_1 and ω_2 , respectively. The CPT phenomenon is studied in this atomic system.	20
Figure 2.3: Flow diagram used in finding steady-state solution for studying the CPT phenomenon in a three-level atomic system.	23
Figure 2.4: Plots showing population ρ_{33} of the excited state calculated using the steady-state (solid line), and the time-dependent (circle) simulation models. Excellent match is obtained between the two models under the same excitation conditions.	25
Figure 2.5: Steady-state simulation result showing broadening of CPT linewidth with increase in Rabi frequency. The model considered equal Rabi frequencies $\Omega_1 = \Omega_2$ for the laser fields with $\delta = 0$ and $\gamma = 0$	26
Figure 2.6: Simulation result showing the effect of ground state decoherence on the CPT linewidth under the conditions $\Omega = \Gamma/30$ and $\delta = 0$	27
Figure 2.7: The real part of coherence terms, ρ_{13} and ρ_{23} plotted with parameters $\Omega = \Gamma/30$, $\delta = 0$ and $\gamma = 0$ to show dispersive characteristic of CPT resonance.	28
Figure 2.8: The real part of coherence terms, ρ_{13} and ρ_{23} plotted with parameters $\Omega_1 = \Omega_2 = \Gamma/30$, $\delta = 0$ and $\gamma = 0$. The plots for $\text{Im}(\rho_{13})$ and $\text{Im}(\rho_{23})$ overlap on each other.	29
Figure 2.9: Timing diagram considered in the simulation for generating Ramsey interference.	29

Figure 2.10: Ramsey fringes obtained with the parameters, $\Omega_1 = \Omega_2 = \Gamma/50$, $\tau_c = 500 \mu s$, $T = 1 ms$, and $\tau_q = 1 \mu s$. The central fringe has the expected linewidth $\Delta\nu = 1/2T = 500 Hz$.	32
Figure 2.11: Ramsey interference obtained with the parameters, $\Omega_1 = \Omega_2 = \Gamma/300$, $\tau_c = 200 \mu s$, $T = 1 ms$, and $\tau_q = 1 \mu s$.	34
Figure 2.12: Ramsey fringes obtained with (a) $T = 500 \mu s$, (b) $T = 1 ms$, and (c) $T = 1.5 ms$. The linewidths change with T as $\Delta\nu = 1/2T$.	34
Figure 2.13: TDRI obtained for different values of Δ , as a function of the query pulse duration [52].	35
Figure 3.1: Raman excitation in a multi-level atomic system consisting of all the energy levels in the D1 manifold of ^{87}Rb atoms. For theoretical modeling, the magnetic sublevels in the F-states are designated by a sequence of numbers from one to sixteen.	39
Figure 3.2: Radiative decay channels corresponding to σ^+ , σ^- , and π transitions from $ F' = 1\rangle$ excited state. All of these decays are considered in formulating H_Γ and L matrices.	43
Figure 3.3: Radiative decay channels corresponding to σ^+ , σ^- , and π transitions from $ F' = 2\rangle$ excited state. All of these decays are considered in formulating H_Γ and L matrices.	44
Figure 3.4: Flow diagram for finding steady state and time-dependent solutions to the density-matrix equations representing a sixteen-level atomic system.	45
Figure 3.5: Calculated and normalized CPT resonance showing a close match between the steady-state and time-dependent solutions. The calculation included x -polarized $lin \parallel lin$ excitation resonant with the $ F' = 1\rangle$ state and the following parameters: $B_z = 5 mG$, $\Omega = \Gamma/60$, $\Gamma = 6 MHz$, and $\gamma_1 = \gamma_2 = 0$.	46
Figure 3.6: Splitting of the central CPT resonance formed by $lin \parallel lin$ excitation at higher axial magnetic field. The following parameters were used in the calculation: $\Omega = \Gamma/60$, $\Gamma = 6 MHz$, and $\gamma_1 = \gamma_2 = 0$.	48
Figure 3.7: (a) Raman transitions in $lin \parallel lin$ excitation forming $(-1, +1)$ and $(+1, -1)$ dark states. (b) Raman transitions created by (σ^+, σ^+) or (σ^-, σ^-) excitation, involving the 0-0 dark state.	48
Figure 3.8: CPT spectrum generated by (σ^+, σ^+) polarized light resonant with the $ F' = 2\rangle$ state. The result shows Zeeman CPT resonances formed by the vector magnetic field B used in the calculation with its magnitude $B_z = 20 mG$. The following parameters were used in the calculation: $\Omega = \Gamma/60$, $\Gamma = 6 MHz$, and $\gamma_1 = \gamma_2 = 3 Hz$.	50
Figure 3.9: CPT spectrum generated by (σ^+, σ^+) polarized light resonant with the $ F' = 2\rangle$ state. The result shows Zeeman CPT resonances formed by the vector magnetic field B	

used in the calculation with its magnitude $B = 20$ mG and angle (a) 5° (b) 10° with respect to the direction of beam propagation in the cell. The following parameters were used in the calculation: $\Omega = \Gamma/60$, $\Gamma = 6$ MHz, and $\gamma_1 = \gamma_2 = 3$ Hz.....52

Figure 3.10: Splitting of the central CPT resonance formed by $lin \perp lin$ excitation resonant with (a) $|F' = 1\rangle$ state, and (b) $|F' = 2\rangle$ state at higher axial magnetic field. The following parameters were used in the calculation: $\Omega = \Gamma/60$, $\Gamma = 6$ MHz, and $\gamma_1 = \gamma_2 = 0$53

Figure 3.11: Splitting of Ramsey fringes formed by $lin \parallel lin$ excitation with axial magnetic fields at $B_z =$ (a) 0, (b) 500 mG, and (c) 1000 mG. The following parameters were used in the calculation: $\tau_c = 400$ μ s, $T = 1$ ms, $\tau_q = 100$ ns, $\Omega = \Gamma/60$, $\Gamma = 6$ MHz, and $\gamma_1 = \gamma_2 = 0$ Hz. For the purpose of visualization, the amplitudes are normalized.....55

Figure 3.12: RR interference spectra generated by (σ^+, σ^+) polarized light resonant with the (a) $|F' = 2\rangle$ and (b) $|F' = 1\rangle$ state. This result shows Zeeman RR interference formed with $B_z = 20$ mG. The following parameters were used in the calculation: $\tau_c = 400$ μ s, $T = 1$ ms, $\tau_q = 100$ ns, $\Omega = \Gamma/60$, $\Gamma = 6$ MHz, and $\gamma_1 = \gamma_2 = 500$ Hz. For the purpose of visualization, the amplitudes are normalized and offset.56

Figure 4.1: (a) Raman excitation in a three-level Λ -system formed in the energy levels of ^{87}Rb atoms, and (b) pulse sequence considered in the model for generating RR interference.60

Figure 4.2: Light shift, ϕ_{LS} versus δ calculated using ρ_{33} . Solid lines represent numerically computed values, and dashed lines show analytical values given in eqn. (4.2). The following parameters were used in the calculations: $\tau_c = 200$ μ s, $T = 1$ ms, $\tau_q = 100$ ns, $\Omega_1 = \Omega_2$, $(\rho_{11} - \rho_{22})^0 = 0.2$ and $\gamma = 0$. The encircled region shows the region of light shift suppression.....64

Figure 4.3: Effect of decoherence γ on the light shift, ϕ_{LS} . The following parameters were used in the calculations: $\tau_c = 200$ μ s, $T = 1$ ms, $\tau_q = 100$ ns, $\Omega_1 = \Gamma/5$, $\Omega_2 = 0.75 \Omega_1$, and $(\rho_{11} - \rho_{22})^0 = 0.2$65

Figure 4.4: RR light shift calculated as a function of the average Rabi frequency, Ω , of the CPT pulse. Solid lines show numerical values, and dashed lines show analytical values obtained using eqn. (3). The following parameters were used in the calculations: $\tau_c = 100$ μ s, $T = 1$ ms, $\tau_q = 100$ ns, $\Omega_1 = \Omega_2 = \Omega$, $(\rho_{11} - \rho_{22})^0 = 0.2$ and $\gamma = 0$. For $\delta = 0$, both numerical and analytical results show zero light shift over the entire range of intensity as expected.66

Figure 4.5: Color-coded 3D plot showing light shift, ϕ_{LS} as functions of average detuning, δ and intensity, I of the CPT pulse. Saturation intensity ($I_{\text{sat}} = 3$ mW/cm 2) for a rubidium atom is considered in converting Ω to an intensity axis. The following parameters were used in the calculations: $\tau_c = 100$ μ s, $T = 1$ ms, $\tau_q = 100$ ns, $\Omega_1 = \Omega_2$, $(\rho_{11} - \rho_{22})^0 = 0.2$ and $\gamma = 0$67

Figure 4.6: Phase shifts associated with $\text{Im}(\rho_{13})$, $\text{Im}(\rho_{23})$, and $\text{Im}(\rho_{13} + \rho_{23})$ plotted as a function of δ . Solid lines represent numerical values, and dashed lines show analytical results. The measured phase shifts cancel each other in $\text{Im}\rho_{13} + \rho_{23}$. The following parameters were chosen in this calculation: $\tau_c = 100 \mu\text{s}$, $T = 1 \text{ ms}$, $\tau_q = 100 \text{ ns}$, $\Omega_1 = \Omega_2$, $(\rho_{11} - \rho_{22})^0 = 0.2$ and $\gamma = 0$68

Figure 4.7: Light shift, φ_{LS} versus δ calculated using ρ_{33} . Solid lines represent the numerically computed values from the multi-level model, and dashed lines show the three-level model values. The following parameters were used in the calculations: $\tau_c = 200 \mu\text{s}$, $T = 1 \text{ ms}$, $\tau_q = 100 \text{ ns}$, $\Omega_1 = \Omega_2$, $(\rho_{11} - \rho_{22})^0 = 0.2$ and $\gamma = 0$. A shift of $0.5 \text{ rad} \equiv 80 \text{ Hz}$70

Figure 4.8: RR Light shift calculated as a function of average Rabi frequency, Ω , of the CPT pulse. Dotted lines represent the numerically computed values from the sixteen-level model, and dashed lines show the three-level model values. The following parameters were used in the calculations: $\tau_c = 100 \mu\text{s}$, $T = 1 \text{ ms}$, $\tau_q = 100 \text{ ns}$, $\Omega_1 = \Omega_2$, $(\rho_{11} - \rho_{22})^0 = 0.2$ and $\gamma = 0$71

Figure 4.9: Line-shape of CPT resonance plotted as a function of Δ . Solid lines represent calculated line-shapes using the solutions to steady-state density-matrix equations with and without velocity-averaging, respectively. Filled dots show the match with the computational model using a long CPT pulse, $\tau_c = 2000 \mu\text{s}$, and parameters, $T = \tau_q = 0$, $\delta = 0$, $\Omega_1 = \Omega_2 = \Gamma/5$ and $\gamma = 0$. The resonance dip is normalized to show effective narrowing due to velocity-averaging.73

Figure 4.10: Calculated velocity-averaged CPT resonance showing a close match between the steady-state and time-dependent solutions. This result considers x -polarized $lin \parallel lin$ excitation resonant with the $|F' = 1\rangle$ state and uses the following parameters in the calculation: $B_z = 5 \text{ mG}$, $\Omega_1 = \Omega_2 = \Gamma/60$, $\Gamma = 6 \text{ MHz}$, and $\gamma_1 = \gamma_2 = 0$74

Figure 4.11: Splitting of the central CPT resonance formed by $lin \parallel lin$ excitation at higher axial magnetic field. The following parameters were used in the calculation: $\Omega_1 = \Omega_2 = \Gamma/60$, $\Gamma = 6 \text{ MHz}$, and $\gamma_1 = \gamma_2 = 0$75

Figure 4.12: CPT spectrum generated by (σ^+, σ^+) polarized light resonant with the $|F' = 2\rangle$ state. The result shows Zeeman CPT resonances formed by the vector magnetic field B used in the calculation with its magnitude $B = 20 \text{ mG}$ and angle (a) 0° (b) 5° (c) 10° with respect to the direction of beam propagation in the cell. For the purpose of illustration, the CPT amplitudes in (b) and (c) are doubled and vertically offset to show the small CPT resonances formed by the TMF component of B . The following parameters were used in the calculation: $\Omega_1 = \Omega_2 = \Gamma/60$, $\Gamma = 6 \text{ MHz}$, and $\gamma_1 = \gamma_2 = 3 \text{ Hz}$77

Figure 4.13: Phase shift calculated in a Doppler-broadened medium and plotted as a function of δ . The following parameters were used in this calculation: $\tau\tau_c = 200 \mu\text{s}$, $T = 1 \text{ ms}$, $\tau_q = 100 \text{ ns}$, $\Omega_1 = \Omega_2$, $(\rho_{11} - \rho_{22})^0 = 0.2$, and $\Delta\nu_{\text{Doppler}} \simeq 1 \text{ GHz}$. Phase shifts for two

single-velocity groups ($kv = \pm 0.1\Gamma$ and $\pm 0.5\Gamma$) are also shown in the figure corresponding to the case $\Omega_1 = \Omega_2 = \Gamma/20$.	78
Figure 5.1: Fabry-Perot analyzer scan depicting carrier-to-sideband ratio change with several different DC V_π settings.	81
Figure 5.2: Picture showing EOM housed in an aluminum enclosure with temperature and bias voltage control.	83
Figure 5.3: (top) EOM bias voltage stabilization servo (bottom) Feedback control signal (green/light trace) and error signal (pink/dark trace) used in controlling EOM DC bias for maintaining a fixed carrier-to-sideband ratio.	84
Figure 5.4: Master oscillator, coupler, PLL board, and embedded RF oscillator used in rubidium clock frequency synthesis.	86
Figure 5.5: Picture showing DAVLL system mounted on a small size breadboard.	88
Figure 5.6: Picture showing the experimental setup developed in the lab for CPT atomic clock using the PPOP scheme	90
Figure 5.7: Schematic of the polarization-based Michelson interferometer introduced in the beam path for implementing $lin \perp lin$ (or PPOP) scheme. The path difference between the two arms of the interferometer is set to $\lambda_{hf}/4$ which is approximately 1.1 cm for ^{87}Rb atoms.	90
Figure 5.8: Schematic and picture of μ -metal chamber on pedestal in the beam path.	93
Figure 5.9: Pictures showing Helmholtz coils and small rubidium cell holder.	95
Figure 5.10: Small vapor cell with rubidium visible, accumulated at the bottom.	95
Figure 5.11: Picture showing rubidium cell in holder between Helmholtz coils with heating wire and thermocouple.	96
Figure 5.12: Picture showing phenolic box enclosure around the rubidium cell.	96
Figure 5.13: CPT contrast measured by varying the cell temperature from 40°C to 61°C in steps of one degree Celsius under the temperature lock condition.	97
Figure 5.14: (left) Solenoid with support fins and mounted vapor cell and (right) Vapor cell wrapped in heating wire alongside aluminum foil insulation and plastic disc cell holders.	98
Figure 5.15: CPT spectrum obtained by (σ^-, σ^-) excitation resonant with $ F' = 2\rangle$ state. The spectrum shows peak-like Zeeman CPT resonances.	99

Figure 5.16: Magnetic shield for a large vapor cell, formed from flat sheets and spot welded.	101
Figure 5.17: (left) Custom made magnetic shield with all three layers and (right) Helmholtz coils and large cell with insulation used with the outer shield only.	101
Figure 5.18: General schematic of Ramsey pulses through a vapor cell. Only the short, query pulses contribute to the Ramsey signal.	102
Figure 5.19: General schematic of Ramsey pulses through a vapor cell. Only the short, query pulses contribute to the Ramsey signal.	103
Figure 5.20: Experimental setup developed for the rubidium CPT clock. A single photodetector distributes the optical signal and produces independent control signals for the laser servo and the clock servo. The dashed box around the $\lambda/2$ plate represents the changeable optical element for implementing $lin \parallel lin$ or (σ, σ) polarization schemes.	105
Figure 5.21: CPT resonances showing narrowing with larger beam diameter, where the off resonant sideband produced asymmetry.	107
Figure 5.22: CPT resonances with three different optical powers, with offset amplitude for relative comparison.	108
Figure 5.23: Magnetic field induced splitting of the central CPT resonance (linewidth = 841 Hz, contrast = 7.5%) generated by $lin \parallel lin$ excitation resonant with $ F' = 1\rangle$ state.	108
Figure 5.24: Magnetic field dependencies of (a) the $(+1, -1)$ CPT resonance, shown in right in figure 5.23 and (b) the $(-1, +1)$ CPT resonance, shown in left in figure 5.23. The dashed lines represent the fittings obtained using the Breit-Rabi equation.	109
Figure 5.25: Differentially detected MOR CPT resonance generated by $lin \parallel lin$ excitation. The signal is dispersive which is evident at higher magnetic field.	110
Figure 5.26: CPT spectrum produced by (σ^-, σ^-) excitation resonant with the $ F' = 2\rangle$ state and $B_z \approx 30$ mG. The inset in the figure shows the central CPT resonance produced with linewidth = 1.04 kHz and contrast = 16.7 %.	113
Figure 5.27: CPT spectrum calculated for (σ^-, σ^-) excitation resonant with $ F' = 1\rangle$ (dashed) and $ F' = 2\rangle$ (solid) states. The two CPT spectra are made to overlap by using background subtraction. CPT contrast was estimated prior to background subtraction. Following parameters were used in our calculation: $\Omega_1 = \Omega_2 = \Gamma/60$, $\Gamma = 6$ MHz, $\gamma_1 = \gamma_2 = 3$ Hz and $B_z = 27$ mG.	113
Figure 5.28: Central CPT resonance produced by $lin \perp lin$ excitation resonant with (a) $ F' = 1\rangle$ state (linewidth = 859 Hz, contrast = 7.8 %) and (b) $ F' = 2\rangle$ state (linewidth = 976 Hz, contrast = 19%). The solid lines correspond to Lorentzian fits to the CPT profiles.	114

Figure 5.29: Ramsey interference fringes for two different optical powers	116
Figure 5.30: Central fringe width of Ramsey interference fringes for different free evolution times.....	116
Figure 5.31: CPT and RR interference resonance width (or central fringe width) with optical power (Rabi frequency)	117
Figure 5.32: CPT light shift vs δ measured at two different total optical powers with polynomial line fit.....	118
Figure 5.33: RR interference light shift vs δ measured with two different free evolution times, with polynomial line fit.....	119
Figure 5.34: CPT and RR interference light shift with optical power (Rabi frequency).....	119
Figure 5.35: VCSEL in a TO-86 package, less than half a cm in diameter.....	121
Figure 5.36: VCSEL ILX mount with TEC and thermistor, the VCSEL is connected to the current source.....	121
Figure 5.37: Schematic of the experimental setup used to generate Ramsey interference in the rubidium atomic clock. The optical beam is pulsed using an AOM and a boxcar integrator is used to perform gated detection and sample averaging to produce the Ramsey fringes by repeated query pulses.....	123
Figure 5.38: Timing diagram showing the pulse cycle with (a) a single query pulse, and (b) repeated query pulses for generating Ramsey interference. The pulse cycle in (b) consists of a periodic train of N query pulses q_N of duration τ_q each and separation $T_N = T/N$. A three-level (Λ -type) atomic system shown in (c) has been used to simulate the Ramsey interference phenomena.....	125
Figure 5.39: Experimentally generated Ramsey fringes by using SQT ($N=1$) and total optical power of (a) $57 \mu\text{W}$ and (b) $90 \mu\text{W}$ in the CPT beams. Simulated Ramsey fringes for Ω equals to (c) $\Gamma/200$, and (d) $\Gamma/100$. The following simulation parameters were also used: $\tau_c = 500 \mu\text{s}$, $T = 1.5 \text{ ms}$, $\tau_q = 1 \mu\text{s}$, $\Gamma = 6 \text{ MHz}$, and $\gamma_1 = \gamma_2 = \gamma = 60 \text{ Hz}$	127
Figure 5.40: Experimental Ramsey fringes collected via RQT with (a) $N=3$ (b) $N=5$, and (c) $N=10$ query pulses. The background biases were electronically subtracted and kept equal when measuring the signal contrast.....	130
Figure 5.41: Variation in fringe contrast and amplitude with query pulses, measured experimentally.....	130
Figure 5.42: Simulated Ramsey fringes with (a) $N=3$ (b) $N=5$, and (c) $N=10$ query pulses. The following simulation parameters were used: $\tau_c = 500 \mu\text{s}$, $T = 1.5 \text{ ms}$, $\tau_q = 1 \mu\text{s}$ and $\Omega = \Gamma/200$	131

Figure 5.43: Amplitude enhancement factor for the Ramsey fringes acquired using N query pulses.....	132
Figure 6.1: Dithered CPT signal shown along with the derivative-like error signal generated by the clock servo.	136
Figure 6.2: Allan deviation (or frequency stability) measured, (a) by locking the synthesizer to the CPT resonance, (b) for the unlocked beat note at 10 MHz, and (c) for a chip-scale atomic clock (CSAC).....	139
Figure 6.3: Allan deviation measurement showing the frequency stability of the CPT clock. ..	140
Figure 6.4: Allan deviation measurement showing the effect of modulation amplitude on frequency stability of the CPT clock.	141
Figure 6.5: Frequency stability performance of the rubidium CPT clock measured by ADEV with three: $lin \parallel lin$, (σ^-, σ^-) and $lin \perp lin$ excitations. Dashed line represents $\sigma_y(\tau) = 3.6 \times 10^{-11} \tau^{-1/2}$	142
Figure 6.6: Frequency stability performance of the rubidium atomic clock measured using ADEV for SQT (green squares) and RQT with N=10 (blue circles). The dashed line represents $\sigma_y(\tau) = 5.58 \times 10^{-11} \tau^{-1/2}$	144
Figure F.1: Model of Helmholtz coils with two slices showing magnetic field strength in mG, and arrows showing the vector direction.	183
Figure F.2: Magnetic flux density through the center of the Helmholtz coils.....	184
Figure G.1: LabVIEW front panel. Radio buttons provide selection of N query pulses up to N=15. The top plot displays the integrated Ramsey signal, and the bottom plot displays the optical query pulse signal or the unaveraged boxcar output signal. Controls allow modification of the gate size to optimize input signal usage in the calculation of fringes.	186
Figure G.2: Block diagram showing the digitizer data collection algorithm and calculation of Ramsey fringes for N query pulses.	187

LIST OF ABBREVIATIONS

σ_y	Allan deviation
$R(\Delta)$	Amplitude of Ramsey interference (analytical)
v	Atom velocity
m	Atomic mass
$\Delta\nu$	Atomic resonance linewidth
δ	Average detuning
μ_B	Bohr magneton
k_B	Boltzmann constant
Δf_{buf}	Buffer gas pressure induced frequency shift
ω_c	Carrier (laser) frequency
σ^+, σ^-	Circularly polarized optical transitions
φ_R	Coherence phase in Cs oven
S	Column vector of solutions
δ_{DS}	Common-mode Doppler shift
a, b	Complex amplitude coefficients
τ_c	CPT pulse duration
ℓ	Cs oven interaction region
ρ_{mn}	Density matrix element
d_{ij}	Dipole transition matrix elements
d	Electric dipole transition matrix element
\vec{E}	Electric field of light
m_e	Electron mass
e	Elementary charge
Γ	Excited state decay
g_J	Fine structure Landé g-factor
T	Free evolution time
δ_{bg}, δ_{be}	Ground and excited state Zeeman shifts
γ	Ground state population exchange
V_π	Half-wave voltage in EOM
g_F	Hyperfine Landé g-factor
ω_{hf}	Hyperfine transition frequency (angular)
ν_{hf}	Hyperfine transition frequency (linear)

Δw	Hyperfine transition frequency for ^{87}Rb D1
λ_{hf}	Hyperfine wavelength
α	Interaction term for the CPT pulse
E_1, E_2	Laser electric field amplitudes
ω_1, ω_2	Laser frequencies
θ	Linear polarization angle
B_X, B_Y, B_Z	Magnetic field along x, y, z directions
M	Matrix of density matrix coefficients
ν_{mw}	Microwave field frequency (Cs oven)
H	Modified Hamiltonian
v_p	Most probable velocity of atom
g_I	Nuclear g-factor
N	Number of atoms or levels (Ch. 2)
N	Number of levels (Ch. 3)
N	Number of query pulses (Ch. 5)
$S_{i,j}$	Outer product matrix
φ_{LS}	Phase angle due to light shift
φ	Phase between dark state and light fields
$\varphi_{13}, \varphi_{23}$	Phase shifts of coherence terms
A	Photon absorption
\hbar	Planck constant
ρ^0	Population difference between ground states
Ψ	Product wave function
Q	Quality factor of atomic resonance $\nu_{\text{hf}}/\Delta\nu$
τ_q	Query pulse duration
Ω_1, Ω_2	Rabi frequencies
Ω	Rabi frequency
W	Reduced matrix
B	Reduced vector of matrix elements
T_N	Repeated query time separation
C	Resonance contrast
S/N	Signal to noise ratio
L	Source matrix
c	Speed of light
τ	Time average interval

F	Total atomic angular momentum
J	Total electron angular momentum
I	Total nuclear angular momentum
B_T	Transverse magnetic field
Δ	Two-photon difference detuning
ψ	Wave function
k	Wavevector
Δ_z	Zeeman shift from axial magnetic field

CHAPTER 1: INTRODUCTION

Timekeeping relies on two primary components: an oscillator and a counter. In a clock, the periodic events of an oscillator are counted to measure its frequency, the inverse of which is time. A typical oscillator has a stability that varies between devices and may depend on ambient conditions. Historically, frequency standards have been developed in the form of sundials, pendulum clocks, mechanical escapement clocks, and quartz clocks, to name a few, depending on the technology at the time. These standards may use the periodic properties of the sun, an oscillating weight, or a crystal that vibrates in response to electrical charge. The accuracy of these standards are limited by both their design and the periodic phenomenon upon which they are formed. For increasingly stable frequency measurements, electro-mechanical oscillators are augmented with more reliable oscillators, atoms.

Atomic frequency standards and clocks in use today commonly implement one of two alkali metals, cesium (Cs) or rubidium (Rb). These types of atomic frequency standards are based on the transition frequency between two ground state energy levels in the atoms. If the atoms involved in the process are made free from external perturbations, they can be assumed to be unchanging in space and time, they will never wear out, and can be finely controlled, making them reliable oscillators upon which a frequency standard can be built [1]. Optical and microwave interrogation of these atoms allows for correction of a relatively less stable electronic oscillator for precise timekeeping applications. Atomically referenced crystal oscillators form the basis of all precise timekeeping in the world today.

Several atomic clock technologies of interest began to develop in the 20th century, two of which are atomic beam clocks and atomic vapor clocks. Over the years, clocks have varied in size

and technique depending on the application and physics involved, from tall fountain clocks for fundamental physics tests to chip scale clocks for field applications [2]. With strict size and power requirements for compact clocks, a tradeoff with precision arises, driving the need for new techniques to further improve compact clock technology.

Atomic clocks are ubiquitous in modern day precision communication and navigation applications, none of which could be possible without a standardized time system. The scientific community adopted the stabilized frequency kept by a particular set of atomic clocks as the frequency (and time) standard for the International System of Units. The official definition of 1 second derived from these clocks was agreed upon in 1967 as “the duration of 9,192,631,770 periods of the radiation corresponding to the transition between the two hyperfine levels of the ground state of the ^{133}Cs atom” [3–5]. With this agreement in place, innumerable applications for atomic clocks arose. Ultra-precise clocks lend themselves to fundamental physics research, such as measurements of the physical constants of nature, very long baseline interferometry (VLBI), relativistic effects, and magnetometry [6]. Beyond precise time keeping, applications of atomic clocks also include navigation systems, power distribution networks, and communications networks, typically in compact forms [7,8].

The global positioning systems (GPS) of the world depend on atomic frequency standards for precise location measurements. Highly accurate measurements of distances are calculated from the time interval that an electromagnetic wave takes to reach a GPS receiver from a satellite. Typical GPS navigation requires four satellites sending out timing and location information, from which the receiver computes three position coordinates (latitude, longitude, altitude) and the time difference. The precision required to accurately calculate the distance from the satellites to a ground receiver is attained through the use of atomic clocks on each satellite. GPS-denied zones

are a common occurrence for first responders and in military operations – atomic clocks assist in precise position determination through triangulation.

Other common applications of compact atomic clocks include secure communications, IED jammers, and high-bandwidth communications. Increased precision of reference oscillators enables enhanced bandwidth in communication networks. Further applications are numerous, such as automobile collision avoidance systems (self-driving cars) and underwater timing applications for data-logging [1,9–11].

Small atomic clocks are also being developed for high performance timekeeping applications in ground- and space-based communications and navigation systems [8,12–16]. Using compact components, these clocks can be made smaller and more widespread for a range of new applications not accessible by large clocks. Vapor cell atomic clocks designed using coherent population trapping (CPT) are suitable for such applications, and have been studied in miniaturized forms for a number of years [17–22]. Pulsed CPT vapor cell clocks, currently in development, offer promising improvements upon CPT clocks.

1.1 Atomic clock technology

All atomic clocks (or frequency standards) conform to the following basic functionality. Figure 1.1 shows the basic building blocks and the control system used in designing a precision atomic clock. It consists of a local oscillator (LO) which has a limited frequency stability which causes the LO frequency to drift to a large extent, thus, making it unsuitable for precision measurements or daily consistency. The LO is referenced to the atomic system and placed in a control loop to correct the frequency error caused with respect to the atomic resonance. The clock frequency matching the atomic ground-state hyperfine frequency (6.834 GHz for ^{87}Rb , or 9.192 GHz for ^{133}Cs) is synthesized from the LO and locked to the peak of atomic resonance using an

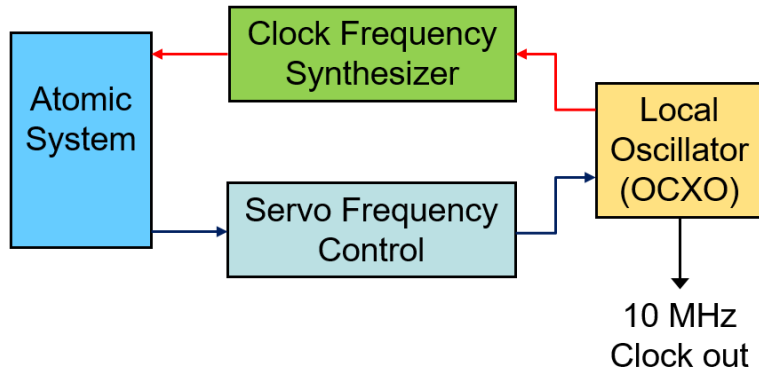


Figure 1.1: Block diagram of the atomic clock

electronic servo. Clock applications often require the clock output to be in a range of 10-100 MHz, so the LO is chosen accordingly and synthesized to match the hyperfine atomic frequency [8]. This constitutes a precision atomic clock. The choice of atomic system depends on the physics of the atomic clock. Separated field Ramsey interference was first studied in atomic beam for clock development, and is discussed next.

1.1.1 Atomic beam and separated field Ramsey interference

Ramsey's invention of the separated oscillatory field method in 1950 provided a method for improving atomic beam clocks by determining the hyperfine transition frequency in atoms with high accuracy [23]. Narrow linewidth interference fringes improve the stability of a beam clock compared with continuous beam excitation, and can be extended to compact clocks using all-optical excitation, while simultaneously overcoming broadening effects and saturation limitation [24]. The first clock was operated in 1955 using microwave excited Ramsey fringes [25] in a Cs atomic beam. Soon after, Cs clocks were constructed as primary frequency standards in many laboratories and industries around the world. The complexity of operation for the Cs clock was later reduced by replacing magnetic state selection with optical pumping. The interrogation

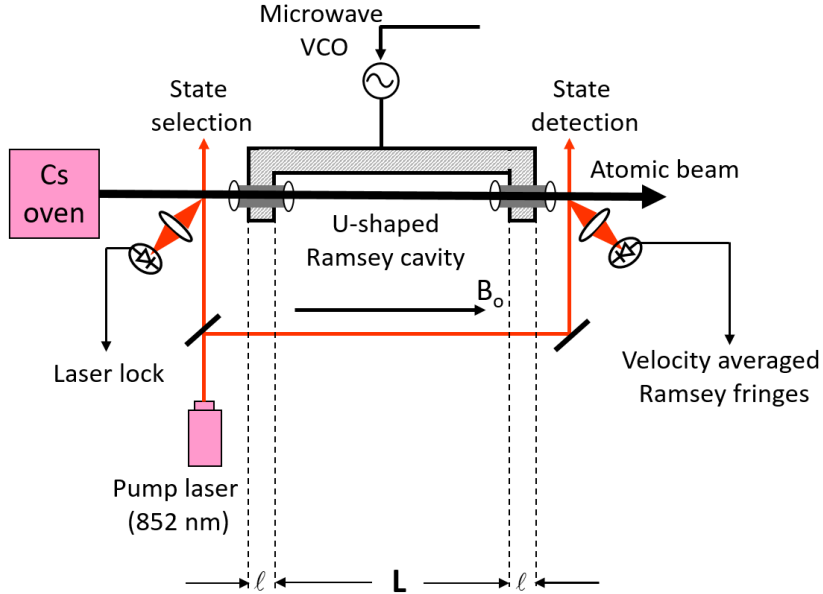


Figure 1.2: Cs atomic beam frequency standard using separated field Ramsey interference.

method in Cs clock uses an atomic beam that interacts with a standing microwave field produced in a microwave Ramsey cavity [26]. As shown in figure 1.2, the atoms generated in Cs-oven travel through an interaction region, ℓ , of the cavity and get exposed to the microwave field for a short period of time. They evolve freely over a distance, L , before entering a second region where they get exposed to the field again. During interaction in the first region, the microwave field whose frequency, ν_{mw} , matches the hyperfine frequency, ν_{hf} , between the ground states in Cs atoms, creates coherence in superposition of the two ground-states. When the atom travels a distance, L , the coherence acquires a phase shift, ϕ_R , which is determined by the hyperfine frequency, ν_{hf} , and the time-of-flight, T , the time the atom takes to travel the distance L . Interaction with the field in the second region causes interference with a condition that depends on the phase difference, ϕ_R , between the field and the coherence. Detuning the frequency, ν_{mw} , away from ν_{hf} changes ϕ_R , and Ramsey fringes (or oscillations) are produced.

In this scheme, Ramsey fringes were detected optically by measuring the population of the ground state in optical fluorescence. Prior to Ramsey interrogation, a laser beam is used at the input to select the atoms in a particular ground-state by optical pumping. The width of fringes observed in this experiment is inversely proportional to the distance, L , or time-of-flight, $T (= L/v)$, between the two arms of the cavity, where v is average velocity of atoms in the beam. In an actual experiment, velocity-averaged Ramsey fringes are observed due to the velocity distribution of atoms. The central fringe corresponding to peak $\Delta (= \nu_{mw} - \nu_{hf})$ equal to zero, is least affected by the velocity averaging. While implementing a Cs frequency standard, the crystal oscillator driving a microwave source is locked to the peak of central fringe using an appropriate modulation technique and feedback control. Design of the two-arm microwave Ramsey cavity poses tight constraint and performance limitations on the clock [27–29]. For example, a small asymmetry in the two cavities at the end of the beam tube by 10^{-4} m can cause large frequency shift of the central fringe by nearly 1 part in 10^{13} . Cavity pulling effect and uniform magnetic field bias (over interaction region) also set the limit on the clock performances. In addition, the cavity volume increases the overall volume and weight of the system. Microwave excited Ramsey method has also been used in laser cooled Cs atoms to build primary frequency standards for applications where volume and weight are not a major concern [30].

1.1.2 Atomic vapor and optically-pumped atomic clocks

Optical pumping in alkali atoms, and microwave resonance methods have been used as standard techniques in early developments of vapor cell clocks [31–33], before the lasers. The energy levels of atoms in the gas phase are mostly unperturbed by environmental factors, so atomic vapor is often chosen for the development of highly stable clocks [8]. The first vapor cell clock

used optical pumping with microwave probes, as described by Kastler in a three-level system [9,34]. Optically-pumped Rb vapor clocks, for example, implement a ^{87}Rb discharge lamp, which outputs two optical lines, separated by the hyperfine frequency of ground states. Because of isotope shift, the transition frequencies of ^{85}Rb have an overlapping component with the discharge lamp. A filter cell of ^{85}Rb after the lamp removes one of the hyperfine lines, leaving a single

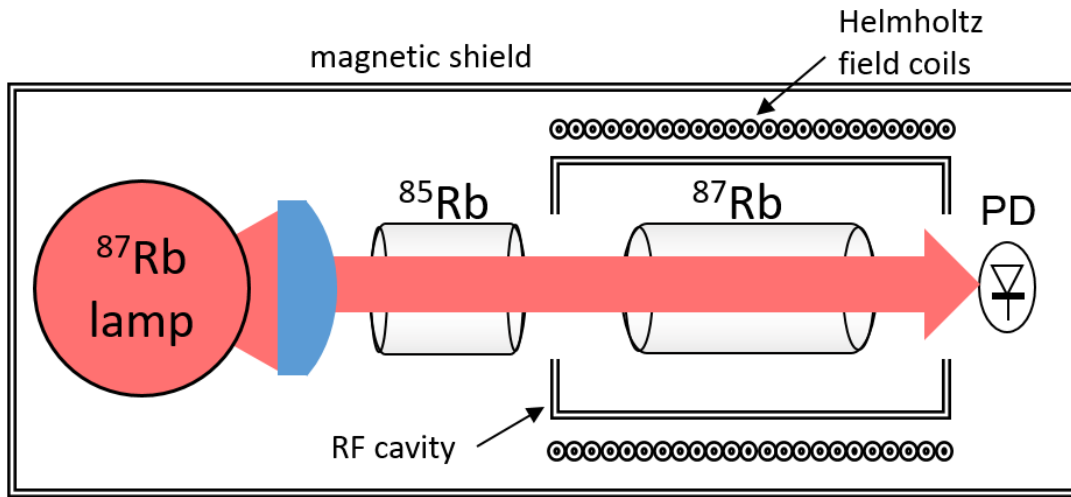


Figure 1.3: Schematic of an optically-pumped ^{87}Rb vapor cell atomic clock.

emission line for optical pumping of a ^{87}Rb cell. The overlap of the spectral lines is improved with buffer gas that induces a shift. A diagram depicting this setup is shown in figure 1.3 [35].

As absorption and re-emission of the pumping light occurs, the ^{87}Rb atoms in the vapor cell are preferentially pumped out of one hyperfine state into the other, which depletes the amount of atoms remaining in the state. The optical intensity rises in this scenario as it is not absorbed or scattered. An applied microwave field induces population transfer between the two hyperfine states, resulting in an equalization of the population, increasing pump light scattering, and a resonance is found as the transmitted intensity drops [2,36]. The microwave field is tuned to that resonance, and the microwave frequency is used to form a clock output.

Moving atoms in vapor cells collide with the cell walls which leads to increased spin-relaxation and decoherence rates, and limits the interaction rate with the optical fields. Inert gases such as nitrogen or neon colliding with the atoms slows the diffusion and increases the interaction time of the atoms with the light. However, a buffer gas pressure and temperature-dependent shift occurs, and the resonance frequency shifts by up to several kHz which becomes sensitive to the cell temperature. This effect can be mitigated by selecting a combination of gases added to the cell which have opposite pressure shifts [32,37–39]. Although, optically-pumped vapor cell atomic clocks can be made compact, the precision of the clock is limited due to the severity of light shift in optical pumping.

During the last few decades, new concepts and technologies have emerged, particularly in developing compact and high-precision atomic clocks using atomic vapor cells [12,40–42]. Narrow laser lines and optical modulation techniques have also paved the way for constructing all-optical frequency standards which do not require microwave cavities to probe the hyperfine resonance. Optical sidebands separated by the hyperfine frequency are now used to create CPT, a narrow resonance, which is used in compact atomic clock development. This study will explore various aspects of CPT resonances formed in the D1 manifold of ^{87}Rb atoms for compact clock development. The following section discusses frequency stability of the atomic clock.

1.1.3 Atomic clock stability

Atomic clock stability is characterized by Allan deviation $\sigma_y(\tau)$ (or Allan variance $\sigma_y^2(\tau)$), which is defined by the fractional frequency stability. While both frequency and phase noise play a role in the frequency stability, frequency noise is discussed here. Many aspects of clocks affect the clock frequency and hence, its stability. Aspects which can be controlled are referred to as

systematic sources of error. These are distinguished from random fluctuations, which are generally uncontrollable [2,8]. For fundamental types of frequency noise, Allan variance has a dependence on time average interval τ in the form of power laws, similar to the noise itself with frequency. The best operating atomic clock should produce a shot-noise limited stability given by

$$\sigma_y(\tau) = \frac{1}{Q} \frac{1}{\text{SNR}} \tau^{-1/2}, \quad (1.1)$$

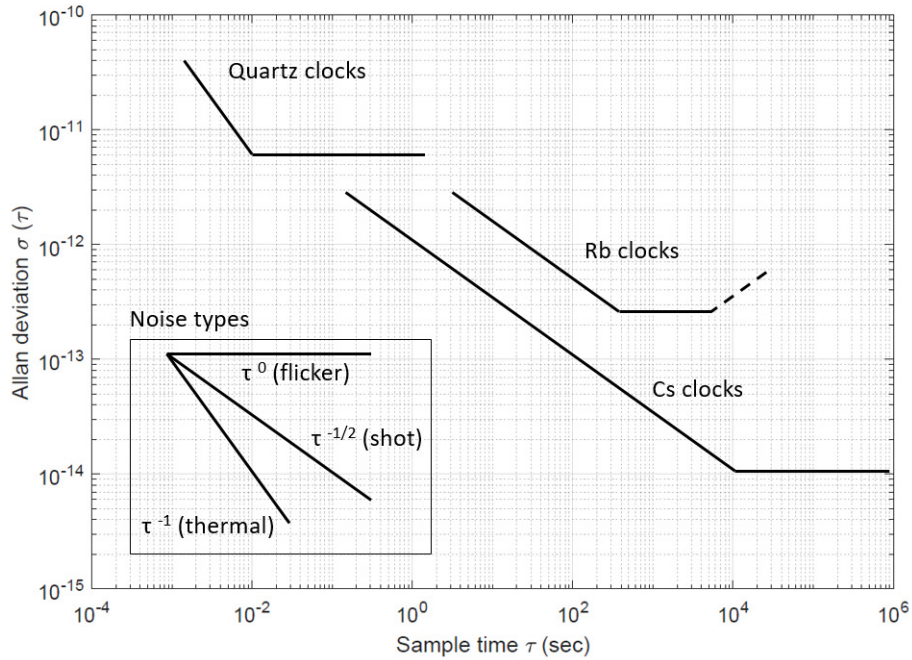


Figure 1.4: Allan deviation plotted as function of time average, τ for different types of frequency standards.

where $Q = \nu_{hf}/\Delta\nu$ represents the quality factor of atomic resonance, and $\text{SNR} = C\sqrt{N}$ where N is the number of photons in the detected beam and C is the contrast of the atomic resonance. As shown in eqn. 1.1, Allan deviation is inversely proportional to ν_{hf} , which pushes precision clock development towards high hyperfine transition frequencies. Fundamental noise sources that appear in clocks include electronic flicker noise ($\sim 1/f$), which affects the stability as τ^0 (i.e. independent of τ). $\sigma_y(\tau)$ flattens out if flicker noise dominates. This produces the “flicker floor” limit in the

stability measurement. Another source is white noise, otherwise known as shot-noise, random fluctuations in the frequency, which dominates after all other sources of noise are minimized to below the shot-noise limit, giving an expected shot-noise limited stability ($\sigma_y \propto \tau^{-1/2}$) [9]. Figure 1.4 inset shows the slope of the noises, with examples of how they might manifest in real atomic clocks. Thermal (or Johnson) noise is nearly white noise for ordinary alkali metal clocks. [2]

The stability of a frequency standard is dependent upon many factors. The most influential factor is the element and method used in the physics package. In figure 1.4, flicker noise dominates the stability of quartz clocks at the short-term time scales, while shot-noise dominates the stability of Cs and Rb standards at longer averaging times until flicker noise takes over. Long term stability is decided by frequency drift in the clock and is proportional to $\tau^{1/2}$. Drift is mostly caused by temperature fluctuations [8]. These characteristics can be used to determine the performance of an atomic clock under test. Limits to the stability can be found, and systematic sources of error can be eliminated [43].

1.2 Miniature atomic clocks

Portable applications require smaller, less expensive, and less power demanding frequency references. While temperature-stabilized crystal oscillators meet some of those requirements, the stability performance is lacking for rigorous applications. Optically-pumped Rb atomic clocks are limited in size due to the size requirement of the microwave cavity and power requirements for the discharge lamp and cell heating. The Rb lamp draws the most power for heating, consuming hundreds of mW. The size bottleneck remains with the microwave cavity, owing to the fact that the microwave wavelength is roughly 4 cm. To minimize the size of a vapor cell clock, the lamp and filter cell must be replaced, and the microwave cavity should be avoided [8].



Figure 1.5: Microsemi (Symmetricom) chip scale atomic clock (CSAC) model SA.31m, employing a VCSEL and CPT, using $<120 \text{ mW @ } 25\text{C}$. The Rb vapor cell is microfabricated. The CSAC has an Allan deviation of $<5 \times 10^{-11}$ at $\tau=1\text{s}$.

Compact clocks are best made with rubidium (Rb) due to the balance of precision, cost, and lower vapor cell heating and pressure requirements. Additionally, Rb is chosen over Cs due to fewer Zeeman sublevels in the ground states involved in the optical excitation [2]. Low power requirements and better performance can be found with Rb because of these characteristics. Similar to microwave cavity clocks, optical pumping can occur between ground states with a directly modulated diode laser to form a CPT resonance. Vertical cavity surface emitting laser (VCSEL) provides a compact light source that allows for direct modulation, to produce optical sidebands separated by a hyperfine transition frequency used in rubidium clocks. Microwave cavities cannot reduce in size below the microwave wavelength so it is challenging to properly miniaturize these types of clocks [8]. CPT is an appropriate choice for miniature vapor cell clocks because of its all-optical excitation. Figure 1.5 shows a commercial example of a chip scale CPT atomic clock constructed using VCSEL and microfabricated Rb cell in a single package.

Typically, in smaller vapor cell, the frequency stability is affected due to increased collision rates of atoms with the cell walls. Additionally, the linewidth of the CPT resonance gets broadened inversely with cell size [8,44]. Buffer gas loading reduces collision, but small vapor cell requires

high buffer gas pressures. The commercial miniaturized CPT clocks attain a short term stability of $\sim 3 \times 10^{-11}$ at $\tau=1$ s and a limited long term stability below 10^{-12} at $\tau=2000$ s [42].

Rb vapor cell clocks including CPT clocks have several challenges which require further development. Factors affecting short-term clock stability beyond the short-term stability of the oscillator are resonance width and signal-to-noise, brought on by buffer gas and optical intensity. The buffer gas mix is a major technical challenge in resonance cells, as well as the frequency dependence of the clock on cell temperature. With improvements in VCSEL technology, some of the issues relating to modulation characteristics of VCSEL can be resolved.

Medium-term stability can be affected by various cell parameters such as temperature drift, and magnetic field variation in the cell environment. Long-term stability is affected by frequency shifts induced by temperature, magnetic field and optical power. It is also limited by light shift which is inherent in atom-field interaction. Although light shift associated with CPT phenomenon is considerably smaller than that with optically-pumped (lamp or laser) atomic clocks, it still causes limitations in attaining the fundamental shot-noise limited performance in the CPT clock.

To mitigate some of the drawbacks associated with miniaturized CPT clock, a variation of CPT, known as pulsed CPT involving pulsed Raman excitations in the time domain was proposed [45]. Ramsey interference is produced by pulsed CPT. This is distinct from the Ramsey interference produced in the atomic beam which was described earlier. Instead of a microwave field, a pulsed frequency modulated laser beam is used to produce Ramsey fringes optically. Rather than separated interaction zones in space, the free evolution time, T , between optical pulses allows the atomic ensemble to evolve freely as in Ramsey method. The width of the measured fringe is given by $1/2T$, which, unlike CPT, is not bound by the optical power [42,45]. This work has extensively studied the properties of CPT and optical Ramsey interference for developing compact,

high-precision atomic clocks. Light shift in Ramsey interference has been investigated to show that it can be highly reduced (or suppressed) for achieving high frequency stability in the Raman clock.

CHAPTER 2: THREE-LEVEL Λ -SYSTEM MODELING

Theoretical simulation of three-level atomic systems provides a fundamental framework for studying CPT and Ramsey interference. This chapter demonstrates a starting point for describing the behavior of the atomic system. The following builds a three-level Λ -system and characterizes CPT and Ramsey interference, which can laser incorporate real parameters of the atomic system.

Atomic absorption of light in a two-level system provides the basis for description of interaction between light and matter. Three-level atomic systems are used to model many different phenomena, including CPT, and are formed in three primary ways: ladder-type, v-type, and Λ -type systems, based on the appearance of the optical transitions with the atomic states. The transitions necessary to form CPT in a Λ -system can be described as an idealized three-level system, which is the system first used in this discussion [46].

To form CPT, two coupling fields are tuned to have a frequency difference which matches that of the frequency separation of ground states in a Λ -system. Under such a condition, the atoms become trapped in a particular superposition of the two ground states such that the light is decoupled from the excited states. The atoms prepared in this superposition state are then no longer able to absorb light; therefore, this superposition state is called a ‘dark state’. If all the atoms in the medium are prepared in the ‘dark state’, the absorption probability is zero, and the light fully passes through the transparent medium. CPT is typically formed with equal optical intensity (or Rabi frequency) for each contributing laser field in the Λ -system. This section describes the theoretical framework developed for investigating CPT formed with continuous excitation and pulsed excitation which leads to the Ramsey interference effect in a three-level atomic system.

2.1 CPT in a three-level Λ -system

Coherent Population Trapping can produce atomic resonance with sub-natural linewidth. Due to its simplicity of generation and small linewidth feature, it is considered promising for atomic clock development, particularly for miniaturized atomic clock technology. Since CPT is formed by preparing the atoms in a non-absorbing dark state, it is less susceptible to energy-level shifts caused by perturbations from the light that generates the state. Due to the long life-time of the hyperfine ground-states in alkali atoms, the dark state does not decohere until perturbed by external influences such as collisions. The following sections describe the quantum-mechanical origin of the dark state and how the CPT phenomenon is modeled from the semi-classical density-matrix equations for light-matter interaction.

2.1.1 Dark state formation

The quantum-mechanical description of CPT relies on calculating the probability amplitude of photon absorption for each frequency of the bichromatic laser field in the superposition of ground states. Figure 2.1 shows two three-level Λ -systems, for the case (a) where both fields are at the one-photon resonance for their frequency, and the case (b) where they are off-resonant.

The condition for two-photon Raman resonance is given by

$$\Delta = (\omega_1 - \omega_2) - \omega_{hf} = 0 \quad (2.1)$$

where ω_1 and ω_2 are the laser frequencies corresponding to $(1 \rightarrow 3)$ and $(2 \rightarrow 3)$ transitions, respectively, and ω_{hf} is the hyperfine frequency separation between the two ground states. To describe the dark state, consider the state $|\psi\rangle$ as a superposition of ground states $|1\rangle$ and $|2\rangle$

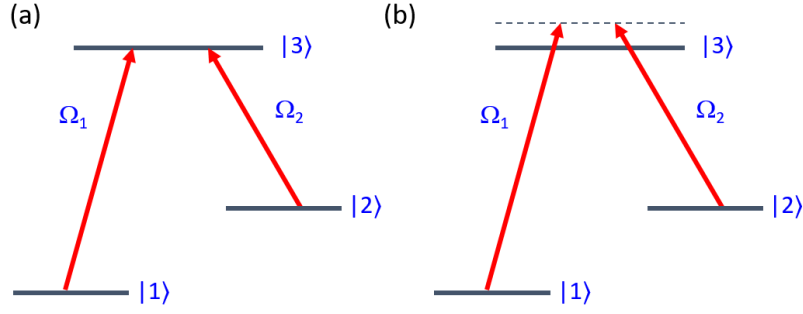


Figure 2.1: Three-level atomic system with two laser fields (a) on resonance and (b) detuned from resonance

$$|\psi\rangle = a|1\rangle + b|2\rangle \quad (2.2)$$

where a and b are complex amplitude coefficients [47]. The probability amplitude of photon absorption A between $|\psi\rangle$ and the excited state $|3\rangle$ is proportional to the expectation value of $(\vec{d} \cdot \vec{E})$ between these two states and is given by

$$\begin{aligned} A &\propto \langle 3 | \vec{d} \cdot \vec{E} | \psi \rangle = a \langle 3 | d | 1 \rangle E_1 + b \langle 3 | d | 2 \rangle E_2 \\ &\Rightarrow A \propto (a d_{13} E_1 + b d_{23} E_2) \end{aligned} \quad (2.3)$$

where d_{ij} is the dipole transition matrix element defining the strength of the atomic transition ($i \rightarrow j$), and $E_{1,2}$ are the amplitudes of the laser electric fields. The Rabi frequencies of the laser fields are defined as

$$\Omega_1 = \frac{d_{13} \cdot E_1}{\hbar} \quad \Omega_2 = \frac{d_{23} \cdot E_2}{\hbar} \quad (2.4)$$

The amplitude, A , vanishes when

$$a d_{13} E_1 = -b d_{23} E_2 \quad (2.5)$$

which along with eqn. (2.4) implies,

$$b = -\frac{d_{13} E_1}{d_{23} E_2} a = -\frac{\Omega_1}{\Omega_2} a \quad (2.6)$$

and so the dark superposition state $|\psi\rangle$ becomes

$$\begin{aligned} |\psi\rangle &= a|1\rangle + -\frac{\Omega_1}{\Omega_2} a|2\rangle \\ \Rightarrow |\psi\rangle &= \frac{a}{\Omega_2} (\Omega_2|1\rangle - \Omega_1|2\rangle) \end{aligned} \quad (2.7)$$

and with normalization, $\langle\psi|\psi\rangle = 1$,

$$\begin{aligned} \Rightarrow \frac{a^2}{\Omega_2^2} (\Omega_2^2 \langle 1|1\rangle + \Omega_1^2 \langle 2|2\rangle) &= 1 \\ \Rightarrow a &= \frac{\Omega_2}{\sqrt{\Omega_1^2 + \Omega_2^2}} \end{aligned} \quad (2.8)$$

This gives the dark state:

$$|\psi_{dark}\rangle = \frac{\Omega_2|1\rangle - \Omega_1|2\rangle}{\sqrt{\Omega_1^2 + \Omega_2^2}} \quad (2.9)$$

The bright state, $|\psi_{bright}\rangle = (\Omega_2|1\rangle + \Omega_1|2\rangle) / (\Omega_1^2 + \Omega_2^2)^{1/2}$, is orthogonal to $|\psi_{dark}\rangle$ such that $\langle\psi_{bright}|\psi_{dark}\rangle = 0$. While $|\psi_{dark}\rangle$ is decoupled to $|3\rangle$, $|\psi_{bright}\rangle$ is coupled to $|3\rangle$. When the atoms are in $|\psi_{dark}\rangle$, they do not interact with either laser field. In the atomic system, the atoms are prepared in the dark state not directly by laser interaction but through spontaneous emission from the excited state. Consider a group of atoms initially in $|1\rangle$, and the laser light is turned on. The atoms can be initially considered to be in a superposition of dark and bright states, defined as

$$|1\rangle = \frac{\Omega_2}{\sqrt{\Omega_1^2 + \Omega_2^2}} |\psi\rangle_{dark} + \frac{\Omega_1}{\sqrt{\Omega_1^2 + \Omega_2^2}} |\psi\rangle_{bright} \quad (2.10a)$$

$$|2\rangle = \frac{\Omega_2}{\sqrt{\Omega_1^2 + \Omega_2^2}} |\psi\rangle_{bright} - \frac{\Omega_1}{\sqrt{\Omega_1^2 + \Omega_2^2}} |\psi\rangle_{dark} \quad (2.10b)$$

The dark component of $|1\rangle$ does not interact with the light but the bright component does. The laser light excites the atom to $|3\rangle$, increasing the population of the state $|2\rangle$. Spontaneous emission of the

excited atoms results in a decay to the $|\psi_{dark}\rangle$ or $|\psi_{bright}\rangle$ of either $|1\rangle$ or $|2\rangle$. Because atoms are not excited from $|\psi_{dark}\rangle$, eventually all the atoms are prepared in $|\psi_{dark}\rangle$. Thus, the dark state is created in a three-level system by optical pumping. Ideally, when the dark state is formed, the atom is decoupled from the laser light and thus, not subjected to light shift. The dark state can also be formed when the laser fields are off-resonant with respect to the single photon resonances as shown in figure 2.1(b). However, in this case, the CPT resonance can be shifted due to the light shift produced by the average detuning of the laser fields.

2.1.2 CPT phenomenon

The coherent population trapping phenomenon has gained significant interest in the development of miniaturized atomic clocks. For this application, achieving high contrast and narrow linewidth in CPT resonance are the two most important factors. Although the previous discussion gave an intuitive explanation for CPT due to the existence of the dark state, it fails to provide other details such as lineshape, linewidth, and the light shift associated with CPT, which are important for atomic clock development. Alkali atoms in which the CPT phenomenon is commonly observed, have multiple energy levels. For simplicity, a density-matrix model involving only three energy levels was developed to investigate various characteristics of CPT resonance. It is discussed in the following section.

2.2 Density matrix

Generally, the density matrix is used to describe the quantum properties of an ensemble of atoms. While Schrödinger's wave function description describes an ensemble that is only fully coherent, the density matrix can describe both partially coherent and incoherent ensembles formed by coherent and incoherent interactions [47]. With density matrix formulation, the ensemble

averaged density matrix, which can contain a mix of coherence states, can be calculated. It can be shown that a mixed state of the ensemble $|\Psi\rangle = \prod_{i=1}^N |\psi^{(i)}\rangle$ is the product of wave function $|\psi^{(i)}\rangle$ for an individual atom in the ensemble, where each wave function $|\psi^{(i)}\rangle$ is described as the superposition of atomic states (represented as $|m\rangle$) as [47]

$$|\psi^{(i)}(t)\rangle = \sum c_m^{(i)}(t) |m\rangle \quad (2.11)$$

The $|m\rangle$ states form an orthonormal basis for the system. The same result is produced by the density matrix element

$$\rho_{mn}^{(i)} = c_m^{(i)}(t) c_n^{(i)}(t)^* \quad (2.12)$$

which contains all necessary information in the wave function $|\psi^{(i)}\rangle$ of the atom to describe its interaction with light. Because the system is typically an ensemble of atoms instead of single atom, one can define the ensemble-averaged density matrix element

$$\rho_{mn} = \frac{1}{N} \sum_{i=1}^N \rho_{mn}^{(i)} \quad (2.13)$$

to describe the average property of the ensemble instead of keeping track of individual quantum states of the atoms in the product state $|\Psi\rangle$. The diagonal terms of the density matrix (ρ_{mm}) describe the population of the atomic states and the off-diagonal terms (ρ_{mn} , $m \neq n$) describe the degree of the coherence between the states $|m\rangle$ and $|n\rangle$.

The time evolution of the density matrix is given by the Liouville equation which is of the form,

$$\frac{\partial \rho}{\partial t} = -\frac{i}{\hbar} [H\rho - \rho H^\dagger] + \dot{\rho}_{src} \quad (2.14)$$

where H is the modified Hamiltonian of the system which is time-independent and non-Hermitian, and $\dot{\rho}_{src}$ accounts for the influx of atoms into the atomic state due to decay from another atomic state.

Figure 2.2 shows a three-level Λ -type atomic system with Raman excitation created by two laser frequencies which are separated by a hyperfine transition frequency, ω_{hf} , between the ground states $|1\rangle$ and $|2\rangle$. The three-level model is considered here to develop a useful physical insight into CPT phenomenon and its properties. The atomic system interacting with laser light is described by the Hamiltonian, H , that consists of both energy and interaction terms. Generally, H is time-dependent. The time-independent form of the Hamiltonian, H can be obtained by applying

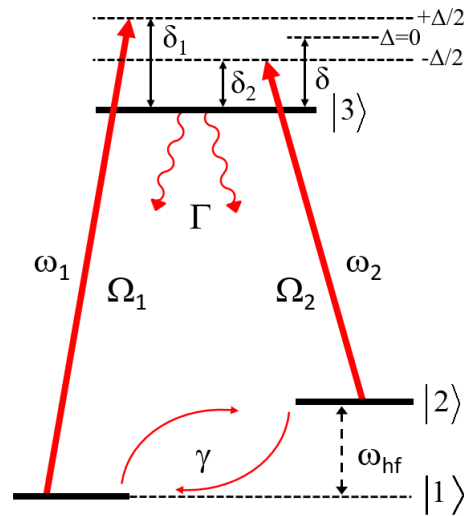


Figure 2.2: Diagram illustrating Raman excitation in a three-level Λ -type atomic system using two laser fields with frequencies, ω_1 and ω_2 , respectively. The CPT phenomenon is studied in this atomic system.

the rotating wave approximation (RWA) and rotating wave transformation (RWT). One can also write the time-independent H by inspection from figure 2.2 without deriving it by applying RWA and RWT as follows [5]:

$$H = \hbar \begin{bmatrix} \frac{\Delta}{2} - \frac{i\gamma}{2} & 0 & -\frac{\Omega_1}{2} \\ 0 & -\frac{\Delta}{2} - \frac{i\gamma}{2} & -\frac{\Omega_2}{2} \\ -\frac{\Omega_1}{2} & -\frac{\Omega_2}{2} & -\delta - \frac{i\Gamma}{2} \end{bmatrix} \quad (2.15)$$

where the diagonal terms of the H matrix are defined in terms of the difference detuning, Δ and the average detuning, δ of the laser frequencies. These detunings can be redefined as $\Delta = (\delta_1 - \delta_2)$ and $\delta = (\delta_1 + \delta_2)/2$ where δ_1 and δ_2 correspond to the single-photon detuning of the two laser fields as shown in figure 2.2. The non-zero off-diagonal terms define the coupling between the states with Rabi frequencies, Ω_1 and Ω_2 . The decay of the amplitudes of the excited state, $|3\rangle$, at the rate $\frac{\Gamma}{2}$, and the two ground states, $|1\rangle$ and $|2\rangle$, each at rate $\frac{\gamma}{2}$, are taken into account by adding complex terms to the diagonal elements of the modified Hamiltonian, H , in eqn. (2.15). This also makes the modified Hamiltonian, H , non-Hermitian. The $\dot{\rho}_{src}$ matrix in eqn. (2.14) is defined as

$$\dot{\rho}_{src} = \begin{bmatrix} \frac{\Gamma}{2}\rho_{33} + \gamma\rho_{22} & 0 & 0 \\ 0 & \frac{\Gamma}{2}\rho_{33} + \gamma\rho_{11} & 0 \\ 0 & 0 & 0 \end{bmatrix} \quad (2.16)$$

The two non-zero diagonal terms in the $\dot{\rho}_{src}$ matrix correspond to the influx of atomic population into the ground states $|1\rangle$ and $|2\rangle$ due to decay (at rate Γ) from the excited state $|3\rangle$ and population exchange (at rate γ) from each ground state. It is assumed that the population of the excited state decays at the same rate $\Gamma/2$ from $|3\rangle$ to $|1\rangle$ and from $|3\rangle$ to $|2\rangle$. This approach of formulating the Hamiltonian, H , and the $\dot{\rho}_{src}$ matrix is generic, and has been used, later, in the next chapter to find H and $\dot{\rho}_{src}$ for a multi-level atomic system representing the energy states of D1 line in ^{87}Rb atoms.

The time-evolution of the three-level system is governed by a set of density-matrix equations which are obtained by substituting H and the $\dot{\rho}_{src}$ in eqn. (2.17) as follows:

$$\begin{aligned}
\dot{\rho}_{11} &= -\left(i\frac{\Omega_1}{2}\rho_{13} + c.c\right) + \frac{\Gamma}{2}\rho_{33} - \gamma(\rho_{11} - \rho_{22}) \\
\dot{\rho}_{22} &= -\left(i\frac{\Omega_2}{2}\rho_{23} + c.c\right) + \frac{\Gamma}{2}\rho_{33} + \gamma(\rho_{11} - \rho_{22}) \\
\dot{\rho}_{33} &= \left(i\frac{\Omega_1}{2}\rho_{13} + c.c\right) + \left(i\frac{\Omega_2}{2}\rho_{23} + c.c\right) - \Gamma\rho_{33} \\
\dot{\rho}_{13} &= -i\frac{\Omega_1}{2}(\rho_{11} - \rho_{33}) - i\frac{\Omega_2}{2}\rho_{12} - \left(\frac{\Gamma}{2} + \frac{\gamma}{2} + i\left(\delta + \frac{\Delta}{2}\right)\right)\rho_{13} \\
\dot{\rho}_{23} &= -i\frac{\Omega_2}{2}(\rho_{22} - \rho_{33}) - i\frac{\Omega_1}{2}\rho_{21} - \left(\frac{\Gamma}{2} + \frac{\gamma}{2} + i\left(\delta - \frac{\Delta}{2}\right)\right)\rho_{23} \\
\dot{\rho}_{12} &= i\frac{\Omega_1}{2}\rho_{32} - i\frac{\Omega_2}{2}\rho_{13} - (\gamma + i\Delta)\rho_{12}
\end{aligned} \tag{2.17}$$

where ρ_{ii} and ρ_{ij} ($i, j = 1, 2, 3$) are density-matrix elements that correspond to atomic population and coherence between the energy-levels, respectively, and $\sum_{i=1}^3 \rho_{ii}$ is constant for a closed system and $c.c$ indicates complex conjugate. The CPT phenomenon is studied by solving the density matrix equations in eqn. (2.17) for the three-level system. Two different computational models are developed for solving these equations. The steady-state model assumes that the atomic system reaches the steady-state condition in interaction. In this model, the time derivatives of all the density matrix elements, $\dot{\rho}_{ij}$, the terms on the left hand side of eqn. (2.17), are set equal to zero. On the other hand, the time-dependent model does not assume the steady-state condition and rigorously solves the density matrix equations in eqn. (2.17) using a numerical method. The time-dependent model gives the flexibility to study CPT under non-steady-state conditions, such as under pulsed excitations, discussed later in this chapter.

Under the steady-state condition, a system of linear and time-dependent equations for the density-matrix elements ρ_{ij} are obtained by setting $\dot{\rho}_{ij}$ in eqn. (2.17) to zero. This system of equations [6] is cast in a matrix-vector form $M\vec{\rho} = 0$, where ρ is a vector consisting of 9 density matrix elements ρ_{ij} (square of the number of levels, $N=3$ in the system) and M is an $(N^2 \times N^2)$ or (9×9) matrix consisting of the coefficients of ρ_{ij} gathered from this system of equations. Using the condition $\sum_{i=1}^3 \rho_{ii} = 1$ for a closed atomic system, one of the first three equations in eqn. (2.17) becomes redundant and the steady-state matrix-vector form $M\vec{\rho} = 0$ is algorithmically reduced to the form $WB = -S$ where matrix W is of reduced dimension $(N^2-1) \times (N^2-1)$ or (8×8) , B is a

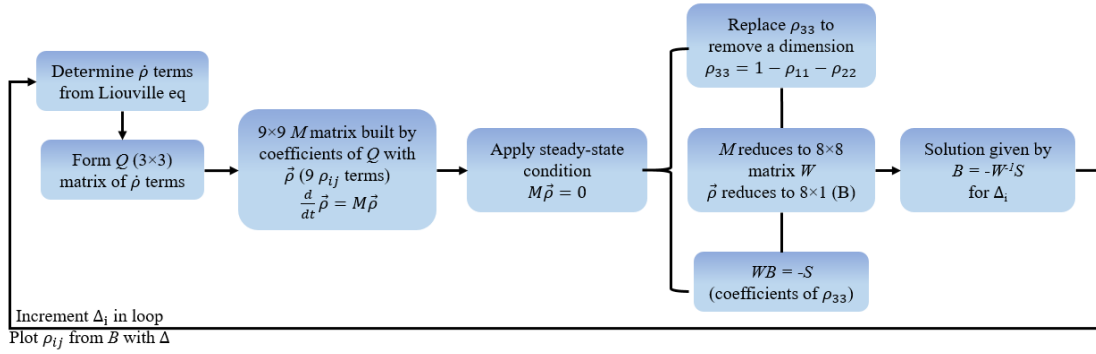


Figure 2.3: Flow diagram used in finding steady-state solution for studying the CPT phenomenon in a three-level atomic system.

vector of only $(N-1) = 8$ density matrix elements ρ_{ij} , and S is a non-zero $(N-1) = 8$ element column vector consisting of $[M_{19}, M_{29}, M_{39}, \dots, M_{89}]^T$. The solutions for the density matrix elements ρ_{ij} are obtained by finding $W^{-1}S$. The CPT spectrum is generated by finding the solutions for ρ_{ij} while choosing different values of the difference detuning, Δ , of the laser fields around the two-photon resonance condition $\Delta = 0$. The following figure 2.3 shows the flow diagram used in the algorithm for calculating the solutions.

In case of the time-dependent model, the solutions for density matrix elements ρ_{ij} are obtained by numerically solving the time-dependent density matrix equations given in eqn. (2.17). The solutions are expressed in terms of a linear combination of the eigenvalues and eigenvectors of the M matrix without reducing its dimension. To verify the accuracy of the time-independent model, the CPT spectrum is obtained by considering excitation with a long CPT ‘pulse’ (i.e. the pulse duration is long enough to ensure reaching the steady-state condition due to interaction with the CPT pulse) and matched with the CPT spectrum calculated using the steady-state model described earlier. Results obtained from both of the models agree very well.

2.3 CPT simulation results

Figure 2.4 shows the plot of the population ρ_{33} of the excited state as a function of the normalized difference detuning Δ/Γ , which is produced using the steady-state (solid line in the figure) and the time-dependent (dots in the figure) simulation models. The MATLAB codes for these simulation models are presented in appendix A. The dip observed at the center of ρ_{33} shows the CPT phenomenon. The value of ρ_{33} gives a measure of atomic fluorescence and shows excellent agreement for both models. The parameters used in this calculation are $\Omega_1 = \Omega_2 = \Omega = \Gamma/2$, $\delta = 0$ and $\gamma = 0$. In the case of the time-dependent model, ρ_{33} is calculated by considering excitation with a sufficiently long CPT pulse with duration $\tau = 1$ second. Due to strong interaction (i.e. large Rabi frequencies of the laser fields), the value of ρ_{33} at the center of the CPT resonance (i.e. $\Delta = 0$) is found to be close to zero indicating zero atomic fluorescence. As seen in figure 2.4, the CPT dip is formed in the middle of the absorption spectrum as expected. The CPT spectrum can also be plotted using other density matrix elements such as the coherence elements i.e. ρ_{13} , ρ_{23} or $(\rho_{13} + \rho_{23})$.

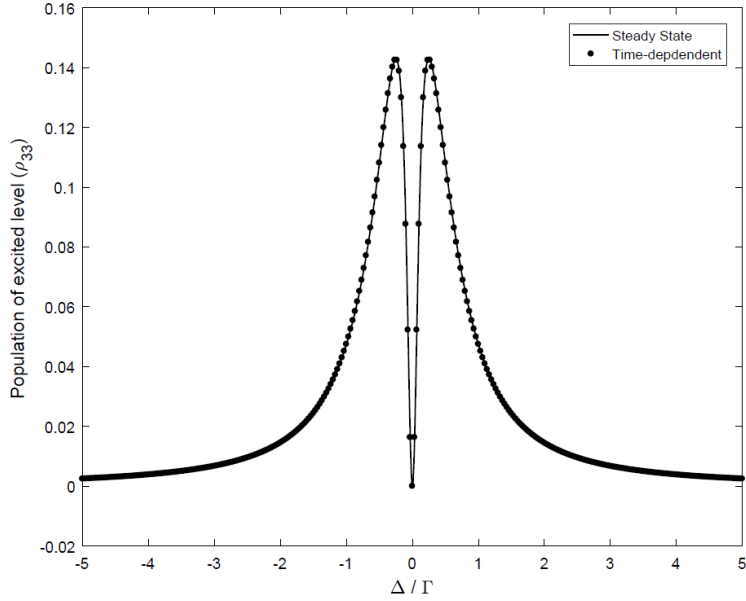


Figure 2.4: Plots showing population ρ_{33} of the excited state calculated using the steady-state (solid line), and the time-dependent (circle) simulation models. Excellent match is obtained between the two models under the same excitation conditions.

Typically, the CPT spectrum in experiment is observed in the transmission of laser light through a vapor medium. Instead of the dip in absorption as seen in figure 2.5, an inverse profile that is a peak in transmission is observed as the atoms entering the dark state cease to absorb the light. In the simulation, this is reflected in the plot of $(1 - \rho_{33})$ instead of ρ_{33} .

Figure 2.5 shows the plots of $(1 - \rho_{33})$ for a small range of Δ/Γ depicting the change in CPT linewidth with increased Rabi frequency from $\Omega = \Gamma/30$ to $\Gamma/10$. The steady-state simulation is used to create these plots. The amplitude $(1 - \rho_{33})$ of the CPT resonance in normalized for observing the effect of increasing Rabi frequency (or optical power) on the CPT linewidth.

The effect of exchange of population and decoherence between the two ground-states on the linewidth of CPT resonance has also been studied through simulation by incorporating a finite decoherence rate, γ in the density matrix equations described earlier in eqn. (2.17). Figure 2.6

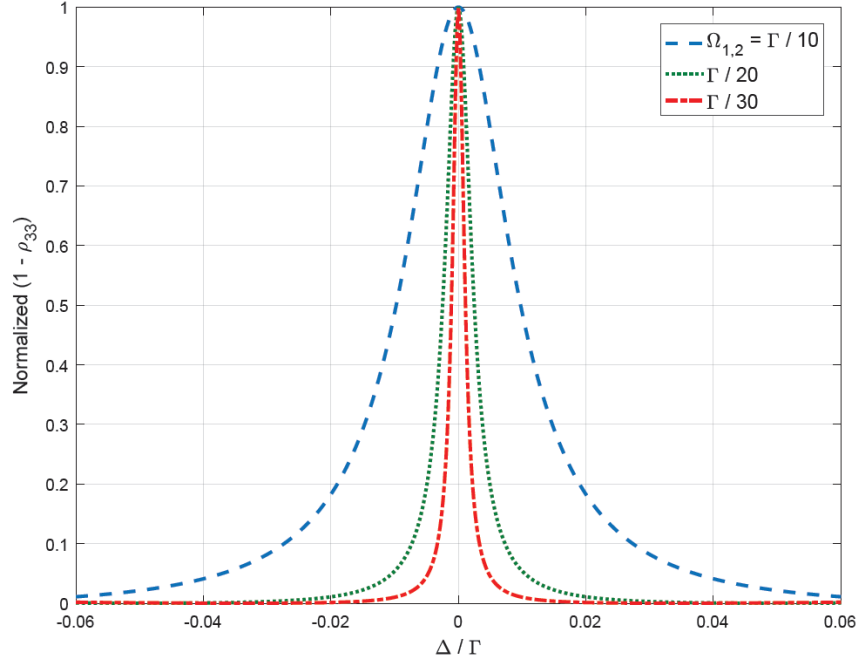


Figure 2.5: Steady-state simulation result showing broadening of CPT linewidth with increase in Rabi frequency. The model considered equal Rabi frequencies $\Omega_1 = \Omega_2$ for the laser fields with $\delta = 0$ and $\gamma = 0$.

shows the effect of decoherence γ on CPT. For the Rabi frequency $\Omega = \Gamma/30$, choosing a non-zero value of γ causes a reduction in the CPT amplitude. The CPT linewidth $\Delta\nu$ is also found to be broadened and limited by γ . As illustrated earlier in figure 2.5, the CPT linewidth primarily depends on the average Rabi frequency, $\Omega = \sqrt{(\Omega_1^2 + \Omega_2^2)}/2$, and therefore gets broadened by Ω . In fact, one can obtain rigorous solutions to the density matrix equations in eqn. (2.17) under the steady-state condition to get an analytic expression for ρ_{33} as

$$\rho_{33} = \frac{\Omega^2}{\Gamma^2} \frac{\Delta^2}{\Delta^2 + \left(\frac{\Omega^2}{\Gamma}\right)^2} \quad (2.18)$$

where it is assumed that $\Omega_1 = \Omega_2 = \Omega$, and $\delta = 0$ and also considers that $\Omega \ll \Gamma$ and $|\Delta| \ll (\Omega, \Gamma)$.

This expression suggests that the CPT resonance has a Lorentzian lineshape with a linewidth $\Delta\nu =$

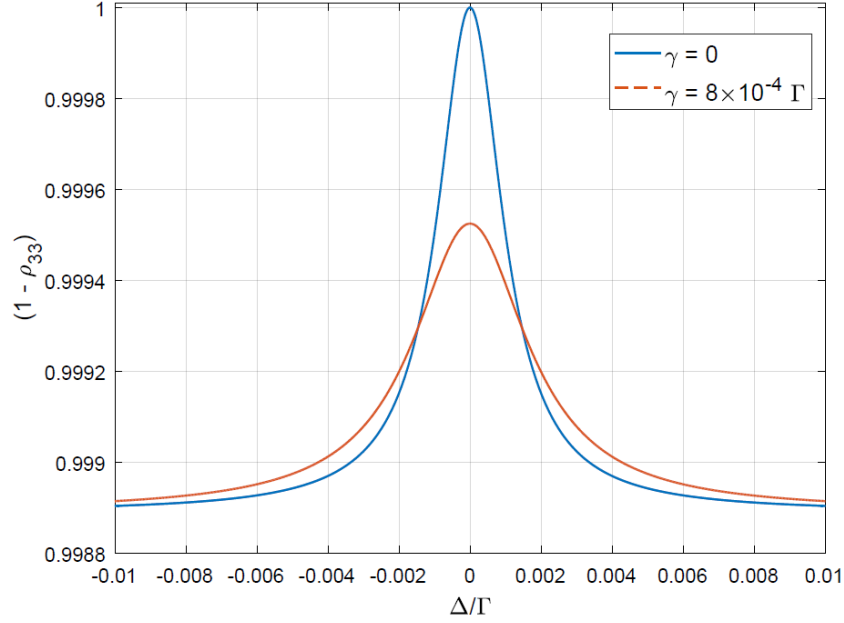


Figure 2.6: Simulation result showing the effect of ground state decoherence on the CPT linewidth under the conditions $\Omega = \Gamma/30$ and $\delta = 0$.

Ω^2/Γ . For $\Omega \ll \Gamma$, this linewidth can be very small. The CPT linewidth is broadened by Ω^2 which is proportional to the total optical power in the laser fields. The linewidths of all simulated CPT plots shown in figure 2.5 match closely with the linewidth predicted from eqn. (2.18). For example, in the case $\Omega = \Gamma/10$, the CPT linewidth will correspond to $\Delta\nu = \Omega^2/\Gamma = \Gamma/100 = (0.01)\Gamma$ which agrees with the simulation result. For a non-zero value of decoherence γ , the linewidth of CPT resonance [3] is modified as [42]

$$\Delta\nu = \gamma + \frac{\Omega^2}{\Gamma} \quad (2.19)$$

which includes the broadening due to γ . This is also consistent with the simulation result shown in figure 2.6 to illustrate the effect of γ . Decoherence is caused by collisions between atoms, and collisions of atoms with the walls in the vapor cell. Furthermore, broadening of CPT linewidth can also be caused by the transit-time of the atoms across the optical beam. This is generally prevented

by expanding the optical beam and adding inert buffer gas to the cell which effectively slows the diffusion of atoms due to frequent collisions of these atoms with the buffer gas atoms.

Figure 2.7 shows the CPT phenomenon observed in plotting the real parts of the coherence terms ρ_{13} and ρ_{23} . These real parts relate to the index of refraction, and show the dispersive characteristic of CPT resonance around $\Delta = 0$. The terms $Re(\rho_{13})$ and $Re(\rho_{23})$ also show opposite dispersion characteristics. Similarly, the imaginary parts of the coherence terms ρ_{13} and ρ_{23} are shown in figure 2.8. The terms $Im(\rho_{13})$ and $Im(\rho_{23})$ relate to the transmission of the light in the medium and, therefore, produce peak-like CPT lineshapes, similar to the one produced by the term $(1 - \rho_{33})$. For equal Rabi frequencies $\Omega_1 = \Omega_2 = \Gamma/30$, the terms $Im(\rho_{13})$ and $Im(\rho_{23})$ have the exact same values and therefore, figure 2.8 shows overlapping plots for $Im(\rho_{13})$ and $Im(\rho_{23})$.

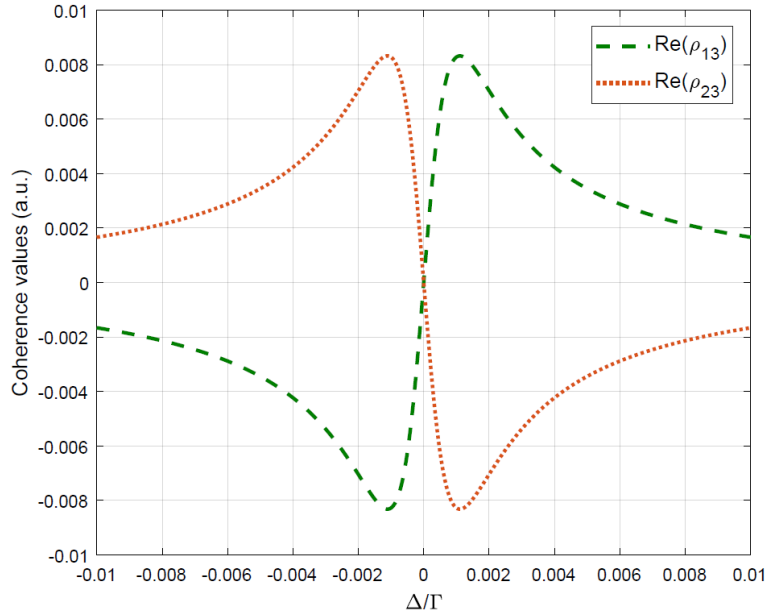


Figure 2.7: The real part of coherence terms, ρ_{13} and ρ_{23} plotted with parameters $\Omega = \Gamma/30$, $\delta = 0$ and $\gamma = 0$ to show dispersive characteristic of CPT resonance.

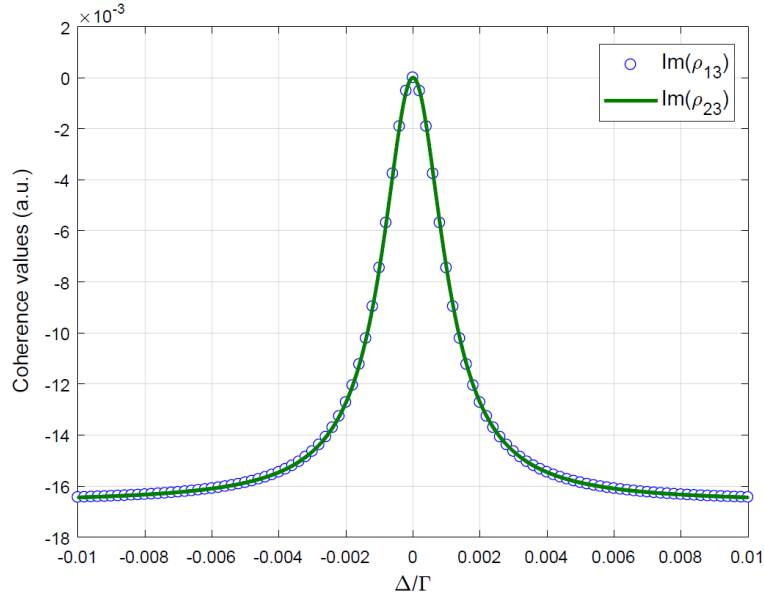


Figure 2.8: The real part of coherence terms, ρ_{13} and ρ_{23} plotted with parameters $\Omega_1 = \Omega_2 = \Gamma/30$, $\delta = 0$ and $\gamma = 0$. The plots for $Im(\rho_{13})$ and $Im(\rho_{23})$ overlap on each other.

2.4 Pulsed CPT and Ramsey interference simulation results

Unlike continuous excitation, pulsed CPT excitation in the three-level Λ -system creates Ramsey interference. In this case, interaction with a long CPT pulse generates atomic coherence by preparing the atoms in the dark state. Subsequently, Ramsey interference is produced by an interaction-free evolution of the atoms followed by a short interaction with the query pulse.



Figure 2.9: Timing diagram considered in the simulation for generating Ramsey interference.

To distinguish this phenomenon from the Ramsey interference commonly observed in a two-level system due to microwave excitation, it is referred to as Raman-Ramsey interference (RR interference) or simply, optical Ramsey interference (section 5.3.4 of [1]). Figure 2.9 shows a typical pulse sequence considered in the time-dependent model to simulate Ramsey interference [48]. This involves Raman interaction with a long CPT pulse of duration τ_c , followed by a free-evolution time T , and another Raman interaction with a short CPT pulse known as the query pulse of duration τ_q . The duration of the long CPT pulse is chosen long to prepare the atoms in the dark state or in other words, drive the atomic system onto the (near) steady-state condition. The interference effect is created during interrogation with the query pulse due to an accumulated phase difference $\Delta\varphi (= \Delta \cdot T)$ between the phase of the evolving dark state and the phase of the Raman fields for the time interval T .

A steady-state analysis cannot be used for investigating pulsed CPT excitation and Ramsey interference. Time-dependent density-matrix equations in eqn. (2.17) need to be solved for three successive time intervals (τ_c, T, τ_q) to calculate the time evolution of all the density-matrix elements, ρ_{ij} , and the Ramsey interference. It is, however, possible to obtain analytic solutions to eqn. (2.17), in particular, $\rho_{33}(t)$, by applying an adiabatic approximation to the evolution of the excited state $|3\rangle$ [49,50]. This approximation is valid in cases where the decay rate Γ is large compared to all other rates in the system (i.e. $\Gamma \gg \Omega_1, \Omega_2, \delta_1, \delta_2, \gamma$). Under this condition, the system can rapidly come to equilibrium with the ground states. In such a case, the system of equations in eqn. (2.17) can be reduced to density matrix equations for an effective two-level system consisting of only the two ground states. Hemmer et al [50] has obtained an analytic solution for ρ_{33} at the end of interaction with the pulse sequence shown in figure 2.9 which is given by

$$\rho_{33}(\tau_c + T + \tau_q) = \alpha e^{-\alpha\Gamma\tau_q} [1 - (1 - e^{-\alpha\Gamma\tau_c}) |\sec(\varphi)| \cos(\Delta T - \varphi_{LS})] \quad (2.20)$$

where $\alpha = \Omega^2/(\Gamma^2 + 3\Omega^2 + 4\delta^2)$ represents the interaction with the CPT pulse, and Ω corresponds to the average Rabi frequency of the CPT pulse. A large value of α will correspond to a strong interaction with the CPT pulse and lead to the pulse saturation effect. In eqn. (2.20), the oscillatory term, $\cos(\Delta T - \varphi_{LS})$, describes Ramsey fringes formed due to Δ . The term φ_{LS} in the argument of the cosine function corresponds to the phase angle due to the light shift associated with Ramsey fringes. For $\varphi_{LS} \neq 0$, the center of Ramsey fringes is shifted from $\Delta = 0$ to $\Delta = \varphi_{LS}/T$. The origin of light shift, φ_{LS} , and its effect on the atomic clock is discussed in more detail later in chapter 4. Eqn. (2.21) also shows that the fringe-width (or linewidth) $\Delta\nu$ of Ramsey fringe is decided by the free-evolution time, T as

$$\Delta\nu = 1/2T \quad (2.21)$$

Unlike CPT linewidth, given in eqn. (2.19), Ramsey fringe width does not depend on the optical power. Thus, Ramsey interference offers the advantage of producing narrow-linewidth without being sensitive to laser power-broadening, an improvement upon CPT. Narrow linewidth can give rise to improved short-term frequency stability in an atomic clock [33,42]. In the atomic vapor, T is limited by the decoherence of the dark state which can be 4 to 5 milliseconds long by adding buffer gas to the vapor cell for preventing frequent atomic collisions. Sub-kilohertz linewidth Ramsey fringes are easily produced in the atomic vapor by using pulsed CPT excitation.

2.4.1 Ramsey interference simulation results

Unlike CPT, a steady-state analysis cannot be used to investigate Ramsey interference. To study Ramsey interference in simulation, the time-dependent density matrix equations, given earlier in eqn. (2.17), are solved for the three successive time intervals, (τ_c, T, τ_q) which

represent the pulse cycle in figure 2.9. A computational eigenvalue method has been used for solving the time-dependent density matrix equations. The following initial conditions are used prior to the CPT pulse: $\rho_{ij(i \neq j)}^0 = \rho_{33} = 0$, $(\rho_{11} + \rho_{22})^0 = 1$ and $(\rho_{11} - \rho_{22})^0 = \rho^0$, where ρ^0 has been assigned a nonzero value to create unequal initial population between the ground states. Solutions for ρ_{ij} obtained at $t = \tau_c$ are used initial values for the density matrix equations during T which are obtained by setting $\Omega_1 = \Omega_2 = 0$. The solutions $\rho_{ij}(\tau_c + T)$ obtained after $t = \tau_c + T$ are then used as initial values for the density matrix equations describing the final interaction with the query pulse of duration τ_q . RR fringes are obtained by repeating the computation for different values of Δ around $\Delta = 0$.

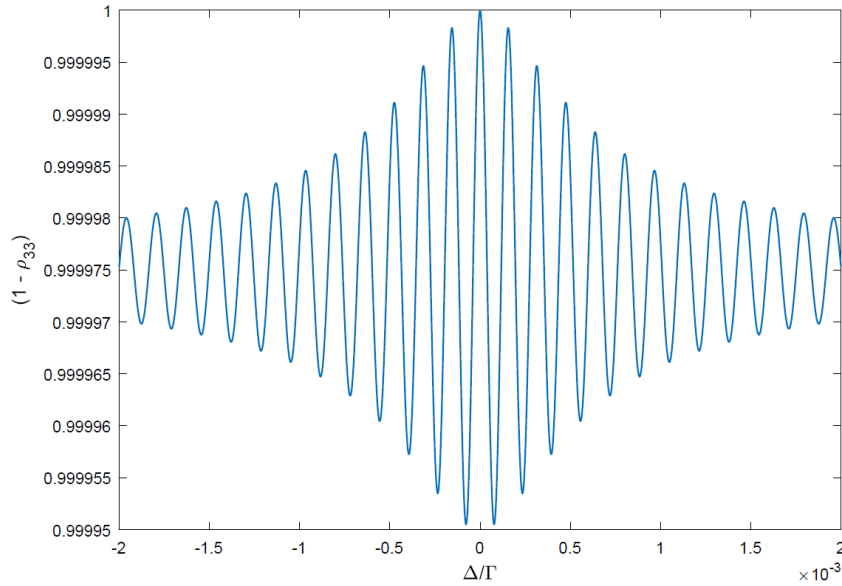


Figure 2.10: Ramsey fringes obtained with the parameters, $\Omega_1 = \Omega_2 = \Gamma/50$, $\tau_c = 500 \mu s$, $T = 1 ms$, and $\tau_q = 1 \mu s$. The central fringe has the expected linewidth $\Delta\nu = 1/2T = 500 Hz$.

Figure 2.10 shows simulated Ramsey fringes for parameters $\tau_c = 500 \mu s$, $T = 1 ms$, $\tau_q = 1 \mu s$, $\Omega_1 = \Omega_2 = \Gamma/50$, $\delta = 0$ and $\gamma = 0$. Unlike CPT which consists of a single resonance, Ramsey interference generates multiple oscillatory resonances (or fringes) as described earlier in eqn.

(2.20). All fringes including the central fringe have a linewidth which is equal to $1/2T$. The fringe envelope corresponds to the single pulse CPT lineshape with a linewidth $\Omega^2/\Gamma = (0.0004)\Gamma$. Figure 2.11 shows simulated Ramsey fringes for $\tau_c = 200 \mu s$ and $\Omega_1 = \Omega_2 = \Gamma/300$ while keeping all other parameters same as before. This result shows a change in the envelope (or profile) of Ramsey fringes (compared to figure 2.10) due to the change in Raman saturation condition defined by the parameter $(\Omega \tau_c)$ of the CPT pulse. The condition $\Omega \tau_c \gg 1$ leads to a steady-state excitation condition [51].

Due to a non-steady state condition, the Ramsey fringe envelope in figure 2.11 shows a pulse-transform limited fringe envelope described by the function $\text{sinc}(\Delta\tau_c/2)$. The result in figure 2.10 has reached the steady state, and shows a linewidth much smaller than the CPT linewidth for the same power. If, however, the condition is not met, the pulse-transform limited fringe envelope becomes apparent, which is described by the function $\text{sinc}(\Delta \tau_c/2)$, assuming the CPT pulse to be a rectangular pulse. Besides the main lobe, the Ramsey fringes in this case are also encased in the sidelobes of the sinc function.

Figure 2.12 shows the change in linewidth of the Ramsey fringes by changing T from $500 \mu s$ to 1.5 ms . Other parameters chosen for this simulation are $\tau_c = 500 \mu s$, $\tau_q = 1 \mu s$, $\Omega_1 = \Omega_2 = \Gamma/100$, $\delta = 0$ and $\gamma = 0$. The linewidths in all three cases were measured and found to match very closely with $\Delta\nu = 1/2T$. It has been also verified that the linewidth of the Ramsey fringe is ultimately limited by γ , which, in experiments, can be made small in atomic vapor by using buffer-gas loaded cells. Detailed discussion and comparison of light shift properties of CPT and Ramsey fringes for atomic clock development is presented in chapter 4.

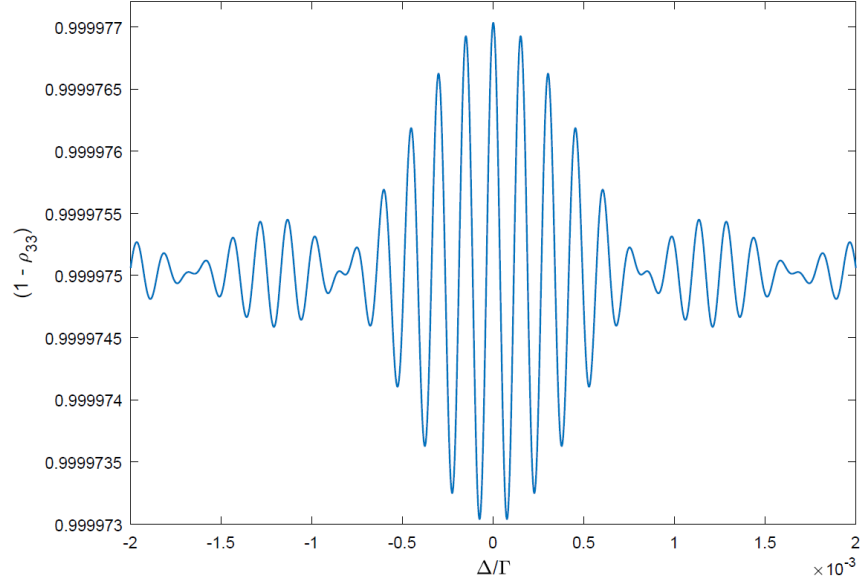


Figure 2.11: Ramsey interference obtained with the parameters, $\Omega_1 = \Omega_2 = \Gamma/300$, $\tau_c = 200 \mu s$, $T = 1 ms$, and $\tau_q = 1 \mu s$.

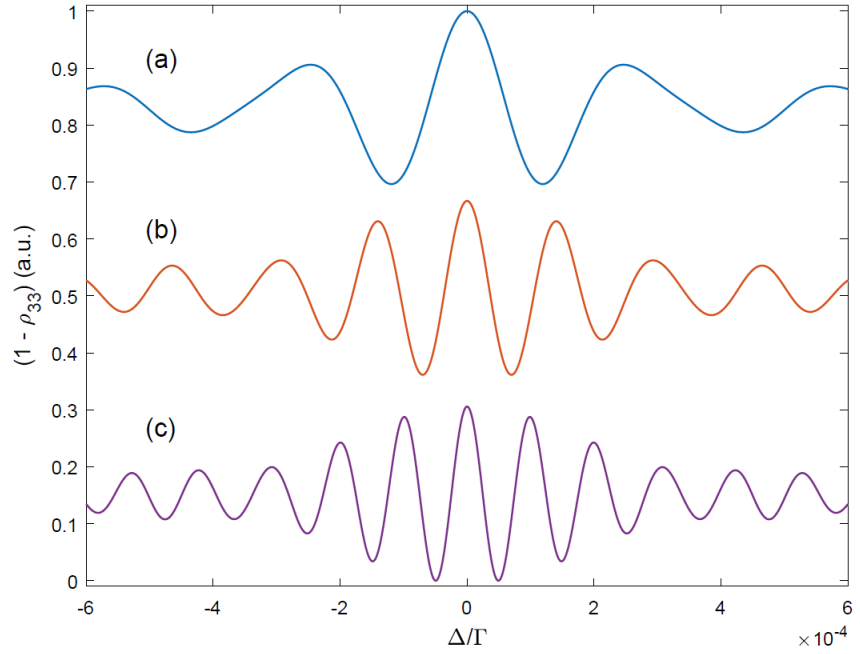


Figure 2.12: Ramsey fringes obtained with (a) $T = 500 \mu s$, (b) $T = 1 ms$, and (c) $T = 1.5 ms$. The linewidths change with T as $\Delta\nu = 1/2T$.

A three-level model gives an ideal representation of the real atom, which in practice is composed of many energy levels. Adding Zeeman levels, magnetic field dependence, velocity parameters, amongst other effects, will strengthen the model and allow for more complicated and useful effects to be predicted.

2.4.2 Time domain Ramsey interference

As described earlier in eqn. (2.20), Ramsey fringes can also be observed by keeping Δ fixed and changing T . These fringes are called time-domain Ramsey interference (TDRI). Alternatively, TDRI can be generated by choosing a highly attenuated (small Rabi frequency) query pulse having a fixed Δ value. In this case, TDRI is observed as oscillations in the amplitude of the query pulse. Figure 2.13 shows the TDRI generated using the time-dependent density matrix simulation by keeping Δ , τ_c , and T fixed and changing the duration of the attenuated query pulse, τ_q . The time

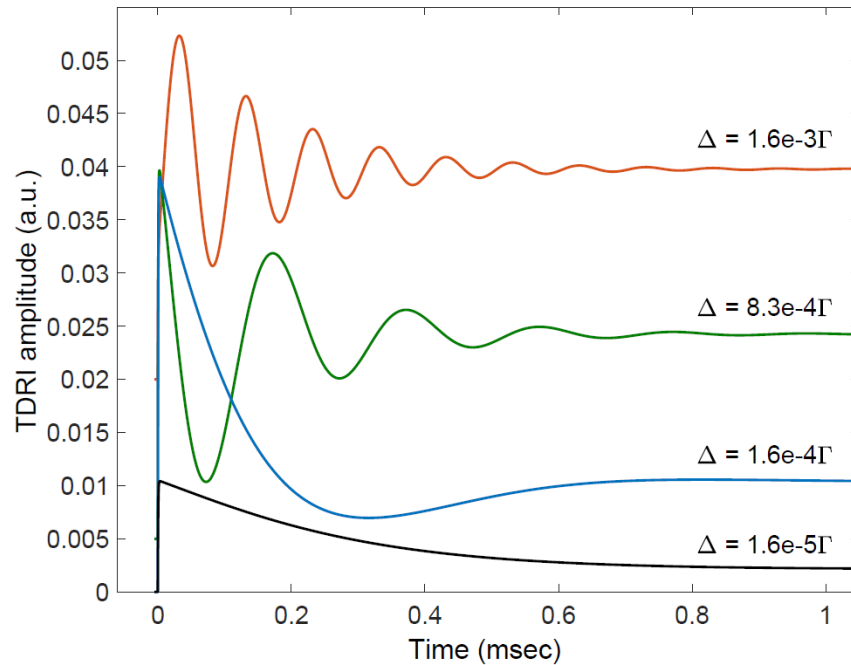


Figure 2.13: TDRI obtained for different values of Δ , as a function of the query pulse duration [52].

period of the oscillation for TDRI in each case matches with $1/\Delta$ as expected. Large Δ produces TDRI with large number of oscillations (or fringes). Increasing the Rabi frequency of the query pulse causes a faster decay of the TDRI fringe amplitude. Negative values of Δ generate the same TDRI fringes as the positive values, but with a π phase shift. This asymmetry and any undesirable variation in the width of the query pulse can potentially create frequency error for the atomic clock.

This chapter described how dark states are formed in a three-level Λ -system along with their properties, explored through the density matrix equations. CPT and Ramsey interference simulation demonstrated the strengths of this model in depicting the general behavior of the schemes. In the next chapter, this simulation will be extended to include more aspects of the atomic system.

CHAPTER 3: MULTI-LEVEL ATOMIC MODELING

The three-level atomic system considered in the previous chapter is only an approximation of the real atom which, in practice, may have laser fields interacting with multiple energy levels. In the case of an atomic clock employing CPT or Ramsey interference, it is necessary to include all the energy levels in the atomic modeling in order to describe the behavior of the atomic clock accurately. Such an inclusive modeling may also be necessary in many other applications such as atom interferometry [53–56], magnetometry [57–63] and laser cooling [18,64–68], etc. This chapter describes a comprehensive theoretical model based on density-matrix equations including all the Zeeman sublevels in the D1 manifold of ^{87}Rb atoms. Laser interaction in this multi-level model explicitly considers all possible Raman transitions formed in the Zeeman sublevels of ^{87}Rb atoms. The model can provide valuable insights on the polarization dependence of CPT and Ramsey interference and their sensitivities to the magnetic field which are important for atomic clock development.

The multi-level model is used here to simulate the relative merits and demerits of using three different optical configurations for a compact rubidium clock using CPT or Ramsey interference. These correspond to the following choices of polarizations for the two Raman beams: $lin \parallel lin$, (σ, σ) , and push-pull optical pumping (PPOP), for the D1 manifold in ^{87}Rb . In the ideal three-level atomic model, described in chapter 2, CPT (or Ramsey interference) is generated by interaction of two resonant laser frequencies with three atomic levels forming a Λ (or Raman) transition. In the multi-level atomic model, properties of CPT (or Ramsey interference) is more accurately described by interaction of two Raman laser frequencies with all sixteen energy levels present in the D1 manifold of ^{87}Rb atoms. Instead of one Λ -transition, multiple Λ -transitions can

be formed in this case. The model considers all possible Λ -transitions that can occur between two hyperfine ground states $|F_g = 1\rangle$ and $|F_g = 2\rangle$ and a common excited state $|F' = 1\rangle$ or $|F' = 2\rangle$. The sixteen-level model also allows one to investigate magnetic field dependence of the CPT spectra produced by different optical excitation schemes.

The optical excitation scheme commonly used in CPT clocks employs circularly (right or left) polarized laser light for interrogating rubidium atoms. Circularly polarized light pumps a significant fraction of the atoms into Zeeman edge (or trap) states, reducing contrast in the CPT signal. This can be prevented by using, on each leg of the Λ system, linearly polarized fields having both right (σ^+) and left (σ^-) circular components. However, a pure dark state cannot be formed in the $m_F = 0$ ground state sublevels of the alkali D1 manifold by a pair of parallel, linearly polarized ($lin \parallel lin$) CPT fields. This is because the dark state corresponding to the right circular fields ($|dark_{\sigma^+}\rangle$) and the dark state corresponding to the left circular fields ($|dark_{\sigma^-}\rangle$) are non-identical, due to opposite signs of matrix element ratios associated with σ^+ and σ^- transitions [69,70]. However, this problem can be circumvented by making use of a pair of orthogonal, linearly polarized ($lin \perp lin$) CPT fields, enabling the formation of a pure dark state in the $m_F = 0$ ground state sublevels, which will be addressed in chapter 5. Alternative methods, such as push-pull optical pumping (PPOP) and counter-propagating circularly polarized beams have been investigated for generating CPT resonance with high contrast [71–75]. The polarization states of the optical fields employed for PPOP scheme are equivalent to those corresponding to the use of $lin \perp lin$ scheme [73]. Keeping this in mind, three primary polarization schemes are considered, (σ, σ) , $lin \parallel lin$, and PPOP (which is the same as $lin \perp lin$) for these theoretical investigations. The results obtained from the model show relative strengths of CPT resonances (or

Ramsey fringes) formed by these polarization schemes. The model is also used to examine the CPT spectrum in the presence of a transverse magnetic field.

3.1 Multi-level atomic model for ^{87}Rb D1 manifold

The comprehensive atomic model is created using the Liouville density-matrix equation [51,76], taking into account all relevant Zeeman sublevels. This model is used to study

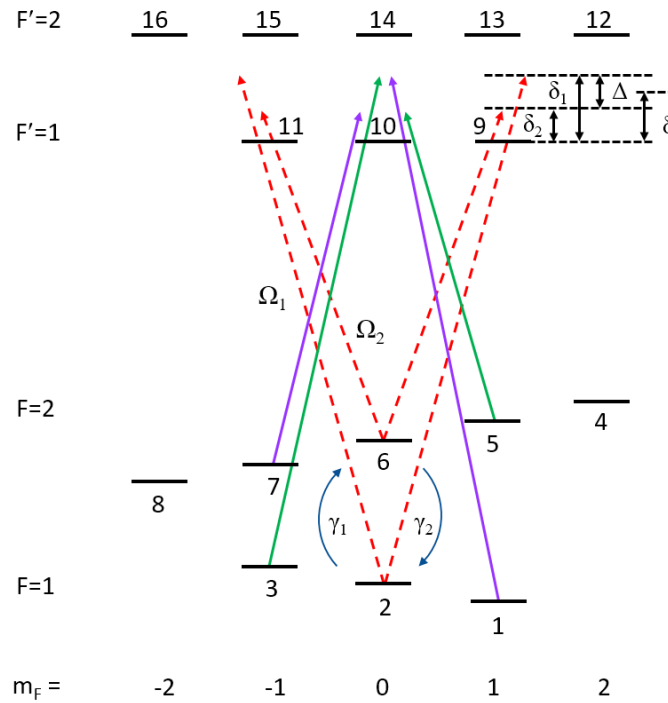


Figure 3.1: Raman excitation in a multi-level atomic system consisting of all the energy levels in the D1 manifold of ^{87}Rb atoms. For theoretical modeling, the magnetic sublevels in the F-states are designated by a sequence of numbers from one to sixteen.

CPT resonances formed by the two-photon Raman excitation with two laser fields at frequencies ω_1 and ω_2 in the D1 manifold of ^{87}Rb atoms. Figure 3.1 shows all sixteen Zeeman sublevels in the model, with the hyperfine ground states $|F = 1, 2\rangle$ coupled to the hyperfine excited states $|F' = 1, 2\rangle$ by the applied laser fields. Each hyperfine state consists of magnetic m_F sublevels which are designated by the number sequence from 1 to 16.

The time evolution of the atomic system is governed by the modified Liouville equation: $\frac{\partial \rho}{\partial t} = -\frac{i}{\hbar} [H\rho - \rho H^\dagger] + L$, where ρ is the density operator, H is the semi-classical, non-Hermitian Hamiltonian, and L represents the source matrix, as defined in detail next.

The non-Hermitian Hamiltonian, $H = H_A + H_B + H_\Gamma$, is expressed as the sum of three parts: H_A represents the internal atomic energy plus the energy due to interaction with the laser fields, H_B represents the energy due to interaction with the magnetic field, and H_Γ (which is complex) accounts for the decays of atomic states. The matrix form of H is given in appendix B. Under the rotating wave approximation, and in the rotating wave picture, H_A (with $\hbar = 1$) for the sixteen-level system can be described as:

$$H_A = \frac{\Delta}{2} \sum_{i=1}^3 s_{i,i} - \frac{\Delta}{2} \sum_{i=4}^8 s_{i,i} - \delta \sum_{i=9}^{16} s_{i,i} + \left(\frac{\Omega_1}{2} \sum_{i=1}^3 \sum_{j=9}^{16} d_{ij} s_{i,j} + \frac{\Omega_2}{2} \sum_{i=4}^8 \sum_{j=9}^{16} d_{ij} s_{i,j} + h.c. \right) \quad (3.1)$$

where $s_{i,j} = |i\rangle\langle j|$ is defined as the outer product matrix with $|i\rangle$ as the i^{th} energy state represented by a (16×1) column vector, $\Delta = \delta_1 - \delta_2$ is the difference frequency detuning between the CPT fields, with δ_1 and δ_2 (shown in figure 3.1) corresponding to respective single photon detuning for the laser frequencies ω_1 and ω_2 , $\delta = (\delta_1 + \delta_2)/2$ is the average (common-mode) laser detuning, d_{ij} represents the normalized dipole matrix element corresponding to the $(i \rightarrow j)$ transition, Ω_1 (Ω_2) is the Rabi frequency of the CPT field at frequency ω_1 (ω_2) corresponding to a transition with a normalized dipole matrix element value of unity, and $h.c.$ stands for Hermitian conjugate. The coupling terms involving Ω_1 (fourth term, to be denoted as $H_A^{(4)}$) and Ω_2 (fifth term, to be denoted as $H_A^{(5)}$) in eqn. (3.1) include σ^+ and σ^- circular transitions, with the values of the normalized

matrix elements depending on the polarization states of the CPT fields. For example, if the CPT fields have \hat{x} -polarized ($lin \parallel lin$) polarization states, the coupling terms in eqn. (3.1) have the following form:

$$H_A^{(4)} = \frac{\Omega_1}{2} \left(-\frac{1}{\sqrt{12}} (s_{2,9} + s_{3,10} + s_{3,14}) - \frac{1}{\sqrt{4}} s_{2,13} - \frac{1}{\sqrt{2}} s_{1,12} \right) \\ + \frac{\Omega_1}{2} \left(\frac{1}{\sqrt{12}} (s_{1,10} + s_{2,11} - s_{1,14}) - \frac{1}{\sqrt{4}} s_{2,15} - \frac{1}{\sqrt{2}} s_{3,16} \right) \quad (3.2)$$

$$H_A^{(5)} = \frac{\Omega_2}{2} \left(\frac{1}{\sqrt{12}} s_{6,9} + \frac{1}{\sqrt{6}} (s_{5,12} + s_{8,15}) + \frac{1}{\sqrt{4}} (s_{7,10} + s_{6,13} + s_{7,14}) + \frac{1}{\sqrt{2}} s_{8,11} \right) \\ + \frac{\Omega_2}{2} \left(\frac{1}{\sqrt{12}} s_{6,11} + \frac{1}{\sqrt{6}} (-s_{4,13} - s_{7,16}) + \frac{1}{\sqrt{4}} (s_{5,10} - s_{5,14} - s_{6,15}) \right) \\ + \frac{1}{\sqrt{2}} s_{4,9} \quad (3.3)$$

The terms in eqn. (3.2) and eqn. (3.3) contain a sum of all σ^+ transitions (the first bracketed term) and σ^- transitions (the second bracketed term). Similarly, the coupling terms for other polarization states corresponding to only (σ^+, σ^+) or (σ^-, σ^-) and $lin \perp lin$ schemes have been formulated.

The Hamiltonian H_B for the sixteen-level system is defined as

$$H_B = B_z [A_1 (s_{1,1} - s_{3,3}) + A_2 (2s_{4,4} + s_{5,5} - s_{7,7} - 2s_{8,8}) \\ + A_3 (s_{9,9} - s_{11,11}) + A_4 (2s_{12,12} + s_{13,13} - s_{15,15} - 2s_{16,16})] \\ + B_T \left[\frac{A_1}{\sqrt{2}} (s_{2,1} + s_{3,2}) + A_2 \left(s_{5,4} + \frac{\sqrt{6}}{2} (s_{6,5} + s_{7,6}) + s_{8,7} \right) \right. \\ \left. + \frac{A_3}{\sqrt{2}} (s_{10,9} + s_{11,10}) + A_4 \left(s_{13,12} + \frac{\sqrt{6}}{2} (s_{14,13} + s_{15,14}) + s_{16,15} \right) \right] \\ + h.c. \quad (3.4)$$

where B_Z corresponds to the longitudinal (or axial) magnetic field (LMF) along the quantization axis, which is chosen to be the z-direction and coincides with the direction of propagation of the laser beam, B_X (B_Y) represents a magnetic field along the x (y) direction, and $B_T = B_X + iB_Y$ is defined as the transverse magnetic field (TMF). In the presence of B_T , the coupling between the magnetic (or Zeeman) sublevels in the ground ($|F = 1\rangle$ and $|F = 2\rangle$) states and similarly, in the excited ($|F' = 1\rangle$ and $|F' = 2\rangle$) states, represented by the off-diagonal terms in H_B , are calculated in appendix C. The parameters $A_n = g_n \mu_B / \hbar$ ($n = 1, 2, 3, 4$) correspond to linear Zeeman shifts of $|F = 1\rangle$, $|F = 2\rangle$, $|F' = 1\rangle$, and $|F' = 2\rangle$ states, respectively, with $g_n = \left(\frac{5g_I - g_J}{4}, \frac{3g_I + g_J}{4}, \frac{5g'_I - g'_J}{4}, \frac{3g'_I + g'_J}{4} \right) = (-0.5017, 0.4997, -0.1677, 0.1657)$ being the respective effective Landé g-factors and μ_B being the Bohr magneton. The model also incorporates the Breit-Rabi equation [70,77,78] to include LMF induced quadratic Zeeman shifts. For $|F = 1\rangle$ and $|F = 2\rangle$ states, the second-order expansion of the Breit-Rabi equation gives the quadratic Zeeman shift coefficient $\frac{(g_J - g_I)^2 (4 - m_F^2) \mu_B^2}{16 \hbar^2 \omega_{hf}}$, where $\hbar \omega_{hf}$ is the energy difference between these two hyperfine states. A similar expression also applies to $|F' = 1\rangle$ and $|F' = 2\rangle$ states. These expressions are derived from the Breit-Rabi equation and presented in appendix C. The decay of atomic levels in the multi-level model is accounted by H_Γ which is defined as [76]

$$H_\Gamma = -\frac{i}{2} \left(\sum_{i=1}^3 \gamma_1 s_{i,i} + \sum_{i=4}^8 \gamma_2 s_{i,i} + \sum_{i=9}^{16} \Gamma s_{i,i} \right) \quad (3.5)$$

where Γ is the total decay rate from each sublevel in the excited states $|F' = 1, 2\rangle$, and γ_1 and γ_2 are the effective decay rates for the ground states $|F = 1\rangle$ and $|F = 2\rangle$, respectively. The source matrix L in the density-matrix equation contains non-zero diagonal elements that account for the influx of atoms decaying from other states:

$$L = \Gamma \sum_{i=1}^8 s_{i,i} \sum_{j=9}^{16} d_{ji}^2 \rho_{jj} + \frac{\gamma_2}{3} \sum_{i=1}^3 s_{i,i} \sum_{j=4}^8 \rho_{jj} + \frac{\gamma_1}{5} \sum_{i=4}^8 s_{i,i} \sum_{j=1}^3 \rho_{jj} \quad (3.6)$$

Here, d_{ji}^2 represents the square of the normalized matrix element for the ($j \rightarrow i$) decay channel.

The expanded form of L is given in appendix B. The source matrix L includes the ground state population influx due to all possible decay channels corresponding to σ^+ , σ^- , and π transitions, as

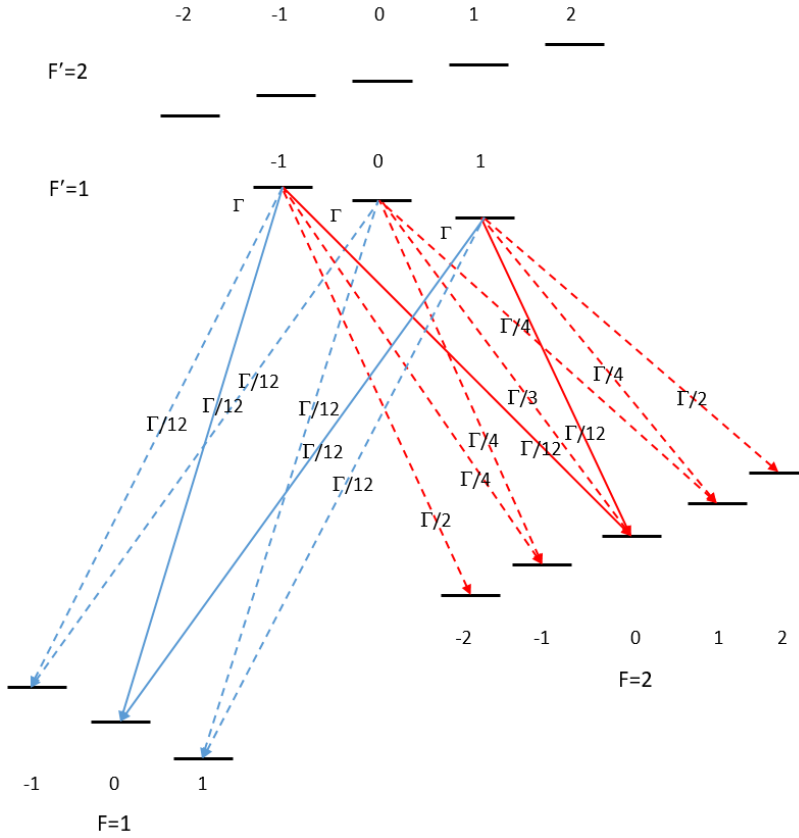


Figure 3.2: Radiative decay channels corresponding to σ^+ , σ^- , and π transitions from $|F' = 1\rangle$ excited state. All of these decays are considered in formulating H_Γ and L matrices.

well as the population exchange between the ground states. The decay channels for the excited states $|F' = 1\rangle$ and $|F' = 2\rangle$ are explicitly shown in figures 3.2 and 3.3. The radiative decay channels follow the selection rules $\Delta m_F = 0, \pm 1$. The total decay from each excited state is

considered as Γ . The strength of an individual decay channel is proportional to the square of the normalized matrix element for that particular decay channel.

A system of linear and time-dependent equations for the density-matrix elements ρ_{ij} are obtained by using H and L matrices given by eqns. (3.1-3.6) in the Liouville equation described previously. This system of equations is recast as a vector-matrix equation in the form $\frac{d}{dt}\rho = M\rho$,

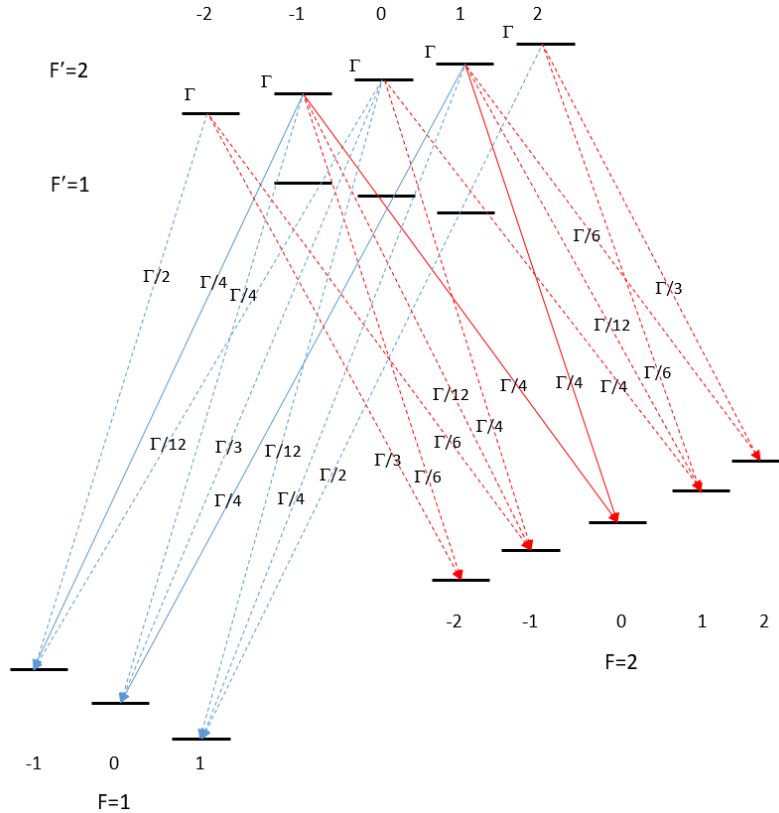


Figure 3.3: Radiative decay channels corresponding to σ^+ , σ^- , and π transitions from $|F' = 2\rangle$ excited state. All of these decays are considered in formulating H_Γ and L matrices.

where ρ is a vector consisting of 256 elements ρ_{ij} and M is a (256×256) matrix consisting of the coefficients of ρ_{ij} gathered from the Liouville equation. A computational model was developed to find time-dependent as well as steady-state solutions for ρ_{ij} for studying CPT using different polarization schemes. Under the steady-state condition, the solutions for ρ are obtained by

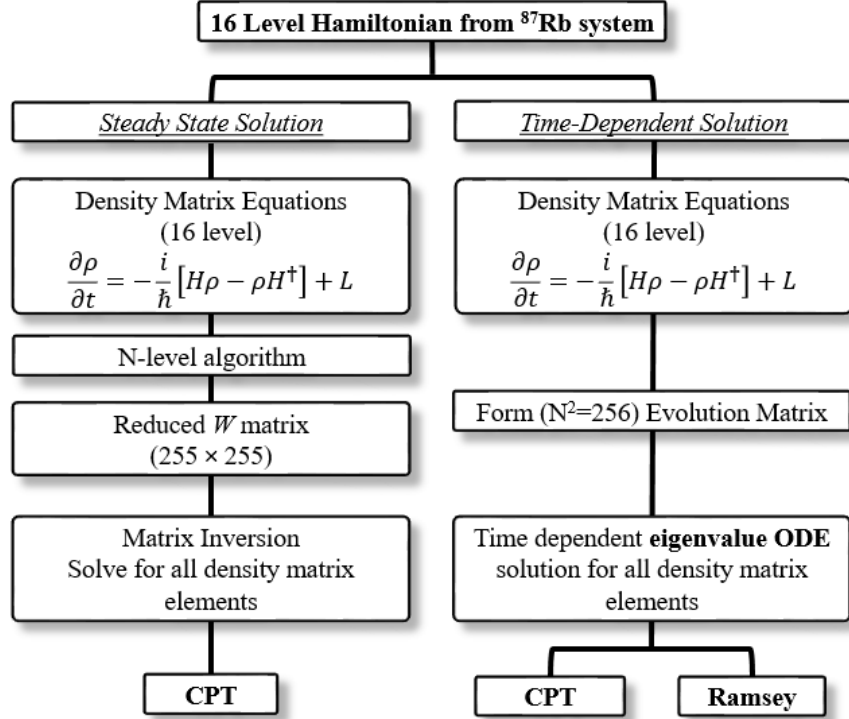


Figure 3.4: Flow diagram for finding steady state and time-dependent solutions to the density-matrix equations representing a sixteen-level atomic system.

equating $\frac{d}{dt}\rho$ to zero, reducing M to a matrix W of reduced dimension (255×255) using the condition $\sum_{i=1}^{16} \rho_{ii} = 1$ for a closed atomic system, and finding W^{-1} . The time-dependent solutions for $\vec{\rho}$ are obtained from the eigenvalues and eigenvectors of the M matrix.

The flow diagram in figure 3.4 shows the steps involved in finding the steady-state and time-dependent solutions for the sixteen-level model. The MATLAB program implementing the algorithm for finding the time-dependent solution is provided in appendix A.

Figure 3.5 shows the CPT resonance produced around $\Delta = 0$, represented by the sum of the populations in states 9 through 11 (i.e., $\sum_{i=9}^{11} \rho_{ii}$) shown in figure 3.1, using steady-state as well as time-dependent solutions, for excitation using \hat{x} -polarized $lin \parallel lin$ CPT fields. The CPT

fields were chosen to be resonant with the $|F' = 1\rangle$ state. For this simulation, the parameters correspond to $\Omega \equiv \sqrt{(|\Omega_1|^2 + |\Omega_2|^2)/2} = \Gamma/60$.

For an ideal three-level system, with the Rabi frequency for leg one being $\Omega_1 \ll \Gamma$ and that for leg two being $\Omega_2 \ll \Gamma$, the linewidth of the CPT signal is expected to be $\sim \Omega^2/\Gamma$. For $\Gamma = 6$ MHz, the linewidth for an ideal CPT system would be ~ 1.7 kHz. The linewidth in figure 3.5 is seen to be somewhat smaller: ~ 0.42 kHz. This is due to a couple factors. First, note that Ω_1 and Ω_2 are defined to be Rabi frequencies corresponding to transitions with normalized matrix elements of unity values. However, the actual matrix elements involved are significantly smaller. Second, the fields are detuned with respect to the $|F' = 2\rangle$ state; the linewidth of a CPT resonance decreases when the excitation is detuned with respect to the intermediate state.

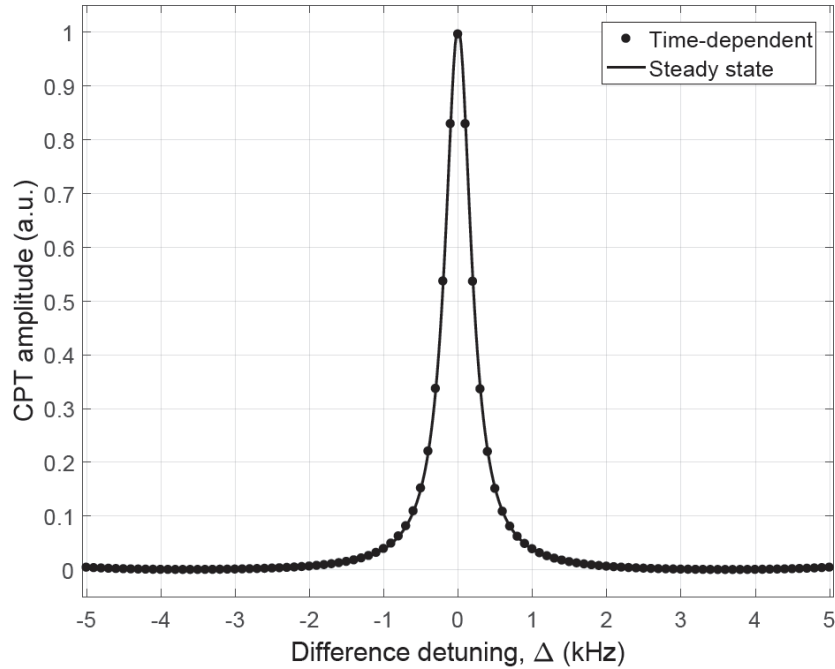


Figure 3.5: Calculated and normalized CPT resonance showing a close match between the steady-state and time-dependent solutions. The calculation included \hat{x} -polarized $lin \parallel lin$ excitation resonant with the $|F' = 1\rangle$ state and the following parameters: $B_z = 5$ mG, $\Omega = \Gamma/60$, $\Gamma = 6$ MHz, and $\gamma_1 = \gamma_2 = 0$.

It should be noted that the solutions obtained from the steady-state and time-dependent models show an excellent match in figure 3.5. A near steady-state solution is obtained from the time-dependent model by considering temporal Raman excitation with a long CPT pulse ($\tau = 2 \text{ ms}$). The time-dependent model is particularly suitable for studying the dark-state CPT resonance under non-steady state conditions and simulating pulsed CPT excitation which produces Raman-Ramsey interference [51,79].

3.2 Optical excitation schemes in CPT

The sixteen-level steady-state model is used to investigate CPT spectra and resonances produced by different optical excitation schemes. First, consider the *lin* \parallel *lin* polarization scheme, which can be created by a single, linearly polarized, modulated laser beam. For simulating excitations using linearly polarized CPT fields, coupling terms for both σ^+ and σ^- transitions with proper relative phase are included in H_A in eqn. (3.1).

Figure 3.6 shows the CPT resonance produced by *lin* \parallel *lin* around $\Delta = 0$ for $B_z = 20 \text{ mG}$ and 400 mG , for resonant excitation with the $|F' = 1\rangle$ excited state, and for $B_z = 20 \text{ mG}$ for resonant excitation with the $|F' = 2\rangle$ excited state. Such a scheme automatically prevents the formation of trap states due to the simultaneous presence of σ^+ and σ^- excitations. As such, the population decay rates for the ground states are taken to be $\gamma_1 = \gamma_2 = 0$ in this case; non-vanishing values of these rates are only used when necessary to prevent trap states, as in the case for purely left circular or purely right circular excitations, to be discussed later.

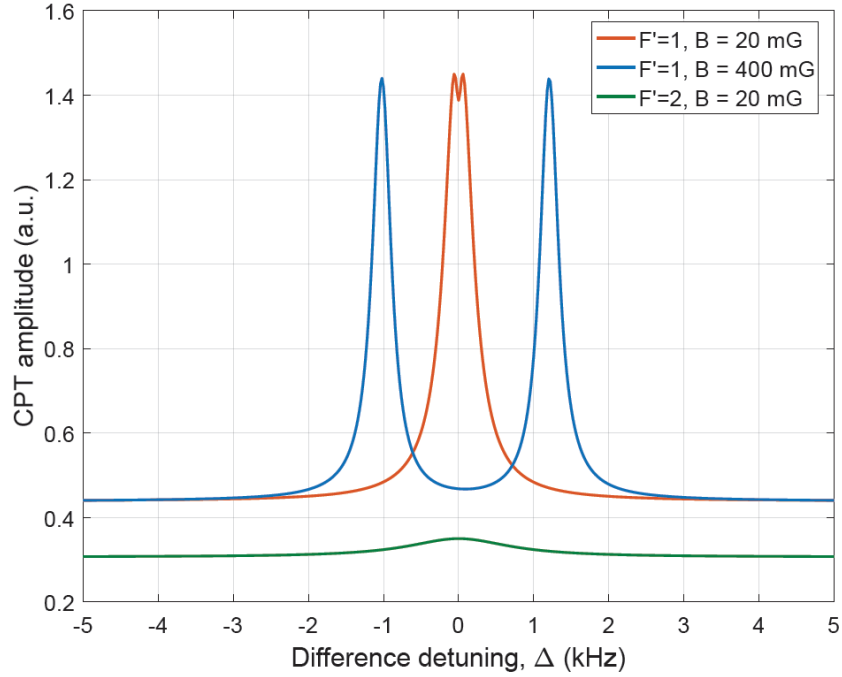


Figure 3.6: Splitting of the central CPT resonance formed by $lin \parallel lin$ excitation at higher axial magnetic field. The following parameters were used in the calculation: $\Omega = \Gamma/60$, $\Gamma = 6$ MHz, and $\gamma_1 = \gamma_2 = 0$.

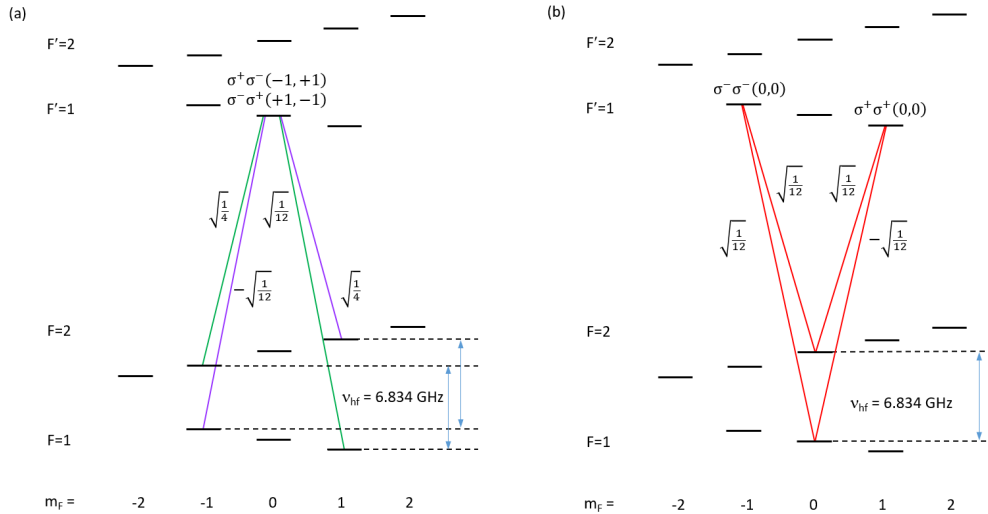


Figure 3.7: (a) Raman transitions in $lin \parallel lin$ excitation forming $(-1, +1)$ and $(+1, -1)$ dark states. (b) Raman transitions created by (σ^+, σ^+) or (σ^-, σ^-) excitation, involving the 0-0 dark state.

For resonant excitation with the $|F' = 1\rangle$ excited state, the splitting of the central CPT resonance in figure 3.6 exhibits high sensitivity to B_z compared to the typical CPT resonance produced by the dark state from a pair of $m_F = 0$ sublevels in $|F = 1\rangle$ and $|F = 2\rangle$ ground states. This can be explained with the following: dark states for $lin \parallel lin$ excitation are produced from a pair of ground-state sublevels $|F = 1, m_F = -1\rangle$, $|F = 2, m_F = +1\rangle$ and $|F = 1, m_F = +1\rangle$, $|F = 2, m_F = -1\rangle$, and are described by [80]

$$\left| Dark_{\begin{smallmatrix} (-1,+1) \\ (+1,-1) \end{smallmatrix}} \right\rangle = C_{\pm} \left[|F = 1, m_F = \mp 1\rangle - \frac{d_{\sigma^{\pm}}^{(1)} E_{\sigma^{\pm}}^{(1)}}{d_{\sigma^{\mp}}^{(2)} E_{\sigma^{\mp}}^{(2)}} |F = 2, m_F = \pm 1\rangle \right] \quad (3.7)$$

where $d_{\sigma^{\pm}}^{(1,2)}$ are σ^+ and σ^- elements of the dipole operator, $E_{\sigma^{\pm}}^{(1,2)}$ are circularly polarized components of the CPT fields, and C_{\pm} are normalization constants. The two dark states in eqn. (3.7) have a linear magnetic field sensitivity arising from the nuclear spin g-factor, g_I , which gives rise to high magnetic field splitting in the presence of B_z . The magnetic field dependencies of the $(-1, +1)$ and $(+1, -1)$ dark states are experimentally measured and discussed later in chapter 5. Figure 3.7a shows the Raman transitions and the normalized matrix elements corresponding to each transition for $lin \parallel lin$ excitation, which form the $(-1, +1)$ and $(+1, -1)$ dark states.

It is also important to note that due to a destructive superposition, a 0-0 dark state cannot be formed in the ground-states $|F = 1, m_F = 0\rangle$ and $|F = 2, m_F = 0\rangle$ by $lin \parallel lin$ excitation, because of differing signs of the relevant dipole matrix elements. High magnetic field sensitivity of $lin \parallel lin$ polarization is unsuitable for producing high frequency stability in the atomic clock. For two-photon excitation resonant with $|F' = 2\rangle$ state, the CPT resonance produced by $lin \parallel lin$ polarization is shown to have a much lower contrast. In this case, states described in eqn. (3.7) are

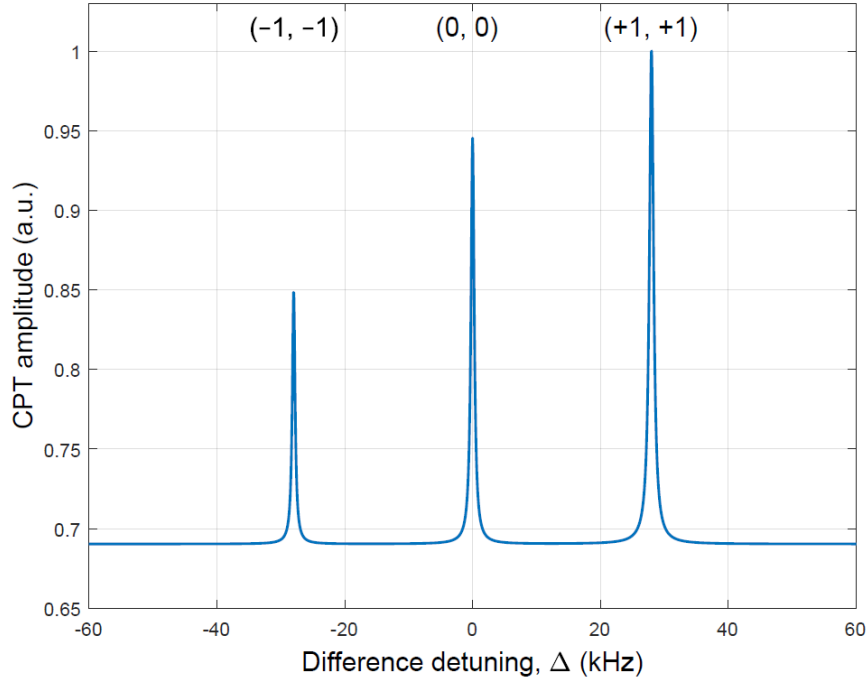


Figure 3.8: CPT spectrum generated by (σ^+, σ^+) polarized light resonant with the $|F' = 2\rangle$ state. The result shows Zeeman CPT resonances formed by the vector magnetic field \vec{B} used in the calculation with its magnitude $B_z = 20$ mG. The following parameters were used in the calculation: $\Omega = \Gamma/60$, $\Gamma = 6$ MHz, and $\gamma_1 = \gamma_2 = 3$ Hz

dark with respect to the $|F' = 1\rangle$ state, as well as the $|F' = 2, m_F = 0\rangle$ state, but see non-vanishing excitations to $|F' = 2, m_F = \pm 2\rangle$ states.

The polarization schemes commonly used in a CPT clock consist of right (σ^+, σ^+) or left (σ^-, σ^-) circularly polarized light. Unlike $lin \parallel lin$ excitation, (σ^+, σ^+) or (σ^-, σ^-) excitation will create Raman transitions only involving the 0-0 dark state which is shown in figure 3.7b, along with the normalized matrix elements.

The multi-level model allows one to simulate and investigate characteristics of CPT spectral resonances for different cases: resonant excitations with (σ^+, σ^+) or (σ^-, σ^-) polarized fields with $|F' = 1\rangle$ or $|F' = 2\rangle$ excited states. Figure 3.8 shows the CPT spectrum generated by (σ^+, σ^+) polarized light for $B_z = 20$ mG and resonant excitation with $|F' = 2\rangle$. The population

decay rates for the ground states are taken to be $\gamma_1 = \gamma_2 = 3$ Hz; non-vanishing values of these parameters must be used in this case in order to prevent trapping of atoms in the extreme Zeeman sublevels.

In addition to the central CPT resonance at $\Delta = 0$, strong $(-1,-1)$ and $(+1,+1)$ Zeeman CPT resonances are formed at $\Delta = \pm 2\Delta_z$, where $\Delta_z \equiv g_F \mu_B B_z$, by a pair of Zeeman-shifted ground-state sublevels $|F = 1, m_F = -1\rangle, |F = 2, m_F = -1\rangle$ and $|F = 1, m_F = +1\rangle, |F = 2, m_F = +1\rangle$. The resonance at $\Delta = 0$ is produced by the 0-0 clock state resulting from a single Λ -transition from $|F = 1, m_F = 0\rangle, |F = 2, m_F = 0\rangle$ to $|F' = 2, m_F = +1\rangle$, which is viable for clock applications, because the 0-0 CPT resonance is insensitive to magnetic fields to first-order. The presence of these additional resonances reduces the contrast of the 0-0 resonance.

A major disadvantage of using circularly polarized light in the CPT clock is the formation of a trap state where a majority of the atoms are accumulated, reducing the contrast (or SNR) of the central CPT resonance in the spectrum.

3.3 Transverse magnetic field effect

The model has been used to study the effect of TMF on the system. A TMF can be produced, for example, by a small angular misalignment between the applied LMF and the direction of optical beam propagation in the cell. Results in figure 3.9 show the effect of TMF on the CPT spectrum generated by the (σ^+, σ^+) polarized light.

The result shows that new CPT resonances are generated at $\Delta = \pm\Delta_z, \pm 3\Delta_z$ in the presence of TMF. The TMF gives rise to population redistribution among the Zeeman sublevels, resulting in new Λ sub-systems formed by effective π -transitions between the ground- and excited-state sublevels [59,81]. Thus, the contrast in the central CPT resonance is further reduced.

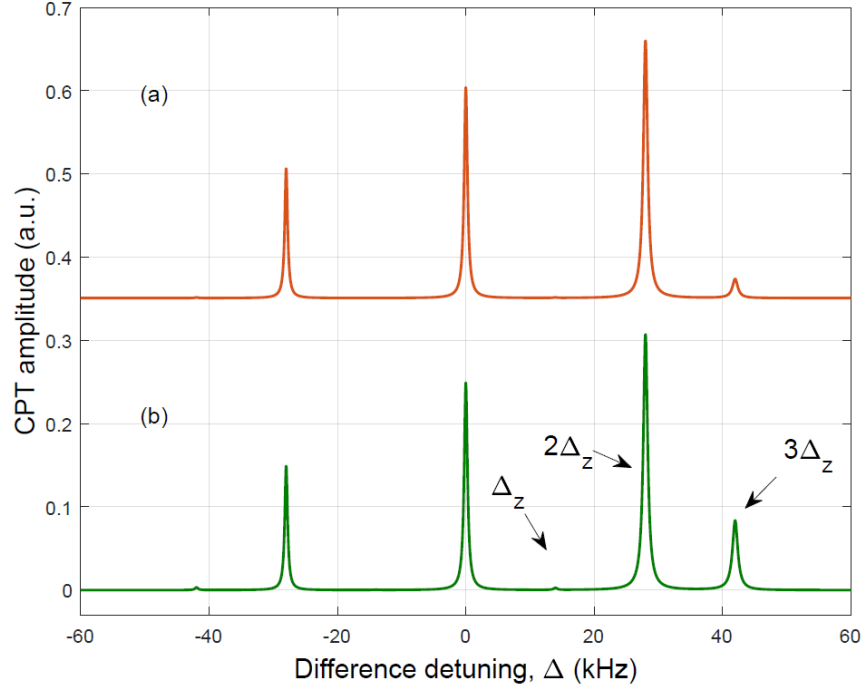


Figure 3.9: CPT spectrum generated by (σ^+, σ^+) polarized light resonant with the $|F' = 2\rangle$ state. The result shows Zeeman CPT resonances formed by the vector magnetic field \vec{B} used in the calculation with its magnitude $B = 20$ mG and angle (a) 5° (b) 10° with respect to the direction of beam propagation in the cell. The following parameters were used in the calculation: $\Omega = \Gamma/60$, $\Gamma = 6$ MHz, and $\gamma_1 = \gamma_2 = 3$ Hz

One of the preferred polarization schemes for producing high contrast CPT resonances in the 0-0 clock state is $lin \perp lin$ where two linear and orthogonal polarizations make up the CPT fields. Such a scheme (as well as the $lin \parallel lin$ scheme, as mentioned earlier) automatically prevents the formation of trap states due to the simultaneous presence of σ^+ and σ^- excitations. As such, the population decay rates for the ground states are taken to be $\gamma_1 = \gamma_2 = 0$ in this case.

In practice, $lin \perp lin$ cannot be directly created from a single, modulated laser beam used in the CPT clock. An alternative method known as push-pull optical pumping (PPOP) using the modulated laser beam in a polarization-based Michelson interferometer can substitute for $lin \perp lin$ [72]. Using a simple analysis of the CPT fields in the modulated laser beam, shown in appendix E that this method is equivalent to $lin \perp lin$ excitation [73]. Figure 3.10 shows the calculated CPT

resonance at $\Delta = 0$ using the model for $lin \perp lin$ excitation. In this case, there is a noticeable difference in CPT characteristics between resonant two-photon excitations with $|F' = 1\rangle$ and $|F' = 2\rangle$ states.

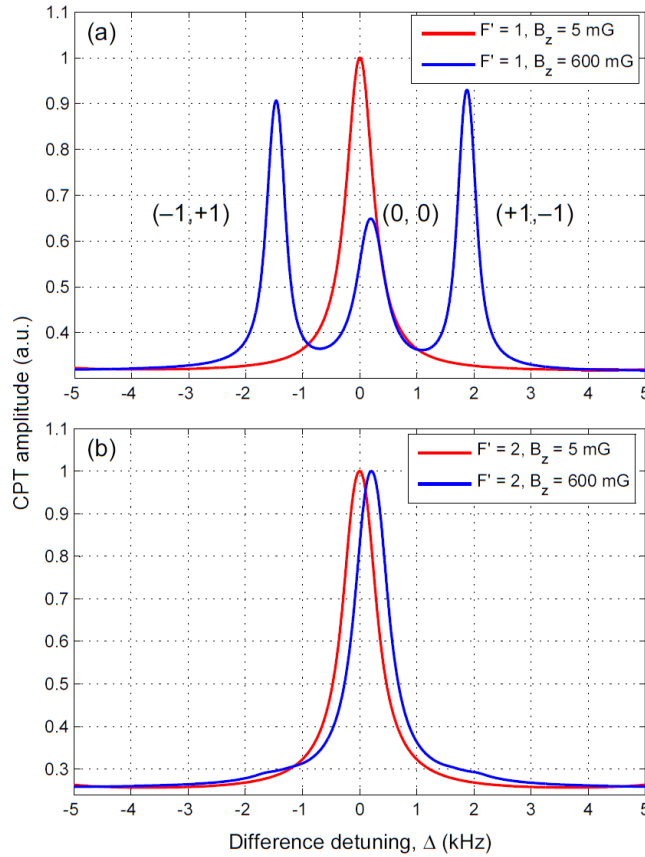


Figure 3.10: Splitting of the central CPT resonance formed by $lin \perp lin$ excitation resonant with (a) $|F' = 1\rangle$ state, and (b) $|F' = 2\rangle$ state at higher axial magnetic field. The following parameters were used in the calculation: $\Omega = \Gamma/60$, $\Gamma = 6$ MHz, and $\gamma_1 = \gamma_2 = 0$.

For a vanishingly small magnetic field ($B_z = 5$ mG), the central CPT resonance in figure 3.10a for resonant $|F' = 1\rangle$ is due to all three dark states: $(0,0)$, $(-1, +1)$ and $(+1, -1)$. However, these dark states produce separated CPT resonances when a significant magnetic field is applied ($B_z = 600$ mG in this case). In contrast, the central CPT resonance in figure 3.10b for resonant $|F' = 2\rangle$ is mainly due to the $(0,0)$ dark state, since the $(-1, +1)$ and $(+1, -1)$ “dark

states” are not fully dark in this case due to coupling to additional Zeeman sublevels in the $|F' = 2\rangle$ state. This is confirmed by using $B_z = 600$ mG which produces a single CPT resonance in figure 3.10b exhibiting the second-order magnetic field sensitivity of the 0-0 dark state; the contributions from the $(-1, +1)$ and $(+1, -1)$ “quasi dark states” appear as small bumps.

3.4 Raman-Ramsey interference

The time-dependent solutions obtained from the multi-level model have been used to simulate Ramsey interference and study its properties with similar optical excitation schemes used earlier in CPT.

Ramsey fringes produced by $lin \parallel lin$ excitation are shown in figure 3.11 for three different strengths of axial magnetic fields. These fringes are generated by considering resonant excitation with the $|F' = 1\rangle$ excited state. At $B_z = 0$, the center of the Ramsey fringes appear at $\Delta = 0$ (3.11a). However, at $B_z = 500$ mG and 1000 mG, the Ramsey interference is separated into two sets of fringes produced by $(-1, +1)$ and $(+1, -1)$ dark states.

Since Ramsey fringes are oscillatory, splitting between the fringes can cause ambiguity in resolving the fringe centers at small axial magnetic fields. At large magnetic field, the two fringe envelopes can be distinguished, showing two separated fringe centers (3.11(b,c)). Due to higher magnetic sensitivity, $lin \parallel lin$ excitation is also undesirable in Ramsey interference for producing high frequency stability in atomic clocks. The model shows that (σ^+, σ^+) or (σ^-, σ^-) excitation forms Ramsey interference in 0-0 dark state with low magnetic field sensitivity. Figure 3.12 shows Ramsey fringes generated by (σ^+, σ^+) excitation resonant with $|F' = 1\rangle$ and $|F' = 2\rangle$ states and for $B_z = 20$ mG. The non-zero magnetic field lifts the Zeeman degeneracy and allows one to

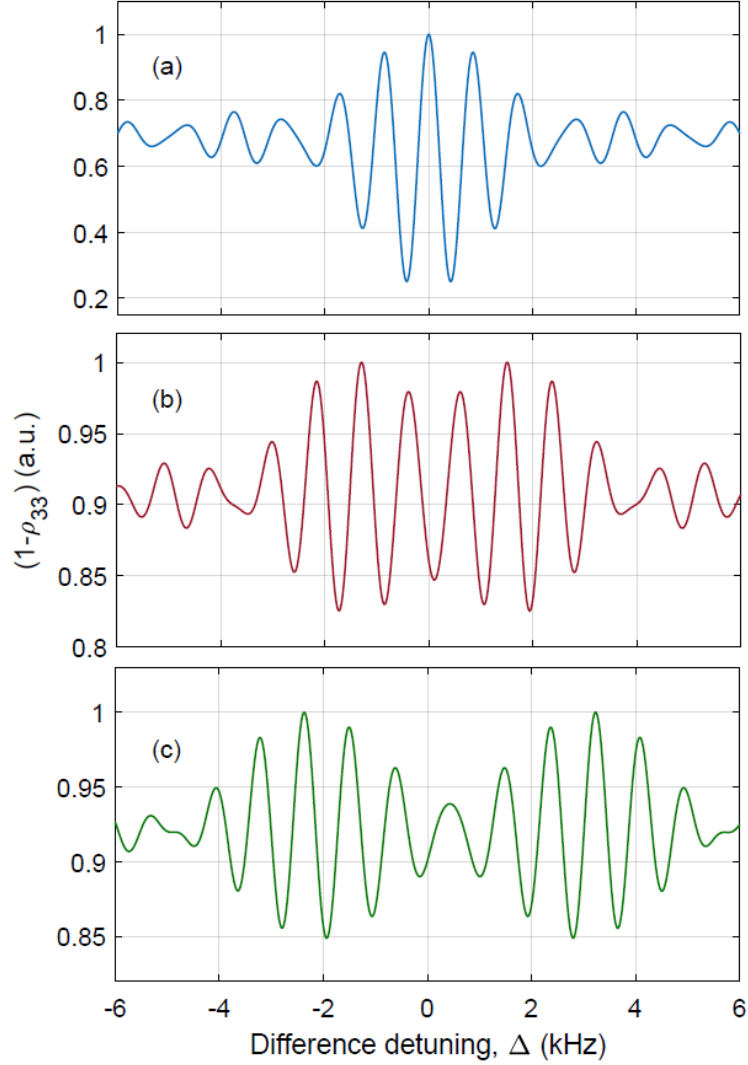


Figure 3.11: Splitting of Ramsey fringes formed by $lin \parallel lin$ excitation with axial magnetic fields at $B_Z =$ (a) 0, (b) 500 mG, and (c) 1000 mG. The following parameters were used in the calculation: $\tau_c = 400 \mu\text{s}$, $T = 1 \text{ ms}$, $\tau_q = 100 \text{ ns}$, $\Omega = \Gamma/60$, $\Gamma = 6 \text{ MHz}$, and $\gamma_1 = \gamma_2 = 0 \text{ Hz}$. For the purpose of visualization, the amplitudes are normalized.

observe Zeeman RR fringes, similar to Zeeman CPT resonances. The amplitude of Ramsey fringes formed at $\Delta = 0$ is found to be small for (σ^+, σ^+) excitation resonant with $|F' = 2\rangle$ state.

The work in this chapter addressed the viability of $lin \parallel lin$, (σ, σ) , and $lin \perp lin$ excitation schemes for producing narrow linewidth, high contrast, magnetically-insensitive CPT resonance in the D1 manifold of ^{87}Rb atoms. The performances of these schemes are studied theoretically.

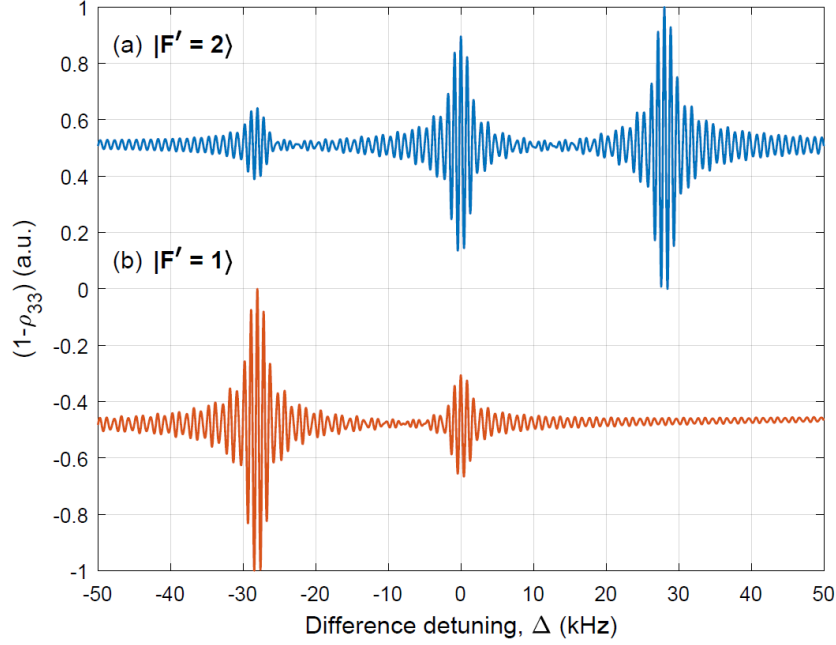


Figure 3.12: RR interference spectra generated by (σ^+, σ^+) polarized light resonant with the (a) $|F' = 2\rangle$ and (b) $|F' = 1\rangle$ state. This result shows Zeeman RR interference formed with $B_Z = 20$ mG. The following parameters were used in the calculation: $\tau_c = 400$ μ s, $T = 1$ ms, $\tau_q = 100$ ns, $\Omega = \Gamma/60$, $\Gamma = 6$ MHz, and $\gamma_1 = \gamma_2 = 500$ Hz. For the purpose of visualization, the amplitudes are normalized and offset.

Our results showed higher magnetic field sensitivity of the CPT resonance produced by $lin \parallel lin$ excitation. For (σ, σ) excitation, we found that the CPT contrast is dependent on the resonant excitation, which reached a maximum value 16.7% for resonant excitation with $|F' = 2\rangle$ state. The theoretical calculations showed that additional Zeeman CPTs could be formed in the presence of a transverse magnetic field component arising from beam alignment with respect to the cell. This simulation provides a more accurate representation of the atoms beyond what is possible with a three-level Λ -system.

CHAPTER 4: LIGHT SHIFT IN RAMAN-RAMSEY INTERFERENCE

A major source of error in atomic clocks is light shift (ac Stark shift). Characterization and understanding can only come from accurate representation of the system. This chapter addresses the problem of light shift through both three- and sixteen- level models demonstrated in the previous chapters.

Raman-Ramsey (RR) interference provides a new avenue for developing compact, high performance atomic clocks [45,48,65,82–85]. Experimentally, RR interference is produced by creating Raman excitation in a three-level Λ -type atomic medium using two optical fields separated in either space or time. In this case, two-photon resonant Raman excitation by the optical fields creates atomic coherence via CPT between the hyperfine ground states in the alkali atoms. Subsequently, RR interference is produced by virtue of an interaction-free evolution of the atoms between the separated optical fields. RR interference has been studied in different types of atomic media ranging from atomic beams and thermal vapor to cold atoms [24,83,84,86–98]. Among these, vapor cell-based RR interference is being studied with significant interest, particularly for developing compact atomic clocks with high frequency-stability performance.

When used as an atomic reference, RR interference offers the advantage of producing narrow-linewidth and high-contrast resonance. This accounts for improved short-term frequency stability of an RR clock which is directly proportional to the resonance linewidth, and inversely proportional to the signal contrast. The long-term frequency stability of the clock is usually dictated by the frequency shifts caused due to a number of factors such as laser frequency drift, laser intensity noise, variations in cell temperature, buffer gas pressure, external magnetic field,

etc. [33,42]. A fundamental limit on the long-term stability is imposed by the light shift. Light shift is caused by electric-dipole interaction between the atoms and the optical fields. Typically, the largest variation in light shift is caused by the fluctuations and drifts in the laser intensity and laser detuning. The slope of the light shift as a function of laser intensity (or laser detuning) affects the long-term stability of the clock.

The sensitivity of light shift to the laser parameters also depends on the type of excitation used in the clock. In many situations, it can be accurately calculated to predict the performance of the clock. For example, in the case of an optically-pumped atomic clock, light shift-related frequency instabilities can be comprehensively modeled by investigating laser interaction with a two-level atomic system [33,99]. Similarly, light shift in a CPT clock can also be modeled using a three-level system interacting with the continuous bichromatic laser fields [42,49,100–102]. The complexity of this model increases for a real atom which generally involves multiple-levels (e.g. hyperfine states and Zeeman sublevels) interacting with the bichromatic laser fields. Additionally, multiple sideband frequencies may need to be considered if a frequency-modulation technique is used to generate the beams in a CPT clock.

It is known that generation of RR interference involves CPT phenomenon, as shown earlier in chapter 2. However, light shift properties of CPT are not directly applicable in the case of RR interference because of the pulsed excitation mechanism used in the RR interference. In a seminal paper, Hemmer *et al* [50] first obtained a closed-form analytic expression for RR light shift by applying an adiabatic approximation. Their results revealed an important, but possibly counterintuitive property, that the RR light shift can be reduced (or suppressed) by utilizing a strong interaction in the first zone. This prediction was verified by experiments using a sodium atomic beam [50]. Unlike an atomic beam experiment, RR interference in the atomic vapor can be

influenced by several additional factors such as off-resonant excitations, rapid ground-state dephasing, and more significantly, by Doppler broadening. Presence of these factors can potentially change the properties of RR light shift for a vapor medium.

The purpose of this chapter is to investigate RR light shift using the computational model based on the density-matrix equations for a generalized three-level system without invoking the adiabatic approximation originally used by Hemmer *et al* [50]. The study also investigates RR light shift calculated using a comprehensive model for a multi-level (16-level) system. Eliminating the adiabatic approximation in a generalized three-level system, allows one to calculate RR light shift and its reduction to greater precision. Results using the model show the dependence of RR light shift on laser detuning and intensity. Results are also obtained to investigate RR phase shifts associated with coherent density-matrix elements as they are relevant to the detection of RR interference in transmission (or absorption).

4.1 Three-level model for Raman-Ramsey interference

Consider a two-photon resonant Raman excitation in a closed three-level Λ -system described earlier in chapter 2 and also shown in figure 4.1a. Such a Raman excitation can be formed in the D1 ($\lambda = 795$ nm) manifold of ^{87}Rb atoms. The Liouville density-matrix equation is used to describe the interaction of the optical fields with the three-level Λ -system. The formulation of the system of density-matrix equations (eqn. 2.18) is described earlier in chapter 2. The density matrix elements ρ_{ii} and ρ_{ij} ($i, j = 1, 2, 3$) correspond to atomic population and coherence between the energy-levels, respectively, and $\sum_{i=1}^3 \rho_{ii}$ is assumed to be constant for a closed system. RR interference is observed using a pulsed interrogation technique. Figure 4.1b shows a typical pulse sequence used in experiments, and also used here in the model to generate RR interference. This

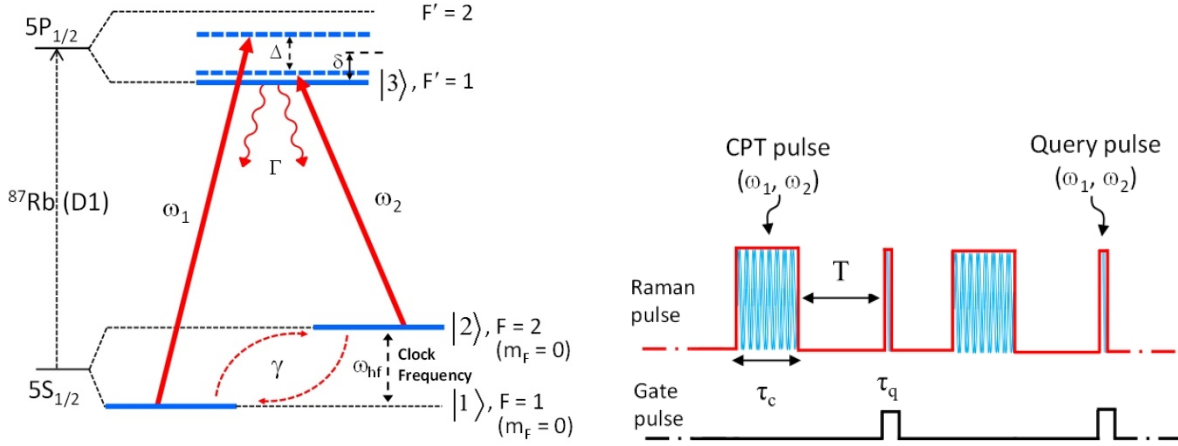


Figure 4.1: (a) Raman excitation in a three-level Λ -system formed in the energy levels of ^{87}Rb atoms, and (b) pulse sequence considered in the model for generating RR interference.

involves Raman interaction with a long pulse, known as the CPT pulse of duration τ_c , followed by a free-evolution time T , and another Raman interaction with a short pulse known as the query pulse of duration τ_q . A steady-state analysis cannot be used to investigate RR interference. Time-dependent density-matrix eqns. (2.18) need to be solved for three successive time intervals (τ_c , T , τ_q) in order to describe the evolution of all density-matrix elements and the dynamics of RR interference. It is possible to obtain analytical solutions to eqns. (2.18) by applying an adiabatic approximation to the evolution of the excited state $|3\rangle$. The analytical expression for the excited state population ρ_{33} at the end of interaction with the Ramsey pulse sequence is given by

$$\rho_{33}(\tau_c + T + \tau_q) = \alpha e^{-\alpha\Gamma\tau_q} [1 - (1 - e^{-\alpha\Gamma\tau_c}) |\sec(\varphi_{LS})| \cos(\Delta T - \varphi_{LS})] \quad (4.1)$$

where $\alpha = \Omega^2/(\Gamma^2 + 3\Omega^2 + 4\delta^2)$ represents the interaction with the CPT pulse, and Ω corresponds to the average Rabi frequency of the CPT pulse. It is also found from eqn. (4.1) that the center of RR interference i.e. $\cos(\Delta T - \varphi_{LS})$ is shifted from $\Delta = 0$ by a phase angle, φ_{LS} , due to light shift (or AC Stark shift), which is given by

$$\Delta v_{LS} = \frac{\varphi_{LS}}{2\pi T} = \frac{1}{2\pi T} \tan^{-1} \left[\left(\frac{e^{-\alpha' \Gamma \tau_c}}{1 - e^{-\alpha \Gamma \tau_c}} \right) (\rho_{11} - \rho_{22})^0 \sin(\alpha' \delta \tau_c) \right] \quad (4.2)$$

where $(\rho_{11} - \rho_{22})^0$ corresponds to the initial population difference between the ground states before excitation, and $\alpha' = \Omega^2 / (\Gamma^2 + 4\delta^2)$. This expression is obtained for equal Rabi frequencies (i.e. $\Omega_1 = \Omega_2 = \Omega$) of the Raman beams in pulsed excitation. It suggests that interaction with the CPT pulse is responsible for creating light shift in RR interference. The arctangent relation also implies that RR light shift can be reduced (or suppressed) by choosing a sufficiently strong interaction with the CPT pulse satisfying the condition $\alpha' \Gamma \tau_c \gg 1$ or, equivalently, by increasing the integrated CPT pulse intensity ($\Omega^2 \tau_c$). Under ideal conditions, light shift can also be completely cancelled if $(\rho_{11} - \rho_{22})^0$ or δ is equal to zero.

Frequency shift produced by RR light shift can be made small by simply increasing the free-evolution time T which, in practice, is limited by the ground-state decoherence γ ($T < 1/\gamma$). The above discussed properties of RR light shift can also be graphically illustrated by using a Bloch vector representation [52,79]. Recall that in a vapor medium, RR interference is usually detected in transmission (or absorption) as opposed to the fluorescence. Absorption is described by the coherent density-matrix terms $\text{Im}(\rho_{13})$ and $\text{Im}(\rho_{23})$, which are given by

$$\begin{aligned} \text{Im} \begin{pmatrix} \rho_{13} \\ \rho_{23} \end{pmatrix} &= \pm \alpha' e^{-\alpha' \Gamma (\tau_c + \tau_q)} (\rho_{11} - \rho_{22})^0 \cos(\alpha' \delta \tau_c) \left[\frac{(\delta \pm \frac{\Delta}{2})}{\Omega} \sin(\alpha' \delta \tau_q) - \frac{\Gamma}{2\Omega} \cos(\alpha' \delta \tau_q) \right] \\ &- \frac{\Gamma}{2\Omega} \alpha' (1 - 3\alpha) e^{-\alpha \Gamma \tau_q} + \left(\frac{\Gamma}{2\Omega} \right) \alpha' (1 - e^{-\alpha \Gamma \tau_c}) e^{-\alpha \Gamma \tau_q} (1 - 3\alpha) |\sec(\varphi_{LS})| \cos(\Delta T - \varphi_{LS}) \quad (4.3) \\ &\mp \alpha' (1 - e^{-\alpha \Gamma \tau_c}) e^{-\alpha' \Gamma \tau_q} \left[\frac{(\delta \pm \frac{\Delta}{2})}{\Omega} \cos(\alpha' \delta \tau_q) + \frac{\Gamma}{2\Omega} \sin(\alpha' \delta \tau_q) \right] |\sec(\varphi_{LS})| \sin(\Delta T - \varphi_{LS}) \end{aligned}$$

Unlike RR interference described in eqn. (4.1), eqn. (4.3) is found to contain oscillating quadrature signals (third and fourth terms). One can simplify these two terms in eqn. (4.3) to find an effective phase shift at the fringe center individually for $\text{Im}(\rho_{13})$ and $\text{Im}(\rho_{23})$, which are given by

$$\begin{pmatrix} \varphi_{13} \\ \varphi_{23} \end{pmatrix} = \pm \tan^{-1} \left[\frac{(2\delta \pm \Delta) \cos(\alpha' \delta \tau_q) + \Gamma \sin(\alpha' \delta \tau_q)}{\Gamma (1 - 3\alpha)} e^{-(\alpha' - \alpha)\Gamma \tau_q} \right] \quad (4.4)$$

The phase shifts φ_{13} and φ_{23} are created by non-zero laser detuning δ and finite duration of the query pulse. If the interference is detected using the absorption of only one Raman beam (while both Raman beams are used in the CPT zone as well as the query zone), these phase shifts will manifest in RR interference as $\cos \left[\Delta T - \varphi_{LS} - \begin{pmatrix} \varphi_{13} \\ \varphi_{23} \end{pmatrix} \right]$. On the other hand, if RR interference is detected via absorption of both Raman beams in the query zone, described by the term $\text{Im}(\rho_{13} + \rho_{23})$, eqn. (4.3) shows that one of the oscillating quadrature signals cancels due to the fact that φ_{13} and φ_{23} have opposite signs and nearly equal values for $\Delta \ll (\delta, \Gamma)$. Thus, RR interference detected using both Raman beams will only be affected by the light shift φ_{LS} similar to the interference described by ρ_{33} . Eqn. (4.4) also provides information regarding the dependence of phase shifts φ_{13} and φ_{23} on laser intensities, detuning, and pulse parameters, etc.

4.2 Computational light shift results and discussions

The density-matrix equations given by eqns. (2.18) in chapter 2 were solved for pulsed excitation to investigate the properties of RR interference. The computational eigenvalue method was used to solve the time-dependent density-matrix equations. The following initial conditions were used prior to the CPT pulse: $\rho_{ij}^0 (i \neq j) = \rho_{33}^0 = 0$, $(\rho_{11} + \rho_{22})^0 = 1$, and $(\rho_{11} - \rho_{22})^0 = \rho^0$, where ρ^0 is assigned a non-zero value to create unequal initial population between the ground-states. Solutions describing $\rho_{33}(\tau_c + T + \tau_q)$, $\text{Im}[\rho_{13}(\tau_c + T + \tau_q)]$ and $\text{Im}[\rho_{23}(\tau_c + T + \tau_q)]$ are obtained by solving the density matrix equations. RR interference is generated by repeating the computation for different values of Δ around $\Delta = 0$. Also, all frequency parameters involved in

the system of density matrix equations are normalized with respect to Γ . Phase shift in the RR fringe is determined by measuring the frequency shift at the fringe center, and using the frequency width of the fringes. A phase shift measurement accuracy of about 1.57 mrad has been achieved by choosing the step-size in Δ to be 250 mHz, and fringe-width $\Delta\nu_{RR} = 500$ Hz. One can also compute an integrated solution (as in experiments [48,86]). For example, $\int_{\tau_c+T}^{\tau_c+T+\tau_q} \rho_{33} dt$ represents an integrated fluorescence over the duration, τ_q , of the query pulse. Although this helps in increasing the SNR in the detection of RR fringes, the phase shift measured from an integrated solution is found to be the same as the one obtained using the instantaneous values. Hence, the computational results presented here are obtained using the instantaneous values of the density-matrix elements.

Next, the phase shifts associated with RR interference are calculated by considering only single (or zero)-velocity group atoms, and compared with the analytic results described section 4.1. Figure 4.2 shows the phase shift measured using ρ_{33} as a function of the average laser frequency detuning, δ . The result is obtained by using different average Rabi frequencies (or intensities) of the CPT pulse, and by considering equal intensities for the Raman beams in the CPT pulse. The following pulse parameters were used: $\tau_c = 200 \mu\text{s}$, $T = 1$ ms and $\tau_q = 100$ ns. An initial ground-state population difference corresponding to $\rho^0 = 0.2$ has been used. The result illustrates reduction in phase/light shift due to pulse saturation (i.e. $\Omega\tau_c \gg 1$) for higher light intensities. The result also shows the comparison between the computational results (solid line) and the analytic results obtained using adiabatic approximation (dashed line). The computational results estimate RR light shift more accurately than those obtained using the adiabatic approximation. RR light shift gets adequately suppressed for $\Omega \geq \Gamma/20$ over a range of δ close to $-\Gamma \leq \delta \leq \Gamma$. Light shift

in the unsaturated region is found to oscillate (between positive and negative values), exhibiting nonlinear dependence on δ . These oscillations can be physically explained by the spiraling of the Bloch vector around its steady-state value in a Bloch vector model [52,79]. The results in figure 4.2 also provide information regarding the long-term frequency stability of a Raman clock limited by the variation in δ , which can be potentially caused by sources such as laser drift, jitter, and linewidth broadening.

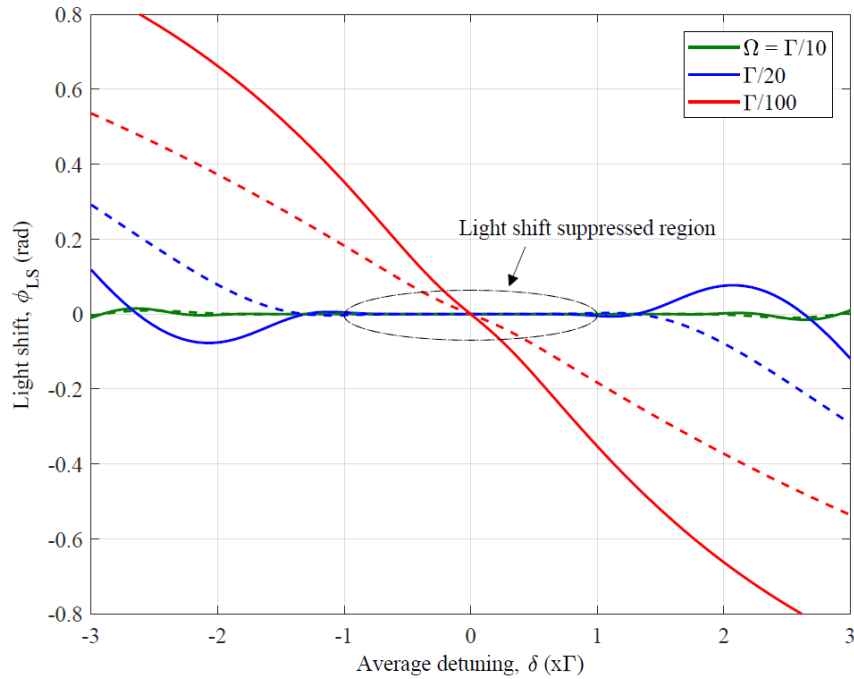


Figure 4.2: Light shift, ϕ_{LS} versus δ calculated using ρ_{33} . Solid lines represent numerically computed values, and dashed lines show analytical values given in eqn. (4.2). The following parameters were used in the calculations: $\tau_c = 200 \mu\text{s}$, $T = 1 \text{ ms}$, $\tau_q = 100 \text{ ns}$, $\Omega_1 = \Omega_2$ ($\rho_{11} - \rho_{22}$)⁰ = 0.2 and $\gamma = 0$. The encircled region shows the region of light shift suppression.

The effect of decoherence due to the incoherent collisional exchange of population between the two ground-states on the RR light shift has also been studied here. The effect of this decoherence is found to be only pronounced in the region where light shift was previously suppressed under the zero-decoherence condition, and more so, for unequal Rabi frequencies (i.e.

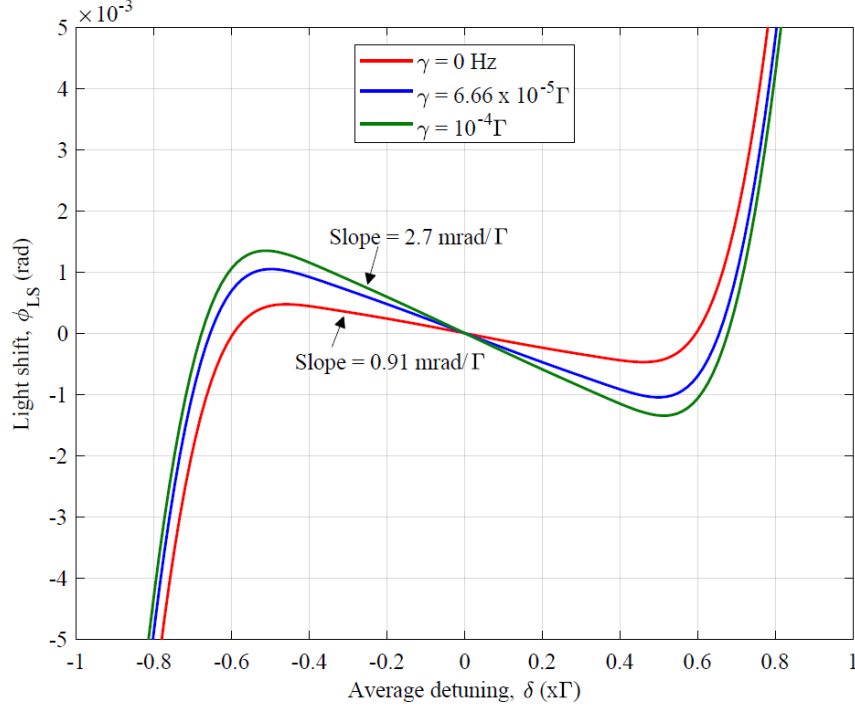


Figure 4.3: Effect of decoherence γ on the light shift, ϕ_{LS} . The following parameters were used in the calculations: $\tau_c = 200 \mu\text{s}$, $T = 1 \text{ ms}$, $\tau_q = 100 \text{ ns}$, $\Omega_1 = \Gamma/5$, $\Omega_2 = 0.75 \Omega_1$, and $(\rho_{11} - \rho_{22})^0 = 0.2$.

$\Omega_1 \neq \Omega_2$) of the CPT pulse. Figure 4.3 shows RR light shifts calculated by choosing $\Omega_1 = \Gamma/5$ and $\Omega_2 = 0.75 \Omega_1$ ($\Omega = \Gamma/5.65$), and by changing the exchange rate γ from zero to $10^{-4}\Gamma$. Although the light shift still remains quite well suppressed over the range $-\Gamma \leq \delta \leq \Gamma$, the slope of light shift is found to increase by nearly three times with increasing γ . Choosing higher values of γ produces significantly modified light shift and, simultaneously, a reduction in RR fringe contrast or signal-to-noise ratio (SNR). The fringe-width $\Delta\nu_{\text{RR}}$ observed in RR interference is also ultimately limited by γ which, in experiments, can be made small (i.e. $\gamma \ll \Gamma$) by using buffer-gas loaded cells.

Figure 4.4 shows the computed RR light shift as a function of Ω of the CPT pulse. RR light shift is close to zero over the whole range of Ω when δ is set equal to zero. This also agrees with the prediction from eqn. (4.2). For large, non-zero values of δ (e.g. $\delta = \pm\Gamma$), oscillation in light

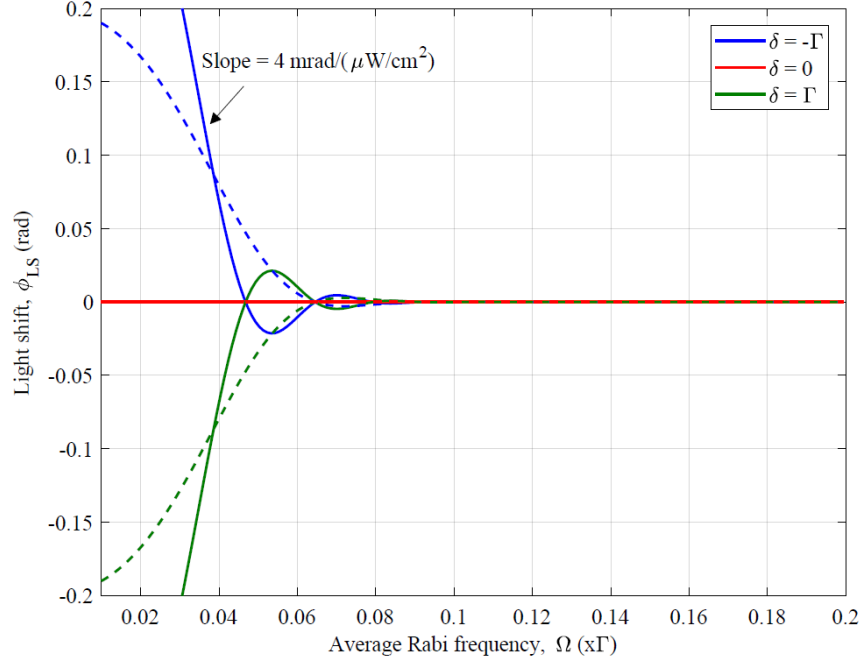


Figure 4.4: RR light shift calculated as a function of the average Rabi frequency, Ω , of the CPT pulse. Solid lines show numerical values, and dashed lines show analytical values obtained using eqn. (3). The following parameters were used in the calculations: $\tau_c = 100 \mu\text{s}$, $T = 1 \text{ ms}$, $\tau_q = 100 \text{ ns}$, $\Omega_1 = \Omega_2 = \Omega$, $(\rho_{11} - \rho_{22})^0 = 0.2$ and $\gamma = 0$. For $\delta = 0$, both numerical and analytical results show zero light shift over the entire range of intensity as expected.

shift with Ω is observed presumably due to weak excitation with the CPT pulse. At higher Ω (or intensity) of the CPT pulse, amplitudes of these oscillations quickly diminish by virtue of the strong interaction. Similar oscillations (shown by dashed lines) are also created by the presence of the term $\sin(\alpha'\delta\tau_c)$ in eqn. (4.2). The result once again shows that RR light shift can be significantly small under strong excitation conditions. Considering mono-velocity atoms and assuming a saturation intensity, I_{sat} , of 3 mW/cm^2 , one can use this result to calculate RR light shift as a function of average intensity, $I \simeq (\Omega/\Gamma)^2 I_{\text{sat}}$, of the CPT pulse. One can also estimate the slope of RR light shift in the unsaturated or saturated regions by using this plot.

Figure 4.5 is a color-coded map generated using the computation to illustrate the properties of RR light shift as a function of both the average detuning, δ , and intensity, I , of the CPT pulse.

The uniformly colored region in the plot where the pulse saturation condition ($\Omega\tau_c \gg 1$) is satisfied, corresponds to a small (close to zero) value of RR light shift. The plot also shows oscillations in light shift (as color change) at lower intensities below $500 \mu\text{W}/\text{cm}^2$ and for $4 \leq |\delta| \leq 18 \text{ MHz}$.

The range of (δ and I) chosen in this map are realistic and can arise in the experiment due to possible laser drift, linewidth broadening, lock instability and/or intensity noise, etc. Therefore, it can be used to get a first-hand estimate of the light shift and long-term frequency stability of the RR clock. For example, the slope of RR light shift can be reduced to an extremely small value below $0.001 \text{ Hz mW}^{-1} \text{ cm}^2$ by using a strong excitation condition.

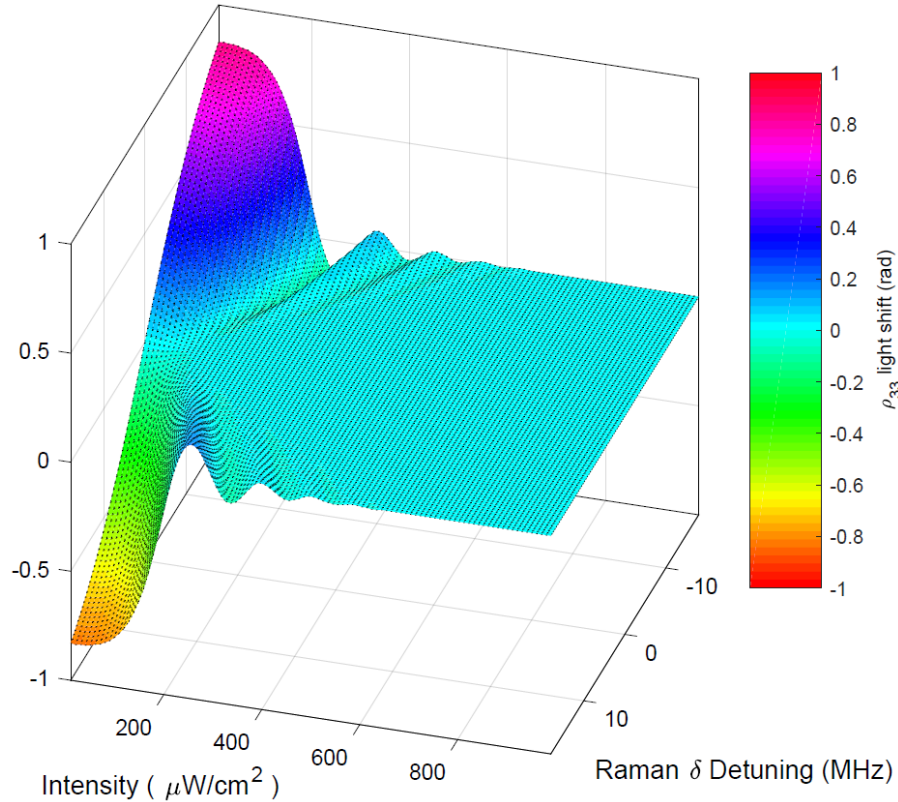


Figure 4.5: Color-coded 3D plot showing light shift, φ_{LS} as functions of average detuning, δ and intensity, I of the CPT pulse. Saturation intensity ($I_{\text{sat}} = 3 \text{ mW}/\text{cm}^2$) for a rubidium atom is considered in converting Ω to an intensity axis. The following parameters were used in the calculations: $\tau_c = 100 \mu\text{s}$, $T = 1 \text{ ms}$, $\tau_q = 100 \text{ ns}$, $\Omega_1 = \Omega_2$, $(\rho_{11} - \rho_{22})^0 = 0.2$ and $\gamma = 0$.

The results presented so far describe RR light shift by using the excited-state population term ρ_{33} . This term only gives a measure of fluorescence intensity for describing RR interference produced in an atomic beam experiment. The computational model has also been used to calculate RR light shift associated with the coherence terms $\text{Im}(\rho_{13})$, $\text{Im}(\rho_{23})$, and $\text{Im}(\rho_{13} + \rho_{23})$ which correspond to detection of RR interference using transmission/absorption of the beams. Figure 4.6

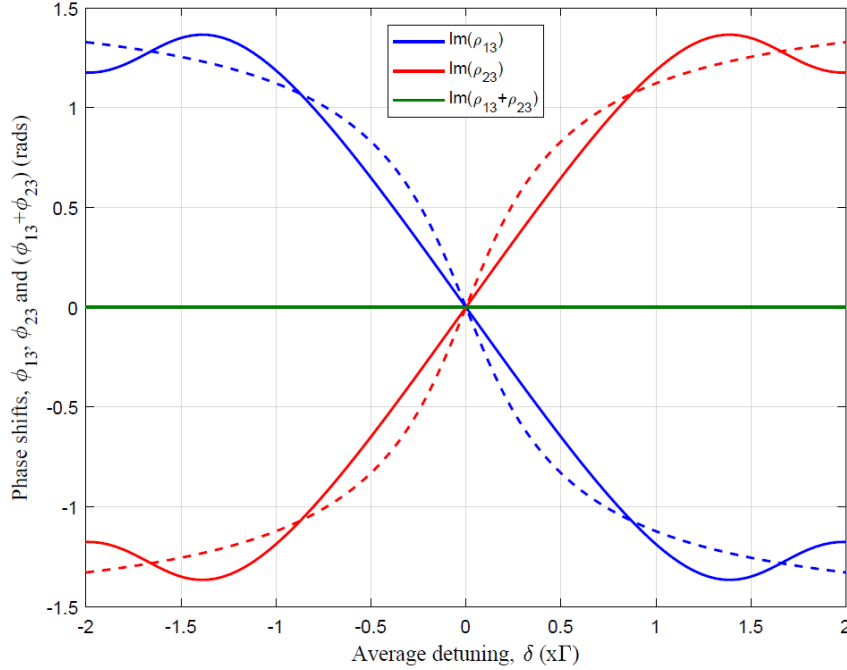


Figure 4.6: Phase shifts associated with $\text{Im}(\rho_{13})$, $\text{Im}(\rho_{23})$, and $\text{Im}(\rho_{13} + \rho_{23})$ plotted as a function of δ . Solid lines represent numerical values, and dashed lines show analytical results. The measured phase shifts cancel each other in $\text{Im}(\rho_{13} + \rho_{23})$. The following parameters were chosen in this calculation: $\tau_c = 200 \mu\text{s}$, $T = 1 \text{ ms}$, $\tau_q = 100 \text{ ns}$, $\Omega_1 = \Omega_2 = \Gamma/5$, $(\rho_{11} - \rho_{22})^0 = 0.2$ and $\gamma = 0$.

shows the phase shifts associated with the coherence terms, plotted as a function of δ . In case of $\text{Im}(\rho_{13} + \rho_{23})$, the phase shift, ϕ_{LS} , due to RR light shift is suppressed to a negligibly small value because of pulse saturation since Ω is set equal to $\Gamma/5$. However, large phase shifts are still produced in $\text{Im}(\rho_{13})$ and $\text{Im}(\rho_{23})$. This is in sharp contrast to the phase shift observed in the

population term ρ_{33} . The origin of these phase shifts were predicted earlier by the analytic theory presented in eqn. (4.4).

The dashed line shows the analytic result in comparison with the computed results. In both cases, a large slope with respect to δ is observed. These phase shifts increase with δ , change sign around $\delta = 0$ and become large (close to $\pm \pi/2$) near $\delta = \pm \Gamma$. It is important to note that since the phase shifts measured in $\text{Im}(\rho_{13})$ and $\text{Im}(\rho_{23})$ are exactly opposite in sign, they cancel each other in the term $\text{Im}(\rho_{13} + \rho_{23})$ as shown in figure 4.6. These results establish the fact that phase shift observed in RR interference is dependent on how the fringe is detected using the transmitted Raman beams. The frequency error caused by this kind of phase shift in a cell-based RR clock can be cancelled by detecting RR fringes via the combined absorption of both Raman beams in the query zone.

4.3 Light shift in multi-level atomic model

The multi-level computational model (discussed in chapter 3) has been used to investigate light shift in RR interference. This model includes all magnetic sublevels in the D1 manifold of ^{87}Rb atoms to show how the properties of RR light shift established here get modified due to the presence of additional off-resonant excitations. Figure 4.7 shows the comparison of light shift between the three-level (dashed) and multi-level (solid) models. The results show a small, but important difference between light shift characteristics. The result obtained from three-level model indicates a reduction in phase/light shift due to pulse saturation which occurs for higher Rabi frequencies ($\Omega \geq \Gamma/20$) or higher light intensity of the CPT pulse. In this case, RR light shift is found to be adequately suppressed over a range of δ close to $-\Gamma \leq \delta \leq \Gamma$.

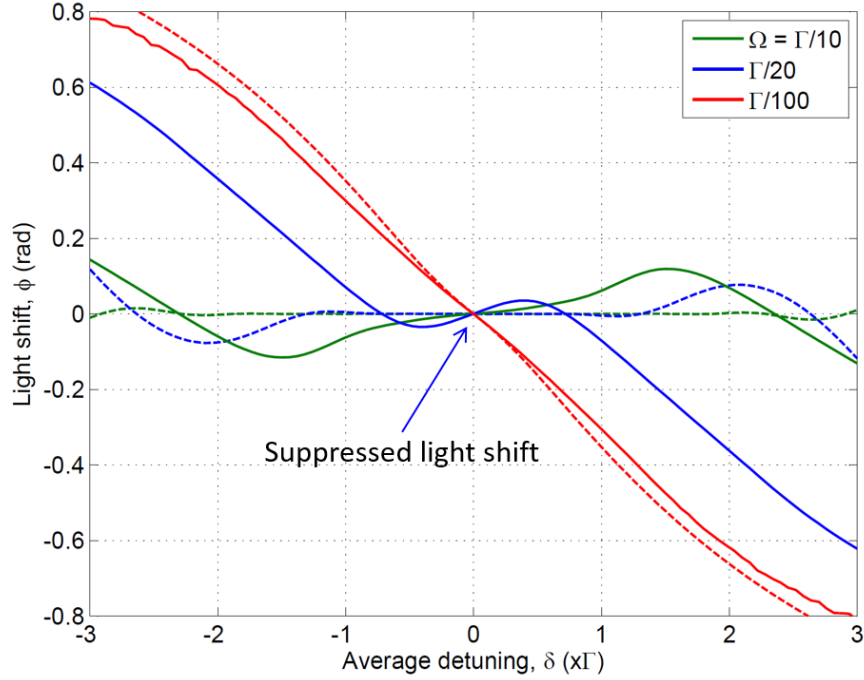


Figure 4.7: Light shift, φ_{LS} versus δ calculated using ρ_{33} . Solid lines represent the numerically computed values from the multi-level model, and dashed lines show the three-level model values. The following parameters were used in the calculations: $\tau_c = 200 \mu\text{s}$, $T = 1 \text{ ms}$, $\tau_q = 100 \text{ ns}$, $\Omega_1 = \Omega_2 (\rho_{11} - \rho_{22})^0 = 0.2$ and $\gamma = 0$. A shift of $0.5 \text{ rad} \equiv 80 \text{ Hz}$.

The sixteen-level calculation shows a similar result, but gives a more accurate result for predicting light shift in real atoms. In this case, it is found that higher CPT pulse intensity is needed to reach saturation, and suppress the light shift to a small value. Light shift in the unsaturated region oscillates and exhibits a nonlinear dependence on δ .

Figure 4.8 shows calculated RR light shift as a function of average Rabi frequency, Ω (or intensity) of the CPT pulse. The result again shows a comparison between three-level model (dashed line) and sixteen-level model (dotted line). In both models, RR light shift is found to be nearly zero over the entire range of Ω when δ is set precisely equal to zero. This agrees with the analytical prediction which was discussed previously. For large, nonzero values of δ (e.g. $\delta = \pm\Gamma$),

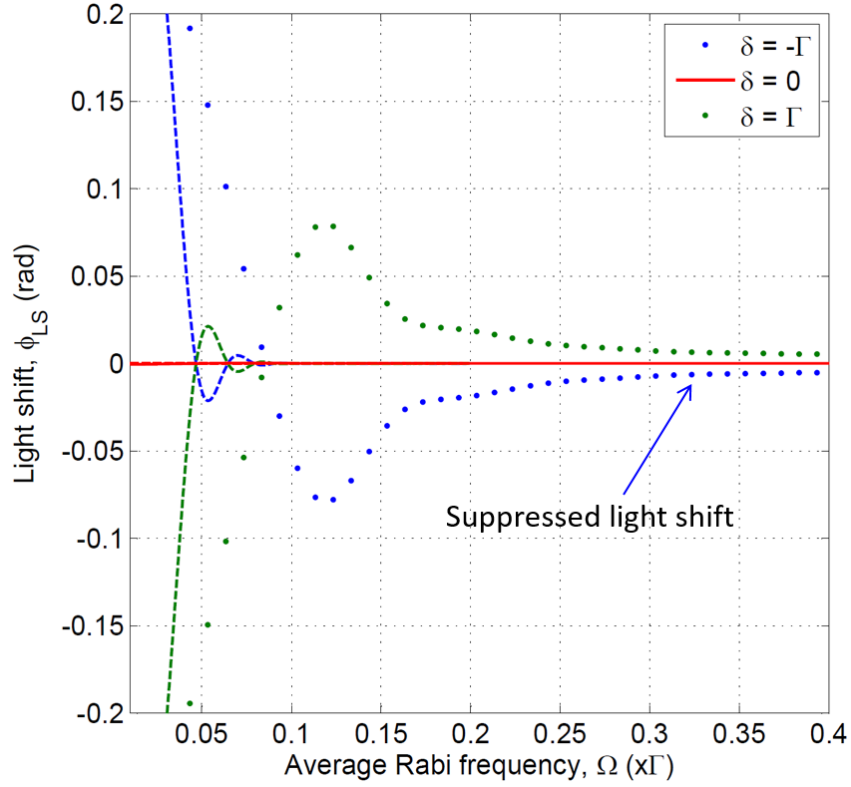


Figure 4.8: RR Light shift calculated as a function of average Rabi frequency, Ω , of the CPT pulse. Dotted lines represent the numerically computed values from the sixteen-level model, and dashed lines show the three-level model values. The following parameters were used in the calculations: $\tau_c = 100 \mu\text{s}$, $T = 1 \text{ ms}$, $\tau_q = 100 \text{ ns}$, $\Omega_1 = \Omega_2$ ($\rho_{11} - \rho_{22}$)⁰ = 0.2 and $\gamma = 0$.

oscillation in light shift with Ω is observed in both models due to weak Raman excitation with the CPT pulse.

At higher Ω (or intensity) of the CPT pulse, amplitudes of these oscillations are found to diminish rapidly in case of three-level model by virtue of strong interaction. However, the amplitude of light shift oscillation is found to be much larger in the sixteen-level case. The period of oscillation is also found to be much longer in this case, possibly due to the presence of multiple off-resonant excitations. However, both models give rise to the same conclusion that RR light shift can be reduced to a small value by using a strong initial CPT pulse. The sixteen-level results, in

general, provide more accurate information regarding the long-term frequency stability of the Raman clock, limited by sources such as laser drift, jitter, and linewidth broadening etc.

4.4 Velocity averaging

Velocity averaging is performed to account for the effect of atomic motion. The computational model is generalized to investigate the RR phase/light shift in the case of Doppler-broadening due to atomic motion. This is done by modifying the single-photon detuning terms in the density matrix equations as $\delta'_{1,2} = \delta_{1,2} \pm \omega_{1,2}(v/c)$ for the individual velocity-groups, and performing a weighted-average of the RR fringes calculated for each individual velocity-group. The weighting is a 1D Maxwell-Boltzmann velocity distribution described by the expression $(1/\sqrt{2\pi}v_p) \exp(-v^2/v_p^2)$, where $v_p = \sqrt{2k_B T/m}$ is the most probable velocity corresponding to atomic mass, m , and sample temperature, T and k_B is the Boltzmann constant. First, the effect of velocity-averaging is shown on the CPT resonance which is created using the three-level model and calculated using the time-dependent solutions to density-matrix equation by assuming interaction with a long CPT pulse of duration τ_c and setting T and τ_q to zero.

As shown in Figure 4.9, velocity-averaging reduces the linewidth of CPT resonance. This rather counter-intuitive result can be understood as follows. First, note that because the Raman beams are co-propagating, the differential Doppler shift is very small. Second, the linewidth for a CPT resonance is determined predominantly by the rate of optical pumping into the dark state. This rate is largest for the zero-velocity atoms, given by $\Omega^2\Gamma/2(\Gamma^2 + 2\Omega^2)$ and is reduced for non-zero velocity atoms by a factor of $(\Omega^2 + \Gamma^2)/(\Gamma^2 + \Omega^2 + 4\delta_{DS}^2)$ where δ_{DS} is the common-mode Doppler shift for these atoms.

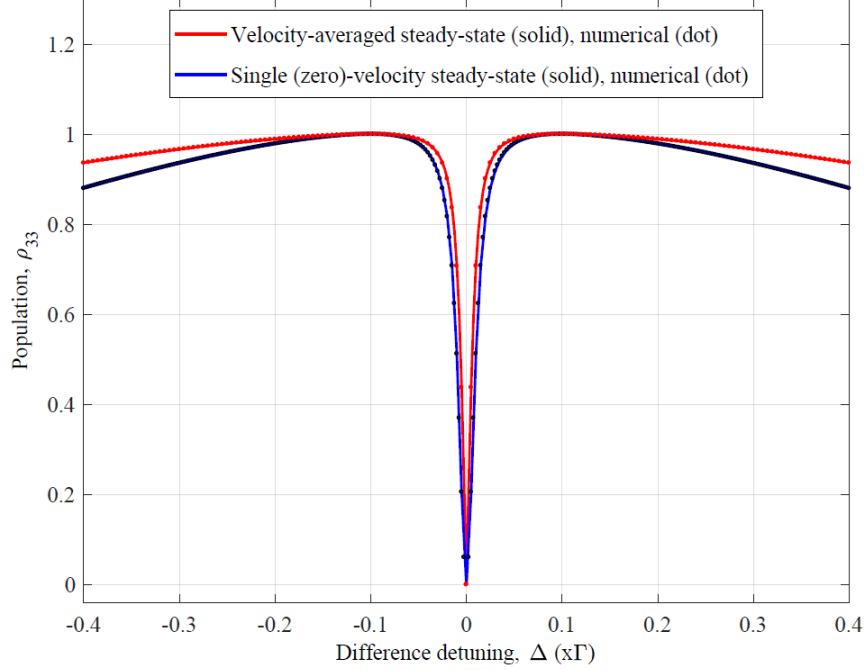


Figure 4.9: Line-shape of CPT resonance plotted as a function of Δ . Solid lines represent calculated line-shapes using the solutions to steady-state density-matrix equations with and without velocity-averaging, respectively. Filled dots show the match with the computational model using a long CPT pulse, $\tau_c = 2000 \mu\text{s}$, and parameters, $T = \tau_q = 0$, $\delta = 0$, $\Omega_1 = \Omega_2 = \Gamma/5$ and $\gamma = 0$. The resonance dip is normalized to show effective narrowing due to velocity-averaging.

A Doppler-broadening close to a frequency-width 1 GHz is considered to simulate the effect of thermally-distributed atoms in a warm rubidium vapor cell. The line-shape of CPT resonance shown in figure 4.9, is calculated using the ρ_{33} term. Unlike CPT, the line-shape of RR fringes (not shown) remain virtually unchanged due to velocity-averaging, because of the fact that the differential Doppler broadening is negligibly small. For Ramsey interference, the time separation, T , is a fixed parameter and remain the same for all velocity group atoms. This is in contrast to the two-zone RR interference produced in an atomic beam, where velocity averaging can cause rapid decay of fringe amplitude since T varies significantly with atomic velocity.

Velocity averaging has also been extended to the multi (sixteen)-level model. This is achieved the same way as the three-level model i.e. by modifying the single-photon detuning terms

in the sixteen-level density matrix equations as $\delta'_{1,2} = \delta_{1,2} \pm \omega_{1,2}(v/c)$, and performing a weighted-average using the Maxwell-Boltzmann velocity distribution.

Figure 4.10 shows the velocity-averaged CPT resonance produced around $\Delta = 0$, represented by the sum of the populations in states 9 through 11 (i.e., $\sum_{i=9}^{11} \rho_{ii}$), using steady-state as well as time-dependent solutions, for excitation using \hat{x} -polarized *lin* || *lin* CPT fields. The CPT fields were chosen to be resonant with the $|F' = 1\rangle$ state. Velocity averaging showed

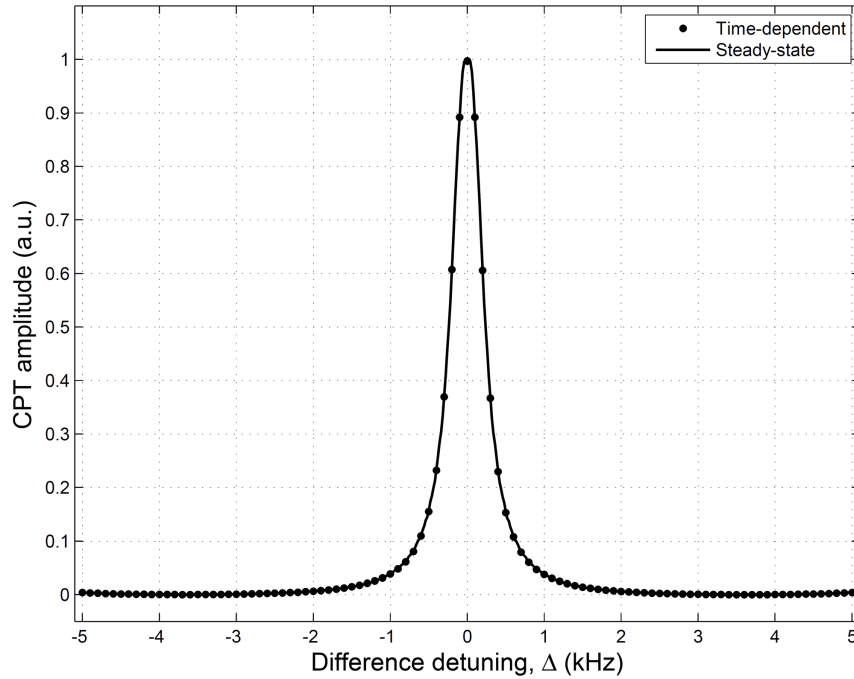


Figure 4.10: Calculated velocity-averaged CPT resonance showing a close match between the steady-state and time-dependent solutions. This result considers \hat{x} -polarized *lin* || *lin* excitation resonant with the $|F' = 1\rangle$ state and uses the following parameters in the calculation: $B_z = 5$ mG, $\Omega_1 = \Omega_2 = \Gamma/60$, $\Gamma = 6$ MHz, and $\gamma_1 = \gamma_2 = 0$.

narrowing of the CPT resonance similar to the result shown in figure 4.9. Significant change in the line-shape (i.e. deviation from the single-velocity Lorentzian line-shape) of CPT resonance is also observed. For this simulation, Rabi frequencies corresponding to $\Omega_1 = \Omega_2 = \Omega \equiv \sqrt{(|\Omega_1|^2 + |\Omega_2|^2)}/2 = \Gamma/60$ were used. For an ideal three-level system, with the Rabi frequency for leg one being $\Omega_1 \ll \Gamma$ and that for the leg two being $\Omega_2 \ll \Gamma$, the linewidth of the

CPT signal is expected to be $\sim \Omega^2 / \Gamma$. For $\Gamma = 6$ MHz, the linewidth for an ideal CPT system would be ~ 1.7 kHz. The linewidth in figure 4.10 is seen to be somewhat smaller: ~ 0.6 kHz.

This is due to several factors. First, note that Ω_1 and Ω_2 are defined to be Rabi frequencies corresponding to transitions with normalized matrix elements of unity values. However, the actual matrix elements involved are significantly smaller. Second, the fields are detuned with respect to the $|F' = 2\rangle$ state; the linewidth of a CPT resonance decreases when the excitation is detuned with respect to the intermediate state. Third, because of the velocity spread, most atoms are detuned away from optical resonance.

As in chapter 3, the velocity-averaged solutions using the steady-state and time-dependent models also show an excellent match in figure 4.10. A near steady-state solution is obtained from the time-dependent model by considering temporal Raman excitation with a long CPT pulse ($\tau =$

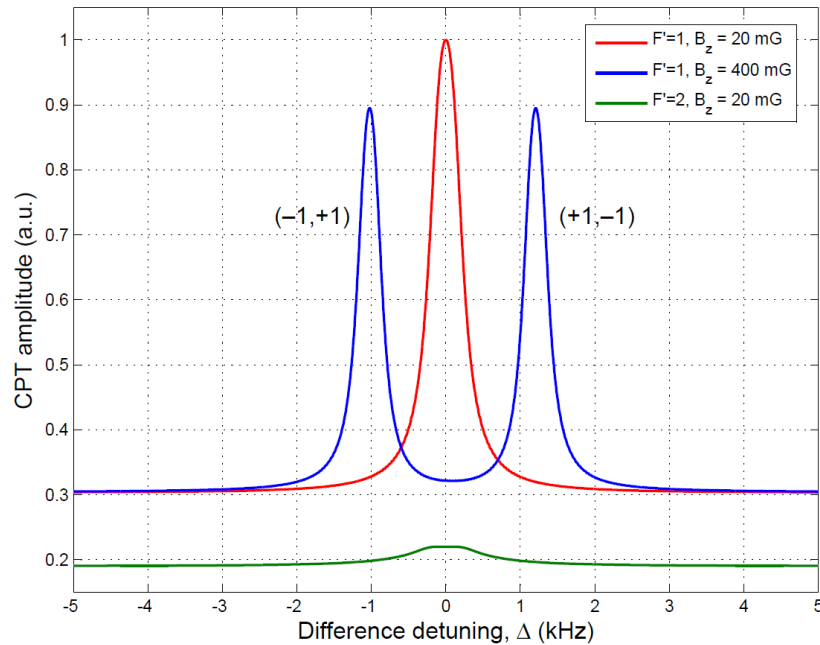


Figure 4.11: Splitting of the central CPT resonance formed by $lin \parallel lin$ excitation at higher axial magnetic field. The following parameters were used in the calculation: $\Omega_1 = \Omega_2 = \Gamma/60$, $\Gamma = 6$ MHz, and $\gamma_1 = \gamma_2 = 0$.

2 ms). The time-dependent model is extensively used in simulating pulsed CPT excitation which produces Raman-Ramsey interference. Similarly, figure 4.11 shows the velocity averaged CPT resonance produced by $lin \parallel lin$ excitation around $\Delta = 0$ for $B_z = 20$ mG and 400 mG, for resonant excitation with the $|F' = 1\rangle$ excited state, and for $B_z = 20$ mG for resonant excitation with the $|F' = 2\rangle$ excited state. Such a scheme automatically prevents the formation of trap states due to the simultaneous presence of σ^+ and σ^- excitations. As such, the population decay rates for the ground states are taken to be $\gamma_1 = \gamma_2 = 0$ in this case; non-vanishing values of these rates are only used when necessary for preventing trap states, as in the case for purely left circular or purely right circular excitations, to be discussed next.

Figure 4.12 shows the velocity averaged CPT spectrum generated by (σ^+, σ^+) polarized light for $B_z = 20$ mG and resonant excitation with $|F' = 2\rangle$. The population decay rates for the ground states are taken to be $\gamma_1 = \gamma_2 = 3$ Hz. In addition to the central CPT resonance at $\Delta = 0$, strong $(-1, -1)$ and $(+1, +1)$ Zeeman CPT resonances are formed at $\Delta = \pm 2\Delta_z$, where $\Delta_z \equiv g_F \mu_B B_z$, by a pair of Zeeman-shifted ground-state sublevels $|F = 1, m_F = -1\rangle, |F = 2, m_F = -1\rangle$ and $|F = 1, m_F = +1\rangle, |F = 2, m_F = +1\rangle$. The result is similar to the result shown in figure 3.9 except that narrowing of CPT resonances are observed due to velocity averaging in figure 4.12. The figure also shows the CPT spectrum due to TMF arising from a vector magnetic field \vec{B} used in the calculation with its magnitude $B = 20$ mG and angle (b) 5° (c) 10° with respect to the direction of beam propagation in the cell.

Figure 4.13 shows computationally measured RR fringe shift obtained using velocity-averaging in a three-level model. For comparison, the figure also shows the phase shifts measured for two non-zero, single-velocity groups corresponding to $\mathbf{k} \cdot \mathbf{v} = \pm 0.2\Gamma$ and $\pm\Gamma$, respectively. Velocity-averaging is found to produce a phase shift (slope $\simeq 0.12 \mu\text{rad}\cdot\text{Hz}^{-1}$ for Rb) that increases

linearly with δ . Even though this is an undesirable effect, the result shows a behavior which is expected from a Doppler-broadened medium.

The following physical argument supports this result: individual velocity-group atoms experience different velocity-induced phase shifts since the Raman detuning, Δ , gets modified as $\Delta' \rightarrow \Delta - (k_1 - k_2)v$ and $k_i = \omega_i/c$, where $i = 1,2$ due to the differential (or residual) Doppler shift caused by the frequency mismatch between the Raman beams. If $\delta = 0$, this creates

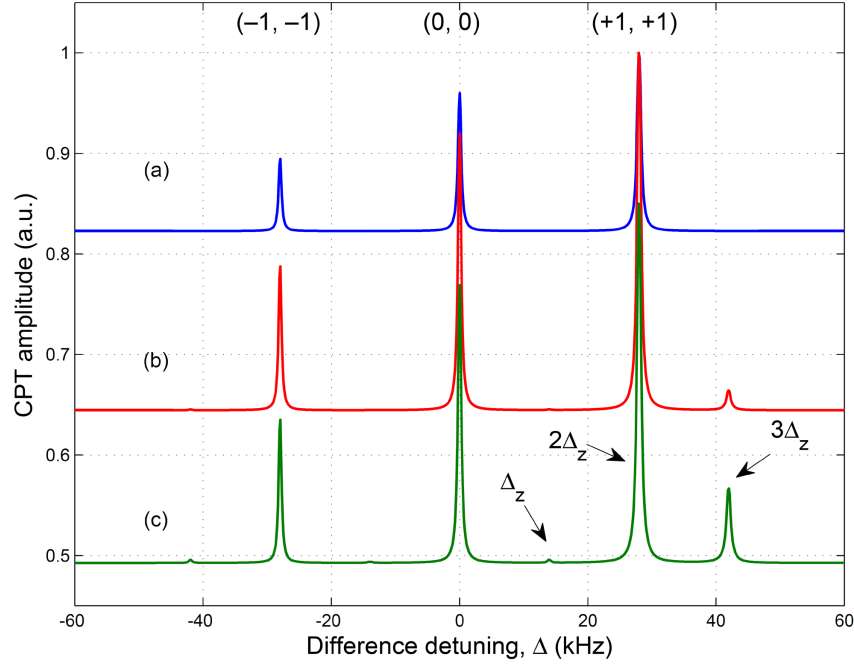


Figure 4.12: CPT spectrum generated by (σ^+, σ^+) polarized light resonant with the $|F' = 2\rangle$ state. The result shows Zeeman CPT resonances formed by the vector magnetic field \vec{B} used in the calculation with its magnitude $B = 20$ mG and angle (a) 0° (b) 5° (c) 10° with respect to the direction of beam propagation in the cell. For the purpose of illustration, the CPT amplitudes in (b) and (c) are doubled and vertically offset to show the small CPT resonances formed by the TMF component of \vec{B} . The following parameters were used in the calculation: $\Omega_1 = \Omega_2 = \Gamma/60$, $\Gamma = 6$ MHz, and $\gamma_1 = \gamma_2 = 3$ Hz.

symmetrically displaced RR fringes produced by non-zero velocity-groups around the RR fringe produced by the zero-velocity group. Therefore, the resultant sum (or average) of these individual velocity-group responses does not create any net phase shift for $\delta = 0$. However, if $\delta \neq 0$, the fringe displacements become asymmetric around the zero-velocity group and, therefore, velocity-

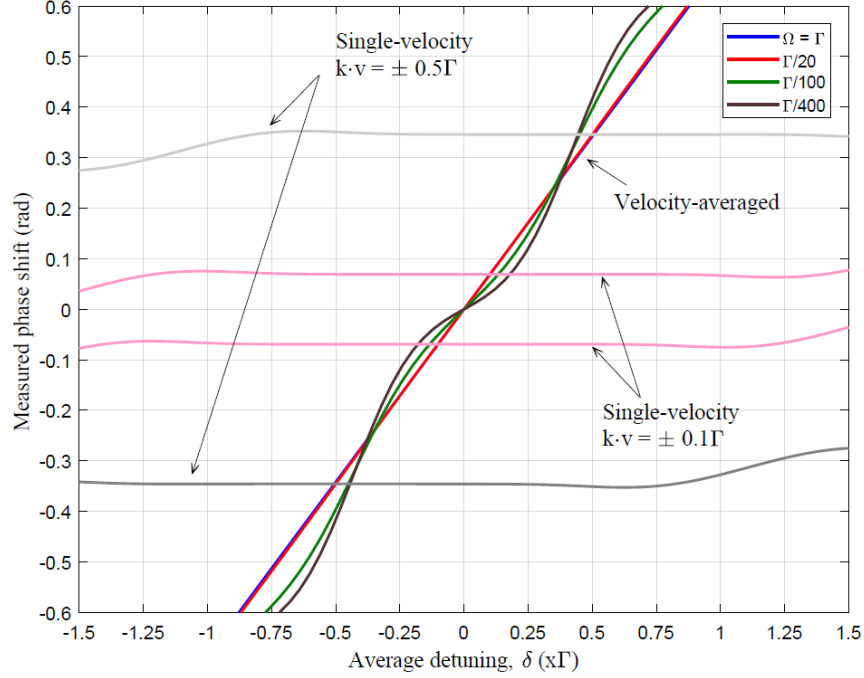


Figure 4.13: Phase shift calculated in a Doppler-broadened medium and plotted as a function of δ . The following parameters were used in this calculation: $\tau_c = 200 \mu\text{s}$, $T = 1 \text{ ms}$, $\tau_q = 100 \text{ ns}$, $\Omega_1 = \Omega_2$, $(\rho_{11} - \rho_{22})^0 = 0.2$, and $\Delta v_{Doppler} \approx 1 \text{ GHz}$. Phase shifts for two single-velocity groups ($kv = \pm 0.1\Gamma$ and $\pm 0.5\Gamma$) are also shown in the figure corresponding to the case $\Omega_1 = \Omega_2 = \Gamma/20$.

averaging creates a net velocity-induced phase shift. Such a phase shift linearly increases with δ and also changes sign with δ . The magnitude of this phase shift is also found to be large compared to the original light shift calculated earlier without velocity averaging.

The velocity-induced phase/frequency shift found here is not specific to RR interference. It will also manifest in any resonance including CPT that involves a resonant Raman excitation in a Doppler-broadened vapor medium. The results in figure 4.13 also shows that velocity-induced shift does not depend on the laser intensity, and can cause a systematic frequency error in a Raman clock provided the uncertainty in laser detuning, δ can be minimized by a precise laser lock. Although, narrowing of CPT resonance is commonly observed when experimenting in atomic vapor, the velocity-induced frequency shift (which manifests in the computation due to the residual

Doppler shift) is suppressed due to buffer-gas loading which forces the two-photon process into the Dicke regime (i.e. $\gamma \gg (k_1 - k_2)v = \Gamma_{res}$) [101]. The sixteen-level simulation also showed RR light shift with an uncharacteristically large slope that does not correspond to the experiment. Therefore, velocity averaging is removed from the light shift calculation. However, it is possible to choose empirically a large value of γ in the velocity averaging which will suppress the velocity-induced frequency shift. This has not been verified.

This chapter considered light shift associated with Raman-Ramsey interference using a computational model based on both a three-level and sixteen-level atomic system. The calculated results for the mono-velocity case confirm that RR light shift can be suppressed by orders of magnitude using the pulse saturation effect. As the results show, high long-term stability in cell-based RR clock can be achieved by suppressing the light shift, which was discovered and characterized through theoretical simulation.

CHAPTER 5: EXPERIMENTAL METHODS AND RESULTS

I have conducted a range of experiments with the goal towards implementing a ^{87}Rb vapor cell-based Raman-Ramsey atomic clock keeping in mind miniaturization requirements, and to compare and validate the theoretical findings. This first required generating two coherent radiation fields that can produce two-photon Raman excitation by coupling two non-degenerate hyperfine ground states to a common excited state in ^{87}Rb atoms. The laser also had to be stabilized to an atomic transition to prevent frequency drift. The electronics and feedback methods were designed for the clock experiment for low noise operation. Finally, the vapor cell environment was tightly controlled in terms of vapor cell characteristics and ambient temperature and magnetic fields. In the following section, I describe our efforts to generate Raman beams using a high-bandwidth electro-optic modulator (EOM), lock the laser to atomic transitions, develop a physics package for the vapor cell, and implement temperature and clock controls for conducting CPT and Raman-Ramsey clock experiments toward a vapor cell Raman clock.

5.1 Raman beam generation with EOM

CPT and Raman-Ramsey interference experiments in atomic vapor are performed by creating two-photon Raman excitation using frequency-modulated laser beams. In these experiments, we generated frequency-modulated laser beams using a high-bandwidth electro-optical modulator (EOM, EOSpace AZ-0S5-10-PFA-PFA-795, bias $V_{\pi} = 1.4$ V). This modulator is an intensity modulator which has a waveguide based Mach-Zehnder interferometric configuration. A large amplitude RF field (~ 20 dB) is used to drive the EOM at either 6.834 GHz (ω_{hf}), the hyperfine frequency for ^{87}Rb , or half that (i.e. 3.417 GHz). This forms modulated

sideband frequencies from the carrier. We also apply a low bias voltage, the DC V_π , to the modulator to change the ratio between the carrier and sideband frequencies. Keeping a fixed RF power at a given frequency, and by changing the DC V_π bias gave us the option to change the carrier-to-sideband intensity ratio, as shown in the figure 5.1, recorded by a 10 GHz bandwidth (or free spectral range) scanning Fabry-Perot etalon (Thorlabs SA210-5B, Scanning Fabry-Perot Interferometer, 10 GHz FSR).

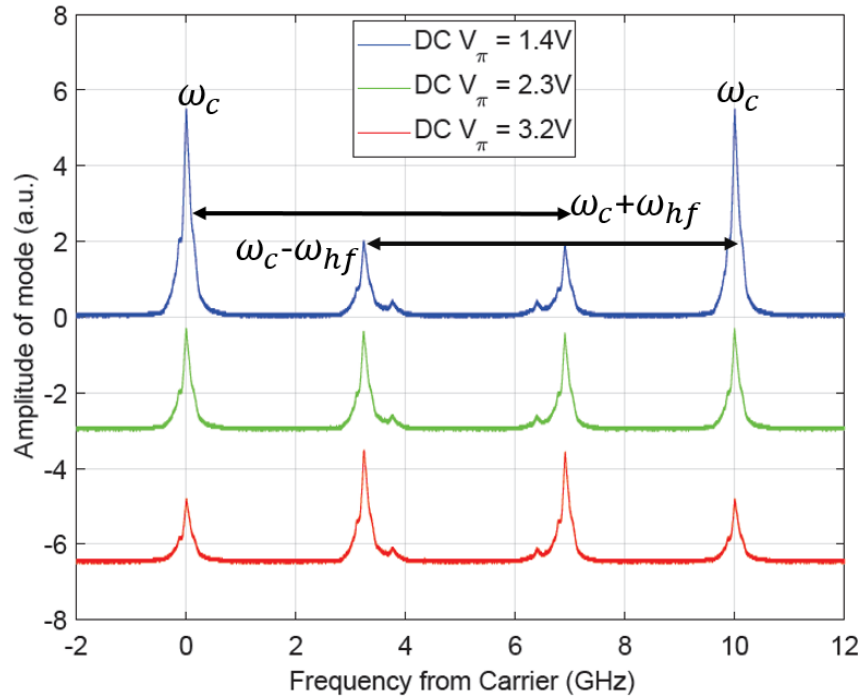


Figure 5.1: Fabry-Perot analyzer scan depicting carrier-to-sideband ratio change with several different DC V_π settings.

There are two possible beam generation schemes used in CPT or RR interference experiments, both of which require two laser fields separated in frequency by 6.834 GHz for two-photon Raman excitation using D1 transition in ^{87}Rb . In one scheme, known as ‘carrier–sideband’, we lock the laser frequency to a saturated absorption peak (see section 5.3), which form one of the contributing Raman frequencies. The beam is passed through the fiber-coupled EOM which is

driven by a 6.834 GHz RF signal to produce amplitude modulation at that frequency. Two shifted coherent laser fields with sideband frequencies (carrier frequency, $\omega_c + 6.834$ GHz) and (carrier frequency, $\omega_c - 6.834$ GHz) are formed. A major benefit of this scheme is its suitability for laser locking, but one of the sidebands can form a significantly large amplitude off-resonant laser field which does not contribute to the CPT or RR interference experiment, and results in producing higher light shift at the clock transition. Another benefit of this scheme is the added ability to independently change the intensities of the two Raman resonant frequencies by adjusting DC V_π to generate symmetric and high-contrast CPT or RR clock signal.

The alternative method requires driving the EOM at 3.414 GHz, half the ^{87}Rb hyperfine frequency, and is known as ‘sideband–sideband’ technique. In this way, the two sidebands (carrier frequency, $\omega_c \pm 3.414$ GHz) are separated by 6.8 GHz and together contribute to two-photon Raman excitation. This technique gives an advantage of suppressing the effect of carrier (or unmodulated laser) on light shift. The carrier is suppressed by applying an appropriate bias voltage to the EOM DC V_π input. However, creating a locking mechanism for sideband frequencies to ^{87}Rb transition using a reference vapor cell proves difficult as there is no available atomic resonance at the unmodulated (suppressed) carrier frequency for the laser to lock to before it enters the EOM. To solve this problem, the modulated beam must be split, and the laser must be conveniently locked using one of the shifted sideband frequencies (see section 5.3).

The EOM has undesirable temperature dependence of its bias voltage. Since the bias voltage controls the optical power in the carrier and the sidebands, any temperature fluctuation in the lab or EOM due to internal heating causes appreciable drift in the carrier power. During operation, the RF signal applied to the EOM results in internal heating which changes the carrier power throughput. The carrier is responsible for producing off-resonant CPT background which

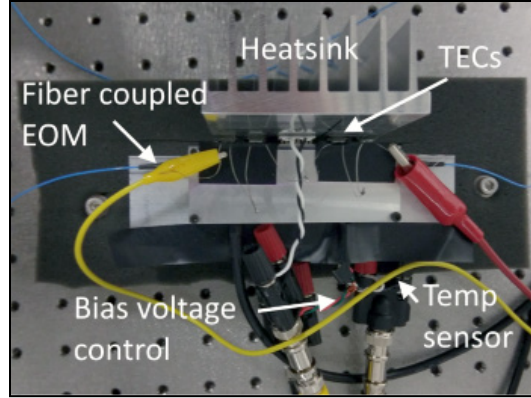


Figure 5.2: Picture showing EOM housed in an aluminum enclosure with temperature and bias voltage control.

can reduce CPT contrast. Maintaining a stable temperature of the EOM ensures a constant carrier-to-sideband ratio, or a minimized carrier. However, this temperature is in balance with the ambient lab temperature, and if the lab temperature changes, the carrier power will inevitably change. This can be remedied by manually changing the DC bias voltage to return the carrier to the desired level.

For a more practical and permanent solution, we have implemented active thermal control for the EOM with a TEC and temperature controller (Wavelength Electronics, WTC3293) to minimize the drift in the EOM bias voltage. Any residual drift in the carrier (or sideband) power is also monitored with a scanning Fabry-Perot etalon (not shown in the figure). Figure 5.2 shows the EOM driven by 3.417 GHz and the thermal controls and V_{π} bias control.

Active feedback control of DC bias is implemented to keep the carrier-to-sideband ratio (or carrier power) fixed (minimized) despite changing ambient temperature [103]. The active feedback of DC bias is made possible by first adding a low frequency dither modulation to the DC bias, picking off and measuring a small amount of power from the modulated beam, implementing an electronic servo by deriving a correction signal from the dithered EOM bias voltage and feeding back to the DC bias input after a PI servo. The signal level changes nonlinearly with applied DC

bias, as seen in figure 5.3, shown by the green trace. By modulating the DC bias at around 4 kHz and then demodulating the picked off beam, we get an error signal (pink trace) that is integrated to send a feedback signal to the EOM DC bias and keeps the carrier-to-sideband ratio set to the minimum output power point, or to any point on the green trace by giving an extra bias voltage. In the sideband-sideband scheme, locking to the minimum point automatically minimizes the carrier power. In early experiments, to remove undesirable modulation from the control signal, we

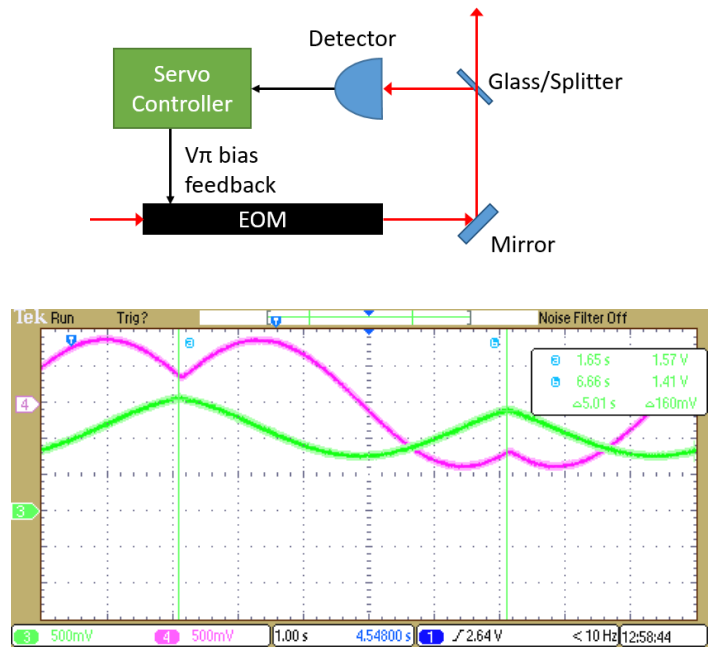


Figure 5.3: (top) EOM bias voltage stabilization servo (bottom) Feedback control signal (green/light trace) and error signal (pink/dark trace) used in controlling EOM DC bias for maintaining a fixed carrier-to-sideband ratio.

instead used a servo to apply a side lock (level lock) technique relying on the slope of the detected signal. This technique allows us to lock to almost any point on the green trace to maintain the desired carrier-sideband ratio, however, it still produced some drift in experiments, and the modulation-based version proved superior.

EOM requires a high power RF driving signal and is an extra element in compact clocks. A compact diode laser (such as a VCSEL), which can be directly modulated, is a preferable option,

but has relatively large linewidth (>10 MHz) and limited stability (power and wavelength) compared to a tunable diode laser and EOM combination, which is discussed later in this chapter.

5.2 Clock frequency synthesis

The generation of the clock frequency has gone through several iterations. In operating a clock, one of a couple schemes can be used to form the necessary RF signal for beam generation: (1) a direct RF signal from a signal generator which can be externally controlled, but is difficult to count, and mixing/beating with a nearby frequency is used to ultimately measure the stability (2) phase-lock two oscillators together, one at the high RF frequency for the hyperfine transition (or half that), one at a smaller, more easily counted (master) frequency.

The frequency synthesis chain for generation and control of the 6.834 GHz or 3.417 GHz EOM modulation signal in the CPT clock begins with a highly stable RF generator. For the first experimental trials with phase locked oscillators, we used the following setup: The master voltage controlled oscillator (VCO) is chosen to oscillate at 213 MHz, which is a low enough frequency to measure using a high-resolution frequency counter (Agilent 53220A). This frequency was chosen due to the availability and simplicity of an integer N phase-locked loop (PLL). A slave RF generator signal at 6.834 GHz (or 3.417 GHz) is sent to a PLL circuit, along with the master VCO output. In this particular PLL, ADF4007 from Analog Devices, the reference signal is divided by integer value 2, and then compared to the RF signal after it has been divided by an integer value 64. Alternatively, if using half the hyperfine frequency for dual sidebands, the integer value can be changed to 32 for 3.417 GHz, or integer 64 can be used with a 106.5 MHz master oscillator. Thus, the PLL compares two signals (i.e. from master and slave) each at about 106 MHz in its phase frequency detector. The charge pump output of the PLL responds to a difference in phase or frequency between the two 106 MHz signals. When the signals are not matched in phase or

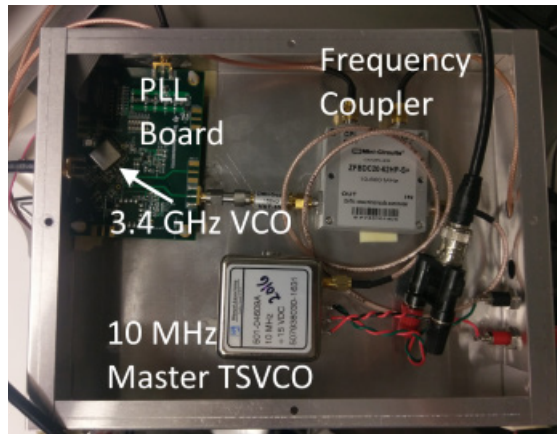


Figure 5.4: Master oscillator, coupler, PLL board, and embedded RF oscillator used in rubidium clock frequency synthesis.

frequency, the PLL charge pump outputs pulses proportional to the magnitude and sign of the mismatch. Sending the charge pump pulses to an integrating servo (loop filter) allows for integration and feedback into the 6.832 GHz (or 3.417 GHz) RF generator to lock it in phase with the master 213 MHz VCO. In this way, any change to the master VCO will result in a proportional change to the RF signal. This also has high bandwidth (hundreds of kHz) of operation suitable for clock frequency generation and control.

The lack of availability of high precision, low noise, low cost VCOs at the specific frequencies needed (213 or 106 MHz) for phase locking required the use of voltage controlled RF signal generators (Stanford Research Systems, SG384) which were not ideal for this application, but sufficiently demonstrated the utility of PLLs in this scheme. Figure 5.4 shows the components ultimately used in synthesizing the rubidium clock frequency (i.e. 3.417 GHz) from a master 10 MHz TSVCO (Wenzel 501-04609A). The output from the master oscillator is used in the PLL. The 10 MHz signal passes through a coupler and into a PLL evaluation board (Texas Instruments, LMX2487E). The coupler routes a fraction of the signal to a frequency counter (phase noise test probe, Microsemi, 3120A) which is referenced to a rubidium frequency standard (Stanford

Research System, FS725) for Allan deviation stability measurements (see chapter 6). The coupler also routes a fraction of the signal to another frequency counter (Keysight, 53220A) for monitoring the frequency. In the PLL evaluation board, the output from the on-board 3.4 GHz VCO (Z-Communications, CRO3412A) is divided by a fractional value for comparison with the 10 MHz TSVCO in the phase frequency detector. The charge pump and the on-board integrating loop filter correct the 3.4 GHz VCO to follow any frequency changes in the master 10 MHz TSVCO, thereby phase locking the high frequency VCO to the master oscillator.

5.3 Laser frequency lock techniques

The precision of atomic clocks is limited by the stability of the laser involved. We expect a laser drift of less than 1 mHz/hr to attain a long-term clock frequency stability below 10^{-12} . As shown in chapter 4, laser detuning causes light shift. Several laser lock methods were employed in the testing. When using the carrier-sideband scheme, the carrier can be locked to the saturated absorption transition before the beam enters the EOM. In standard saturated absorption experiments using counter-propagating carrier beams (a pump and a probe), a non-Doppler broadened atomic transition can be measured and used as an atomic reference to maintain the laser frequency on that transition, using a low frequency dither modulation technique with a lock-in amplifier and integrating servo. This method, however, requires an extra vapor cell beyond the experiment cell and two photodiodes (or a balanced detector) for subtraction to produce a high contrast signal, and only works in the carrier-sideband scheme. Working toward simplification and compactness, the following laser lock methods were used, which are more compatible with the sideband-sideband scheme and compactness.

5.3.1 Dichroic atomic vapor laser lock

As an alternative to common saturated absorption spectroscopy, we have employed a dichroic atomic vapor laser lock (DAVLL) scheme to stabilize the laser frequency to the Doppler broadened absorption line in ^{87}Rb D1 transition. This is achieved by taking a small fraction of the laser beam's power, and passing it through a reference rubidium cell as shown in the picture in figure 5.5. A strong longitudinal magnetic field is applied to the reference cell such that absorption for the linearly polarized laser light is oppositely shifted in frequency for its circular polarization

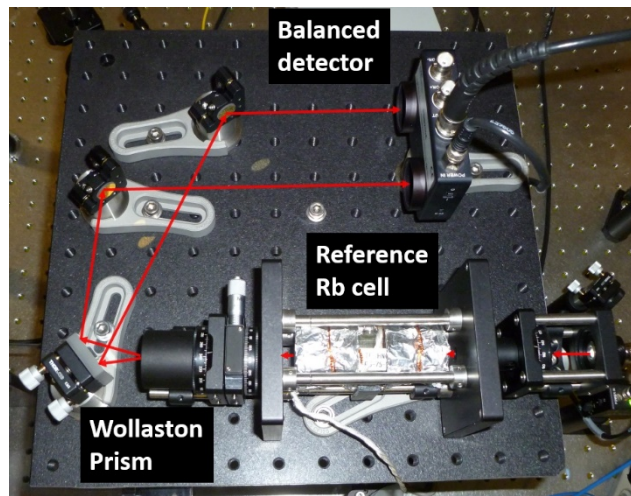


Figure 5.5: Picture showing DAVLL system mounted on a small size breadboard components [104]. The beam is then split into two circular polarization components using a Wollaston prism, and measured using a balanced photodetector. The output from the balanced photodetector forms a zero-crossing which is used as a discriminant signal in a PI controller based frequency servo for laser frequency stabilization.

While this scheme is well suited for the carrier laser frequency in the carrier-sideband scheme, splitting off the single modulated beam (sideband-sideband) and directing it to the DAVLL is not. When the two sidebands are used with the DAVLL, it does not produce a zero

crossing or slope which can be locked that is not highly detuned. Further, this is not suited for a compact clock application due to the requirement of another vapor cell beyond the test cell in the physics package.

5.3.2 Single detector laser lock

The laser can be frequency locked to the ^{87}Rb D1 absorption maximum created by resonant excitations of the modulated laser beam with $|F' = 1\rangle$ and $|F' = 2\rangle$ simultaneously, when passing through the experimental rubidium cell [21,105]. This allows the use of a single photodetector and single vapor cell for implementing the laser lock as well as the CPT clock (see chapter 6). The laser lock is implemented via dither modulation, lock-in amplifier, and a laser servo controller. The laser servo and the clock servo operate independently with different dither modulation frequencies for preventing lock instability caused by interference. This method lends itself to compact clock applications by requiring the least components and optical power and giving the clock components a dual purpose.

5.4 Implementation of push-pull optical pumping scheme

Another aspect of beam generation and preparation is the polarization state selection of the laser light. In the experiment, the polarization states for these frequencies are controlled using a wave plate in the beam path. In the case of $lin \parallel lin$ excitation, properly oriented half-wave ($\lambda/2$) plate establishes a particular linear polarization state for the CPT fields. To choose pure circularly polarized CPT fields, the $\lambda/2$ plate is replaced by a quarter-wave ($\lambda/4$) plate. However, to employ $lin \perp lin$ (or PPOP), a polarization-based Michelson interferometer (picture and schematic shown in figures 5.6 and 5.7) is used in the beam path. Each arm of the interferometer consists of a $\lambda/4$

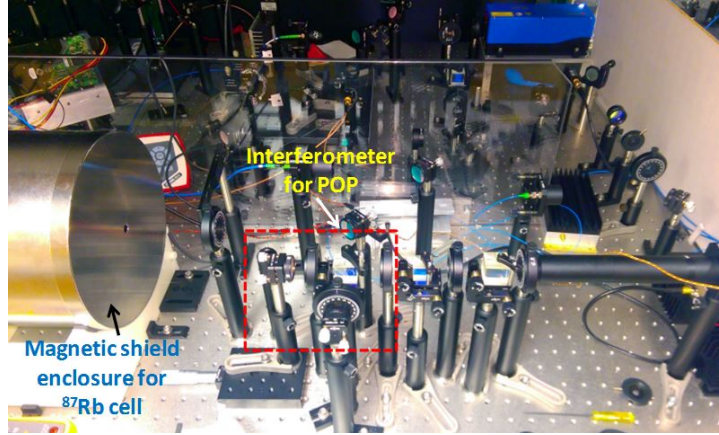


Figure 5.6: Picture showing the experimental setup developed in the lab for CPT atomic clock using the PPOP scheme

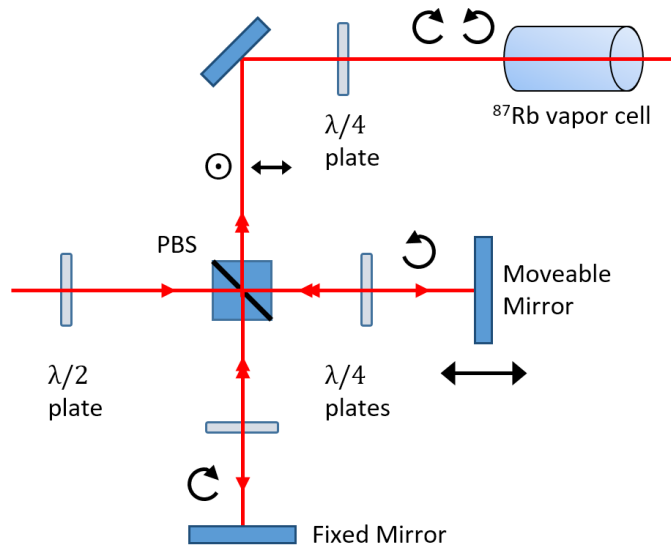


Figure 5.7: Schematic of the polarization-based Michelson interferometer introduced in the beam path for implementing $lin \perp lin$ (or PPOP) scheme. The path difference between the two arms of the interferometer is set to $\lambda_{hf}/4$ which is approximately 1.1 cm for ^{87}Rb atoms.

plate and a retro-reflecting mirror. The $\lambda/4$ plates change the beam polarization from linear to circular during the forward pass, and from circular to an orthogonal linear polarization during the return. The beams are combined at the polarizing beam splitter (PBS) and emerge with orthogonal horizontal and vertical linear polarization states from the two arms of the interferometer. Finally, a $\lambda/4$ plate at the output of the interferometer converts the modulated laser beams to right circular

polarization (RCP) and left circular polarization (LCP). One of the interferometer arms is changed to set the path difference between the two arms by one quarter of a wavelength λ_{hf} corresponding to the ^{87}Rb hyperfine ground state frequency 6.834 GHz. This is approximately 1.1 cm. Since the beam travels twice along the interferometer arm, the overall path difference is $\lambda_{hf}/2$. This ensures that the modulated laser beams emerging from the interferometer have a 90° phase difference with their electric fields after the $\lambda/4$ plate described as

$$\vec{E}_{CPT}^{(1)} = 2E_0 \cos\left(\frac{k_1 - k_2}{2}z_1 - \frac{\omega_1 - \omega_2}{2}t\right) [\hat{x} \cos(\bar{k}z_1 - \bar{\omega}t) + \hat{y} \sin(\bar{k}z_1 - \bar{\omega}t)] \quad (5.1a)$$

$$\vec{E}_{CPT}^{(2)} = 2E_0 \sin\left(\frac{k_1 - k_2}{2}z_1 - \frac{\omega_1 - \omega_2}{2}t\right) [\hat{x} \cos(\bar{k}z_2 - \bar{\omega}t) - \hat{y} \sin(\bar{k}z_2 - \bar{\omega}t)] \quad (5.1b)$$

where $\bar{k} = (k_1 + k_2)/2$ and $\bar{\omega} = (\omega_1 + \omega_2)/2$ are average values of the propagation constant and angular frequency of the modulated laser beam, respectively. Equal amplitude E_0 has been considered for the RCP and LCP fields. Eqn. (5.1) shows that the CPT beams have orthogonal circular polarizations and their amplitudes oscillate at half the ^{87}Rb hyperfine frequency ν_{hf} with a quadrature phase difference. Thus, when the intensity (time-averaged) of RCP (or σ^+) beam is maximum, the intensity of LCP (or σ^-) beam is zero and vice versa. This produces alternate excitations and optical pumping using σ^+ and σ^- polarization states, which is known as push-pull optical pumping (PPOP) that gives rise to high contrast in the CPT signal [72,73]. One can also show the equivalence between PPOP and $lin \perp lin$ by superposing the modulated laser fields together in eqn. (5.1) to obtain the following expression:

$$\begin{aligned}
\vec{E}_T &= \vec{E}_{CPT}^{(1)} + \vec{E}_{CPT}^{(2)} \\
&= 2E_0[\{\hat{x} \cos \theta + \hat{y} \sin \theta\} \cos(k_1 z' - \omega_1 t) \\
&\quad + \{\hat{x} \sin \theta - \hat{y} \cos \theta\} \cos(k_2 z' - \omega_2 t)]
\end{aligned} \tag{5.2}$$

where $z' = (z_1 + z_2)/2$ is the average distance and $\theta = k_1|z_1 - z_2|/2 = k_1(\lambda_{hf}/4)$ that corresponds to the angle of the linear polarization state of the electric field at frequency ω_1 and ω_2 . The curly bracketed terms in eqn. (5.2) represent the two orthogonal linear polarization CPT fields $lin \perp lin$ at frequencies ω_1 and ω_2 , respectively. Thus, $lin \perp lin$ excitation scheme is implemented using the polarization interferometer shown in figure 5.7. The $lin \perp lin$ excitation scheme can also be implemented without the polarization interferometer by using counter-propagating σ^+ and σ^- polarized modulated laser beams through a cell [71,106]. In this case, one can show

$$\begin{aligned}
\vec{E}_T &= \vec{E}_{CPT}^{(\sigma^+, +z)} + \vec{E}_{CPT}^{(\sigma^-, -z)} \\
&= 2E_0[\{\hat{x} \cos \theta_1 + \hat{y} \sin \theta_1\} \cos(\theta - \omega_1 t) \\
&\quad - \{\hat{x} \sin(\theta_1 - \theta'(z_1)) + \hat{y} \cos(\theta_1 - \theta'(z_1))\} \sin(\theta - \omega_2 t)]
\end{aligned} \tag{5.3}$$

where $\theta_1 = k_1(z_1 + z_2)/2$ corresponds to the angle of the linear polarization state at frequency ω_1 (see appendix E). The curly bracketed terms in eqn. (5.3) show two linear polarization states with standing wave fields at frequencies ω_1 and ω_2 which are orthogonal provided $\theta'(z_1) = 2\pi z_1/\lambda_{hf}$ is an integer multiple of π for a particular location z_1 inside the cell. If orthogonality is satisfied at z_1 , it will not be strictly satisfied at other locations inside the cell for which z_1 deviates by a distance $\ll \lambda_{hf}/4$ ($\simeq 1.1$ cm). Thus, $lin \perp lin$ excitation scheme cannot be implemented with counter-propagating σ^+ and σ^- beams in relatively long cells, like ours which is 2 cm long. The scheme is more suitable for microcells which are typically used in compact CPT clock [71,106].

5.5 Small cell physics package

The ambient environment around the experiment vapor cell significantly determines the clock stability. Factors such as stray magnetic fields, temperature gradients, inhomogeneous applied magnetic field, buffer induced shift, temperature induced shift, all contribute to the hyperfine transition frequency the experiment measures. Continual improvements to the physics package were made as time and funding allowed, based on the quality of experimental results and potential improvements. The first small cell physics package that was implemented is described here followed by a recent revision for improved heating and magnetic field stability, which was ultimately used in the experimental results, except where indicated.

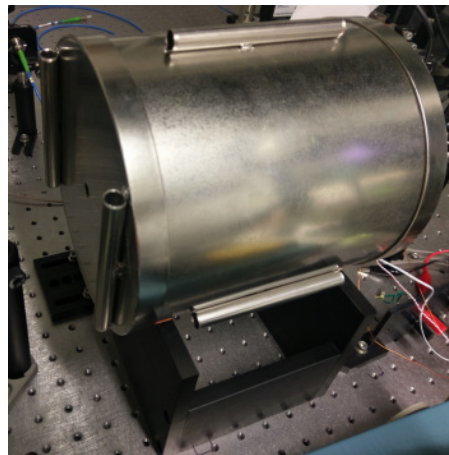
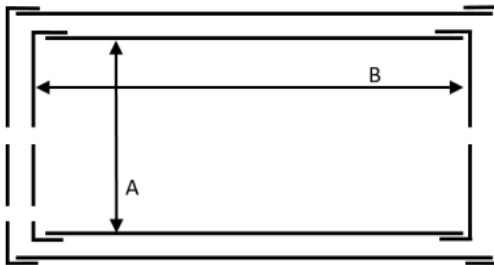


Figure 5.8: Schematic and picture of μ -metal chamber on pedestal in the beam path.

For small cell studies, we used a pure-isotope ^{87}Rb vapor cell (optical length = 2.3 cm, diameter = 1 cm), filled with 10 Torr of neon buffer gas. In small vapor cells, an appreciable buffer gas induced frequency shift is evident. This shift is also temperature dependent and can thus change with cell temperature instability. One possible technique to compensate for this shift is the use of two complementary buffer gases with opposite shifts such that the net shift is small and unchanging with temperature, such as neon and argon together in a specific ratio [12,107].

The physics package for the vapor cell has an approximate cylindrical volume of 7000 cubic cm. This is composed of a dual layer μ -metal magnetic shield enclosure surrounding the cell for mitigating residual magnetic fields resulting from the Earth and the local environment by approximately 50 dB. The μ -metal magnetic shielding chamber has an internal diameter of 16.5 cm (A) and length of 19 cm (B). There are through-holes for the laser beam on both sets of endcaps and through-holes for wires on one set of endcaps, shown in figure 5.8 schematic. The dual layer shields each have a thickness of 0.16 cm and are separated by 1.27 cm spacers. A plastic pedestal supports the chamber.

Figure 5.8 shows the chamber *in situ*, and the spacers on the outside allow it to fit into a third shield, if needed. In this low B-field environment, we used a pair of Helmholtz coils mounted inside the enclosure to apply a small uniform axial magnetic field ($B \approx 30$ mG) to lift the Zeeman degeneracy of the ^{87}Rb atomic states. Appendix F demonstrates an example of how the coils were modeled before fabrication to ensure a homogenous magnetic field. The Helmholtz coils are lathed from plastic, which have 44 turns of copper wire per coil. The Helmholtz coils have a diameter of ~ 16.4 cm and are ~ 1.8 cm wide, with an inner separation of ~ 8.5 cm.

Maintaining the separation of the two coils is a horizontal plastic support serving as a base for the plastic pillar which is bolted to a plastic enclosure comprised of a base and a lid which fits on with aluminum pins, shown in figure 5.9. The enclosure contains the aluminum heatsink which holds the small rubidium cell as shown in the picture. Figure 5.10 shows the vapor cell with rubidium accumulated at the bottom. The cell must be heated sufficiently to remove the atoms from the glass and into a vapor form. Bifilar twisted nichrome wire is wrapped around two aluminum tubes which are set in place to hold the rubidium cell very close to the windows using set screws. This ensures that the primary heat reaches the rubidium cell at the windows, preventing

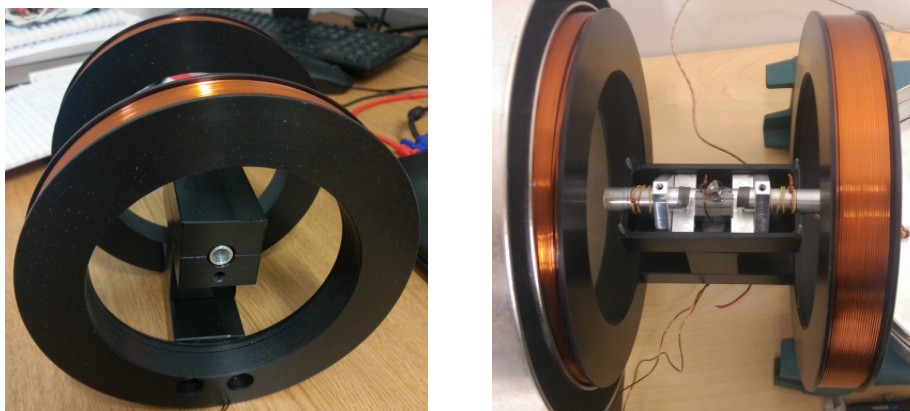


Figure 5.9: Pictures showing Helmholtz coils and small rubidium cell holder.

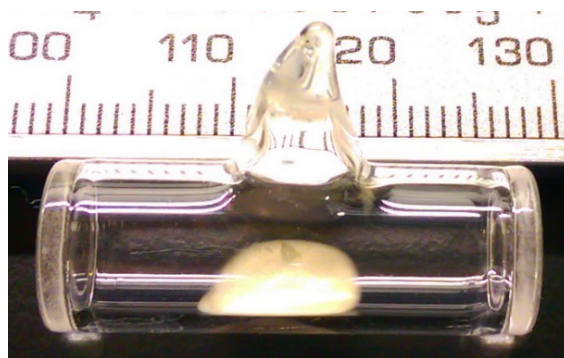


Figure 5.10: Small vapor cell with rubidium visible, accumulated at the bottom.

rubidium accumulation on the windows. Double sided thermally conductive tape further secures the rubidium cell and facilitates heat transfer as shown in the picture in figure 5.11. The glass stem, being furthest away from the heating surfaces, is susceptible to collection of rubidium, risking loss of vapor density, and required further insulation. The cell is covered in aluminum foil and further insulated with a porous foam.

The heating wire is secured to the aluminum tubes with small lengths of copper wire with ends twisted to tighten them into place. Similarly, a K-type thermocouple is bent to touch the glass surface of the vapor cell and held in place with a copper wire, ends twisted until taut. A programmable temperature controller (PTC) (Stanford Research Systems, PTC10) uses PID

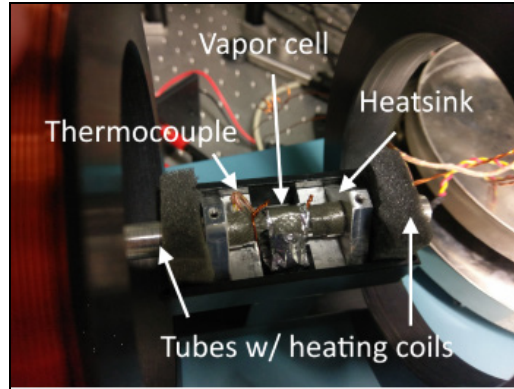


Figure 5.11: Picture showing rubidium cell in holder between Helmholtz coils with heating wire and thermocouple

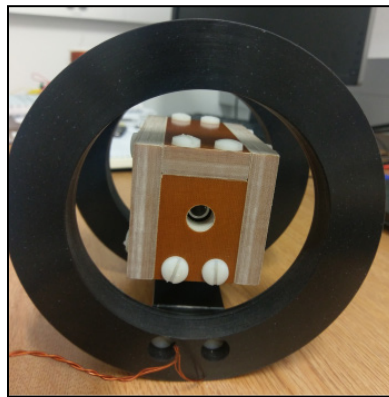


Figure 5.12: Picture showing phenolic box enclosure around the rubidium cell.

control to stabilize the temperature by applying varying levels of current to the resistive wires. The vapor cell has active temperature control within $\Delta T \approx 100$ mK with bifilar-twisted resistive nichrome heating wire and a standard K-type thermocouple sensor. The K-type thermocouple is susceptible to magnetic fields, which could disrupt the homogeneity of the applied magnetic field and induce frequency shifts.

One major benefit of this design is the large bulk of metal reduces the speed of thermal dissipation so that any ambient temperature change is rapidly compensated by the controller. A drawback surfaces, however, when changing the temperature or while optimizing the temperature

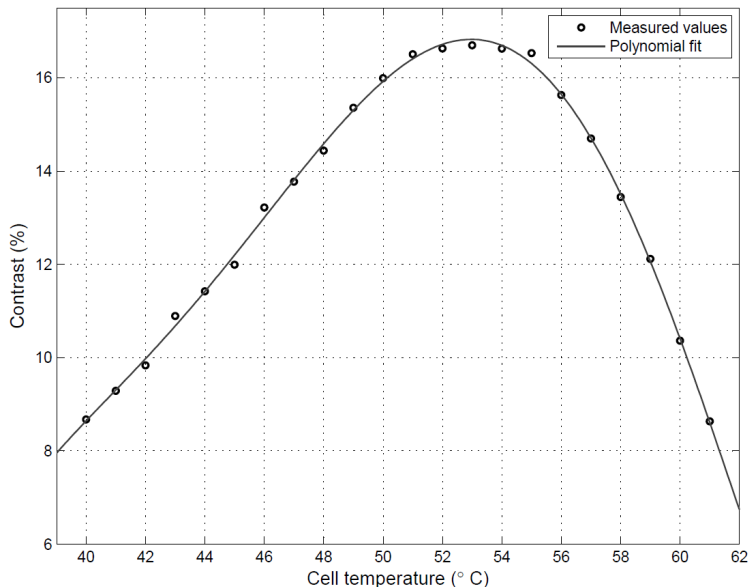


Figure 5.13: CPT contrast measured by varying the cell temperature from 40°C to 61°C in steps of one degree Celsius under the temperature lock condition.

lock, the response time is very slow – several thermocouple locations were tried before settling on the position atop the glass cell. During the process of experimenting for improving the temperature stability, we surrounded the plastic enclosure with a phenolic box (fiberglass and resin) (see figure 5.12), but that resulted in preventing the controller from locking the desired temperature – the response time was severely diminished.

To achieve a magnetic field strength of 30 mG, the Helmholtz coils are driven with a current of about 7 mA from a low noise current driver (ILX, LDC3714C). In order to find an optimum cell temperature, we measured the contrast in the CPT signal with varying cell temperature. Figure 5.13 shows CPT contrast as a function of the cell temperature. The cell is thus kept at a steady and optimum temperature of 53° C. Thus, for studies in section 5.7 and 5.8 (except where noted), the cell is actively maintained at a steady and optimal temperature of 53°C where the contrast is found to be close to its maximum. The modulated laser beam from the EOM is expanded and collimated to an approximate diameter of 8 mm before passing it through the

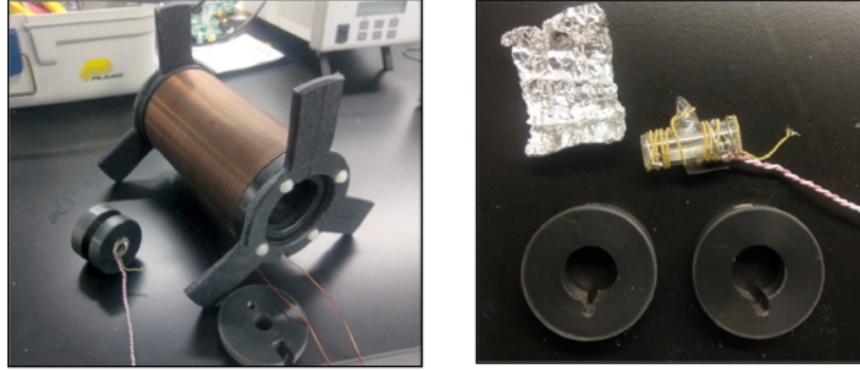


Figure 5.14: (left) Solenoid with support fins and mounted vapor cell and (right) Vapor cell wrapped in heating wire alongside aluminum foil insulation and plastic disc cell holders

rubidium cell. Expanded beam size and frequent collisions with buffer gas atoms increase the interaction time between the photons and ^{87}Rb atoms for observing narrow linewidth CPT resonance. Sub-kilohertz linewidth CPT resonances, limited by the optical power, are observed in transmission by scanning the modulation frequency around the two-photon resonant frequency i.e. 6.834 GHz.

Upon using the previously described physics package, it became evident that we needed to revise the heating and magnetic field design for the small rubidium vapor cell. For better temperature control and reduction of magnetic field gradient, we made the following modifications. A solenoid with 60 turns of copper wire replaces the Helmholtz coils in the new design, see figure 5.14. A spiraled groove cut into the plastic solenoid tube prevents the coiled wire from slipping and helps creating a uniform magnetic field. Three fins on either end of the tube, allow it to be centered in the μ -metal chamber. The solenoid produces a magnetic field with strength of roughly 40 mG with about 7 mA applied current. To increase the temperature responsivity, the cell is directly wrapped in bifilar twisted nichrome heating wire. In an attempt to remove the K-type thermocouple, a platinum thin-film temperature sensor (thermistor) is placed in contact with the glass cell. It has a small amount of magnetically-susceptible metal, and is

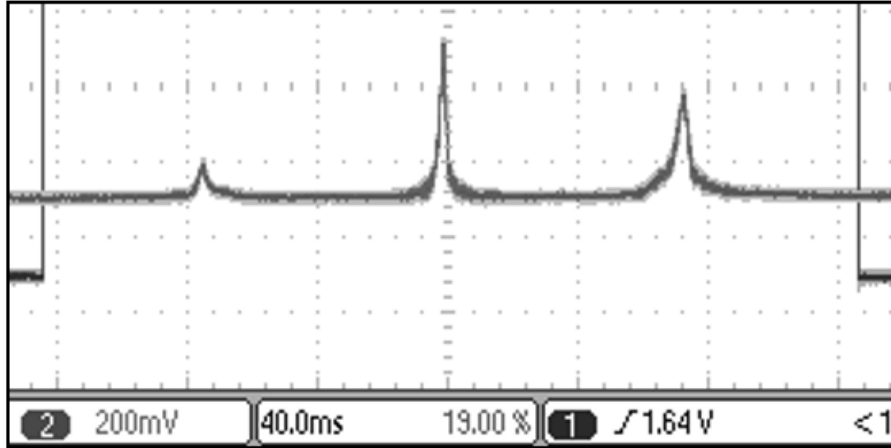


Figure 5.15: CPT spectrum obtained by (σ^-, σ^-) excitation resonant with $|F' = 2\rangle$ state. The spectrum shows peak-like Zeeman CPT resonances.

connected to copper leads, to minimize magnetic field disturbance. The cell is wrapped in aluminum foil to retain the applied heat and reduce the amount of current needed to maintain a steady temperature; the components are laid out in figure 5.14. A thermistor-based controller (Thorlabs, TC200) was used instead of the previous K-type controller, which is primarily intended for use with vapor cell heating applications.

However, this configuration did not provide a stable temperature control and the system was returned to the K-type controller setup. Securing the vapor cell within the solenoid tube requires two plastic discs with plastic set-screws. The disc assembly remains stationary in the tube via pressure. Plastic end caps with holes for the laser beam and wires close off the tube to further reduce the temperature gradient and maintain higher temperature stability. The CPT spectrum obtained with the new cell enclosure design shows little to no evidence of magnetic field distortion from the solenoid, evident in figure 5.15.

5.5.1 Magnetic shield revisions

While a Helmholtz coil or solenoid is placed around the vapor cell, generating a magnetic field to lift the degeneracy of the ground-state Zeeman sublevels, the cell and coils are also placed in a magnetic shield to ensure a consistent magnetic field without external perturbations [8,9]. These shields are built from a high magnetic permeability material, such as μ -metal from the Magnetic Shield Corporation, which essentially ‘redirects’ magnetic fields away from sensitive components when designed properly. After construction, the shields are annealed at high temperatures to increase the shielding efficiency. Several magnetic shielding designs were used depending on vapor cell size and available materials.

The first magnetic shield was designed for a large vapor cell (2.5 cm diameter, 10 cm long), and made to fit a set of Helmholtz coils with the vapor cell mounted in the center, which is shown in figure 5.16. This shield was formed from flat sheets of μ -metal and is composed of two layers, without spacing. The shield was not annealed after construction and did not have high performance as expected.

The final shield, described partly in section 5.5.1, was custom designed, fabricated, and annealed by the Magnetic Shield Corporation. The shielding factor for the inner two shields was estimated to be approximately 50 dB. Up to three layers can be used with this custom made chamber, and the outer layer was dual purposed for further large cell tests. Figure 5.17 shows the three nested shields with two endcaps removed, and an example of how the outer shield was implemented for a large cell.

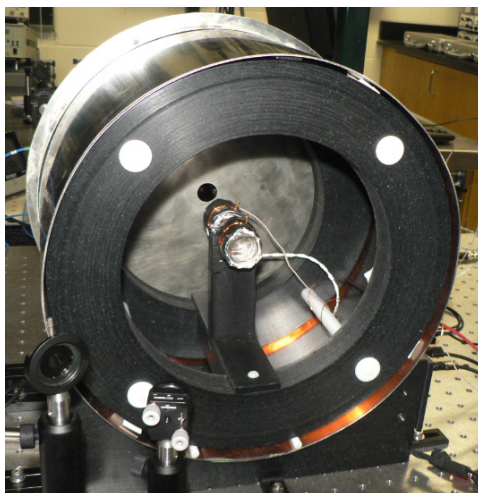


Figure 5.16: Magnetic shield for a large vapor cell, formed from flat sheets and spot welded.

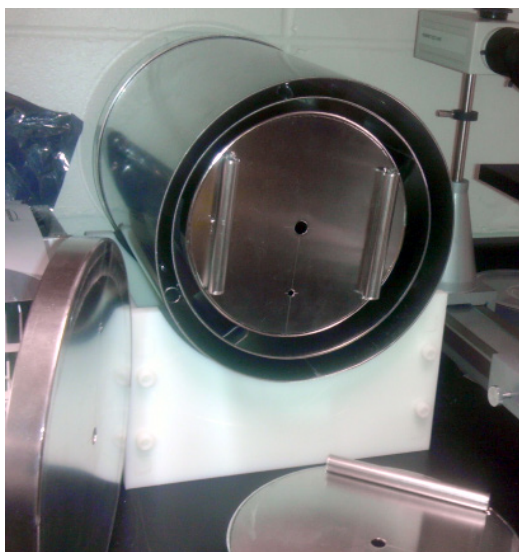


Figure 5.17: (left) Custom made magnetic shield with all three layers and (right) Helmholtz coils and large cell with insulation used with the outer shield only.

5.6 Ramsey pulse switching with AOM

For communication and navigation, atomic clock technology relies on creating optical resonances with narrow linewidth and high S/N ratio. Continuous optical pumping in alkali atoms produces stable and coherent atomic dark state resonances with some limitations [8,42,108]. In Ramsey interference, a CPT pulse is used to prepare the atoms in the ‘dark state’. Interference is subsequently produced through an interaction free evolution of the dark state for time T and its superposition with the short query (or interrogation) pulse [45,48,84,88,109]. The fringe-width of

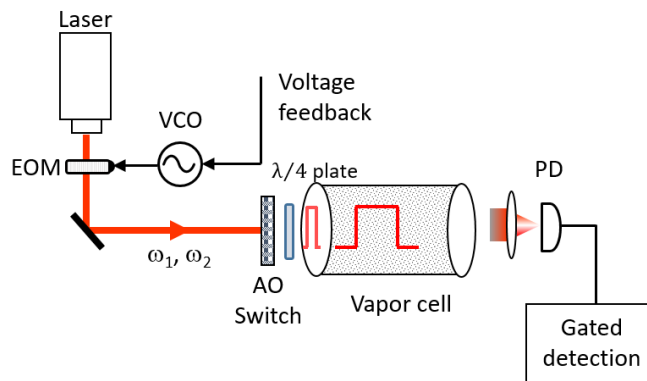


Figure 5.18: General schematic of Ramsey pulses through a vapor cell. Only the short, query pulses contribute to the Ramsey signal.

Ramsey interference is decided by the free-evolution time, T (i.e. $\Delta\nu = 1/2T$). The fringe-width can be narrow with large T in order to produce high short-term frequency stability in the atomic clock due to the increased Q factor. The other advantage of Ramsey interference is light shift, which can be reduced by using a strong interaction with the CPT preparation pulse [50,51,86,92].

A free-space acousto-optic modulator (AOM) is placed before the EOM and is used as a switching element, as shown in figure 5.18. The AOM shifts the optical frequency by 80 MHz relative to the original laser frequency. A pulse generator is used to switch the Bragg diffracted beam from the AOM off and on by sending voltage pulses from the pulse generator to the

modulation input of the AOM driver. This allows us to create the optical pulse sequence needed for generating Ramsey interference. The rise time of the AOM and minimum duration of the optical pulse is decided by its bandwidth and the beam size at the AOM. Query pulses with minimum duration $\tau_q = 1\text{-}2 \mu\text{s}$ are produced by the AOM. The pulsed and modulated optical beam in our experiment is passed through a quarter-wave ($\lambda/4$) plate to create circularly polarized CPT fields (for example). It is then passed through a pure-isotope ^{87}Rb vapor cell filled with neon buffer gas. For a single query pulse, the pulse cycle (shown in figure 5.19) is defined by the CPT pulse (duration τ_c), free-evolution time T , and the query pulse of duration τ_q .

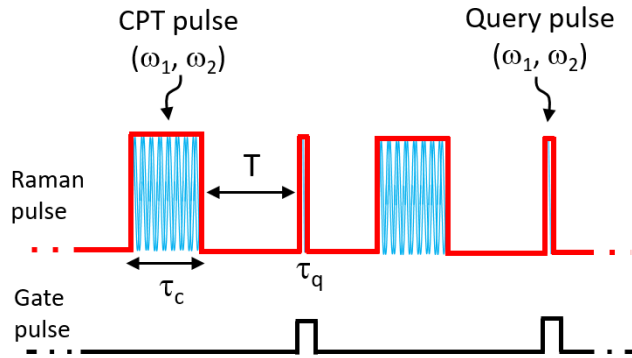


Figure 5.19: General schematic of Ramsey pulses through a vapor cell. Only the short, query pulses contribute to the Ramsey signal.

The pulse generator is programmed to switch the AOM on and off at these intervals. In the experiments, τ_c is generally chosen to be near $500 \mu\text{s}$ to prepare the atoms in the dark state. The free-evolution time T is chosen to be 1 to 1.5 ms which is decided on the basis of decoherence of the dark state. The duration of the query pulse τ_q is chosen to be short (i.e. $1 \mu\text{s}$) to minimize destructive read-out of the dark state coherence. A boxcar integrator is used to gate the electronic signal produced by the photodetector during the query pulse for observing the interference effect. Ramsey fringes are generated by repeating the pulse cycle and slowly changing the frequency

difference between the CPT fields around the two-photon resonant frequency (i.e. $\omega_{hf} = 6.834$ GHz, the ^{87}Rb hyperfine ground-state frequency).

Additionally, the optical query pulses can be collected and integrated digitally with a computer digitizer instead of a boxcar integrator. This method is implemented and discussed in section 5.8.

5.7 Experimental results

The diagram in figure 5.20 depicts the experimental setup used in investigating CPT characteristics by employing the previously discussed optical excitation schemes, the small vapor cell, custom made magnetic shield, and phase-locked loop. The setup is also used as a CPT clock to measure the frequency stability using all three polarization schemes. A tunable diode laser (DL PRO, Toptica Photonics) with linewidth less than 1 MHz is used as the light source. The laser beam is sent through the fiber-coupled waveguide EOM driven by an RF oscillator to produce the frequency-modulated laser beam for CPT and Ramsey experiments. The EOM is modulated at approximately half the hyperfine ground-state frequency of ^{87}Rb (i.e. 3.417 GHz) accounting for the buffer gas pressure induced frequency shift ($\Delta f_{buf} = 3.022$ kHz from neon buffer gas at 10 Torr) in the 2 cm long rubidium cell. The EOM is driven by approximately 22 dBm RF power to produce optical sidebands around the laser carrier frequency. The difference in frequency between the first two sidebands is matched close to 6.834 GHz for creating two-photon resonant Raman excitation in the rubidium cell. The laser lock is implemented via dither modulation and a laser servo controller shown in figure 5.20 to the absorption maximum detected with both beams in the single detector. The dither modulation frequencies used in the laser servo and clock servo are chosen to prevent lock instability caused by interference or beating.

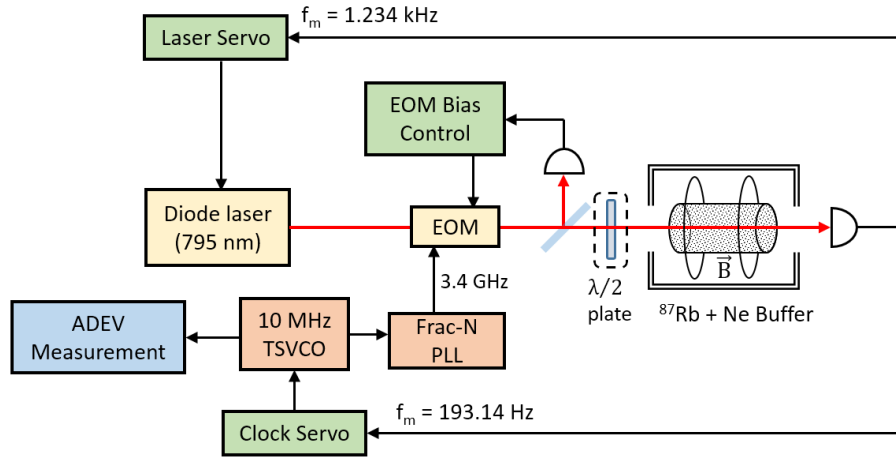


Figure 5.20: Experimental setup developed for the rubidium CPT clock. A single photodetector distributes the optical signal and produces independent control signals for the laser servo and the clock servo. The dashed box around the $\lambda/2$ plate represents the changeable optical element for implementing $lin \parallel lin$ or (σ, σ) polarization schemes.

For the following results, we used the small vapor cell in a two layer magnetic shield. In this low B-field environment, we used a pair of Helmholtz coils (diameter = 16.5 cm) mounted inside the enclosure to apply a small uniform axial magnetic field ($B \approx 30$ mG) for lifting the Zeeman degeneracies of the ^{87}Rb atomic states. The rubidium cell is actively temperature controlled ($\Delta T \approx 100$ mK) with bifilar-twisted resistive nichrome heating wire and a standard K-type thermocouple sensor. The laser beam emerging from the EOM is expanded using a fiber-end collimator to an approximate diameter of 8 mm before passing it through the rubidium cell. A combination of the expanded beam size and frequent collisions of ^{87}Rb atoms with buffer gas atoms, increase the interaction time between the laser fields and ^{87}Rb atoms for observing narrow linewidth CPT resonance. Sub-kilohertz linewidth CPT resonance, limited by the optical power, is observed by scanning the laser modulation frequency (sweeping the TSVCO) around the two-photon resonant frequency.

For polarization state preparation, either a quarter- or half- waveplate is used for linear or circular polarization, respectively. This is shown as a changeable polarizing optical element in figure 5.20 which is sufficient to create either $lin \parallel lin$ or (σ, σ) excitation. However, to employ $lin \perp lin$ (or PPOP), the polarization-based Michelson interferometer is used in the beam path, as described in section 5.4.

5.7.1 CPT results

Two primary characteristics of CPT that are important for clock stability are linewidth and contrast. The first two results are prepared with a single sideband scheme in a large vapor cell to demonstrate these characteristics in CPT. As noted previously, increased beam size increases the interaction time of the atoms with the laser and produces a narrow resonance, as shown in figure 5.21. The CPT resonances here were measured with a fixed optical power and three beam sizes using single sideband modulation at 6.834 GHz. The modulated laser beam exits a fiber and is collimated with a 15.29mm focal length aspheric lens and then expanded up to 8mm.

Contrast and linewidth of CPT resonances are also impacted by optical power, as discussed in chapters 2 and 3. Figure 5.22 shows CPT resonances for three beam powers. While the linewidth decreases with less optical power, contrast is also lost.

For investigations of polarization schemes, we prepared the modulated laser beam in the $lin \parallel lin$ polarization state, and measured the characteristics of CPT resonance. Figure 5.23 shows the central CPT resonance observed with $lin \parallel lin$ excitation resonant with $|F' = 1\rangle$ state for two different axial magnetic field strengths. With low axial magnetic field ($B_z \simeq 30$ mG), a single-

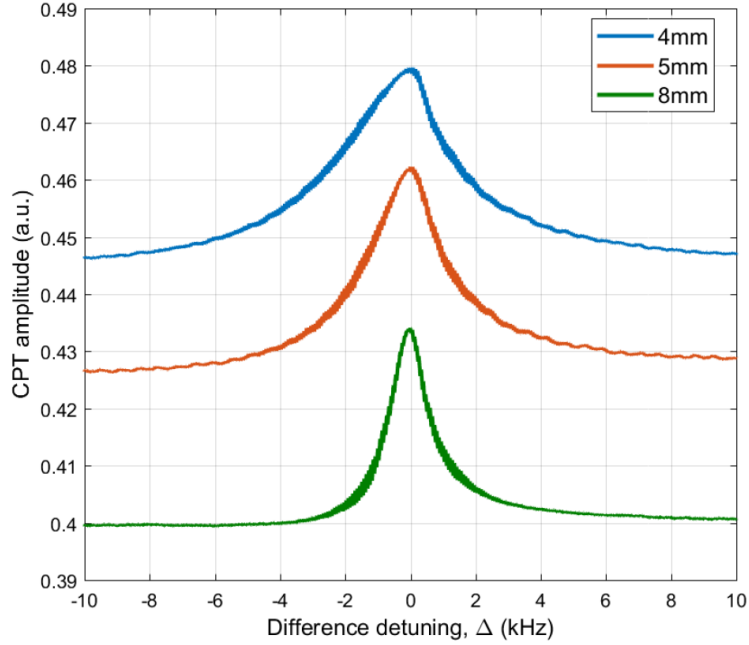


Figure 5.21: CPT resonances showing narrowing with larger beam diameter, where the off resonant sideband produced asymmetry.

peaked CPT resonance with linewidth of 841 Hz and contrast of 7.5% is observed. CPT contrast is measured by calculating $(V_P - V_B) / V_P$ where V_P and V_B are defined as the respective peak and background voltage levels of the CPT signal.

The total optical power used in the modulated laser beam was approximately $70 \mu\text{W}$. At higher magnetic field ($B_z \approx 900 \text{ mG}$), the CPT resonance is split into two separate resonances. The central CPT resonance consists of two dark states formed by $(-1, +1)$ and $(+1, -1)$ ground state m_F sublevels in ^{87}Rb . These dark states have higher magnetic field sensitivity than the conventional 0-0 dark state. Figure 5.24 shows the magnetic field dependencies of $(-1, +1)$ and $(+1, -1)$ CPT resonances produced by the $lin \parallel lin$ scheme. These measurements are obtained by slowly changing the current in the Helmholtz coil while keeping the laser modulation frequency locked to the peak of CPT resonance using an electronic servo, and measuring the shift in the modulation frequency with a frequency counter. These measurements could only be taken when

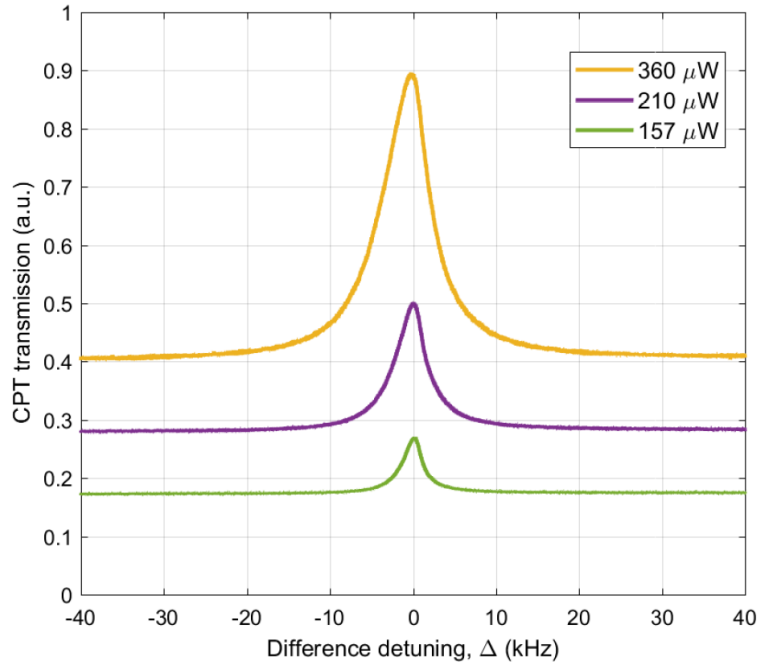


Figure 5.22: CPT resonances with three different optical powers, with offset amplitude for relative comparison.

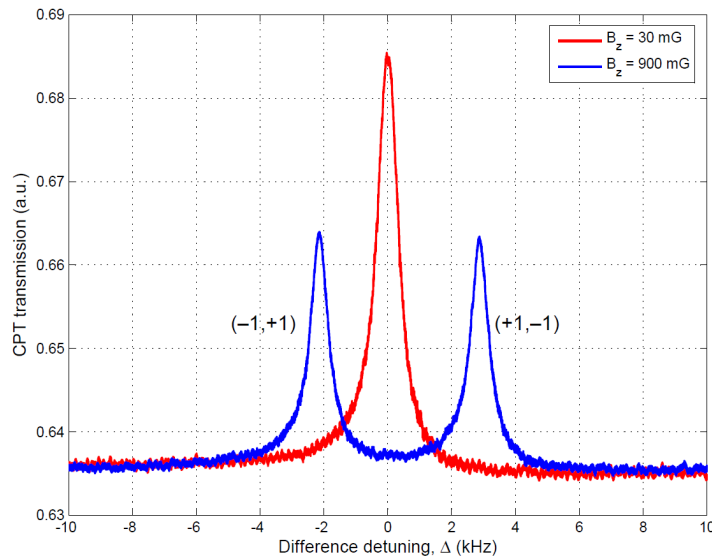


Figure 5.23: Magnetic field induced splitting of the central CPT resonance (linewidth = 841 Hz, contrast = 7.5%) generated by $lin \parallel lin$ excitation resonant with $|F' = 1\rangle$ state.

the $(-1, +1)$ and $(+1, -1)$ resonances were sufficiently separated by B_z allowing the servo to lock.

The two resonances split asymmetrically as B_z is gradually increased. As expected, the splitting

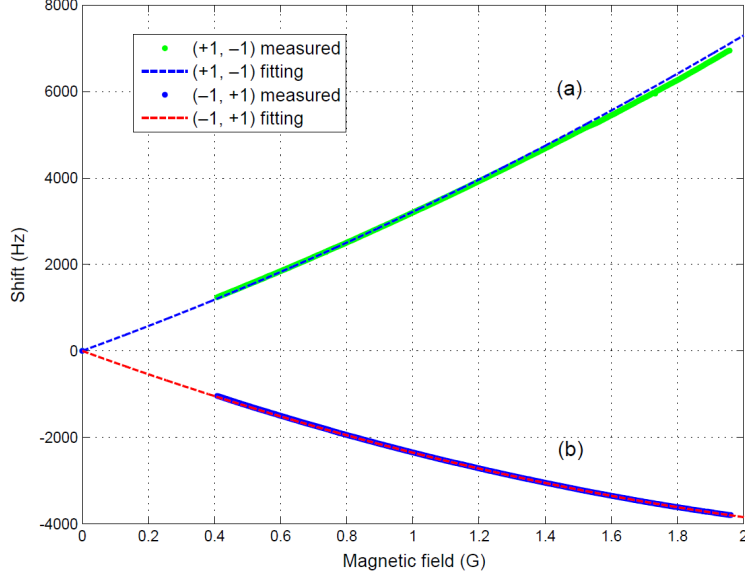


Figure 5.24: Magnetic field dependencies of (a) the (+1, -1) CPT resonance, shown in right in figure 5.23 and (b) the (-1, +1) CPT resonance, shown in left in figure 5.23. The dashed lines represent the fittings obtained using the Breit-Rabi equation.

also exhibits a nonlinear dependence on B_z . The experimental trends agreed very well with the magnetic field dependencies shown in dashed lines in figure 5.24 as theoretical fittings obtained from the Breit-Rabi equation [70,77]:

$$\Delta_{\substack{+1,-1 \\ -1,+1}} = \omega_{hf} \pm \left(\frac{2g_I\mu_B}{\hbar} \right) B_z + \left(\frac{3}{4} \frac{(g_J - g_I)^2 \mu_B^2}{2\hbar^2 \omega_{hf}} \right) B_z^2 \quad (5.4)$$

where g_I is the nuclear spin g-factor and g_J is the electron spin g-factor. See appendix C for more detail on the Breit-Rabi equation. We measured the coefficients of linear and quadratic shifts (i.e. the bracketed terms in eqn. (5.4)), and found them to be in close agreement with published values of 2785.6 Hz/G and 430.94 Hz/G², respectively [65,110]. These measurements confirmed higher magnetic field sensitivities of (-1, +1) and (+1, -1) resonances. They can be indirectly used in estimating the atomic g-factors.

Alternatively, magneto-optical rotation (MOR) measurement can be performed in *lin* || *lin* excitation scheme for observing MOR CPT resonance with high contrast [111–114]. In this case,

the $lin \parallel lin$ polarized beam is transformed to $45^\circ lin \parallel lin$ using the $\lambda/2$ plate before the cell and differential detection is performed by subtracting the horizontal (H) and vertical (V) components

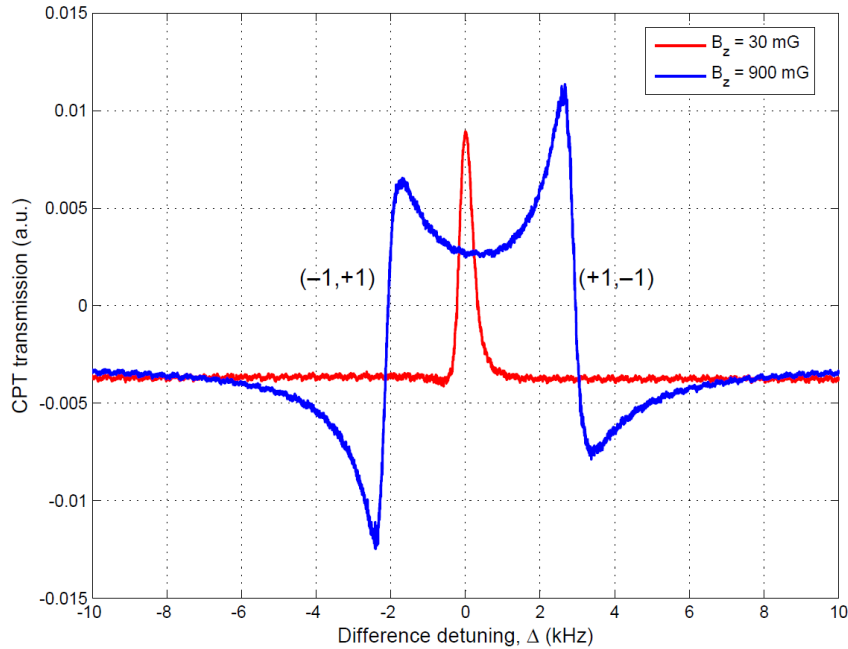


Figure 5.25: Differentially detected MOR CPT resonance generated by $lin \parallel lin$ excitation. The signal is dispersive which is evident at higher magnetic field.

of the polarized field after the cell using a polarimeter consisting of a polarizing beam splitter (PBS), two (H and V) photodetectors, and a high-speed electronic subtractor. Figure 5.25 shows the MOR CPT resonance observed at the output of the subtractor. With low magnetic field ($B_z \approx 30$ mG), the signal is formed with a single peak, but with a higher magnetic field ($B_z \approx 900$ mG), the dispersive nature of the MOR CPT resonance is evident in the separated resonances formed by $(-1, +1)$ and $(+1, -1)$ dark states. Differential detection used in MOR gives the advantage of generating background-free CPT resonance with high contrast (close to 100%) and also cancels the common-mode laser and electronic noises. However, it suffers from the same limitation as the direct detection $lin \parallel lin$ excitation, exhibiting high magnetic field sensitivity, leading to clock instability.

Polarization Scheme	Contrast		Linewidth		Clock transition	Shot Noise Limited Stability
	$F' = 1$	$F' = 2$	$F' = 1$	$F' = 2$		$\sigma_y(\tau = 1 \text{ s})$
$lin \parallel lin$	7.5%	N/A	841 Hz	N/A	$(-1, +1), (+1, -1)$	1.4×10^{-13} ($F' = 1$)
(σ^-, σ^-)	4.2%	16.7%	780 Hz	1040 Hz	0-0	7.7×10^{-14} ($F' = 2$)
$lin \perp lin$	7.8%	19.0%	859 Hz	976 Hz	0-0	6.4×10^{-14} ($F' = 2$)

Table 5.1: Experimentally measured CPT characteristics for different polarization schemes

Traditionally, circular polarization in the form of (σ^+, σ^+) or (σ^-, σ^-) has been used in commercial CPT clocks [115–117]. Figure 5.26 shows the CPT spectrum produced by (σ^-, σ^-) excitation resonant with $|F' = 2\rangle$ state in ^{87}Rb . The central CPT resonance at $\Delta = 0$ is only formed by the 0-0 dark state as shown earlier in our simulation result in figure 3.8. Figure 5.26 also shows frequency-shifted Zeeman CPT resonances formed by $(-1, -1)$ and $(+1, +1)$ dark states with frequency shifts proportional to the applied B_z (≈ 30 mG). The broadening of Zeeman CPT resonances is attributed to the inhomogeneity of B_z across the cell length. The strengths of Zeeman CPT resonances are indicative of the atomic population in the $(-1, -1)$ and $(+1, +1)$ dark states. The inset in figure 5.26 shows the central CPT resonance using a narrow frequency scan (20 kHz) around the two-photon resonance. The linewidth $\Delta\nu$ and contrast C of the central CPT resonance are found to be approximately 1.04 kHz and 16.7%, respectively. We observed that (σ^-, σ^-) excitation resonant with $|F' = 1\rangle$ state produced central CPT resonance with significantly low contrast ($C \approx 4.2\%$).

We used the atomic model (described in chapter 3) to simulate CPT spectra and compare their contrast for (σ^-, σ^-) excitation resonant with $|F' = 1\rangle$ and $|F' = 2\rangle$ states. These results are as shown in figure 5.27. For the choice of parameters used in our calculation (i.e. $\Omega_1 = \Omega_2 = \Gamma/60$, Γ

= 6 MHz, $\gamma_1 = \gamma_2 = 3$ Hz and $B_z = 27$ mG), the central CPT resonance for $|F' = 2\rangle$ shows a contrast of 13.7% while the one for $|F' = 1\rangle$ shows reduced contrast 5.3%. This reduction in contrast could be caused due to effective trapping of rubidium atoms in the Zeeman end state $|F = 2, m_F = 2\rangle$ for resonant excitation with $|F' = 1\rangle$ state. Although, the results obtained from our simulation reflect the reduction in contrast, the absolute values of contrast obtained from these results do not match with our experiment. This is because in actual experiment, magnetic field inhomogeneity, beam propagation in the medium, and buffer gas filling can influence CPT contrast, and these effects are not included in our model. Our observations suggest that (σ, σ) excitation resonant with $|F' = 2\rangle$ state is suitable for rubidium CPT clock for producing CPT resonance with high contrast and low magnetic field sensitivity.

Finally, we investigated $lin \perp lin$ excitation scheme by installing the polarization-based interferometer in our experiment setup as described earlier in section 5.4. Figure 5.28 shows the central CPT resonance (with a Lorentzian fit) produced by $lin \perp lin$ excitation resonant with $|F' = 1\rangle$ and $|F' = 2\rangle$ states, respectively. For comparing the linewidth and contrast of the CPT resonance, the total optical power used in the laser beam is kept the same ($\approx 70 \mu\text{W}$) as for $lin || lin$ and (σ^-, σ^-) excitations discussed earlier. The measured values of linewidth and contrast for different excitation schemes are listed in table 5.1. The central CPT resonance in $lin \perp lin$ excitation resonant with $|F' = 2\rangle$ is mainly formed by the 0-0 dark state as seen earlier in our simulation result in figure 3.10. The estimated shot noise limited stability values are given in table 5.1.

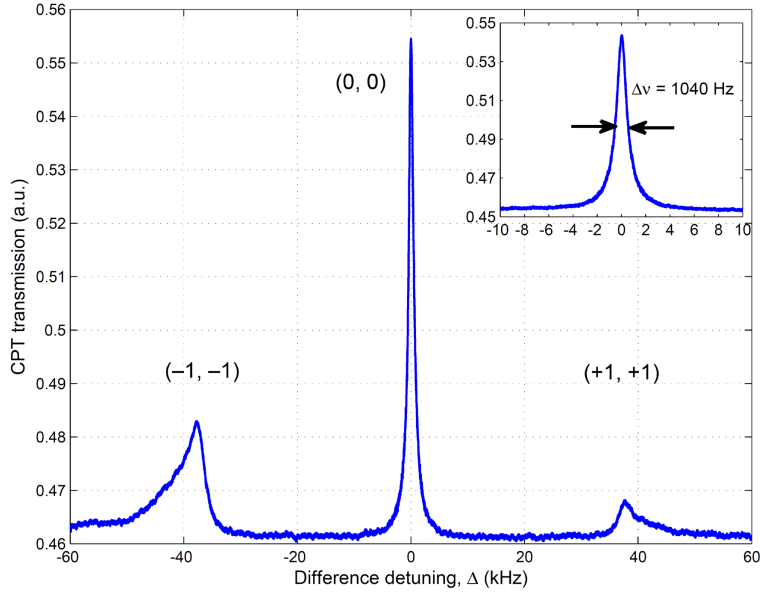


Figure 5.26: CPT spectrum produced by (σ^-, σ^-) excitation resonant with the $|F' = 2\rangle$ state and $B_z \approx 30$ mG. The inset in the figure shows the central CPT resonance produced with linewidth = 1.04 kHz and contrast = 16.7 %.

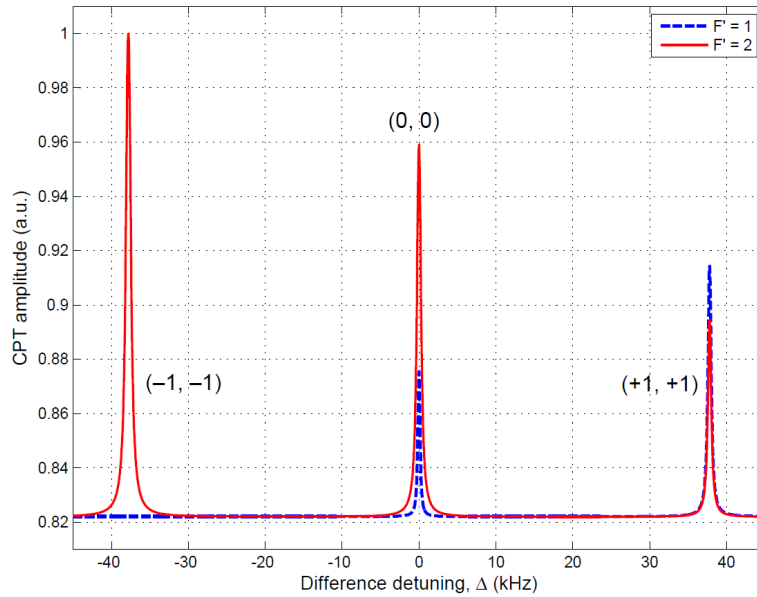


Figure 5.27: CPT spectrum calculated for (σ^-, σ^-) excitation resonant with $|F' = 1\rangle$ (dashed) and $|F' = 2\rangle$ (solid) states. The two CPT spectra are made to overlap by using background subtraction. CPT contrast was estimated prior to background subtraction. Following parameters were used in our calculation: $\Omega_1 = \Omega_2 = \Gamma/60$, $\Gamma = 6$ MHz, $\gamma_1 = \gamma_2 = 3$ Hz and $B_z = 27$ mG.

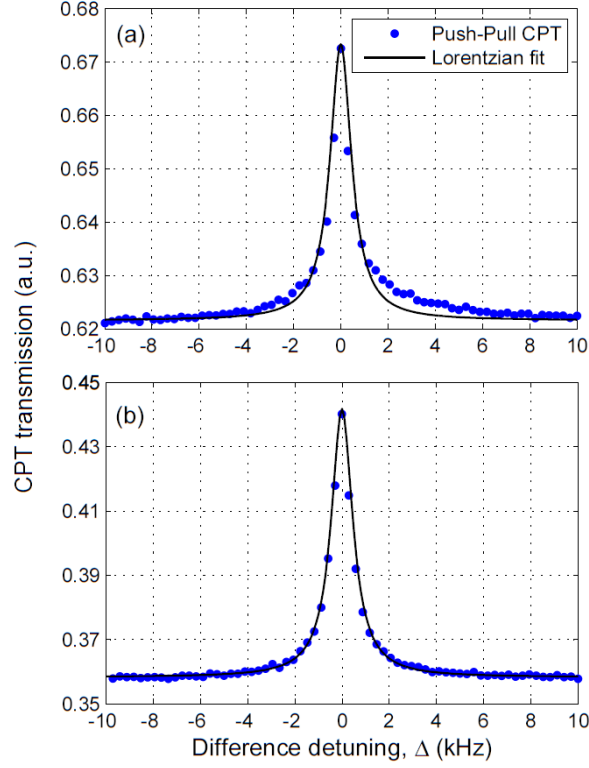


Figure 5.28: Central CPT resonance produced by $lin \perp lin$ excitation resonant with (a) $|F' = 1\rangle$ state (linewidth = 859 Hz, contrast = 7.8 %) and (b) $|F' = 2\rangle$ state (linewidth = 976 Hz, contrast = 19%). The solid lines correspond to Lorentzian fits to the CPT profiles.

We optimized the path difference between the arms of the interferometer to achieve a maximum contrast of 19% for resonant excitation with $|F' = 2\rangle$ state. This is nearly 2.4 times higher than resonant $|F' = 1\rangle$ excitation. However, the observed linewidth for $|F' = 1\rangle$ state is found to be slightly smaller than $|F' = 2\rangle$ state due to the difference in their matrix elements involved in excitation. While the advantages of $lin \perp lin$ excitation are evident in comparison to $lin || lin$ and (σ, σ) excitation, adding the interferometer to the cell physics package may give rise to additional complexity (in terms of volume and weight), thus, making $lin \perp lin$ unsuitable for compact clock design. However, as mentioned before, a counter-propagating σ^+ and σ^- excitation scheme with similar advantages can be adopted in compact clock design.

5.7.2 Ramsey results

RR interference produced with the method described in section 5.6 exhibits the characteristics detailed previously, such as linewidth dependence on T and insensitivity to optical power change. Figure 5.29 shows RR interference fringes for two different optical powers demonstrating the change in contrast with little to no change in central fringe width.

Figure 5.30 shows how the central fringe linewidth of RR interference fringes changes with free evolution time. For this particular optical power ($\sim 500 \mu\text{W}$) and system (large vapor cell), the width may be limited by dephasing, despite the linewidth dependence on $1/2T$. Figure 5.31 demonstrates the slope of linewidth with optical power for both CPT and RR interference. As expected, CPT linewidth is more susceptible to power than RR interference, as it has a slope five times larger. These results need to be retaken in future studies with parameters closer to ideal system settings for improved characterization. Implementing both an experimental and full multi-level model characterization of RR interference light shift properties could bring to light aspects of light shift reduction or suppression. Ramsey interference is further explored in the context of the repeated query pulse technique in section 5.8.

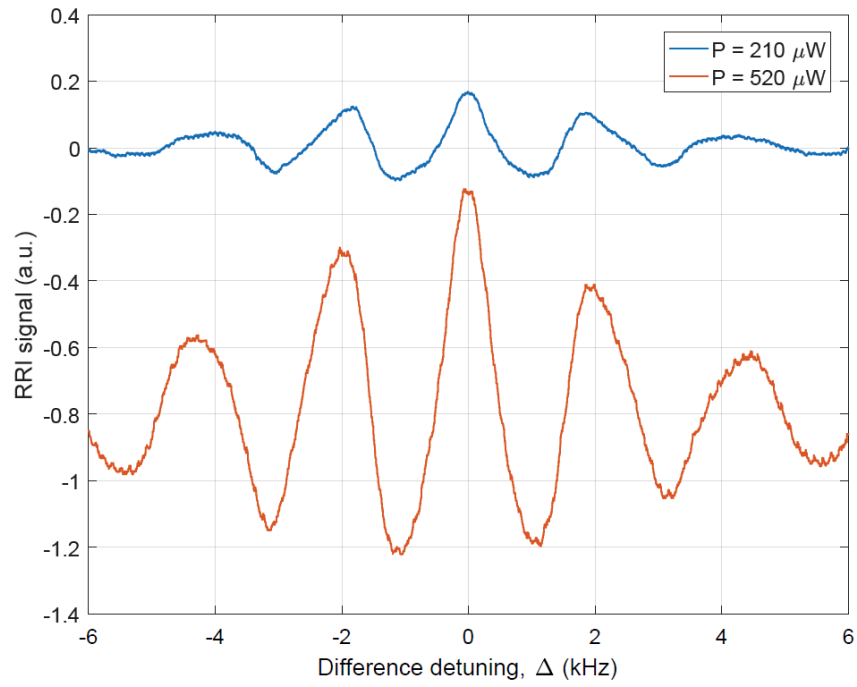


Figure 5.29: Ramsey interference fringes for two different optical powers

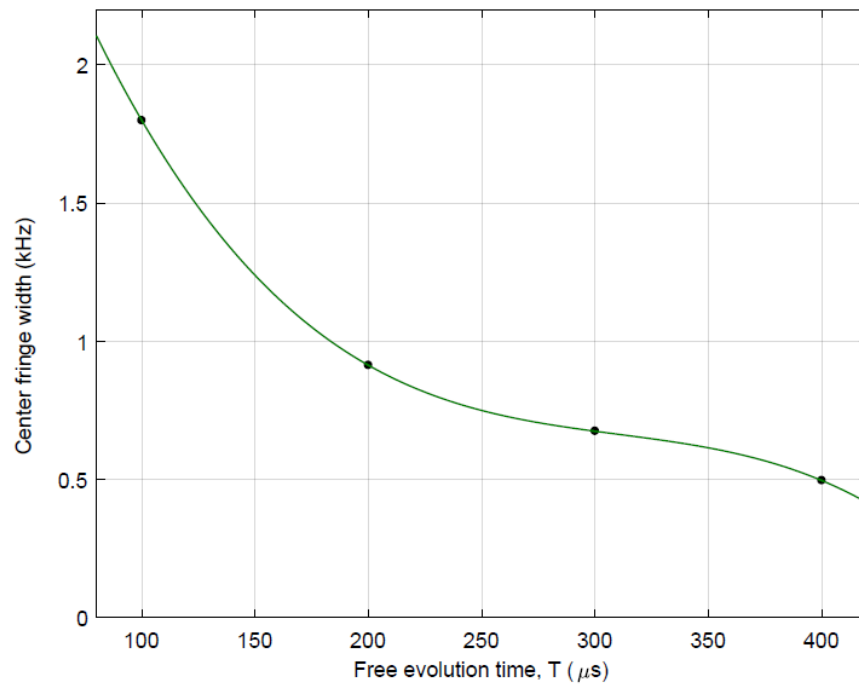


Figure 5.30: Central fringe width of Ramsey interference fringes for different free evolution times.

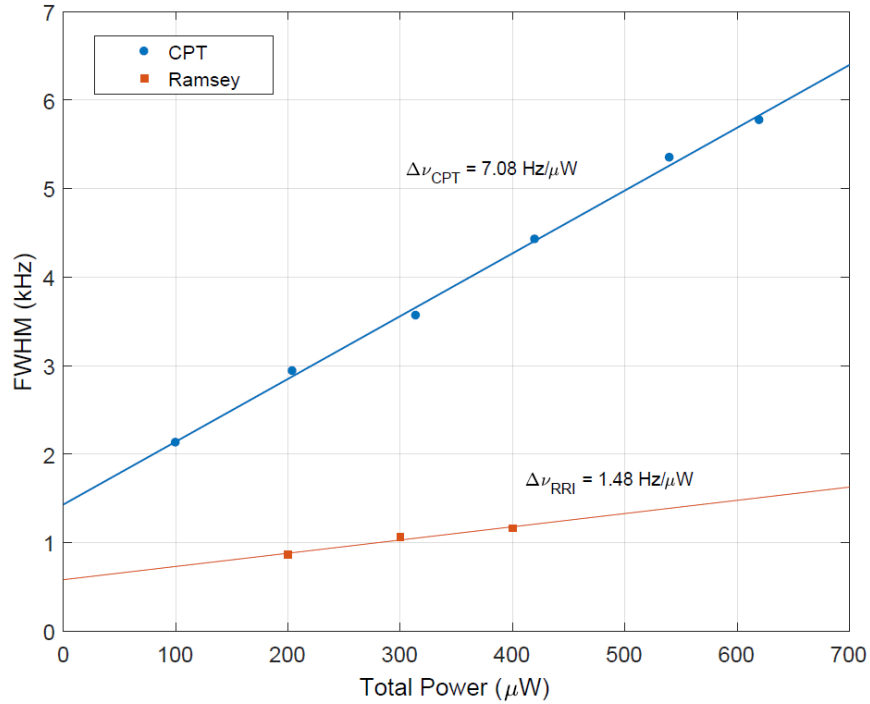


Figure 5.31: CPT and RR interference resonance width (or central fringe width) with optical power (Rabi frequency)

5.7.3 Light shift measurements

As predicted by the theoretical model in chapter 4, the pulsed interrogation scheme used in the CPT clock will be less susceptible to light shift error caused by long-term drift (or fluctuation) in laser power and frequency. Figure 5.32 shows experimental measurements of light shift with single photon laser detuning for the CPT clock. Figure 5.33 shows the light shift measurement with detuning for the Ramsey (pulsed CPT) clock. These measurements were performed using a locked TSVCO in a large vapor cell, using the carrier and single sideband with a separation of 6.834 GHz to form the CPT beam. The off-resonant sideband contributes a significant fraction of background light to the total optical power. The measurements were collected by locking the

TSCVCO to the peak of the atomic resonance, unlocking the laser and slowly sweeping the laser frequency around the highest contrast point for CPT, and finding the frequency offset from the locked CPT or Ramsey clock frequency when the laser fields are on resonance. The slope of the CPT light shift (figure 5.32) is found to be 0.37 Hz/MHz while using an optical power of 210 μW . The slope of Ramsey light shift (figure 5.33) is found to be significantly reduced to 0.05 Hz/MHz

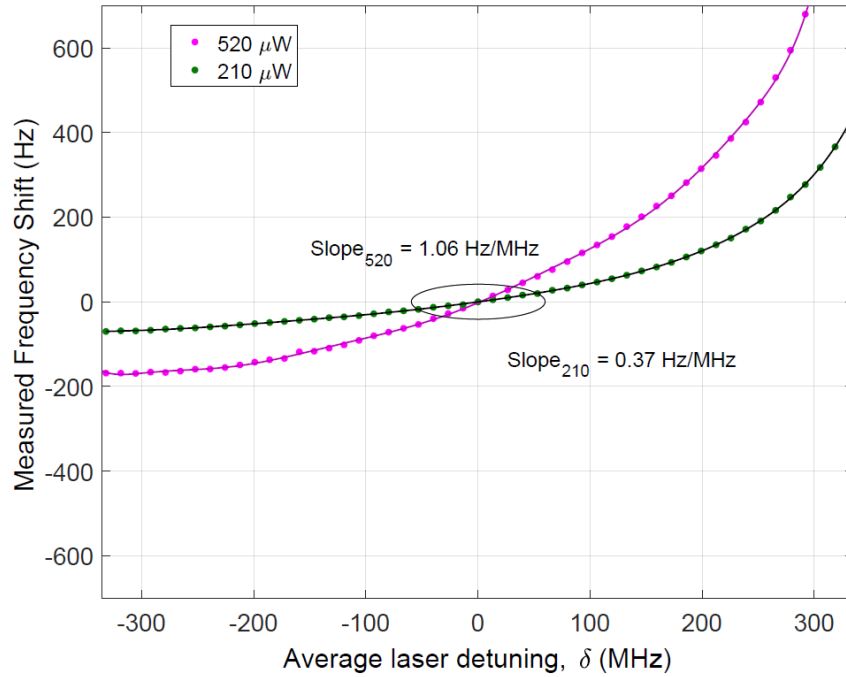


Figure 5.32: CPT light shift vs δ measured at two different total optical powers with polynomial line fit.

by using a pulse separation T equal to 800 μs . This slope can be further reduced by exploiting the pulse saturation condition.

Optical power affecting CPT and RR interference light shift is shown in figure 5.34. With a few data points, it is clear that the frequency dependence of RR interference on optical power is significantly less affected. CPT light shift with power has a slope of 0.27 Hz/ μW , while RR interference light shift with power has a slope of 0.12 Hz/ μW , less than half. Power fluctuations

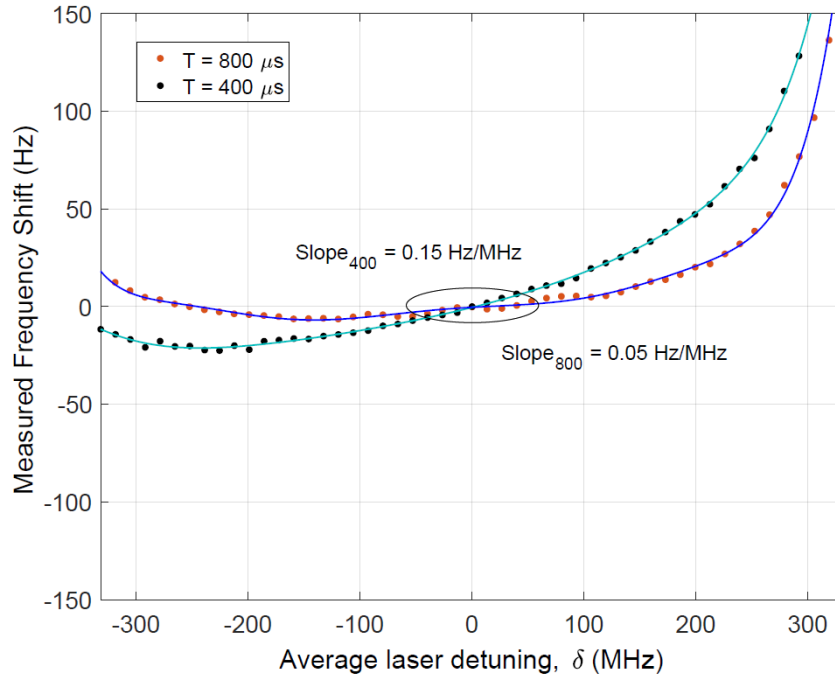


Figure 5.33: RR interference light shift vs δ measured with two different free evolution times, with polynomial line fit.

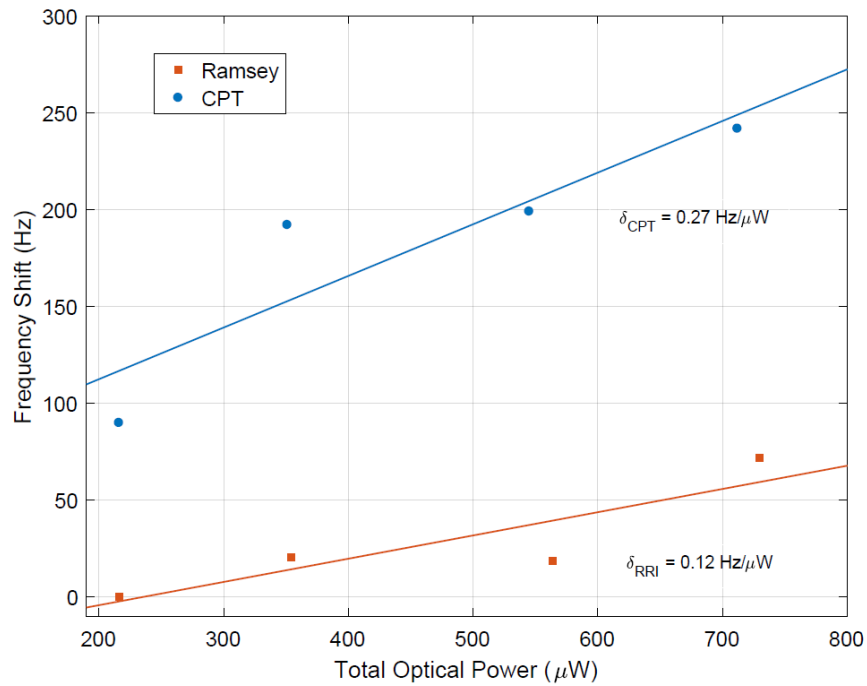


Figure 5.34: CPT and RR interference light shift with optical power (Rabi frequency)

would thus affect RR interference less than CPT. Fine tuning the parameters of this experiment would allow for better characterization of light shift with power and Rabi frequency in the system.

5.7.4 VCSEL characterization

For compactness and low power consumption, the tunable laser and EOM should be replaced by a vertical cavity surface emitting laser (VCSEL), which can be directly modulated at RF frequencies. We have begun preliminary studies with a VCSEL (M2 Photonics VCSEL, APM2101013300) to characterize its modulation behavior and performance for generating CPT and RR interference fringes. The VCSEL is current-driven and temperature controlled with an ILX laser controller with a 5 mA/V current tuning slope and a measured wavelength and frequency tuning of $\lambda/I = 0.6646$ nm/mA or 103 GHz/mA. Because of this sensitivity, a very low noise current driver is required. The size of a VCSEL diode (figure 5.35) makes it an ideal option for size and power requirements in compact clocks. The VCSEL linewidth, however, is around 30 MHz, which is significantly higher than a tabletop tunable diode laser (~ 1 MHz) and will reduce the performance of the clock.

The VCSEL frequency is tuned by both current and temperature, therefore precise temperature control is also implemented. Figure 5.36 shows the TEC heating block and diode mount used in the setup. For VCSEL sideband modulation, a bias-tee is used to combine the DC current from the low-noise current driver and the RF signal at 3.417 GHz from a VCO.

Preliminary measurements of modulated VCSEL with the Fabry-Perot scanning etalon showed a high sensitivity to RF amplitude. However, at an RF power of 10 dBm, the carrier is sufficiently suppressed and optical sidebands separated by 6.834 GHz were visible, though noisy. Further study is needed for sideband generation and application of VCSEL to our schemes.



Figure 5.35: VCSEL in a TO-86 package, less than half a cm in diameter

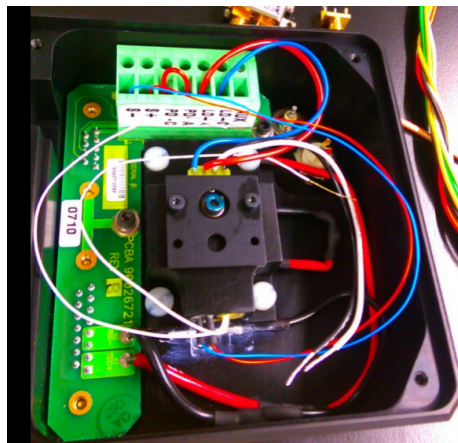


Figure 5.36: VCSEL ILX mount with TEC and thermistor, the VCSEL is connected to the current source.

5.8 Repeated query technique

In a vapor medium, rapid decoherence of the dark state occurs due to atomic collisions. This leads to an exponential decay of the Ramsey signal amplitude with T and thus, creates a trade-off between choosing a large T to simultaneously produce narrowest fringe-width and high S/N ratio in Ramsey interference. For example, a typical vapor cell filled with buffer gas can produce sub-kilohertz fringe-width for T extending up to 5 to 6 milliseconds, but with significantly low contrast ($< 10\%$). Indirect detection of Ramsey interference fringes using magneto-optical rotation

can improve the signal contrast up to 90% [118,119]. However, this scheme can only be used with $lin \parallel lin$ polarized CPT fields which generally have a high sensitivity to the magnetic field. Guérandel et al [2007] introduced a phase-stepping method for generating high contrast Ramsey fringes which exhibits a dispersive characteristic at the center (or two-photon resonant) frequency [85,120]. However, phase-stepping requires precise adjustment of the relative phase between two laser frequencies during each pulse, which can potentially create phase (or frequency) errors.

In this section, we demonstrate a repeated query technique (RQT) for interrogation to generate narrow fringe-width and high S/N ratio in Ramsey interference. Typically Ramsey fringes produced by a single query pulse, have nearly uniform amplitude around the center of the frequency sweep. This also makes the central fringe nearly indistinguishable from the adjacent fringes. However, the results show that RQT enhances the central fringe amplitude and suppresses the side fringes. Implementation of RQT requires simple electronic modifications in the setup for generating the pulse sequence and integrating the signal after detection. It is therefore suitable for compact Ramsey clock development. We carried out our experiments using a small (2 cm long), isotopically pure and buffer-gas filled rubidium cell. We measured the line shapes of Ramsey interference produced due to RQT and compared the line shapes with those estimated from solving density-matrix equations for a three-level (Λ -type) atomic system. The results show simultaneous narrowing of fringe-width and improvement in S/N ratio with N , where N represents the number of repeated query pulses. We have measured the frequency stability of the Ramsey clock and compared the frequency stability of the clock with RQT and single query technique (SQT).

Figure 5.37 shows the schematic of the experimental setup used in investigating the characteristics of Ramsey interference with SQT and RQT. The setup is also used as a clock to

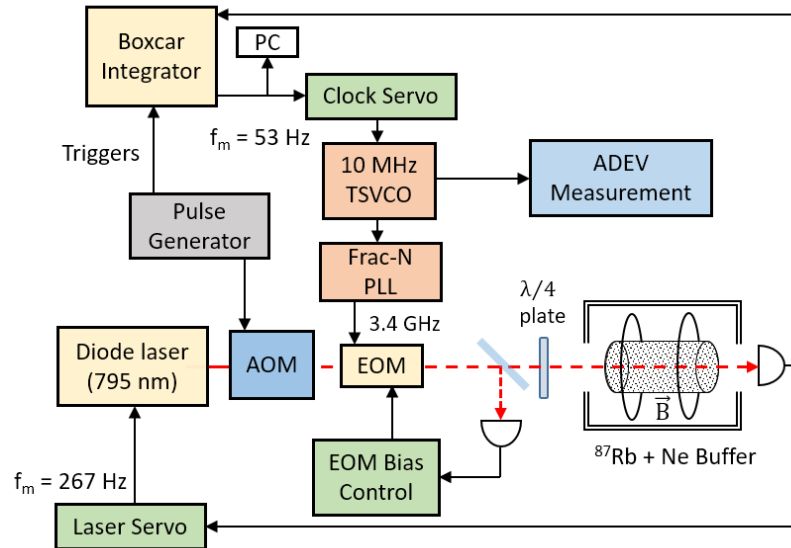


Figure 5.37: Schematic of the experimental setup used to generate Ramsey interference in the rubidium atomic clock. The optical beam is pulsed using an AOM and a boxcar integrator is used to perform gated detection and sample averaging to produce the Ramsey fringes by repeated query pulses.

measure the frequency stability performances of the clock with SQT and RQT. The RF signal driving the EOM, which is synthesized from a 10 MHz temperature-stabilized voltage controlled oscillator (TSVCO) locked to an RF VCO by a fractional phase-locked loop (PLL), is shown in figure 5.37. When the setup is used as a clock, the TSVCO output frequency is locked to the center of the Ramsey fringe by a clock servo, and its frequency stability is measured using the Allan deviation (ADEV) measurement test probe.

The schematic for the single and repeated query pulse Ramsey interference measurements including the pulsing AOM is shown in figure 5.37. The pulsed and modulated optical beam in our experiment is passed through a quarter-wave ($\lambda/4$) plate to create circularly polarized CPT fields. It is then passed through a pure-isotope ^{87}Rb vapor cell (length = 2 cm, diameter = 1 cm) filled with 10 Torr neon buffer gas. The physics package of the vapor cell is comprised of a dual layer μ -metal magnetic shield enclosure surrounding the cell to reduce the effect of residual magnetic

field on rubidium atoms. A pair of Helmholtz coils is mounted inside the enclosure to apply a small uniform axial magnetic field ($B \simeq 30$ mG) which lifts the Zeeman degeneracy of the ^{87}Rb atomic states. The vapor cell is also actively temperature controlled ($\Delta T \simeq 100$ mK) with bifilar-twisted resistive nichrome heating wire and a standard K-type thermocouple temperature sensor.

During the experiment, the laser frequency is locked to the ^{87}Rb D1 absorption maximum corresponding to resonant excitation with $|F' = 2\rangle$ state [21,105]. The output from a single photodetector is used to implement both the laser servo and the clock servo as shown in figure 5.37. The laser beam is dithered (or modulated) by the EOM at two different frequencies ($f_m = 267$ Hz and 53 Hz, respectively) for the laser servo and clock servo to operate independently. The servo consisted of a lock-in-amplifier for generating the error signal by demodulating the output from the photodetector at the corresponding dither frequency. The servo also used a proportional-integral (PI) controller for generating the control signal. Due to the long duty-cycle of the optical pulse ($T_c = 1\text{-}2$ ms) sequence used in our experiments, dither frequencies and servo time constants were chosen properly to produce low noise error signals.

Figures 5.38 (a,b) show the schematic of the optical pulse cycle such as the pulse widths, time separation, and periodic repetition of the query pulses used in generating Ramsey interference. For the single query pulse technique (SQT), the pulse lengths are set as $\tau_c = 500 \mu\text{s}$, $T = 1.5$ ms, and $\tau_q = 1 \mu\text{s}$.

Figure 5.38b shows the modified pulse cycle for RQT using N repeated query pulses. In this case, the free evolution time T for SQT is divided into N equal time periods (i.e. $T_1 = T_2 \dots = T_N = T/N$) as shown in figure 5.38b. Therefore, a single pulse cycle of RQT consists of one CPT pulse of duration τ_c followed by a periodic train of N free-evolution times ($T_1, T_2 \dots T_N$) and N query pulses ($q^{(1)}, q^{(2)} \dots q^{(N)}$) each with duration τ_q . Ramsey interference effects are generated

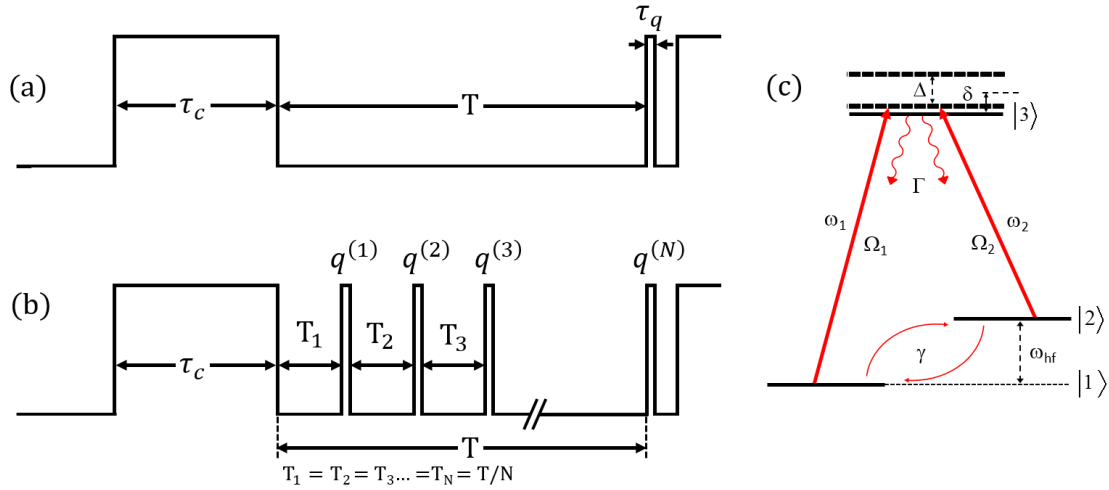


Figure 5.38: Timing diagram showing the pulse cycle with (a) a single query pulse, and (b) repeated query pulses for generating Ramsey interference. The pulse cycle in (b) consists of a periodic train of N query pulses $q^{(N)}$ of duration τ_q each and separation $T_N = T/N$. A three-level (Λ -type) atomic system shown in (c) has been used to simulate the Ramsey interference phenomena.

by each query pulse used in RQT. The boxcar integrator is triggered by the electronic query pulse triggers for observing the Ramsey interference effects produced by each query pulse. The combined Ramsey interference due to N query pulses in RQT is produced by setting the number of samples for rolling average in the boxcar integrator equal to N . Ramsey fringe due to RQT is produced by repeating the pulse cycle shown in figure 5.38b and changing the two-photon resonant frequency. As a simpler alternative, we used a fast digitizer board interfaced with LabVIEW to acquire Ramsey fringes. Appendix G shows the LabVIEW program for pulse integration and visualization of the data. The digitizer allowed us to perform real-time sampling and signal integration without the boxcar integrator. This method can also be used to introduce real-time signal processing in data acquisition to reduce ‘noise’ in the Ramsey signal.

Figures 5.39(a,b) show experimentally observed Ramsey fringes obtained with a single query pulse, and by increasing the optical power in the CPT beams from $57 \mu\text{W}$ to $90 \mu\text{W}$. We

used a pulse cycle with $\tau_c = 500 \mu\text{s}$, $T = 1.5 \text{ ms}$ and $\tau_q = 1 \mu\text{s}$. Ramsey fringes were generated by scanning the frequency difference $\Delta = [(\omega_1 - \omega_2) - \omega_{hf}]$ between the CPT fields of frequencies ω_1 and ω_2 , at a rate 20 mHz around $\Delta = 0$. The fringe-width is found to be consistent with $\Delta\nu (= 1/2T) \simeq 333 \text{ Hz}$ and it is also found to be independent of the optical power as expected.

The central Ramsey fringe in figure 5.39a exhibits a contrast $C (= T_A/T_p)$ of about 80% with its transmitted amplitude $T_A \simeq 0.4$ and peak amplitude, $T_p \simeq 0.5$ for the fringe. Figure 5.39b shows Ramsey fringes with higher contrast ($C \simeq 90\%$) and higher transmitted amplitude ($T_A \simeq 0.8$), or S/N ratio, obtained due to increased (i.e. approximately double) optical power. It is also observed that Ramsey fringes adjacent to the center have high contrast (i.e. close to 76% in figure 5.39b). This can make them indistinguishable when identifying the central fringe for the atomic clock.

We investigated Ramsey fringes theoretically by modeling the optical excitations in a three-level atomic system (shown in figure 5.38c) with time-dependent density-matrix equations $\frac{\partial \rho}{\partial t} = -\frac{i}{\hbar} [H\rho - \rho H^\dagger] + L$, where ρ is the density operator, H is the semi-classical, non-Hermitian Hamiltonian, and L represents the source matrix for possible relaxations (i.e. Γ and γ) between the atomic states [51] (see chapter 2). The Hamiltonian H for the atomic system is described by

$$\begin{pmatrix} \frac{\Delta}{2} - \frac{i\gamma}{2} & 0 & -\frac{\Omega_1}{2} \\ 0 & -\frac{\Delta}{2} - \frac{i\gamma}{2} & -\frac{\Omega_2}{2} \\ -\frac{\Omega_1}{2} & -\frac{\Omega_2}{2} & -\delta - \frac{i\Gamma}{2} \end{pmatrix} \quad (5.5)$$

where Ω_1 and Ω_2 represent the CPT field Rabi frequencies, $\delta = (\delta_1 + \delta_2)/2$ is the average frequency detuning with δ_1 and δ_2 representing the single-photon detuning of the respective CPT fields, and $\Delta = \delta_1 - \delta_2$ corresponds to difference (or Raman) detuning between the two CPT

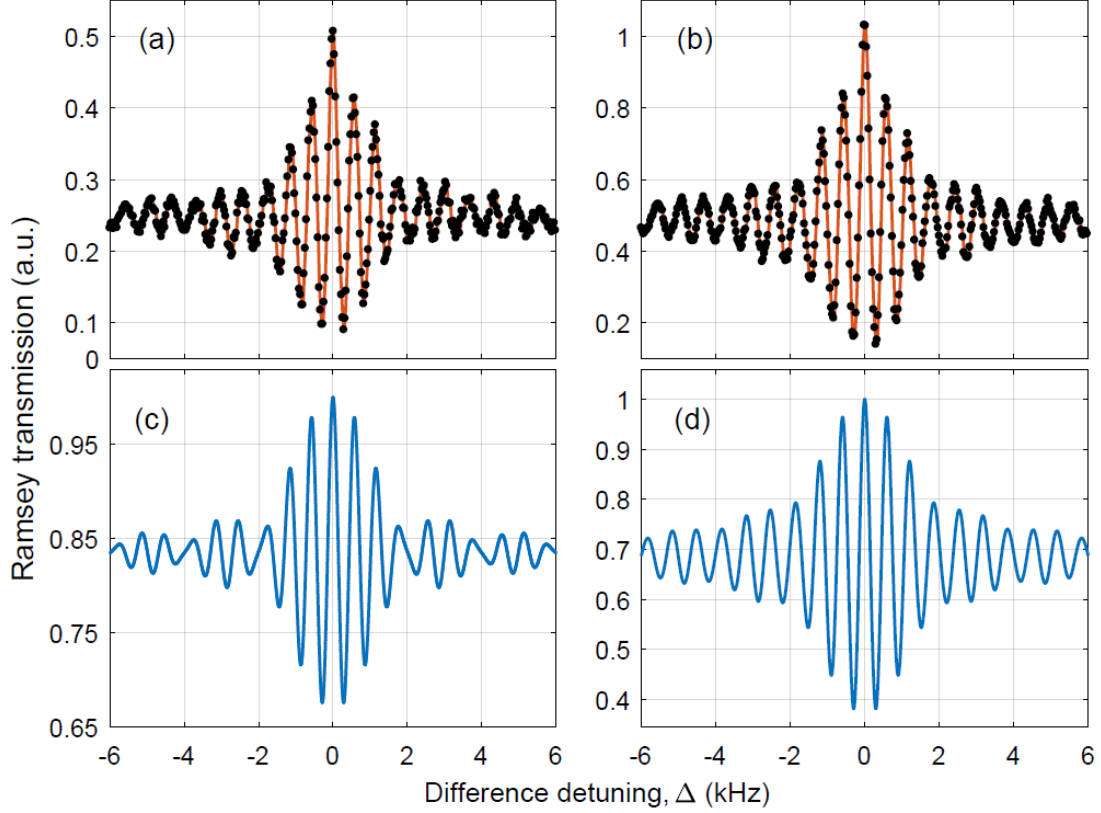


Figure 5.39: Experimentally generated Ramsey fringes by using SQT ($N=1$) and total optical power of (a) $57 \mu\text{W}$ and (b) $90 \mu\text{W}$ in the CPT beams. Simulated Ramsey fringes for Ω equals to (c) $\Gamma/200$, and (d) $\Gamma/100$. The following simulation parameters were also used: $\tau_c = 500 \mu\text{s}$, $T = 1.5 \text{ ms}$, $\tau_q = 1 \mu\text{s}$, $\Gamma = 6 \text{ MHz}$, and $\gamma_1 = \gamma_2 = \gamma = 60 \text{ Hz}$.

fields. For simplicity, the Rabi frequencies are chosen to be equal (i.e. $\Omega_1 = \Omega_2 = \Omega$) for our theoretical calculations. The density-matrix equations are used to calculate Ramsey fringes

produced by pulsed optical excitations i.e. $\begin{cases} \Omega \neq 0, & t = \tau_c, \tau_q \\ \Omega = 0, & t = T \end{cases}$. While simulating Ramsey

interference with a single query pulse, numerical solutions are obtained for ρ for three sequential time intervals τ_c , T , and τ_q during the pulse cycle. Ramsey fringes are generated by repeating our numerical calculations for many pulse cycles, calculating the fringes for values of Δ around zero.

For simplicity, we only chose the density-matrix element ρ_{33} (corresponds to excited-state population) to represent the Ramsey fringe. Similarly, our calculation is extended to simulate

Ramsey fringes due to RQT by including N query pulses during each pulse cycle. In this case, ρ is calculated N successive times for intervals (T/N and τ_q) and the calculated values of ρ obtained after each query pulse $q^{(i)}, i = 1..N$ are added to generate the Ramsey fringes.

Figures 5.39(c,d) show theoretically calculated Ramsey fringes for single query pulse (i.e. $N = 1$) and the simulation parameters: $\tau_c = 500 \mu\text{s}$, $T = 1.5 \text{ ms}$, $\tau_q = 1 \mu\text{s}$, and $\Gamma = 6 \text{ MHz}$ which corresponds to the decay rate of the rubidium excited state. We chose two different Rabi frequencies, Ω , and introduced an empirical ground-state decoherence rate $\gamma = 60 \text{ Hz}$ in each case. Ramsey fringes shown in figure 5.39(c,d) demonstrate a significant change in the line shape of Ramsey fringes due to change in Ω from $\Gamma/200$ to $\Gamma/100$ (which is equivalent to doubling the optical power in the experiment) or change in Raman saturation parameter ($\Omega \tau_c$) of the CPT pulse. The condition $\Omega \tau_c \gg 1$ leads to a steady-state excitation condition [51]. Figure 5.39c shows the line shape for $\Omega = \Gamma/200$ encased with a pulse-transform limited fringe envelope described by the function $\text{sinc}(\Delta\tau_c/2)$.

This also shows similarity with the experimental line shape in figure 5.39a. The contrast of the central Ramsey fringe in figure 5.39c is approximately 32.4%. Figure 5.39d shows the line shape of Ramsey fringes for $\Omega = \Gamma/100$ which is found to be relatively smooth without having any sidelobes. The fringes are also observed to be sinusoidal across its line shape. The central fringe contrast is found to be higher ($\approx 61.8\%$) than the previous case due to higher Raman saturation effect. As our theoretical model considers an ideal three-level atomic system, the results obtained here cannot be used to obtain exact match with the experimental results. However, they still exhibit the general characteristics of Ramsey interference.

Using our experimental setup (described earlier in Section 2), we implemented RQT by electronically changing the number of query pulses in the pulse cycle. Figure 5.40a-c shows Ramsey fringes produced by RQT for $N = 3, 5,$ and 10 respectively.

In all three cases, a single-peaked fringe emerges in the Ramsey spectrum produced by RQT. Unlike the single query Ramsey spectrum in figure 5.39, all the side fringes are suppressed due to the combined interference of N query pulses, and the peak amplitude of the central Ramsey fringe also increased in proportion with N . This is a desirable effect as the central fringe is used to create the discriminant signal for the atomic clock. It is also observed that increase in the peak amplitude is accompanied by a small increase in the fringe-width and substantial increase in the overall bias with N . As the bias is created by the electronic addition of query pulse signals, we compensated it electronically.

We then measured the contrast of the Ramsey signal by defining it as $(T_p - T_b)/T_p$ and keeping the bias T_b the same for all N . The contrasts were found to be approximately 31%, 65%, 72%, and 83% for $N=1, 3, 5,$ and 10 query pulses, respectively. Figure 5.41 shows the variation in contrast and peak (or signal) amplitude as a function of N . While the signal amplitude continues to grow linearly, the contrast reaches a maximum value 87% at around $N = 15$. The result suggests that RQT can produce a discriminant signal with significantly high contrast and S/N ratio, as needed to achieve high short-term frequency stability in the atomic clock.

We simulated the Ramsey fringes produced due to RQT using our atomic model. Figure 5.42a-c shows the simulated Ramsey spectra using repeated query pulses with $N = 3, 5,$ and $10,$ respectively. All other simulation parameters are kept the same as SQT except the free-evolution time between the query pulses are chosen to be $T_1 = T_2 \dots = T/N$ with $T = 1.5$ ms. Theoretical Ramsey spectra obtained with RQT for $\Omega = \Gamma/200$ show striking similarity with our

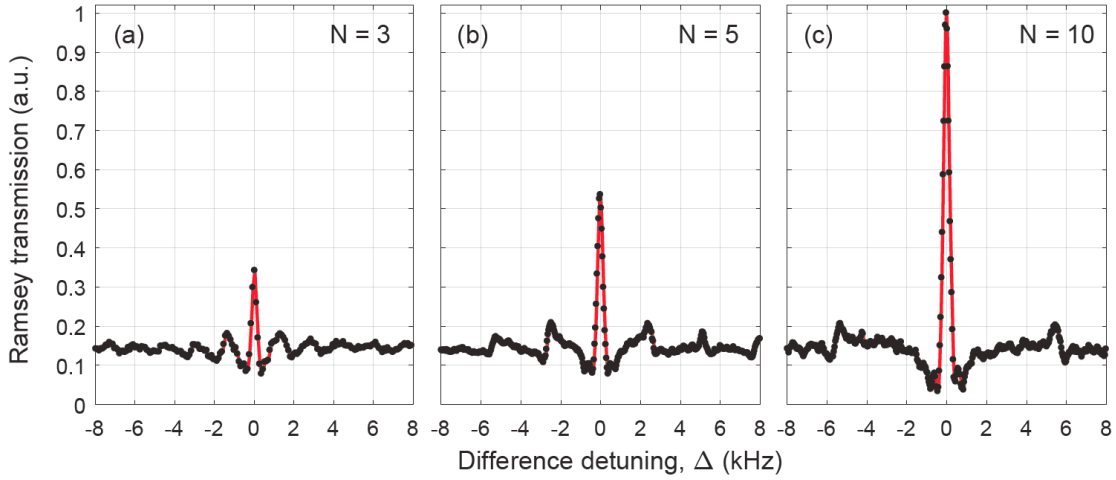


Figure 5.40: Experimental Ramsey fringes collected via RQT with (a) $N=3$ (b) $N=5$, and (c) $N=10$ query pulses. The background biases were electronically subtracted and kept equal when measuring the signal contrast.

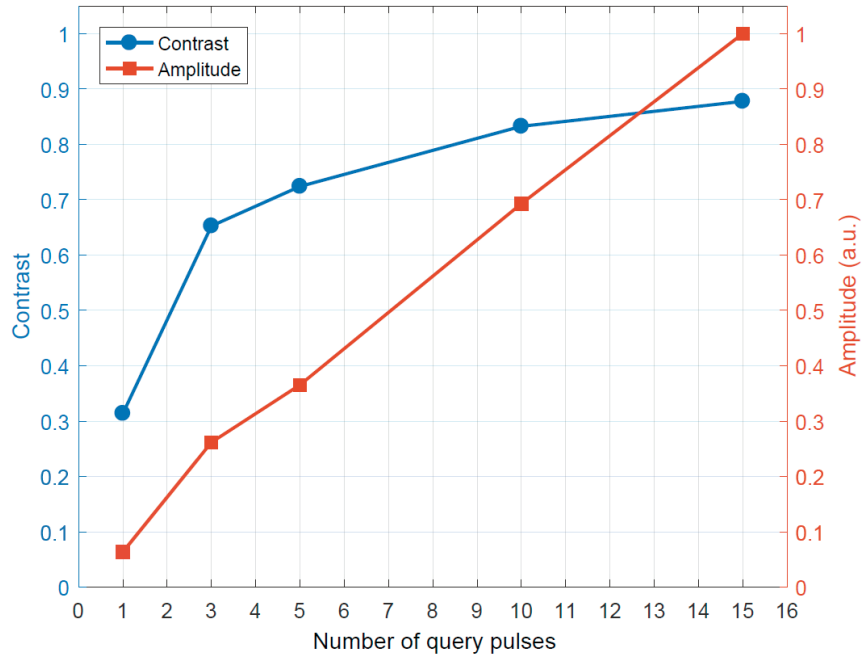


Figure 5.41: Variation in fringe contrast and amplitude with query pulses, measured experimentally.

experimental results in figure 5.40. Due to constructive interference of all query pulses at the fringe center $\Delta = 0$, a single-peaked Ramsey fringe with narrow fringe-width ($\Delta\nu$ comparable to $1/2T$)

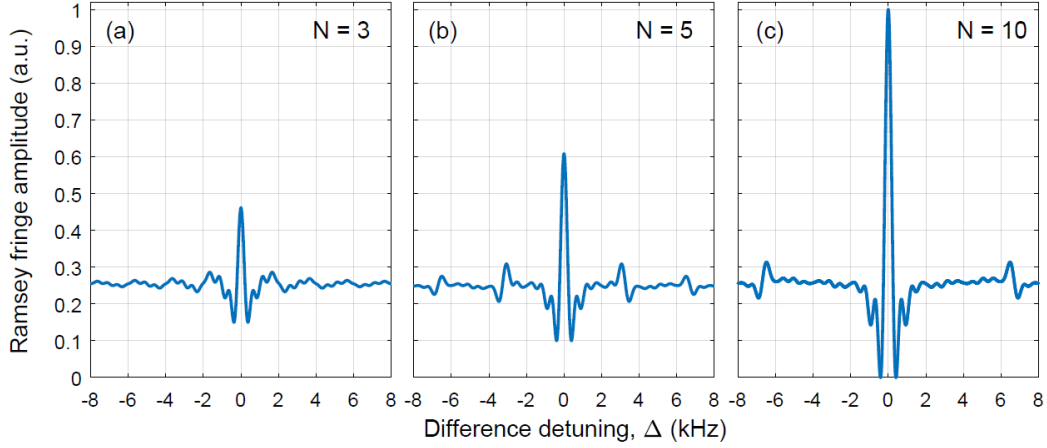


Figure 5.42: Simulated Ramsey fringes with (a) $N=3$ (b) $N=5$, and (c) $N=10$ query pulses. The following simulation parameters were used: $\tau_c = 500 \mu\text{s}$, $T = 1.5 \text{ ms}$, $\tau_q = 1 \mu\text{s}$ and $\Omega = \Gamma/200$.

$= 333 \text{ Hz}$) is produced. Increasing bias resulting from addition of repeated query signals, has been suppressed while plotting the Ramsey spectra in figure 5.42. As in experiment, the fringe amplitude enhancement has been confirmed from the simulation which, in practice, leads to improvement in contrast and S/N ratio in RQT. As in experiment, the fringe amplitude enhancement has been confirmed from the simulation which, in practice, leads to improvement in contrast and S/N ratio in RQT.

A general understanding about fringe amplitude enhancement due to RQT can be developed by finding the following analytical expression as the weighted sum of periodic Ramsey signals from N query pulses as

$$\begin{aligned}
 R(\Delta) &= \sum_{n=1}^N \cos\left(\frac{n \Delta T}{N}\right) e^{-\frac{n \gamma T}{N}} \\
 &= \frac{e^{-\gamma T} \left\{ \cos\left[\frac{(N+1)\Delta T}{N}\right] - e^{-\frac{\gamma T}{N}} \cos(\Delta T) \right\} - \cos\left(\frac{\Delta T}{N}\right) + \cosh\left(\frac{\gamma T}{N}\right) - \sinh\left(\frac{\gamma T}{N}\right)}{2 \left[\cos\left(\frac{\Delta T}{N}\right) - \cosh\left(\frac{\gamma T}{N}\right) \right]} \quad (5.6)
 \end{aligned}$$

where $R(\Delta)$ represents the amplitude of Ramsey interference, the fringe line shapes are assumed to be uniform, and the fringe amplitudes are assumed to decay at the rate γ . For $\gamma = 0$, the expression reduced to the familiar line shape function $\frac{\sin[(N+1/2) \Delta T/N]}{\sin[\Delta T/2N]}$ which has a maximum value N at $\Delta = 0$ indicating that the signal amplitude will be N times larger. Due to non-zero γ , the enhancement factor is found from eqn. (5.6) to be $\frac{e^{\gamma T} - 1}{e^{\gamma T/N} - 1}$ for N queries. This analytical model

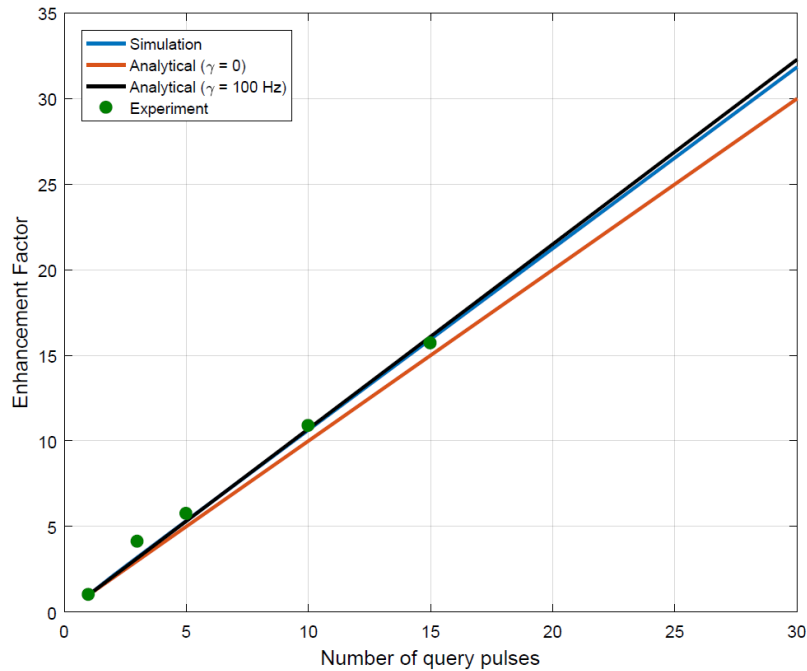


Figure 5.43: Amplitude enhancement factor for the Ramsey fringes acquired using N query pulses.

does not consider the destructive read-out effect of the query pulses on the fringe amplitude enhancement. Figure 5.43 shows the plots of enhancement factors estimated from eqn. (5.6) and our simulation for comparison purpose. Both simulation and the analytical model show higher slopes

for the enhancement factor compared to the case $\gamma = 0$. The solid dots in figure 5.43 show our experimental measurements with slope which agrees closely with the analytical model and the

simulation for small N . The observed discrepancy in the slope may be due to the choice of simulation parameters, particularly γ and Ω not matching the experiment. Degradation in the enhancement factor due to the destructive read-out effect of the query pulses is found to be significant for large N exceeding 30 pulses or so.

This chapter demonstrated the experimental methods and techniques used to characterize and implement a CPT and RR interference rubidium vapor cell atomic clock with various schemes. The results address the viability of $lin \parallel lin$, (σ, σ) , and $lin \perp lin$ excitation schemes for producing narrow linewidth, high contrast, magnetically-insensitive CPT resonance in the D1 manifold of ^{87}Rb atoms. They showed higher magnetic field sensitivity of the CPT resonance produced by $lin \parallel lin$ excitation. For (σ, σ) excitation, it was shown that the CPT contrast is dependent on the resonant excitation, which reached a maximum value 16.7% for resonant excitation with $|F' = 2\rangle$ state. Theoretical calculations matching experimental measurements revealed and verified magnetic field dependence of the central CPT resonance formed by different excitations. CPT contrast close to 20% was measured using $lin \perp lin$ excitation which is shown to be equivalent to PPOP. We also demonstrated the repeated query technique as a CPT interrogation scheme for generating Ramsey interference with a single-peaked central fringe of high contrast and S/N ratio. The experimental results showed that significant enhancements in contrast, peak amplitude as well as narrowing of fringe-width are achieved by using RQT with only 5 to 10 query pulses. The theoretical model estimated the line shapes of Ramsey fringes with different N which agreed closely with our experiments.

CHAPTER 6: CLOCK STABILITY RESULTS

Oscillators are characterized by, among other parameters, the stability of the output frequency. The frequency inevitably fluctuates over time from many factors. The stability is calculated from adjacent frequency values measured over time instead of deviation from the mean. Chapter 1 introduced and discussed Allan deviation in section 1.1.3.

A primary goal of these studies is to demonstrate an experimental testbed of CPT and RR interference clocks for reaching a long term Allan deviation of 10^{-13} . While the clocks demonstrated here have not yet reached that limit, the study of techniques show promising results toward improving the clock stability, especially with improved electronics and physics package environment controls.

6.1 Shot-noise limited stability estimation

Fractional frequency stability of a clock can be estimated through measurement of the resonance linewidth. By taking the ratio of linewidth to hyperfine transition frequency used for the resonance,

$$\sigma_y(\tau) \approx \frac{\Delta\nu}{\nu_{\text{hf}}} \tau^{-1/2} \quad (6.1)$$

For example, if the linewidth of a CPT resonance, $\Delta\nu$, is 500 Hz, in ^{87}Rb with 6.834 GHz hyperfine transition, ν_{hf} , one can expect a stability (at $\tau=1\text{s}$) of at least $\sigma_y(\tau)=7.3\times 10^{-8}$. This estimate improves by considering the contrast, C , such that

$$\sigma_y(\tau) = \frac{1}{Q} \frac{1}{\text{SNR}} \tau^{-1/2}, \quad (6.2)$$

where $Q = \nu_{hf}/\Delta\nu$ represents the quality factor of atomic resonance, and $SNR = C\sqrt{N}$ where N is the number of photons in the detected beam and C is the contrast of the atomic resonance. So for the same resonance with a contrast $C = 20\%$ (realistic), and a detected optical power of $15 \mu\text{W}$ ($\sim 6 \times 10^{13}$ photons/sec), the estimate improves to $\sigma_y(\tau) = 4.7 \times 10^{-14}$ in this example. However, because of other noise sources this estimate is too high, but does provide a theoretical limit before considering electronic noise and system drifts.

Experimentally, the Allan deviation measurement calculates the change in frequency over an averaging or integration time, τ to determine how much the frequency deviates in that time. VCOs that are not atomically referenced tend toward high instability at longer integration times beyond 1000 seconds (10^3 s), while atomic clocks will flatten or decrease in instability.

6.2 Clock servo

Different methods of electronic feedback exist for locking oscillators to atomic resonances, such as frequency stepping [121], frequency modulation [122], and dispersive signal generation. The Raman clock experiments described here use frequency modulation and phase-sensitive detection to form a correction signal to steer the VCO toward the peak of the resonance. Figures 5.20 and 5.37 in the previous chapter show the entirety of the clock configuration including lock electronics for CPT and Ramsey interference Raman clocks.

Figure 6.1 shows the dithered CPT signal along with the error signal (derivative-like) generated by the lock-in amplifier. The zero-crossing of the error signal corresponds to the peak of the CPT resonance. The error signal is further integrated using a proportional-integrator (PI) circuit to generate a correction signal, which is then used to electronically lock the frequency of

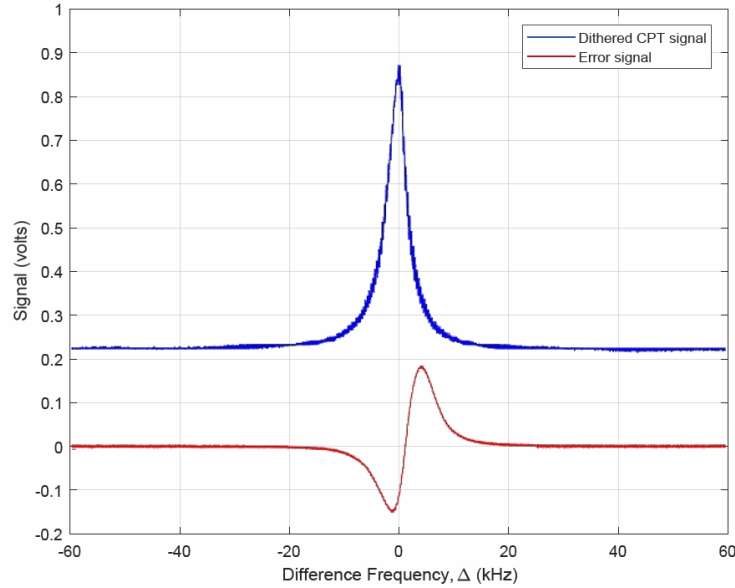


Figure 6.1: Dithered CPT signal shown along with the derivative-like error signal generated by the clock servo.

the RF synthesizer to the atomic clock transition. The error signal and correction signal corresponding to RR interference are also generated using the same electronic principle.

After the frequency synthesis chain described in the previous chapter (section 5.2), the RF signal is sent to an amplifier. Power amplification of the 3.4 GHz VCO occurs just before the EOM to provide enough RF power for the sideband generation. Sidebands are generated at ± 3.417 GHz from the laser carrier frequency. Sweeping the two optical sidebands, separated by 6.834 GHz, allow detection of CPT resonances. A low frequency modulation signal is applied to the master oscillator, transferred via PLL to result in modulation of the VCO and optical sidebands. By demodulating the central CPT resonance with a lock-in amplifier (Stanford Research Systems, SR830) at the modulation frequency, an error signal is formed. The error signal is integrated via an external PI servo (loop filter, New Focus, LB1005) and the CPT clock is operated by sending the correction signal to the master 10 MHz TSVCO for electronically locking it to the peak of the CPT resonance. For RR interference, the same is applied to the central fringe. The frequency

stability (or Allan deviation, ADEV, σ_y) of the locked 10 MHz TSVCO is measured using an ADEV/phase-noise measurement test probe (Microsemi, 3120A) by referencing it to a rubidium standard (SRS, FS725, $\sigma_y < 2 \times 10^{-11}$ at $\tau = 1$ sec).

While Ramsey interference can be locked in the same way, much lower dither modulation frequencies are used. In the pulsed scheme, the light and thus the modulation is not detected for most of the time the clock operates. Only proper selection of modulation frequency maintains a tight lock on the central fringe of Ramsey interference.

6.3 CPT clock stability results

The clock stability is measured for different physics packages and excitation schemes to determine the performance of the clock. By analyzing the Allan deviation, sources of error and low performance can be identified and addressed.

6.3.1 Preliminary (large cell) ^{85}Rb CPT clock results

The experimental setup has also been operated as a clock to test the performance of a CPT clock using the ^{85}Rb cell. This section shows clock results for the first magnetic shield and large (10 cm) ^{85}Rb vapor cell.

Figure 6.2 shows the measured short-, medium- and long-term frequency stabilities of the locked synthesizer by locking it to the CPT resonance. For comparison, the figure also shows the measured frequency stability of the same synthesizer (down-converted to a 10 MHz output) operating in the free-running mode.

This preliminary result indicates that the performance of the locked oscillator is severely degraded due to various limiting factors such as instability caused in the external feedback and

control of the synthesizer, additional phase noise introduced by various electronic components used in clock servo control, and temperature and magnetic-field variation present in the cell environment. In this configuration, the design of the Rb cell physics package is not optimized for CPT or RR interference clock operation. In order to achieve ultimate performance, the physics package must be highly isolated from environmental fluctuations such as temperature and magnetic field etc. This effort is demonstrated in sections 6.3.3 and 6.3.4. ADEV measured for longer sample period ($\tau \geq 100$ sec) give a measure of the long-term performance of the clock. Figure 6.2 shows measured ADEV for a commercially available chip-scale atomic clock (CSAC). Frequency stability of CSAC is found to reach one part in 10^{11} for τ close to 200 sec. The clock not only has short term stability above that of the RF generators, due to numerous drifts and noise in the system but is also limited by flicker noise in the short term. We expect that an optimized RR interference rubidium clock will be able to achieve two-orders of magnitude higher stability than CSAC by using ^{87}Rb atoms, and mitigating various physical effects that are limit the performance of the clock.

6.3.2 Clock results using integer PLL and large ^{87}Rb cell

Using the custom made magnetic shield and a pure isotope (7.5 cm long) ^{87}Rb vapor cell, a clock servo is implemented which controls the master 213 MHz VCO by electronically locking it to the peak of CPT resonance. A 1 kHz modulation signal with a small amplitude is applied to the control voltage on the master VCO, which in turn drives a 1 kHz modulation on the slave VCO. The slave VCO which drives the EOM, modulates the laser beam, thus, creating 1 kHz modulation on the CPT signal. After detection, a lock-in amplifier demodulates the CPT signal and passes the discriminant back to the servo for integration and feedback to the master VCO. This closes the

loop and results in a frequency-locked master VCO which is an atomically referenced to the peak of CPT resonance.

Frequency stability of the master VCO (or clock output) is measured with a gated frequency counter, externally referenced to a highly stable rubidium atomic clock for comparison. The counter measures the 213 MHz signal for a gate time 1 second, and records the average frequency for that time. This measurement is taken for 2 hours or more, and analyzed in a

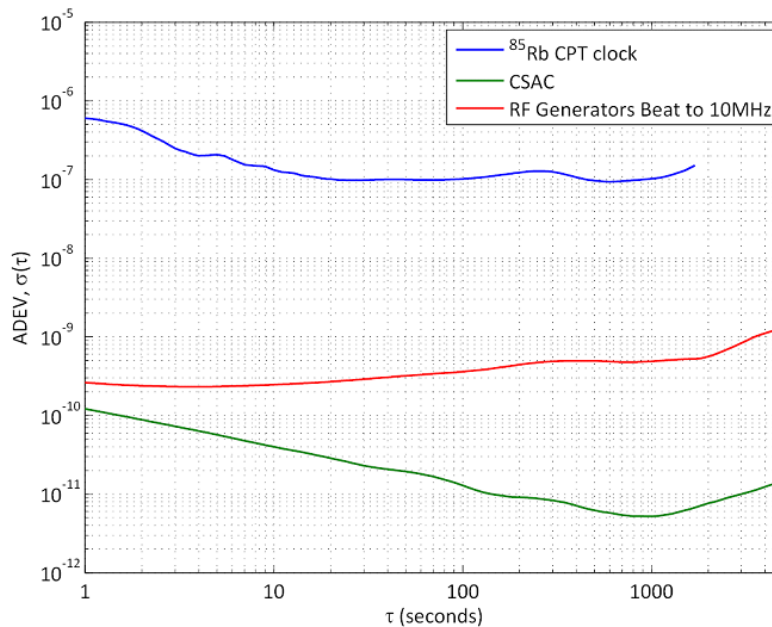


Figure 6.2: Allan deviation (or frequency stability) measured, (a) by locking the synthesizer to the CPT resonance, (b) for the unlocked beat note at 10 MHz, and (c) for a chip-scale atomic clock (CSAC).

MATLAB script to calculate the Allan deviation of the master VCO as a function of averaging time, τ . Figure 6.3 depicts a comparison of the free-running master VCO frequency stability (red trace) with the atomic clock stability (blue trace) where the master VCO is atomically referenced to the peak of CPT resonance via the clock servo (time constant $\cong 34$ ms). While taking this measurement, Raman excitation in ⁸⁷Rb atomic system is done by the carrier and the 6.8 GHz downshifted sideband, using the push-pull optical pumping scheme, at 50 μ W total optical power,

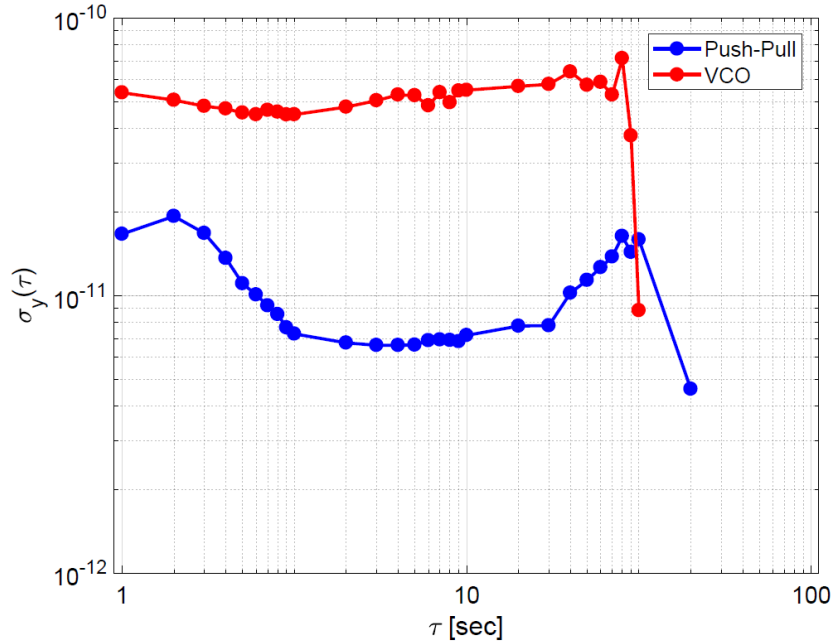


Figure 6.3: Allan deviation measurement showing the frequency stability of the CPT clock.

with a small axial magnetic field applied using Helmholtz coil placed inside the magnetic-shield enclosure, and with the vapor cell package shielded from external magnetic fields by two layers of magnetic shield (attenuation > 30 dB). The flicker floor is evident in the clock measurement and long term drift results in the rising ADEV measurement after the 300 second average time. Many noise sources contribute to this measurement, and this preliminary data hints at the experiment approaching high stability.

6.3.3 Stability dependence on modulation amplitude

We also investigated the effect of modulation amplitude on clock stability, which impacts clock frequency [123]. As shown in figure 6.4, increasing the amplitude above 150 mV results in decreased short term stability, so this amplitude is somewhat optimized for the given modulation frequencies. This result was obtained with a small vapor cell, (σ, σ) , dual sideband with RF synthesized from 10 MHz, 193 Hz modulation frequency for the clock, and 1.234 kHz modulation

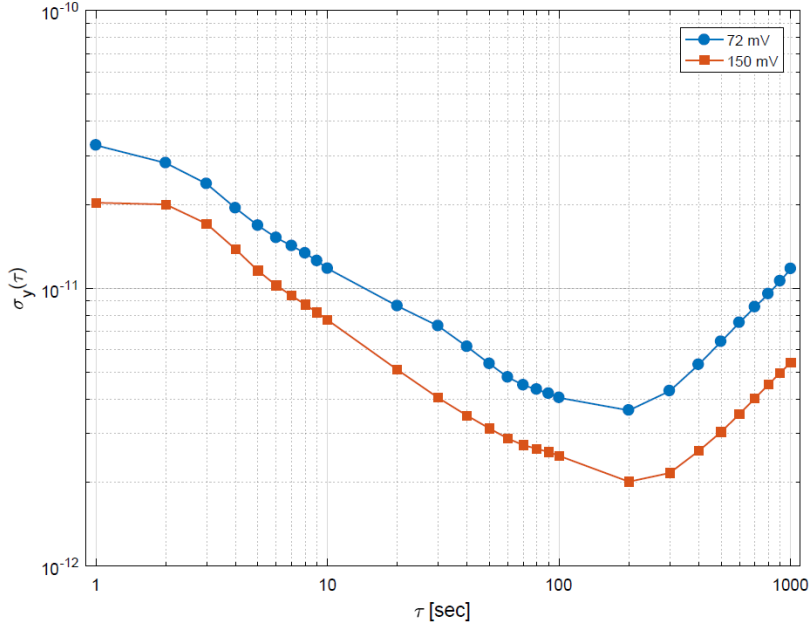


Figure 6.4: Allan deviation measurement showing the effect of modulation amplitude on frequency stability of the CPT clock.

frequency for the laser lock. The slope of the Allan deviation measurement is close to $\tau^{-1/2}$ until 200 seconds when it turns around and drift in the system reduces the stability of the clock.

6.3.4 Clock stability with CPT in small ^{87}Rb cell

We measured the frequency stability of our rubidium CPT clock prototype by employing all three: $lin \parallel lin$, (σ^-, σ^-) and $lin \perp lin$ excitation schemes. The CPT clock is operated by electronically locking the 10 MHz TSVCO to the peak of central CPT resonance. The frequency stability (or Allan deviation, ADEV, σ_y) of the locked oscillator is measured using a phase-noise measurement test probe (Microsemi, 3120A) by referencing it to a rubidium standard (SRS, FS725, $\sigma_y < 2 \times 10^{-11}$ at integration time, $\tau = 1$ sec). Figure 6.5 shows a comparison of frequency stabilities for $lin \parallel lin$, (σ^-, σ^-) and $lin \perp lin$ with the free-running oscillator stability (blue line). The operating conditions are the same as the polarization schemes that were described in

section 5.7.1. The free-running oscillator exhibits a short-term stability, $\sigma_y \approx 1.4 \times 10^{-11}$ at $\tau = 1$ sec and relatively high instability at longer integration time, for example, $\sigma_y \approx 1.9 \times 10^{-10}$ at $\tau = 1000$ sec. The CPT locked oscillator shows improved long-term stabilities for all excitations, for example, $\sigma_y \approx 4.7 \times 10^{-12}$ at $\tau = 100$ sec using (σ^-, σ^-) excitation.

The dashed line drawn in Figure 6.5 shows the expected shot-noise limited stability (i.e. $\sigma_y \propto \tau^{-1/2}$) for the (σ^-, σ^-) excitation with a starting stability $\sigma_y \approx 3.6 \times 10^{-11}$ at $\tau = 1$ sec. The

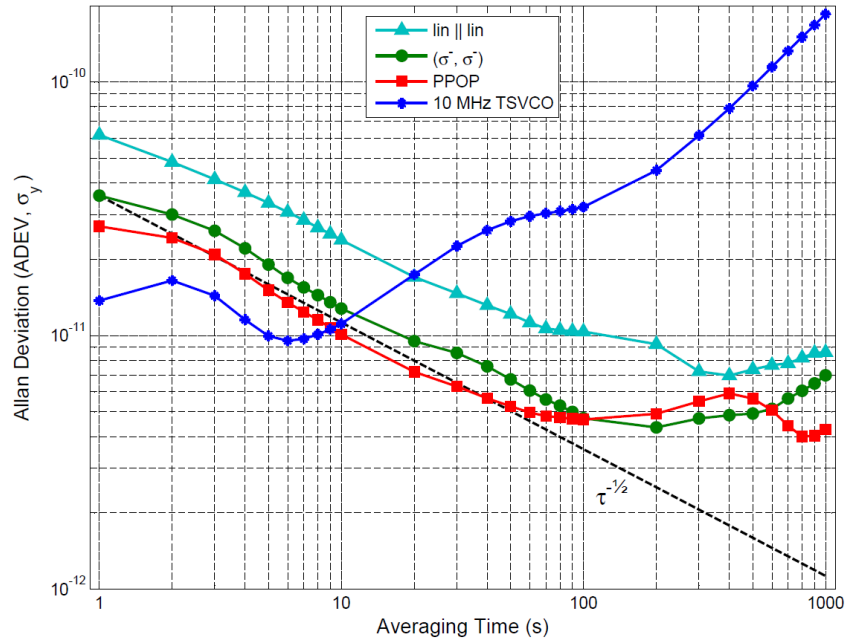


Figure 6.5: Frequency stability performance of the rubidium CPT clock measured by ADEV with three: $lin \parallel lin$, (σ^-, σ^-) and $lin \perp lin$ excitations. Dashed line represents $\sigma_y(\tau) = 3.6 \times 10^{-11} \tau^{-1/2}$

CPT clocks for all three excitations do not seem to produce shot-noise limited stability for τ exceeding 100 sec. Frequency stability in the order of 10^{-13} has been reached in rubidium CPT clocks at τ exceeding 1000 sec [12,119]. The performance of our CPT clock is currently limited by various sources of long-term frequency drifts in the system. The major source of frequency drift is related to optical power drift associated with the fiber pigtailed EOM. The power drift is caused by stress and temperature-induced polarization rotation in the fiber, coupled with polarization-

dependent modulation properties of the EOM. Other sources of frequency drifts originating from the cell environment such as cell temperature instability and magnetic field fluctuation are also affecting the long-term stability performance of our CPT clock. A major contributing factor is light shift in CPT, possibly due to drift in the laser frequency.

Under this circumstance, a comparison of frequency stabilities shown in Figure 6.5 indicate that $lin \parallel lin$ excitation exhibits the poorest performance of all, possibly due to its high magnetic field sensitivity. A long-term stability $\sigma_y \simeq 9 \times 10^{-12}$ for $\tau \simeq 150$ sec is found in this case. The highest short-term stability ($\sigma_y \simeq 2.7 \times 10^{-11}$) is found in the case of $lin \perp lin$ excitation due to higher CPT contrast in comparison to (σ^-, σ^-) excitation. The long-term stability performance of the PPOP CPT clock is found to be comparable, if not much worse, to the (σ^-, σ^-) scheme based CPT clock. This is likely due to polarization leakage in the interferometer which caused power drift and fluctuation due to vibration and thermal expansion in the interferometer. This affected the long-term performance of the $lin \perp lin$ (PPOP) CPT clock.

6.4 Clock stability results using Ramsey interference

We measured the frequency stability of the clock prototype to compare the performance of RQT with SQT in the Ramsey atomic clock. The boxcar integrator was used to acquire the Ramsey fringes. The frequency of the TSVCO was locked to the center of Ramsey fringe using the clock servo shown earlier in chapter 5. The frequency stability (or ADEV, σ_y) of the locked TSVCO was measured with the ADEV measurement test probe by referencing it to a rubidium frequency standard. Figure 6.6 shows ADEV, σ_y as a function of the averaging (or integration) time τ for $N = 1$ and 10 query pulses. Under the same condition, RQT with $N=10$ provided better short term

stability ($\sigma_y \approx 5.6 \times 10^{-11}$ at $\tau = 1$ sec) compared to the SQT ($N = 1$) case. The short-term stability of the clock can be estimated by

$$\sigma_y(\tau) = \frac{1}{Q \cdot SNR} \sqrt{\frac{T_c}{N \tau_q}} \tau^{-\frac{1}{2}} \quad (6.3)$$

where $Q = \nu_{hf}/\Delta\nu$ represents the quality factor of the central Ramsey fringe, $\Delta\omega$ corresponds to the central fringe-width, and ν_{hf} representing the rubidium hyperfine frequency. Due to pulsed operation of the Ramsey clock, σ_y in eqn. (6.3) includes a factor in the square root as the ratio of

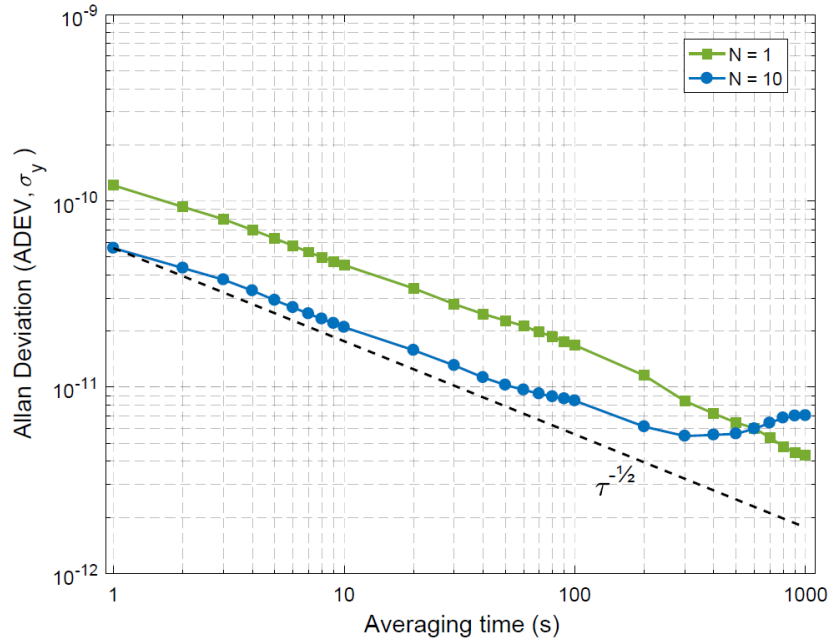


Figure 6.6: Frequency stability performance of the rubidium atomic clock measured using ADEV for SQT (green squares) and RQT with $N=10$ (blue circles). The dashed line represents $\sigma_y(\tau) = 5.58 \times 10^{-11} \tau^{-1/2}$.

pulse cycle time $T_c (= \tau_c + T + \tau_q)$ to the detection time $N\tau_q$. Thus, in the case of RQT, besides improvement in SNR, one can expect an additional improvement in σ_y by a factor \sqrt{N} . Contrary to these expected improvements, we observed much less improvement (nearly by a factor 2) in the frequency stability, possibly due to various sources of noise in our experiments.

However, improved frequency stability with RQT was observed in σ_y for τ ranging up to nearly 100 seconds (Figure 6.6). Our experimental system has significant noise and drift arising from the cell temperature control and the residual magnetic field. These can be reduced in the future with a better design of the cell physics package to conclusively verify the performance of RQT in the Ramsey clock.

This chapter demonstrated improved clock stability with either increased contrast in CPT and RR interference, or decreased linewidth, or both. Additionally, low noise electronics for generating the requisite RF frequency lowered the flicker floor and allowed for the clock stability to approach a $\tau^{-1/2}$ slope. Frequency stability performances of the rubidium clock prototype were measured by employing $lin \parallel lin$, (σ^-, σ^-) and $lin \perp lin$ excitation schemes. In a laboratory demonstration, which showed a short-term stability $\sigma_y \simeq 2.7 \times 10^{-11}$ for $\tau = 1$ sec and a long-term stability $\sigma_y \simeq 4.3 \times 10^{-12}$ for $\tau = 1000$ sec by adopting $lin \perp lin$ excitation in the clock prototype for CPT. Incorporation of the VCSEL to replace the bulky and temperature sensitive EOM and the laser in our system, and improving the design for the cell physics package will minimize the system noise and drift, for improving the long-term stability of the rubidium clock.

CHAPTER 7: CONCLUSION AND FUTURE WORK

In this dissertation, research on CPT and Ramsey interference based atomic clocks using Rb vapor cells was presented. To support and confirm the experimental results multi-level simulation models were implemented demonstrating characterization of the atomic system behavior. CPT is shown as a basis for Ramsey interference (pulsed CPT) and characterized to determine optimal clock operation parameters. Ramsey interference methods are introduced as improvements to CPT for light shift reduction and increased clock stability from smaller linewidths and reduced sensitivity to optical intensity fluctuations. In characterizing the atomic system for clock development, the following experiments and simulations were performed.

Chapter 2 depicts the strengths of using a model to predict interaction between Raman laser transitions and atoms. Building on steady-state models, we are able to build a theoretical modeling system which provides a basis for meaningful simulation. Extension of three level modeling of a continuous Raman interaction to a pulsed Raman excitation scheme enables theoretical study for Ramsey interference fringes, and the dependence of signal shape on optical intensity and free evolution time.

In chapter 3, we demonstrated an extension of the three-level atomic model to 16 Zeeman sublevels, a multilevel atomic model. We thus investigated the comparative properties of $lin \parallel lin$, (σ, σ) , and $lin \perp lin$ excitation schemes for producing narrow linewidth, high contrast, magnetically-insensitive CPT resonances in the D1 manifold of ^{87}Rb atoms. The performances of these schemes were studied theoretically, keeping in mind their application in compact and high-performance CPT clock development using a vapor cell. The results show higher magnetic field sensitivity of the CPT resonance produced by $lin \parallel lin$ excitation. The theoretical calculations

characterize the magnetic field dependence of the central CPT resonance formed by different excitations, and also show that additional Zeeman CPTs could be formed in the presence of a transverse component of a bias magnetic field, arising from imperfect alignments of the optical fields.

In chapter 4, we investigated light shift associated with Raman–Ramsey interference using a computational model based on a three–level atomic system as described in chapter 2. Light shift is accurately calculated without invoking the adiabatic approximation. We also investigated the coherent density-matrix elements and the phase shifts associated with them, which is relevant for the case where RR interference is detected via absorption. The calculated results for the mono-velocity case confirm that RR light shift can be suppressed by orders of magnitude using the pulse saturation effect. The study has also been extended to investigate light shift in the presence of Doppler-broadening in a medium. Although the light shift suppression remained valid in a Doppler-broadened medium by ensuring pulse saturation, additional velocity-induced phase/frequency shift is found to be associated with RR fringe center, which is later found to not be a real effect in the physical system, and thus more study is needed. Previously, based on the computational results, we also predicted that this would create a newly recognized source of frequency error for all vapor cell-based Raman clocks, which is being reconsidered. As the results show, high long-term stability (below 10^{-13}) in a cell-based RR clock can be achieved by suppressing the light shift, and simultaneously reducing the impact of velocity-induced shift by a precise laser lock.

In chapter 5, experimental setups and results were presented. The experimental results confirm the simulation characteristics and show higher magnetic field sensitivity of the CPT resonance produced by $lin \parallel lin$ excitation. For (σ, σ) excitation, we found that the CPT contrast

is dependent on the transition used for locking the laser frequency, and reached a maximum value 16.7% for lasers resonant with the $|F' = 2\rangle$ state. The experimental studies were carried out in a clock prototype consisting of a laboratory scale Rb vapor cell physics package. CPT contrast close to 20% was measured using the $lin \perp lin$ excitation.

Also in chapter 5, we demonstrated the repeated query technique as a CPT interrogation scheme for generating Ramsey interference with a single-peaked central fringe of high contrast and S/N ratio. These experimental results showed that significant enhancements in contrast, peak amplitude as well as narrowing of fringe-width are achieved by using RQT with only 5 to 10 query pulses. The theoretical model estimated the line shapes of Ramsey fringes with different N which agreed closely with the experiments. Typically, in a vapor medium, dephasing due to atomic collisions limits the largest possible free-evolution time, T and hence, the narrowest possible fringe-width. In a buffer gas filled vapor cell, T can be extended up to 5 to 6 milliseconds to produce sub-kilohertz fringe-width, but the fringes are often produced with significantly low contrast. Due to the long duty-cycle of the optical pulse ($T_C = 1-2$ ms) sequence used in the experiments, dither frequencies and servo time constants were chosen properly to produce low noise error signals.

In chapter 6, clock stability measurements are shown. Frequency stability performances of the rubidium clock prototype were measured by employing $lin \parallel lin$, (σ^-, σ^-) and $lin \perp lin$ excitation schemes. We attained a short-term stability $\sigma_y \approx 2.7 \times 10^{-11}$ for $\tau = 1$ sec and a long-term stability $\sigma_y \approx 4.3 \times 10^{-12}$ for $\tau = 1000$ sec for the $lin \perp lin$ excitation. We employed RQT in the rubidium clock experiment and measured the frequency stability of the clock in comparison with the conventional single query pulse scheme, and found an improvement in the stability of the RQT clock.

Future directions for this work include detailed experimental comparison of CPT and Ramsey interference under the same conditions, using a directly modulated VCSEL. By eliminating the bulky tunable diode laser and the EOM, power and size can be reduced, at the expense of laser stability and laser linewidth, which can be mitigated with stricter controls. Furthermore, for a compact clock, an AOM is bulky and draws a significant amount of electrical power, so a suitable switching scheme for Ramsey interference with a VCSEL is needed. For optical switching, RF/microwave switching of the RF modulator has been considered [88,124], however must be tuned and pulsed appropriately to avoid disrupting the modulation characteristics of the VCSEL. More detailed experimental light shift measurements need to be completed, demonstrating the predicted benefit of all-optical Ramsey interference over CPT in rubidium vapor clocks.

Some improvements to the multi-level atomic model remain, such as incorporating analysis of the transverse magnetic field effect for magnetometry simulations, along with more accurate Doppler averaging for light shift calculations, and propagation effect for atomic vapor density-dependent calculations. Precise simulation of light shift for Ramsey interference in a 16 level atom must also be calculated. With a more complete model, simulations of atomic vapor based clocks can more accurately verify experimental results.

REFERENCES

1. J. Vanier and C. Audoin, *The Quantum Physics of Atomic Frequency Standards* (1989).
2. F. G. Major, *The Quantum Beat*, 2nd ed. (Springer-Verlag New York, 2007).
3. "Resolution 1 of the 13th CGPM," *Metrologia* **4**, 41–45 (1968).
4. D. Allan, N. Ashby, and C. Hodge, *The Science of Timekeeping* (1997).
5. W. Markowitz, R. G. Hall, L. Essen, and J. V. L. Parry, "Frequency of cesium in terms of ephemeris time," *Phys. Rev. Lett.* **1**, 105–107 (1958).
6. R. F. C. Vessot, "Applications of Highly Stable Oscillators To Scientific Measurements," *Proc. IEEE* **79**, 1040–1053 (1991).
7. M. a Lombardi, T. P. Heavner, and S. R. Jefferts, "NIST Primary Frequency Standards and the Realization of the SI Second," *NCSL Int. Meas.* **2**, 74 (2007).
8. S. Knappe, "MEMS atomic clocks," in *Comprehensive Microsystems*, Y. Gianchandani, O. Tabata, and H. Zappe, eds. (Elsevier, 2007), Vol. 3, pp. 571–612.
9. F. Riehle, *Frequency Standards* (Wiley-VCH Verlag GmbH & Co. KGaA, 2003).
10. R. Lutwak, "Principles of Atomic Clocks," *Ifcs-Eftf 2011* (2011).
11. P. R. Gerry, "Microsemi CSAC webinar," (2014).
12. M. Merimaa, T. Lindvall, I. Tittonen, and E. Ikonen, "All-optical atomic clock based on coherent population trapping in 85 Rb," *JOSA B* **20**, 273–279 (2003).
13. S. Knappe, P. Schwindt, V. Shah, L. Hollberg, J. Kitching, L. Liew, and J. Moreland, "A chip-scale atomic clock based on 87Rb with improved frequency stability," *Opt. Express* **13**, 1249–1253 (2005).
14. M. Bloch, I. Pascaru, C. Stone, and T. McClelland, "Subminiature rubidium frequency standard for commercial applications," 1993 *IEEE Int. Freq. Control Symp.* 164–177 (1993).
15. J. Ho, I. Pascaru, C. Stone, and T. McClelland, "New rubidium frequency standard designs for telecommunications applications," *IEEE Int. Freq. Control Symp.* 80–83 (1998).
16. J. D. Prestage and G. L. Weaver, "Atomic Clocks and Oscillators for Deep-Space Navigation and Radio Science," *Proc. IEEE* **95**, 2235–2247 (2007).
17. Y. Koyama, H. Matsuura, K. Atsumi, K. Nakamuta, and I. Maruyama, "An Ultra-Miniature Rubidium Frequency Standard," in *IEEE/EIA International Frequency Control Symposium and Exhibition* (2000), pp. 694–699.
18. F.-X. Esnault, E. A. Donley, J. Kitching, and E. N. Ivanov, "Status of a compact cold-atom CPT frequency standard," 2011 *Jt. Conf. IEEE Int. Freq. Control Eur. Freq. Time Forum Proc.* 1–3 (2011).
19. S. A. Zibrov, I. Novikova, D. F. Phillips, R. L. Walsworth, A. S. Zibrov, V. L. Velichansky, A. V. Taichenachev, and V. I. Yudin, "Coherent-population-trapping resonances with linearly polarized light for all-optical miniature atomic clocks," *Phys. Rev. A - At. Mol. Opt. Phys.* **81**, 1–7 (2010).
20. R. Boudot, P. Dziuban, M. Hasegawa, R. K. Chutani, S. Galliou, V. Giordano, and C. Gorecki, "Coherent population trapping resonances in Cs-Ne vapor microcells for miniature clocks applications," *J. Appl. Phys.* **109**, 14912 (2011).
21. S. Goka, "85Rb D1-line coherent-population-trapping atomic clock for low-power

- operation," *Jpn. J. Appl. Phys.* **49**, 0628011–0628014 (2010).
22. Y. Zhang, W. Yang, Z. Shuangyou, and J. Zhao, "Rubidium chip-scale atomic clock with improved long-term stability through light intensity optimization and compensation for laser frequency detuning," *J. Opt. Soc. Am. B* **33**, 1756–1763 (2016).
 23. N. F. Ramsey, "A molecular beam resonance method with separated oscillating fields," *Phys. Rev.* **78**, 695 (1950).
 24. T. Zanon, S. Trémine, S. Guérandel, E. de Clercq, D. Holleville, N. Dimarcq, and A. Clairon, "Observation of Raman-Ramsey fringes with optical CPT pulses," *IEEE Trans. Instrum. Meas.* **54**, 776–779 (2005).
 25. L. Essen and J. V. L. Parry, "An Atomic Standard of Frequency and Time Interval: A Cæsium Resonator," *Nature* **176**, 280–282 (1955).
 26. A. G. Mungall, H. Daams, and J.-S. Boulanger, "Design, Construction, and Performance of the NRC CsVI Primary Cesium Clocks," *Metrologia* **17**, 123–145 (1981).
 27. A. G. Mungall, "Cavity Phase Dependent Frequency Shifts in Cesium Beam Frequency Standards," *Metrologia* **8**, 28–32 (1971).
 28. A. De Marchi and G. P. Bava, "On Cavity Phase Shift in Commercial Caesium-Beam Frequency Standards," *Metrologia* **20**, 33–36 (1984).
 29. J. Vanier and C. Audoin, "The classical caesium beam frequency standard: fifty years later," *Metrologia* **42**, S31–S42 (2005).
 30. A. Clairon, C. Salomon, S. Guellati, and W. D. Phillips, "Ramsey Resonance in a Zacharias Fountain," *Eur. Lett* **16**, 165–170 (1991).
 31. G. Mileti, J. Deng, F. L. Walls, D. A. Jennings, and R. E. Drullinger, "Laser-pumped rubidium frequency standards: New analysis and progress," *IEEE J. Quantum Electron.* **34**, 233–237 (1998).
 32. C. Affolderbach, F. Droz, and G. Mileti, "Experimental demonstration of a compact and high-performance laser-pumped Rubidium gas cell atomic frequency standard," *IEEE Trans. Instrum. Meas.* **55**, 429–435 (2006).
 33. J. Vanier and C. Mandache, "The passive optically pumped Rb frequency standard: the laser approach," *Appl. Phys. B* **87**, 565–593 (2007).
 34. A. Kastler, "Quelques suggestions concernant la production optique et la détection optique d'une inégalité de population des niveaux de quantification spatiale des atomes. Application à l'expérience de Stern et Gerlach et à la résonance magnétique," *J. Phys. Radium* **11**, 255–265 (1950).
 35. E. C. Beaty, P. L. Bender, and A. R. Chi, "Narrow Hyperfine Absorption Lines of Cs-133 in Various Buffer Gases," *Phys. Rev.* **112**, 450–451 (1958).
 36. M. E. Packard and B. E. Swartz, "The Optically Pumped Rubidium Vapor Frequency Standard," *IRE Trans. Instrum.* **I-11**, 215–223 (1962).
 37. R. Lutwak, D. Emmons, W. Riley, and R. M. Garvey, "The chip-scale atomic clock coherent population trapping vs conventional interrogation," 34th Annu. Precise Time Time Interval Meet. 539–550 (2002).
 38. O. Kozlova, S. Guérandel, and E. De Clercq, "Temperature and pressure shift of the Cs clock transition in the presence of buffer gases: Ne, N₂, Ar," *Phys. Rev. A - At. Mol. Opt. Phys.* **83**, 62714 (2011).
 39. R. Boudot, D. Miletic, P. Dziuban, C. Affolderbach, P. Knapkiewicz, J. Dziuban, G. Mileti, V. Girodano, and C. Gorecki, "First-order cancellation of the Cs clock frequency

- temperature-dependence in Ne-Ar buffer gas mixture.," *Opt. Express* **19**, 3106–14 (2011).
40. N. Cyr, M. Tetu, and M. Breton, "All-optical microwave frequency standard: a proposal," *IEEE Trans. Instrum. Meas.* **42**, 640–649 (1993).
 41. S. Knappe, V. Shah, P. D. D. Schwindt, L. Hollberg, J. Kitching, L. A. Liew, and J. Moreland, "A microfabricated atomic clock," *Appl. Phys. Lett.* **85**, 1460–1462 (2004).
 42. J. Vanier, "Atomic clocks based on coherent population trapping: a review," *Appl. Phys. B* **81**, 421–442 (2005).
 43. D. W. Allan, M. A. Weiss, and J. L. Jespersen, "A frequency-domain view of time-domain characterization of clocks and time and frequency distribution systems," in *Forty-Fifth Annual Symposium on Frequency Control* (1991), pp. 667–678.
 44. J. Kitching, S. Knappe, and L. Hollberg, "Miniature vapor-cell atomic-frequency references," *Appl. Phys. Lett.* **81**, 553–555 (2002).
 45. T. Zanon, S. Guerandel, E. De Clercq, D. Holleville, N. Dimarcq, and A. Clairon, "High contrast ramsey fringes with coherent-population-trapping pulses in a double lambda atomic system," *Phys. Rev. Lett.* **94**, 193002 (2005).
 46. E. Arimondo, "Coherent Population Trapping," in *Progress in Optics* (1996), Vol. 35, pp. 257–354.
 47. D. Budker, D. Kimball, and D. DeMille, *Atomic Physics: An Exploration through Problems and Solutions* (Oxford University Press, 2008).
 48. G. S. Pati, K. Salit, R. Tripathi, and M. S. Shahriar, "Demonstration of Raman-Ramsey fringes using time delayed optical pulses in rubidium vapor," *Opt. Commun.* **281**, 4676–4680 (2008).
 49. T. Zanon-Willette, E. De Clercq, and E. Arimondo, "Ultrahigh-resolution spectroscopy with atomic or molecular dark resonances: Exact steady-state line shapes and asymptotic profiles in the adiabatic pulsed regime," *Phys. Rev. A - At. Mol. Opt. Phys.* **84**, 1–17 (2011).
 50. P. R. Hemmer, M. S. Shahriar, V. D. Natoli, and S. Ezekiel, "Ac Stark shifts in a two-zone Raman interaction," *J. Opt. Soc. Am. B* **6**, 1519 (1989).
 51. G. S. Pati, Z. Warren, N. Yu, and M. S. Shahriar, "Computational studies of light shift in a Raman – Ramsey interference-based atomic clock," *J. Opt. Soc. Am. B* **32**, 388–394 (2015).
 52. G. S. Pati, F. K. Fatemi, and M. S. Shahriar, "Observation of query pulse length dependent Ramsey interference in rubidium vapor using pulsed Raman excitation.," *Opt. Express* **19**, 22388–401 (2011).
 53. D. Döring, J. E. Debs, N. P. Robins, C. Figl, P. A. Altin, and J. D. Close, "Ramsey interferometry with an atom laser," *Opt. Express* **17**, 20661–20668 (2009).
 54. D. Butts, J. Kinast, K. Kotru, A. Radojevic, B. Timmons, and R. Stoner, "Coherent population trapping in Raman-pulse atom interferometry," *Phys. Rev. A* **84**, 1–8 (2011).
 55. B. Cheng, P. Gillot, S. Merlet, and F. Pereira Dos Santos, "Coherent population trapping in a Raman atom interferometer," *Phys. Rev. A - At. Mol. Opt. Phys.* **93**, 1–5 (2016).
 56. J. E. Debs, D. Döring, N. P. Robins, C. Figl, P. a Altin, and J. D. Close, "A two-state Raman coupler for coherent atom optics.," *Opt. Express* **17**, 2319–25 (2009).
 57. D. Budker, D. Kimball, S. Rochester, V. Yashchuk, and M. Zolotarev, "Sensitive magnetometry based on nonlinear magneto-optical rotation," *Phys. Rev. A* **62**, 1–7 (2000).
 58. V. I. Yudin, A. V. Taichenachev, Y. O. Dudin, V. L. Velichansky, A. S. Zibrov, and S. A. Zibrov, "Vector magnetometry based on electromagnetically induced transparency in linearly polarized light," *Phys. Rev. A - At. Mol. Opt. Phys.* **82**, 1–7 (2010).

59. K. Cox, V. I. Yudin, A. V. Taichenachev, I. Novikova, and E. E. Mikhailov, "Measurements of the magnetic field vector using multiple electromagnetically induced transparency resonances in Rb vapor," *Phys. Rev. A - At. Mol. Opt. Phys.* **83**, 2–5 (2011).
60. S.-Q. Liang, G.-Q. Yang, Y.-F. Xu, Q. Lin, Z.-H. Liu, and Z.-X. Chen, "Simultaneously improving the sensitivity and absolute accuracy of CPT magnetometer," *Opt. Express* **22**, 6837 (2014).
61. M. O. Scully and M. Fleischhauer, "High-sensitivity magnetometer based on index-enhanced media," *Phys. Rev. Lett.* **69**, 1360–1363 (1992).
62. P. D. D. Schwindt, S. Knappe, V. Shah, L. Hollberg, J. Kitching, L. A. Liew, and J. Moreland, "Chip-scale atomic magnetometer," *Appl. Phys. Lett.* **85**, 6409–6411 (2004).
63. M. Stähler, S. Knappe, C. Affolderbach, W. Kemp, and R. Wynands, "Picotesla magnetometry with coherent dark states," *Europhys. Lett.* **54**, 323–328 (2001).
64. F.-X. Esnault, E. Donley, and J. Kitching, "Towards a compact cold atom frequency standard based on coherent population trapping," 2010 IEEE Int. Freq. Control Symp. 465–469 (2010).
65. F.-X. Esnault, E. Blanshan, E. N. Ivanov, R. E. Scholten, J. Kitching, and E. A. Donley, "Cold-atom double- Λ coherent population trapping clock," *Phys. Rev. A* **88**, 42120 (2013).
66. J. D. Kleykamp, a. J. Hachtel, D. G. Kane, M. D. Marshall, N. J. Souther, P. K. Harnish, and S. Bali, "Measurement of sub-natural linewidth AC Stark shifts in cold atoms: An experiment for an advanced undergraduate laboratory," *Am. J. Phys.* **79**, 1211 (2011).
67. H. J. Metcalf and P. van der Straten, "Laser cooling and trapping of atoms," *J. Opt. Soc. Am. B* **20**, 887 (2003).
68. M. Kasevich and S. Chu, "Laser cooling below a photon recoil with three-level atoms," *Phys. Rev. Lett.* **69**, (1992).
69. S. Zibrov, V. L. Velichansky, A. S. Zibrov, A. V. Taichenachev, and V. I. Yudin, "Experimental Investigation of the Dark Pseudoresonance on the D1 Line of the 87Rb Atom Excited by a Linearly Polarized Field," *J. Exp. Theor. Phys. Lett.* **82**, 5 (2005).
70. G. Kazakov, B. Matisov, I. Mazets, G. Mileti, and J. Delporte, "Pseudoresonance mechanism of all-optical frequency-standard operation," *Phys. Rev. A - At. Mol. Opt. Phys.* **72**, 1–6 (2005).
71. S. V Kargapol'tsev, J. Kitching, L. Hollberg, A. V. Taichenachev, V. L. Velichansky, and V. I. Yudin, "High-contrast dark resonance in σ^+ - σ^- optical field," *Laser Phys. Lett.* **1**, 495–499 (2004).
72. Y. Y. Jau, E. Miron, A. B. Post, N. N. Kuzma, and W. Happer, "Push-pull optical pumping of pure superposition states," *Phys. Rev. Lett.* **93**, 160802 (2004).
73. X. Liu, J. M. Mérolla, S. Guérandel, C. Gorecki, E. De Clercq, and R. Boudot, "Coherent-population-trapping resonances in buffer-gas-filled Cs-vapor cells with push-pull optical pumping," *Phys. Rev. A - At. Mol. Opt. Phys.* **87**, 1–12 (2013).
74. M. Abdel Hafiz and R. Boudot, "A coherent population trapping Cs vapor cell atomic clock based on push-pull optical pumping," *J. Appl. Phys.* **118**, 124903 (2015).
75. E. Breschi, Z. D. Grujić, P. Knowles, and A. Weis, "A high-sensitivity push-pull magnetometer," *Appl. Phys. Lett.* **104**, 1–5 (2014).
76. M. S. Shahriar, Y. Wang, S. Krishnamurthy, Y. Tu, G. S. Pati, and S. Tseng, "Evolution of an N-level system via automated vectorization of the Liouville equations and application to optically controlled polarization rotation," *J. Mod. Opt.* **61**, 351–367 (2014).

77. S. Zibrov, V. L. Velichansky, A. S. Zibrov, A. V. Taichenachev, and V. I. Yudin, "Experimental Investigation of the Dark Pseudoresonance on the D1 Line of the 87Rb Atom Excited by a Linearly Polarized Field," *J. Exp. Theor. Phys. Lett.* **82**, 5 (2005).
78. D. A. Steck, "Rubidium 87 D line data," (2001).
79. M. S. Shahriar, P. R. Hemmer, D. P. Katz, A. Lee, and M. G. Prentiss, "Dark-state-based three-element vector model for the stimulated Raman interaction," *Phys. Rev. A* **55**, 2272–2282 (1997).
80. A. V. Taichenachev, V. I. Yudin, V. L. Velichansky, and S. A. Zibrov, "On the unique possibility to increase significantly the contrast of dark resonances on D1 line of 87Rb," *J. Exp. Theor. Phys. Lett.* **82**, 398–403 (2005).
81. L. Margalit, M. Rosenbluh, and A. D. Wilson-Gordon, "Coherent-population-trapping transients induced by a modulated transverse magnetic field," *Phys. Rev. A - At. Mol. Opt. Phys.* **88**, (2013).
82. P. R. Hemmer, S. Ezekiel, and C. C. Leiby, "Stabilization of a microwave oscillator using a resonance Raman transition in a sodium beam.," *Opt. Lett.* **8**, 440–2 (1983).
83. P. R. Hemmer, M. S. Shahriar, H. Lamela-Rivera, S. P. Smith, B. E. Bernacki, and S. Ezekiel, "Semiconductor laser excitation of Ramsey fringes by using a Raman transition in a cesium atomic beam," *J. Opt. Soc. Am. B* **10**, 1326–1329 (1993).
84. I. Yoshida, N. Hayashi, K. Fujita, S. Taniguchi, Y. Hoshina, and M. Mitsunaga, "Line-shape comparison of electromagnetically induced transparency and Raman Ramsey fringes in sodium vapor," *Phys. Rev. A - At. Mol. Opt. Phys.* **87**, 2–7 (2013).
85. P. Yun, Y. Zhang, G. Liu, W. Deng, L. You, and S. Gu, "Multipulse Ramsey-CPT interference fringes for the 87 Rb clock transition," *EPL (Europhysics Lett.)* **97**, 63004 (2012).
86. G. S. Pati, F. K. Fatemi, M. Bashkansky, and S. M. Shahriar, "Optical Ramsey Interference and its Performance in D1 Line Excitation in Rubidium Vapor for Implementation of a Vapor Cell Clock," in *SPIE Proc.* (2011), Vol. 7949, pp. 794910–12.
87. Y. Yano and S. Goka, "Pulse excitation method of coherent-population-trapping suitable for chip-scale atomic clock," *Jpn. J. Appl. Phys.* **51**, 1–4 (2012).
88. X. Liu, J. Mérolla, and S. Guérandel, "Ramsey spectroscopy of high-contrast CPT resonances with push-pull optical pumping in Cs vapor," *Opt. Express* **21**, 12451–12459 (2013).
89. J. E. Thomas, P. R. Hemmer, S. Ezekiel, C. C. Leiby, R. H. Picard, and C. R. Willis, "Observation of Ramsey fringes using a stimulated, resonance Raman transition in a sodium atomic beam," *Phys. Rev. Lett.* **48**, 867–870 (1982).
90. E. Kuchina, E. E. Mikhailov, and I. Novikova, "Effect of atomic diffusion on the Raman-Ramsey CPT resonances," *J. Opt. Soc. Am. B* **33**, 610–614 (2016).
91. N. Castagna, R. Boudot, S. Guérandel, E. De Clercq, N. Dimarcq, and A. Clairon, "Investigations on continuous and pulsed interrogation for a CPT atomic clock," *IEEE Trans. Ultrason. Ferroelectr. Freq. Control* **56**, 246–253 (2009).
92. E. Blanshan, S. M. Rochester, E. A. Donley, and J. Kitching, "Light shifts in a pulsed cold-atom coherent-population-trapping clock," *Phys. Rev. A - At. Mol. Opt. Phys.* **91**, 1–6 (2015).
93. C. Xi, Y. Guo-Qing, W. Jin, and Z. Ming-Sheng, "Coherent Population Trapping-Ramsey Interference in Cold Atoms," *Chinese Phys. Lett.* **27**, 113201 (2010).

94. Y. Feng, H. Xue, X. Wang, S. Chen, and Z. Zhou, "Observation of Ramsey fringes using stimulated Raman transitions in a laser-cooled continuous rubidium atomic beam," *Appl. Phys. B Lasers Opt.* **118**, 139–144 (2014).
95. G. Theobald, V. Giordano, N. Dimarcq, and P. Cerez, "Observation of narrow Ramsey-type resonances in a caesium beam due to Zeeman coherences," *J. Phys. B At. Mol. Opt. Phys.* **24**, 2957–2966 (1991).
96. A. S. Zibrov, I. Novikova, and A. B. Matsko, "Observation of Ramsey fringes in an atomic cell with buffer gas.," *Opt. Lett.* **26**, 1311–1313 (2001).
97. G. S. Pati, F. K. Fatemi, M. Bashkansky, and S. Shahriar, "Prospect for development of a pulsed CPT Raman Ramsey clock using atomic vapor," **7612**, 76120D–76120D–25 (2010).
98. B. Yan, Y. Ma, and Y. Wang, "Formation of Ramsey fringes based on pulsed coherent light storage," *Phys. Rev. A* **79**, 63820 (2009).
99. B. H. McGuyer, Y. Y. Jau, and W. Happer, "Simple method of light-shift suppression in optical pumping systems," *Appl. Phys. Lett.* **94**, 25–27 (2009).
100. M. Zhu and L. S. Cutler, "Theoretical and experimental study of light shift in a CPT-based Rb vapor cell frequency standard," 32nd Annu. Precise Time Time Interval Meet. 311–323 (2000).
101. A. Taichenachev, V. Yudin, R. Wynands, M. Stähler, J. Kitching, and L. Hollberg, "Theory of dark resonances for alkali-metal vapors in a buffer-gas cell," *Phys. Rev. A* **67**, 1–11 (2003).
102. M. Crescimanno and M. Hohensee, "N⁺ CPT clock resonance," *JOSA B* **25**, 2130–2139 (2008).
103. J. Snoddy, Y. Li, F. Ravet, and X. Bao, "Stabilization of electro-optic modulator bias voltage drift using a lock-in amplifier and a proportional-integral-derivative controller in a distributed Brillouin sensor system," *Appl. Opt.* **46**, 1482 (2007).
104. K. L. Corwin, Z. T. Lu, C. F. Hand, R. J. Epstein, and C. E. Wieman, "Frequency-stabilized diode laser with the Zeeman shift in an atomic vapor," *Appl. Opt.* **37**, 3295–3298 (1998).
105. S. Goka, "85 Rb Coherent-Population-Trapping Atomic Clock with Low Power Consumption," *Jpn. J. Appl. Phys.* **48**, 82202 (2009).
106. A. V. Taichenachev, V. I. Yudin, V. L. Velichansky, S. V. Kargapoltsev, R. Wynands, J. Kitching, and L. Hollberg, "High-contrast dark resonances on the D1 line of alkali metals in the field of counterpropagating waves," *J. Exp. Theor. Phys. Lett.* **80**, 236–240 (2004).
107. P. L. Bender, E. C. Beaty, and A. R. Chi, "Optical Detection of Narrow Rb-87 Hyperfine Absorption Lines," *Phys. Rev. Lett.* **1**, 311–313 (1958).
108. E. E. Mikhailov, T. Horrom, N. Belcher, and I. Novikova, "Performance of a prototype atomic clock based on lin||lin coherent population trapping resonances in Rb atomic vapor," *J. Opt. Soc. Am. B* **27**, 6 (2009).
109. J. Yang, Y. Tian, B. Tan, P. Yun, and S. Gu, "Exploring Ramsey-coherent population trapping atomic clock realized with pulsed microwave modulated laser," *J. Appl. Phys.* **115**, (2014).
110. D. A. Steck, "Rubidium 87 D Line Data," available online at <http://steck.us/alkalidata>, revision 2.1.5, 13 January (2015).
111. B. Tan, Y. Tian, H. Lin, J. Chen, and S. Gu, "Noise suppression in coherent population-trapping atomic clock by differential magneto-optic rotation detection," *Opt. Lett.* **40**, 3703–6 (2015).

112. M. Rosenbluh, V. Shah, S. Knappe, and J. Kitching, "Differentially detected coherent population trapping resonances excited by orthogonally polarized laser fields," *Opt. Express* **14**, 6588–6594 (2006).
113. M. U. Momeen, G. Rangarajan, and P. C. Deshmukh, "Magneto Optical Rotation in the Doppler-broadened Spectrum of Rb atoms in intermediate fields," *J. Phys. Conf. Ser.* **80**, 1–7 (2007).
114. A.-L. Yang, G.-Q. Yang, Y.-F. Xu, and Q. Lin, "High contrast atomic magnetometer based on coherent population trapping," *Chin. Phys. B* **23**, 2012–2015 (2014).
115. J. Deng, P. Vlitaz, D. Taylor, L. Perletz, and R. Lutwak, "A commercial CPT rubidium clock," *Proc. Eur. Freq. Time Forum (EFTF)*(Toulouse, FR, 22-25 April 2008) E3B01-0099 (2008).
116. R. Lutwak, D. Emmons, W. Riley, and R. Garvey, "The chip-scale atomic clock-coherent population trapping vs. conventional interrogation," 539–550 (2003).
117. R. Lutwak, "The chip-scale atomic clock - Recent developments," in *2009 IEEE International Frequency Control Symposium Joint with the 22nd European Frequency and Time Forum* (2009), pp. 573–577.
118. X. L. Sun, J. W. Zhang, P. F. Cheng, C. Xu, L. Zhao, and L. J. Wang, "Investigation of Ramsey spectroscopy in a lin-par-lin Ramsey coherent population trapping clock with dispersion detection," *Opt. Express* **24**, 4532 (2016).
119. J. Lin, J. Deng, Y. Ma, H. He, and Y. Wang, "Detection of ultrahigh resonance contrast in vapor-cell atomic clocks.," *Opt. Lett.* **37**, 5036–8 (2012).
120. S. Guérandel, T. Zanon, N. Castagna, F. Dahes, E. de Clercq, N. Dimarcq, and A. Clairon, "Raman-Ramsey interaction for coherent population trapping Cs clock," in *IEEE Transactions on Instrumentation and Measurement* (2007), Vol. 56, pp. 383–387.
121. C. E. Calosso, S. Micalizio, A. Godone, E. K. Bertacco, and F. Levi, "Electronics for the pulsed rubidium clock: design and characterization.," *IEEE Trans. Ultrason. Ferroelectr. Freq. Control* **54**, 1731–40 (2007).
122. I. Ben-Aroya, M. Kahanov, and G. Eisenstein, "Optimization of FM spectroscopy parameters for a frequency locking loop in small scale CPT based atomic clocks.," *Opt. Express* **15**, 15060–5 (2007).
123. D. F. Phillips, I. Novikova, C. Y.-T. Wang, R. L. Walsworth, and M. Crescimanno, "Modulation-induced frequency shifts in a coherent-population-trapping-based atomic clock," *J. Opt. Soc. Am. B* **22**, 305 (2005).
124. Y. Tian, B.-Z. Tan, J. Yang, Y. Zhang, and S.-H. Gu, "Ramsey-CPT spectrum with the Faraday effect and its application to atomic clocks," *Chinese Phys. B* **24**, 63302 (2015).

APPENDIX A: MATLAB CODES

The following MATLAB scripts and functions calculate solutions to the density matrix equations using initial input values, and allow determination of the system response to frequency detuning and other effects in many different circumstances. All values are defined in terms of excited state decay rate, Γ . When necessary, the calculated results reincorporate Γ to acquire measurable values and trends.

A.1 Three-level CPT solver – steady state solution

The steady-state solver calculates the density matrix values by following the steps outlined in chapter 2.

```
%% Steady-state solution for 3-level atomic system in 87Rb

%% Define decay frequency
    gm = 6; % MHz
    gamma3 = gm/gm;

%% Rabi frequency
    omega1 = 1/3 * gamma3;
    omega2 = omega1;

    delta = 0; % delta (common-mode detuning)

% Delta scan
    ulimit = 36/gm; step = 2*ulimit; R = 1001; % R = # of points
    del = -ulimit:step/(R-1):ulimit;

%% Initialization of variables for algorithm
    N = 3; % number of energy levels
    M = zeros(N^2,N^2); % M-matrix
    rho = zeros(N,N); % density matrix
    H = zeros(N,N); % Hamiltonian with decay
    W = zeros((N^2-1),(N^2-1)); % W-matrix
    S = zeros((N^2-1),1); % S-vector
    B = zeros((N^2-1),1); % B-vector
    A = zeros(N^2,R); % A=vectors, for all detunings
    He = zeros(16,16);
    Hsp = He;
    Hsm = He;
    Hp = He;

%% Ground state dephasing (GSD) (decoherence)
    dec = 0.005/gm; % 5 kHz
```

```

for m=1:R % start the Delta (difference detuning) loop
    Delta = del(1,m);
    % Define Hamiltonian
    H=[Delta/2 - 1i*dec/2, 0, -omega1/2; ...
        0, -Delta/2-1i*dec/2, -omega2/2; ...
        -omega1/2, -omega2/2, -delta-1i*gamma3/2];
%% Algorithm
for n=1:N^2 % start the outer-loop for finding elements of M
    for p=1:N^2 % start inner-loop for finding elements of M
        % finding alpha and beta
        remain=rem(n,N);
        if remain==0
            beta=N;
        else
            beta=remain;
        end
        alpha=(1+(n-beta)/N);
        % finding epsilon and sigma
        remain=rem(p,N);
        if remain==0
            sigma=N;
        else
            sigma=remain;
        end
        epsilon=(1+(p-sigma)/N);

        rho=zeros(N,N); % reset rho to all zeros
        rho(epsilon,sigma)=1; % pick on element to unity
        % find first part of Q matrix
        Q = (H*rho-rho*conj(H))*(0-1i);

        % add pop source term to Q
        Q(1,1) = Q(1,1)+gamma3/2*rho(3,3)+dec*rho(2,2);
        Q(2,2) = Q(2,2)+gamma3/2*rho(3,3)+dec*rho(1,1);

        M(n,p) = Q(alpha, beta);
    end % end the inner-loop for finding elements of M
end % end the outer-loop for finding elements of M

S=M(1:(N^2-1),N^2:N^2); % find S-vector
W=M(1:(N^2-1),1:(N^2-1)); % initialize W-matrix

% update W by subtracting from selected columns
for d=1:(N-1)
    W(:,((d-1)*N+d)=W(:,((d-1)*N+d))-S;
end

B=(W\S)*(-1); % find B-vector: primary solution

rhonn=1; % initialize pop of N-th state
for f=1:(N-1) % determine pop of N-th state
    rhonn=rhonn-B(((f-1)*N+f),1);
end

A(1:(N^2-1),m) = B;

```

```

    A(N^2,m)=rhonn;
end % end of Delta detuning loop

figure;
%% Plot excited state population term
plot(del,real(A(9,:)));
xlabel('\Delta/\Gamma')
ylabel('Excited state population \rho_{33}')
```

```

figure;
%% Plot coherence terms result
plot(del,imag(A(3,:)));
hold on;
plot(del,imag(A(6,:)));
xlabel('\Delta/\Gamma')
ylabel('Coherence terms \rho_{13} and \rho_{23} (index of refraction)')
```

```

figure;
plot(del,real(A(3,:)));
hold on;
plot(del,real(A(6,:)));
xlabel('\Delta/\Gamma')
ylabel('Coherence terms \rho_{13} and \rho_{23} (absorption)')
```

A.2 Three-level CPT/Ramsey solver – time-dependent method

The time-dependent solver uses a matrix method to solve a coupled system of equations.

Unlike the steady state solver, this method requires that the $N^2 \times N^2$ matrix is generated and placed into the function to be directly solved. Both the script and the function are presented here.

Script:

```

%% Time-dependent solution for 3-level atomic system in 87Rb
%% Define decay frequency
    gm = 6; % MHz (or 2*pi*6 MHz -> 26.5 ns lifetime, 87Rb)
    gamma3 = gm/gm;

%% Define long CPT "pulse" duration for CPT:
    tcpt = 500e-6/(26.5e-9); % increase pulse length proportional to gm

%% Include T and t_q for Ramsey:
    tfree = 0.5e-3/(26.5e-9);
    tquery = 1000e-9/(26.5e-9);

%% Beginning population distribution, 50% in each ground state
    rho11 = 0.5;
    rho22 = 0.5;

%% Ground state dephasing (GSD) (decoherence)
    decl = .0001/gm; % 100 Hz
    dec2 = decl;
```

```

delta = 0*gamma3;    % delta (common-mode detuning)

% Delta scan
ulimit = .036/gm;
step = 2*ulimit;
pd = -ulimit:step/1000:ulimit;

prcoher1=zeros(1,length(pd));

% initial rho-vector state
% [rho11,12,13,21,22,23,31,32,33]
rho0=[rho11,0,0,0,rho22,0,0,0,0]';

% parallelized loop calculates faster
% (replace with 'for' if no parallel toolbox)
parfor q=1:length(pd),
    Delta=pd(q);

    %% Rabi frequency
    omega1 = 1/50*gamma3;
    omega2 = omega1;

    % CPT Pulse
    t = tcpt;
    [rho] = fn3lv19x9(t, rho0, omega1, omega2, gamma3, delta, Delta, decl);

    %% enable the next two function calls for Ramsey:
    % Free evolution time, T
    t=tfree;
    omega1=0;
    omega2=0;
    [rho] = fn3lv19x9(t, rho, omega1, omega2, gamma3, delta, Delta, decl);

    % Query pulse
    t=tquery;
    omega1=(1/200)*gamma3;    % weak t_query probe pulse
    omega2=omega1;
    [rho] = fn3lv19x9(t, rho, omega1, omega2, gamma3, delta, Delta, decl);

    %% Collect terms
    % Excited state population
    prcoher1(q) = real(rho(9));
    % Coherence terms (absorption)
    prcoher13r(q) = real(rho(3));
    prcoher23r(q) = real(rho(6));
    % Coherence terms (index of refraction)
    prcoher13i(q) = imag(rho(3));
    prcoher23i(q) = imag(rho(6));
end
figure; hold all;
plot(pd,prcoher1);
% plot(pd,prcoher13r,'g'); % uncomment to enable coherence plots
% plot(pd,prcoher23r,'r');
xlabel('\Delta\Gamma')

```

```
ylabel('Population of excited state (\rho_3_3)')
```

Function:

```
function rho=fn3lv19x9(t,rho0,omega1,omega2,gamma3,delta,Delta,dec)

% N^2 x N^2 matrix of coefficients from Liouville equation
nsquare= ...
[-dec,0,-(omega1*1i)/2,0,dec,0,(omega1*1i)/2,0,gamma3/2;
0,-Delta*1i-dec,-(omega2*1i)/2,0,0,0,(omega1*1i)/2,0;
-(omega1*1i)/2,-(omega2*1i)/2,-(Delta*1i)/2-dec/2-delta*1i-
gamma3/2,0,0,0,0,(omega1*1i)/2;
0,0,0,Delta*1i-dec,0,-(omega1*1i)/2,(omega2*1i)/2,0,0;
dec,0,0,0,-dec,-(omega2*1i)/2,0,(omega2*1i)/2,gamma3/2;
0,0,0,-(omega1*1i)/2,-(omega2*1i)/2,(Delta*1i)/2-dec/2-delta*1i-
gamma3/2,0,0,(omega2*1i)/2;
(omega1*1i)/2,0,0,(omega2*1i)/2,0,0,(Delta*1i)/2-dec/2+delta*1i-gamma3/2,0,-
(omega1*1i)/2;
0,(omega1*1i)/2,0,0,(omega2*1i)/2,0,0,-(Delta*1i)/2-dec/2+delta*1i-gamma3/2,-
(omega2*1i)/2;
0,0,(omega1*1i)/2,0,0,(omega2*1i)/2,-(omega1*1i)/2,-(omega2*1i)/2,-gamma3];

% Determine eigenvalues and eigenvectors
[ve, va] = eig(nsquare,'nobalance');
[~,q] = size(nsquare); % get length of rho vector

% calculation begins at t0 and ends at t (tcpt, tfree, tquery)
t0 =0;

% initialize vectors
rhon = zeros(q,1);
rho_prime = rhon;

% calculate rho vector one rho_ij at a time
for m = 1:q
    % calculate new rho from e-values and e-vectors
    rhon(:,m) = exp(va(m,m)*t0)*ve(:,m);
    % calculate new rho from solved equation to pass to new time
    rho_prime(:,m) = exp(va(m,m)*t)*ve(:,m);
end

% solve for coefficients with initial rho values (rho0)
% equations:(rho0=rhon*alpha); alpha=inv(rhon)*rho0
% alpha = [A;B;C;D;E;F;G;H;I] % coefficients of the equations
alpha= rhon\rho0; % same as inv(rhon)*rho0

% pass result to script
rho = rho_prime*alpha;
end
```

A.3 16-level CPT solver – steady state solution

The parameters in this script are set to plot the sum of the excited state populations with a 20 mG axial magnetic field, RCP light, and a Rabi frequency $\Omega = \Gamma/60$, resonant with the $F' = 2$ state.

```
%% Steady-state solution for 16-level atomic system in 87Rb
%% Define decay frequency
    gm = 6; % Gamma, MHz
gamma3 = gm/gm;

%% Rabi frequency (in units of Gamma)
omega1 = 1*gamma3/60;
omega2 = omega1;

% Excited state hyperfine splitting
Deltahf = 814.5/gm;
% common-mode detuning -Deltahf for F'=1, 0 for F'=2
    delta = -Deltahf * 0;

% Delta scan
ulimit= .005/gm; step = 2*ulimit; R = 1001; % R = # of points
del = -ulimit:step/(R-1):ulimit;

%% Magnetic field strengths (Gauss) (explicit)
% Ground state transverse coupling
Bx = 0.000;
By = 0.000;
Bz = 0.005;
% Transverse Magnetic Field (misaligned axial field) (calculated)
    B = 0.02; % fixed total magnitude
    Bangle = 0.00; % angle of magnetic field
    Bxs = B * sind(Bangle); % x component
    Bzs = B * cosd(Bangle); % z component
    Bx = Bxs;
    Bz = Bzs;

%% Polarization Selection
% Ground state transverse coupling (1) or Pi-polarization induced (-1)
    Btype = 1;
% Optical polarization
linear = 0; % circular (0), lin||lin (1), linperplin (2)
% E-field polarization vector angle from vertical for lin||lin
    alpha = 0; % degrees from x (vertical)
% circular polarization handedness
    circ = 1; % RCP (1) or LCP (-1)

%% Initialization of variables for algorithm
    N = 16; % number of energy levels
    M = zeros(N^2,N^2); % M-matrix
rho = zeros(N,N); % density matrix
```

```

H = zeros(N,N); % Hamiltonian with decay
W = zeros((N^2-1),(N^2-1)); % W-matrix
S = zeros((N^2-1),1); % S-vector
B = zeros((N^2-1),1); % B-vector
A = zeros(N^2,R); % A=vectors, for all detunings
He = zeros(16,16);
Hsp = He;
Hsm = He;
Hp = He;

%% Ground state dephasing (GSD) (decoherence)
gup = 0.0001/gm*1/5;
gdown = 0.00006/gm*1/3;

%% decay terms (hand coded)
Q_source= ...
[0 0 0 gdown gdown gdown gdown gdown 1/12 1/12 0 1/2 1/4 1/12 0 0;
0 0 0 gdown gdown gdown gdown gdown 1/12 0 1/12 0 1/4 1/3 1/4 0;
0 0 0 gdown gdown gdown gdown gdown 0 1/12 1/12 0 0 1/12 1/4 1/2;
gup gup gup 0 0 0 0 0 1/2 0 0 1/3 1/6 0 0 0;
gup gup gup 0 0 0 0 0 1/4 1/4 0 1/6 1/12 1/4 0 0;
gup gup gup 0 0 0 0 0 1/12 1/3 1/12 0 1/4 0 1/4 0;
gup gup gup 0 0 0 0 0 0 1/4 1/4 0 0 1/4 1/12 1/6;
gup gup gup 0 0 0 0 0 0 0 1/2 0 0 0 1/6 1/3;
0 0 0 0 0 0 0 0 0 0 0 0 0 0 0 0;
0 0 0 0 0 0 0 0 0 0 0 0 0 0 0 0;
0 0 0 0 0 0 0 0 0 0 0 0 0 0 0 0;
0 0 0 0 0 0 0 0 0 0 0 0 0 0 0 0;
0 0 0 0 0 0 0 0 0 0 0 0 0 0 0 0;
0 0 0 0 0 0 0 0 0 0 0 0 0 0 0 0;
0 0 0 0 0 0 0 0 0 0 0 0 0 0 0 0];

%% Magnetic Field dependency
%% Calculate all B-field shifts for H (LMF And TMF)
muB = 1.399624604; % MHz/Gauss Bohr magneton
gfl = 1/2*muB/gm; % gF Lande factor. MHz/Gauss for lower states
gfu = 1/6*muB/gm; % gF Lande factor. MHz/Gauss for upper states
deltabg = abs(gfl) * Bz; % energy level shifts for Hamiltonian
deltabe = abs(gfu) * Bz;
deltabg = 0; % not used, hardcoded into Hamiltonian

btg = 1/2*muB/gm * (Bx + 1i*By);
bte = 1/6*muB/gm * (Bx + 1i*By);
btgc = 1/2*muB/gm * (Bx - 1i*By);
btec = 1/6*muB/gm * (Bx - 1i*By);

% pi-polarized transitions replace off-diagonal coupling terms
if Btype == -1,
    btg = 0;
    bte = 0;
    btgc = 0;
    btec = 0;
end

```

```

%% loop calculation
for m=1:R % start the Delta (difference detuning) loop
    %% F=1 He diagonal
    He(1,1) = del(1,m)/2 - deltabg - li*gup*5/2 - 0.702369/gm*Bz -
0.00021568/gm*Bz^2;
    He(1,2) = -btgc/sqrt(2);
    He(2,1) = -btg/sqrt(2);
    He(2,2) = del(1,m)/2 - li*gup*5/2 - 0.000287573/gm*Bz^2;
    He(2,3) = -btgc/sqrt(2);
    He(3,2) = -btg/sqrt(2);
    He(3,3) = del(1,m)/2 + deltabg - li*gup*5/2 + 0.702369/gm*Bz -
0.00021568/gm*Bz^2;
    %% F=2 He diagonal
    He(4,4) = - del(1,m)/2 + 2*deltabg - li*gdown*3/2 + 1.39917/gm*Bz;
    He(4,5) = btgc;
    He(5,4) = btg;
    He(5,5) = - del(1,m)/2 + deltabg - li*gdown*3/2 + 0.699583/gm*Bz +
0.00021568/gm*Bz^2;
    He(5,6) = sqrt(3/2)*btgc;
    He(6,5) = sqrt(3/2)*btg;
    He(6,6) = - del(1,m)/2 - li*gdown*3/2 + 0.000287573/gm*Bz^2;
    He(6,7) = sqrt(3/2)*btgc;
    He(7,6) = sqrt(3/2)*btg;
    He(7,7) = - deltabg - del(1,m)/2 - li*gdown*3/2 - 0.699583/gm*Bz +
0.00021568/gm*Bz^2;
    He(7,8) = btgc;
    He(8,7) = btg;
    He(8,8) = - 2*deltabg - del(1,m)/2 - li*gdown*3/2 - 1.39917/gm*Bz;
    %% F'=1 He diagonal
    He(9,9) = - delta - Deltahf - deltabe - (gamma3*li)/2;
    He(9,10) = -btec/sqrt(2);
    He(10,9) = -bte/sqrt(2);
    He(10,10) = - delta - Deltahf - (gamma3*li)/2;
    He(10,11) = -btec/sqrt(2);
    He(11,10) = -bte/sqrt(2);
    He(11,11) = - delta - Deltahf + deltabe - (gamma3*li)/2;
    %% F'=2 He diagonal
    He(12,12) = - delta + 2*deltabe - (gamma3*li)/2;
    He(12,13) = btec;
    He(13,12) = bte;
    He(13,13) = - delta + deltabe - (gamma3*li)/2;
    He(13,14) = sqrt(3/2)*btec;
    He(14,13) = sqrt(3/2)*bte;
    He(14,14) = - delta - (gamma3*li)/2;
    He(14,15) = sqrt(3/2)*btec;
    He(15,14) = sqrt(3/2)*bte;
    He(15,15) = - delta - deltabe - (gamma3*li)/2;
    He(15,16) = btec;
    He(16,15) = bte;
    He(16,16) = - delta - 2*deltabe - (gamma3*li)/2;
    %% optional pi transitions
    % F=1
    Hp(1,13) = -omega1/2*sqrt(1/4);
    Hp(2,14) = -omega1/2*sqrt(1/3);
    Hp(3,15) = -omega1/2*sqrt(1/4);

```

```

Hp(13,1) = -omega1/2*sqrt(1/4);
Hp(14,2) = -omega1/2*sqrt(1/3);
Hp(15,3) = -omega1/2*sqrt(1/4);
% F=2
Hp(4,12) = -omega2/2*sqrt(1/3);
Hp(5,13) = -omega2/2*sqrt(1/12);
Hp(6,14) = -omega2/2*0;
Hp(7,15) = -omega2/2*(-sqrt(1/12));
Hp(8,16) = -omega2/2*(-sqrt(1/3));
Hp(12,4) = -omega2/2*sqrt(1/3);
Hp(13,5) = -omega2/2*sqrt(1/12);
Hp(14,6) = -omega2/2*0;
Hp(15,7) = -omega2/2*(-sqrt(1/12));
Hp(16,8) = -omega2/2*(-sqrt(1/3));
%% Sigma Plus only
Hsp(1,12) = -omega1/2*(-sqrt(1/2));
Hsp(2,13) = -omega1/2*(-sqrt(1/4));
Hsp(3,14) = -omega1/2*(-sqrt(1/12));
  Hsp(2,9) = -omega1/2*(-sqrt(1/12));
Hsp(3,10) = -omega1/2*(-sqrt(1/12));
Hsp(12,1) = -omega1/2*(-sqrt(1/2));
Hsp(13,2) = -omega1/2*(-sqrt(1/4));
Hsp(14,3) = -omega1/2*(-sqrt(1/12));
  Hsp(9,2) = -omega1/2*(-sqrt(1/12));
Hsp(10,3) = -omega1/2*(-sqrt(1/12));
Hsp(5,12) = -omega2/2*sqrt(1/6);
Hsp(6,13) = -omega2/2*sqrt(1/4);
Hsp(7,14) = -omega2/2*sqrt(1/4);
Hsp(8,15) = -omega2/2*sqrt(1/6);
  Hsp(6,9) = -omega2/2*sqrt(1/12);
Hsp(7,10) = -omega2/2*sqrt(1/4);
Hsp(8,11) = -omega2/2*sqrt(1/2);
Hsp(12,5) = -omega2/2*sqrt(1/6);
Hsp(13,6) = -omega2/2*sqrt(1/4);
Hsp(14,7) = -omega2/2*sqrt(1/4);
Hsp(15,8) = -omega2/2*sqrt(1/6);
  Hsp(9,6) = -omega2/2*sqrt(1/12);
Hsp(10,7) = -omega2/2*sqrt(1/4);
Hsp(11,8) = -omega2/2*sqrt(1/2);
%% Sigma Minus Only
Hsm(1,10) = -omega1/2*sqrt(1/12);
Hsm(1,14) = -omega1/2*(-sqrt(1/12));
Hsm(2,11) = -omega1/2*sqrt(1/12);
Hsm(2,15) = -omega1/2*(-sqrt(1/4));
Hsm(3,16) = -omega1/2*(-sqrt(1/2));
Hsm(10,1) = -omega1/2*sqrt(1/12);
Hsm(14,1) = -omega1/2*(-sqrt(1/12));
Hsm(11,2) = -omega1/2*sqrt(1/12);
Hsm(15,2) = -omega1/2*(-sqrt(1/4));
Hsm(16,3) = -omega1/2*(-sqrt(1/2));
%% omega2 in SigmaMinus, - for parallel, + for perp
if linear == 0 || linear == 1, % linparlin
  Hsm(4,9) = -omega2/2*sqrt(1/2);
  Hsm(4,13) = -omega2/2*(-sqrt(1/6));
  Hsm(5,10) = -omega2/2*sqrt(1/4);

```

```

Hsm(5,14) = -omega2/2*(-sqrt(1/4));
Hsm(6,11) = -omega2/2*sqrt(1/12); %
Hsm(6,15) = -omega2/2*(-sqrt(1/4));
Hsm(7,16) = -omega2/2*(-sqrt(1/6));
  Hsm(9,4) = -omega2/2*sqrt(1/2);
Hsm(13,4) = -omega2/2*(-sqrt(1/6));
Hsm(10,5) = -omega2/2*sqrt(1/4);
Hsm(14,5) = -omega2/2*(-sqrt(1/4));
Hsm(11,6) = -omega2/2*sqrt(1/12); %
Hsm(15,6) = -omega2/2*(-sqrt(1/4));
Hsm(16,7) = -omega2/2*(-sqrt(1/6));
else % linperplin
  Hsm(4,9) = omega2/2*sqrt(1/2);
  Hsm(4,13) = omega2/2*(-sqrt(1/6));
  Hsm(5,10) = omega2/2*sqrt(1/4);
  Hsm(5,14) = omega2/2*(-sqrt(1/4));
  Hsm(6,11) = omega2/2*sqrt(1/2);
  Hsm(6,15) = omega2/2*(-sqrt(1/4));
  Hsm(7,16) = omega2/2*(-sqrt(1/6));
  Hsm(9,4) = omega2/2*sqrt(1/2);
  Hsm(13,4) = omega2/2*(-sqrt(1/6));
  Hsm(10,5) = omega2/2*sqrt(1/4);
  Hsm(14,5) = omega2/2*(-sqrt(1/4));
  Hsm(11,6) = omega2/2*sqrt(1/2);
  Hsm(15,6) = omega2/2*(-sqrt(1/4));
  Hsm(16,7) = omega2/2*(-sqrt(1/6));
end
%% Add H components based on interaction polarization
if linear == 0 && circ == 1, % RCP
  H = He + Hsp*1 + Hsm*0;
elseif linear == 0 && circ == -1, % LCP
  H = He + Hsp*0 + Hsm*1;
else
  H = He + Hsp + Hsm; % lin||lin or lin perp lin
end
%% pi-polarization induced transitions from transverse B field
if Btype == -1,
  H = He + Hsp*1 + Hsm*1 + Hp;
end
%% Algorithm
col=0; % index for column of M-matrix that will be filled.
index1 = 1:N;
index2 = 1:N:N*(N-1)+1;
index3 = 1:N+1:N^2;
% n keeps track of where in the M matrix the
% elements of Ham have to be entered
for n=1:N
  for p=1:N % p picks the pth column of the Ham
    col=col+1;
    M(index1+(n-1)*N,col)=1i*conj(H(:,p));
    M(index2+p-1,col)=M(index2+p-1,col)-1i*(H(:,n));
    if n==p,
      M(index3,col)=M(index3,col)+Q_source(:,n);
    end
  end
end % end the inner-loop for finding elements of M

```

```

end
S=M(1:(N^2-1),N^2:N^2);      % find S-vector
W=M(1:(N^2-1),1:(N^2-1));

% update W by subtracting from selected columns
for d=1:(N-1)
    W(:,((d-1)*N+d)=W(:,((d-1)*N+d))-S;
end
B=(W\S)*(-1);                % find B-vector: primary solution!

rhonn = 1;                    % initialize population of Nth state
for f=1:(N-1)
    rhonn=rhonn-B(((f-1)*N+f),1);
end

A(1:(N^2-1),m) = B;
A(N^2,m)=rhonn;
M=zeros(N^2,N^2);
end                            % end of Delta detuning loop

%% Collect excited state population values
prcoherf1 = real( A((171),:) + A((154),:) + A((137),:));
prcoherf2 = real( A((256),:) + A((239),:) + A((222),:) + A((205),:) +
A((188),:));

%% Plot either F'=2 or F'=1 result (resonant)
if delta == 0,
    %% F' = 2 total
    plot(del*gm*1e3,prcoherf2);
else
    %% F' = 1 total
    plot(del*gm*1e3,prcoherf1);
end
xlabel('Difference detuning, \Delta (kHz)')
ylabel('Excited states total population')

```

APPENDIX B: MULTI-LEVEL HAMILTONIAN AND SOURCE MATRIX

The non-Hermitian Hamiltonian, H , on the following page consists of all three parts, H_A , H_B , and H_Γ , as described in chapter 3. The coupling terms defined by the σ^+ and σ^- transitions are colored blue and red, respectively. Frequency shifts of the Zeeman sublevels that are caused by the axial magnetic field are included in terms of δ_{bg} for ground state shifts and δ_{be} for excited state shifts.

H	(1, +1)	(1, 0)	(1, -1)	(2, +2)	(2, +1)	(2, 0)	(2, -1)	(2, -2)	(1', +1)	(1', 0)	(1', -1)	(2', +2)	(2', +1)	(2', 0)	(2', -1)	(2', -2)
(1, +1)	$\frac{\Delta - \delta_{bg}}{2} \frac{t_{r1}}{t_{r2}} - \frac{1}{2}$	$-\frac{\mu_B B_T}{2} \frac{1}{\sqrt{2}}$	0	0	0	0	0	0	0	$\frac{1}{\sqrt{2}} \frac{\Omega_1}{2}$	0	$-\frac{1}{\sqrt{2}} \frac{\Omega_1}{2}$	0	$-\frac{1}{\sqrt{2}} \frac{\Omega_1}{2}$	0	0
(1, 0)	$-\frac{\mu_B B_T}{2} \frac{1}{\sqrt{2}}$	$\frac{\Delta - t_{r1}}{2} - \frac{1}{2}$	$-\frac{\mu_B B_T}{2} \frac{1}{\sqrt{2}}$	0	0	0	0	0	$-\frac{1}{\sqrt{2}} \frac{\Omega_1}{2}$	0	$\frac{1}{\sqrt{2}} \frac{\Omega_1}{2}$	0	$-\frac{1}{\sqrt{2}} \frac{\Omega_1}{2}$	0	$-\frac{1}{\sqrt{2}} \frac{\Omega_1}{2}$	0
(1, -1)	0	$-\frac{\mu_B B_T}{2} \frac{1}{\sqrt{2}}$	$\frac{\Delta + \delta_{bg}}{2} \frac{t_{r1}}{t_{r2}} - \frac{1}{2}$	0	0	0	0	0	$-\frac{1}{\sqrt{2}} \frac{\Omega_1}{2}$	$-\frac{1}{\sqrt{2}} \frac{\Omega_1}{2}$	0	0	0	$-\frac{1}{\sqrt{2}} \frac{\Omega_1}{2}$	0	$-\frac{1}{\sqrt{2}} \frac{\Omega_1}{2}$
(2, +2)	0	0	$\frac{\mu_B B_T}{2}$	$-\frac{\Delta}{2} + \frac{2\delta_{bg}}{t_{r2}} - \frac{1}{2}$	$\frac{\mu_B B_T}{2}$	0	0	0	$\frac{1}{\sqrt{2}} \frac{\Omega_2}{2}$	0	0	0	0	0	0	0
(2, +1)	0	0	0	$\frac{\mu_B B_T}{2}$	$-\frac{\Delta + \delta_{bg}}{2} \frac{t_{r2}}{t_{r1}} - \frac{1}{2}$	$\frac{\mu_B}{2} \sqrt{\frac{3}{2}} B_T$	0	0	$\frac{1}{\sqrt{2}} \frac{\Omega_2}{2}$	$\frac{1}{\sqrt{2}} \frac{\Omega_2}{2}$	0	$-\frac{1}{\sqrt{2}} \frac{\Omega_2}{2}$	0	$-\frac{1}{\sqrt{2}} \frac{\Omega_2}{2}$	0	0
(2, 0)	0	0	0	0	$\frac{\mu_B}{2} \sqrt{\frac{3}{2}} B_T$	$-\frac{\Delta - t_{r2}}{2} - \frac{1}{2}$	$\frac{\mu_B}{2} \sqrt{\frac{3}{2}} B_T$	0	$\frac{1}{\sqrt{2}} \frac{\Omega_2}{2}$	0	$\frac{1}{\sqrt{2}} \frac{\Omega_2}{2}$	0	$\frac{1}{\sqrt{2}} \frac{\Omega_2}{2}$	0	$-\frac{1}{\sqrt{2}} \frac{\Omega_2}{2}$	0
(2, -1)	0	0	0	0	0	$-\frac{\Delta - \delta_{bg}}{2} \frac{t_{r2}}{t_{r1}} - \frac{1}{2}$	$\frac{\mu_B B_T}{2}$	$\frac{\mu_B B_T}{2}$	$\frac{1}{\sqrt{2}} \frac{\Omega_2}{2}$	$\frac{1}{\sqrt{2}} \frac{\Omega_2}{2}$	0	0	0	$\frac{1}{\sqrt{2}} \frac{\Omega_2}{2}$	0	$-\frac{1}{\sqrt{2}} \frac{\Omega_2}{2}$
(2, -2)	0	0	0	0	0	$-\frac{\Delta}{2} - \frac{2\delta_{bg}}{t_{r2}} - \frac{1}{2}$	$\frac{\mu_B B_T}{2}$	$-\frac{\Delta}{2} - \frac{2\delta_{bg}}{t_{r2}} - \frac{1}{2}$	0	0	$\frac{1}{\sqrt{2}} \frac{\Omega_2}{2}$	0	0	0	$\frac{1}{\sqrt{2}} \frac{\Omega_2}{2}$	0
(1', +1)	0	$-\frac{1}{\sqrt{2}} \frac{\Omega_1}{2}$	0	$\frac{1}{\sqrt{2}} \frac{\Omega_2}{2}$	0	$\frac{1}{\sqrt{2}} \frac{\Omega_2}{2}$	0	0	$-\frac{\Delta_{hf}}{6} \frac{t\Gamma}{\delta_{bc}} - \frac{1}{2}$	$-\frac{\mu_B B_T}{6} \frac{1}{\sqrt{2}}$	0	0	0	0	0	0
(1', 0)	$\frac{1}{\sqrt{2}} \frac{\Omega_1}{2}$	0	$-\frac{1}{\sqrt{2}} \frac{\Omega_1}{2}$	0	$\frac{1}{\sqrt{2}} \frac{\Omega_2}{2}$	0	0	0	$-\frac{\Delta_{hf}}{6} \frac{t\Gamma}{\delta_{bc}} - \frac{1}{2}$	$-\frac{\mu_B B_T}{6} \frac{1}{\sqrt{2}}$	$-\frac{\mu_B B_T}{6} \frac{1}{\sqrt{2}}$	0	0	0	0	0
(1', -1)	0	$\frac{1}{\sqrt{2}} \frac{\Omega_1}{2}$	0	0	0	$\frac{1}{\sqrt{2}} \frac{\Omega_2}{2}$	0	$\frac{1}{\sqrt{2}} \frac{\Omega_2}{2}$	$-\frac{\Delta_{hf}}{6} \frac{t\Gamma}{\delta_{bc}} - \frac{1}{2}$	$-\frac{\mu_B B_T}{6} \frac{1}{\sqrt{2}}$	$-\frac{\Delta_{hf}}{6} \frac{t\Gamma}{\delta_{bc}} - \frac{1}{2}$	0	0	0	0	0
(2', +2)	$-\frac{1}{\sqrt{2}} \frac{\Omega_1}{2}$	0	0	0	$\frac{1}{\sqrt{2}} \frac{\Omega_2}{2}$	0	0	0	0	0	0	$-\frac{\delta}{6} + \frac{2\delta_{bc}}{t\Gamma} - \frac{1}{2}$	$\frac{\mu_B B_T}{6}$	0	0	0
(2', +1)	0	$-\frac{1}{\sqrt{2}} \frac{\Omega_1}{2}$	0	$-\frac{1}{\sqrt{2}} \frac{\Omega_2}{2}$	0	$\frac{1}{\sqrt{2}} \frac{\Omega_2}{2}$	0	0	0	0	0	$\frac{\mu_B B_T}{6}$	$-\frac{\delta + \delta_{bc}}{2} \frac{t\Gamma}{\delta_{bc}}$	$\frac{\mu_B}{6} \sqrt{\frac{3}{2}} B_T$	0	0
(2', 0)	$-\frac{1}{\sqrt{2}} \frac{\Omega_1}{2}$	0	$-\frac{1}{\sqrt{2}} \frac{\Omega_1}{2}$	0	$-\frac{1}{\sqrt{2}} \frac{\Omega_2}{2}$	0	$\frac{1}{\sqrt{2}} \frac{\Omega_2}{2}$	0	0	0	0	0	$\frac{\mu_B}{6} \sqrt{\frac{3}{2}} B_T$	$-\frac{\delta - t\Gamma}{2}$	$\frac{\mu_B}{6} \sqrt{\frac{3}{2}} B_T$	0
(2', -1)	0	$-\frac{1}{\sqrt{2}} \frac{\Omega_1}{2}$	0	0	0	$-\frac{1}{\sqrt{2}} \frac{\Omega_2}{2}$	0	$\frac{1}{\sqrt{2}} \frac{\Omega_2}{2}$	0	0	0	0	0	$-\frac{\delta - \delta_{bc}}{6} \frac{t\Gamma}{\delta_{bc}}$	$-\frac{\mu_B B_T}{6}$	$\frac{\mu_B B_T}{6}$
(2', -2)	0	0	$-\frac{1}{\sqrt{2}} \frac{\Omega_1}{2}$	0	0	0	$-\frac{1}{\sqrt{2}} \frac{\Omega_2}{2}$	0	0	0	0	0	0	0	$\frac{\mu_B B_T}{6}$	$-\frac{\delta}{2} \frac{2\delta_{bc}}{t\Gamma} - \frac{1}{2}$

Table B.1: 16-level non-Hermitian Hamiltonian

The diagonal elements of the source matrix L are defined as:

$$L_{11} = \frac{\gamma_2}{3}(\rho_{4,4} + \rho_{5,5} + \rho_{6,6} + \rho_{7,7} + \rho_{8,8}) + \frac{\Gamma}{12}\rho_{9,9} + \frac{\Gamma}{12}\rho_{10,10} + \frac{\Gamma}{2}\rho_{12,12} \\ + \frac{\Gamma}{4}\rho_{13,13} + \frac{\Gamma}{12}\rho_{14,14}$$

$$L_{22} = \frac{\gamma_2}{3}(\rho_{4,4} + \rho_{5,5} + \rho_{6,6} + \rho_{7,7} + \rho_{8,8}) + \frac{\Gamma}{12}\rho_{9,9} + \frac{\Gamma}{12}\rho_{11,11} + \frac{\Gamma}{4}\rho_{13,13} \\ + \frac{\Gamma}{3}\rho_{14,14} + \frac{\Gamma}{4}\rho_{15,15}$$

$$L_{33} = \frac{\gamma_2}{3}(\rho_{4,4} + \rho_{5,5} + \rho_{6,6} + \rho_{7,7} + \rho_{8,8}) + \frac{\Gamma}{12}\rho_{10,10} + \frac{\Gamma}{12}\rho_{11,11} + \frac{\Gamma}{12}\rho_{14,14} \\ + \frac{\Gamma}{4}\rho_{15,15} + \frac{\Gamma}{2}\rho_{16,16}$$

$$L_{44} = \frac{\gamma_1}{5}(\rho_{1,1} + \rho_{2,2} + \rho_{3,3}) + \frac{\Gamma}{2}\rho_{9,9} + \frac{\Gamma}{3}\rho_{12,12} + \frac{\Gamma}{6}\rho_{13,13}$$

$$L_{55} = \frac{\gamma_1}{5}(\rho_{1,1} + \rho_{2,2} + \rho_{3,3}) + \frac{\Gamma}{4}\rho_{9,9} + \frac{\Gamma}{4}\rho_{10,10} + \frac{\Gamma}{6}\rho_{12,12} + \frac{\Gamma}{12}\rho_{13,13} + \frac{\Gamma}{4}\rho_{14,14}$$

$$L_{66} = \frac{\gamma_1}{5}(\rho_{1,1} + \rho_{2,2} + \rho_{3,3}) + \frac{\Gamma}{12}\rho_{9,9} + \frac{\Gamma}{3}\rho_{10,10} + \frac{\Gamma}{12}\rho_{11,11} + \frac{\Gamma}{4}\rho_{13,13} + \frac{\Gamma}{4}\rho_{15,15}$$

$$L_{77} = \frac{\gamma_1}{5}(\rho_{1,1} + \rho_{2,2} + \rho_{3,3}) + \frac{\Gamma}{4}\rho_{10,10} + \frac{\Gamma}{4}\rho_{11,11} + \frac{\Gamma}{4}\rho_{14,14} + \frac{\Gamma}{12}\rho_{15,15} + \frac{\Gamma}{6}\rho_{16,16}$$

$$L_{88} = \frac{\gamma_1}{5}(\rho_{1,1} + \rho_{2,2} + \rho_{3,3}) + \frac{\Gamma}{2}\rho_{11,11} + \frac{\Gamma}{6}\rho_{15,15} + \frac{\Gamma}{3}\rho_{16,16}$$

$$L_{ij}|_{i=j} = 0 \quad \begin{cases} i = 9 \dots 16 \\ j = 9 \dots 16 \end{cases}$$

$$L_{ij}|_{i \neq j} = 0 \quad \begin{cases} i = 1 \dots 16 \\ j = 1 \dots 16 \end{cases}$$

(B.1)

The off-diagonal elements of the source matrix L are all zero.

APPENDIX C: TRANSVERSE MAGNETIC FIELD INTERACTIONS

For the magnetic interaction calculation, the following values are defined for ^{87}Rb D1 line:

$$\text{Bohr magneton: } \mu_B = \frac{e \hbar}{2 m_e} \Rightarrow \frac{\mu_B}{\hbar 2 \pi} \cong 1.4 \text{ MHz/G}$$

Landé	$5^2S_{1/2}$		$5^2P_{1/2}$	
g-factors	$F = 1$	$F = 2$	$F' = 1$	$F' = 2$
g_F	-1/2	+1/2	-1/6	+1/6

Table C.1: Landé g-factors for the ground and excited states of D1 line of ^{87}Rb

$$\text{Interaction Hamiltonian: } \hat{H}_I = g_F \frac{\mu_B}{\hbar} \vec{F} \cdot \vec{B}$$

The Zeeman shift is calculated as the following when \vec{B} is parallel to the quantization direction \hat{z} (axial magnetic field):

$$\vec{B} = \hat{z} B_0 \tag{C.1}$$

$$\Rightarrow \vec{F} \cdot \vec{B} = F_z B_0$$

$$\Rightarrow \hat{H}_I = g_F \frac{\mu_B}{\hbar} \hat{F}_z B_0; \{ \hat{F}_z |F, m_F\rangle = \hbar m_F |F, m_F\rangle \} \tag{C.2}$$

$$\Rightarrow \langle F, m_F | \hat{H}_I | F, m'_F \rangle = g_F \mu_B B_0 m'_F \delta_{\{m_F, m'_F\}}$$

For the example of the Zeeman sublevels in $5^2S_{1/2}$, $F = 1$, $m_F = +1, 0, -1$ the shift is calculated

as:

$$\langle \frac{\hat{H}_I}{\hbar} \rangle = -\frac{1}{2} \frac{\mu_B}{\hbar} B_0 \tag{C.3}$$

This corresponds to a shift of the frequency by $-\frac{1}{2} \times 1.4 \text{ MHz}$ or -0.7 MHz for an axial magnetic field of 1 Gauss. Likewise, the axial magnetic field induced shift is calculated for the other m_F levels in the two ground and excited states:

$$5^2 S_{1/2}, F = 1 \left(g_F = -\frac{1}{2} \right) \text{ or } 5^2 P_{1/2}, F' = 1 \left(g_F = -\frac{1}{6} \right)$$

$\frac{\hat{H}_I}{\hbar} =$	$m'_F = +1$	$m'_F = 0$	$m'_F = -1$	(C.4)
$m_F = +1$	+1	0	0	
$m_F = 0$	0	0	0	
$m_F = -1$	0	0	-1	

$\times g_F \frac{\mu_B}{\hbar} B_0$

$$5^2 S_{1/2}, F = 2 \left(g_F = +\frac{1}{2} \right) \text{ or } 5^2 P_{1/2}, F' = 2 \left(g_F = +\frac{1}{6} \right)$$

$\frac{\hat{H}_I}{\hbar} =$	$m'_F = +2$	$m'_F = +1$	$m'_F = 0$	$m'_F = -1$	$m'_F = -2$	(C.5)
$m_F = +2$	+2	0	0	0	0	
$m_F = +1$	0	+1	0	0	0	
$m_F = 0$	0	0	0	0	0	
$m_F = -1$	0	0	0	-1	0	
$m_F = -2$	0	0	0	0	-2	

$\times g_F \frac{\mu_B}{\hbar} B_0$

For the general case where \vec{B} is in an arbitrary direction, the following are defined:

$$\vec{B} = B_X \hat{x} + B_Y \hat{y} + B_Z \hat{z} \tag{C.6}$$

$$\begin{aligned}\hat{H}_I &= g_F \frac{\mu_B}{\hbar} \vec{F} \cdot \vec{B} \\ &= \alpha_F (\hat{F}_x B_X + \hat{F}_y B_Y + \hat{F}_z B_Z)\end{aligned}\tag{C.7}$$

where $\alpha_F \equiv g_F \frac{\mu_B}{\hbar}$.

For a given F :

$$\begin{aligned}\langle F, m_F | \hat{H}_I | F, m'_F \rangle \\ = \alpha_F \{ B_X \langle F, m_F | \hat{F}_x | F, m'_F \rangle + B_Y \langle F, m_F | \hat{F}_y | F, m'_F \rangle + B_Z \langle F, m_F | \hat{F}_z | F, m'_F \rangle \}\end{aligned}\tag{C.8}$$

The third term is the same as in the axial (\hat{z}) calculation above:

$$\langle F, m_F | \hat{F}_z | F, m'_F \rangle = \hbar m'_F \delta_{\{m_F, m'_F\}}\tag{C.9}$$

To calculate the first and second terms:

$$\hat{F}_+ |F, m_F\rangle = \hbar [F(F+1) - m_F(m_F+1)]^{\frac{1}{2}} |F, m_F+1\rangle\tag{C.10}$$

$$\hat{F}_- |F, m_F\rangle = \hbar [F(F+1) - m_F(m_F-1)]^{\frac{1}{2}} |F, m_F-1\rangle\tag{C.11}$$

where

$$\hat{F}_+ \equiv \hat{F}_x + i\hat{F}_y\tag{C.12}$$

$$\hat{F}_- \equiv \hat{F}_x - i\hat{F}_y\tag{C.13}$$

$$\Rightarrow \hat{F}_+ = \frac{\hat{F}_+ + \hat{F}_-}{2}\tag{C.14}$$

$$\Rightarrow \hat{F}_y = \frac{1}{2i}(\hat{F}_+ - \hat{F}_-)\tag{C.15}$$

These relations are true for any angular momentum.

So, the following is found:

$$\begin{aligned} \hat{F}_x |F, m_F\rangle = & \left\{ \frac{\hbar}{2} [F(F+1) - m_F(m_F+1)]^{\frac{1}{2}} |F, m_F+1\rangle \right. \\ & \left. + \frac{\hbar}{2} [F(F+1) - m_F(m_F-1)]^{\frac{1}{2}} |F, m_F-1\rangle \right\} \end{aligned} \quad (\text{C.16})$$

$$\begin{aligned} \hat{F}_y |F, m_F\rangle = & \left\{ \frac{\hbar}{2i} [F(F+1) - m_F(m_F+1)]^{\frac{1}{2}} |F, m_F+1\rangle \right. \\ & \left. + \frac{\hbar}{2i} [F(F+1) - m_F(m_F-1)]^{\frac{1}{2}} |F, m_F-1\rangle \right\} \end{aligned} \quad (\text{C.17})$$

After coupling the states,

$$\begin{aligned} \langle F, m_F | \hat{F}_x | F, m'_F \rangle & \\ & = \frac{\hbar}{2} [F(F+1) - m'_F(m'_F+1)]^{\frac{1}{2}} \delta_{\{m_F, (m'_F+1)\}} \\ & \quad + \frac{\hbar}{2} [F(F+1) - m'_F(m'_F-1)]^{\frac{1}{2}} \delta_{\{m_F, (m'_F-1)\}} \end{aligned} \quad (\text{C.18})$$

$$\begin{aligned} \langle F, m_F | \hat{F}_y | F, m'_F \rangle & \\ & = -\frac{i\hbar}{2} [F(F+1) - m'_F(m'_F+1)]^{\frac{1}{2}} \delta_{\{m_F, (m'_F+1)\}} \\ & \quad + \frac{i\hbar}{2} [F(F+1) - m'_F(m'_F-1)]^{\frac{1}{2}} \delta_{\{m_F, (m'_F-1)\}} \end{aligned} \quad (\text{C.19})$$

The main result for the interaction Hamiltonian is expressed as:

$$\begin{aligned}
& \langle F, m_F | \hat{H}_I | F, m'_F \rangle \\
&= \hbar \alpha_F \left\{ \frac{B_X}{2} \left[\{F(F+1) - m'_F(m'_F+1)\}^{\frac{1}{2}} \delta_{\{m_F, (m'_F+1)\}} \right. \right. \\
&+ \left. \left. \{F(F+1) - m'_F(m'_F-1)\}^{\frac{1}{2}} \delta_{\{m_F, (m'_F-1)\}} \right] \right. \\
&- \frac{iB_Y}{2} \left[\{F(F+1) - m'_F(m'_F+1)\}^{\frac{1}{2}} \delta_{\{m_F, (m'_F+1)\}} \right. \\
&\left. \left. - \{F(F+1) - m'_F(m'_F-1)\}^{\frac{1}{2}} \delta_{\{m_F, (m'_F-1)\}} \right] + B_Z m'_F \delta_{\{m_F, m'_F\}} \right\}
\end{aligned} \tag{C.20}$$

Thus the interaction Hamiltonian can be written as a matrix with the magnetic field coupling. For the coupling between Zeeman sublevels of the $5^2 S_{1/2}, F = 1$ state (where $\alpha_F = -\frac{1}{2} \frac{\mu_B}{\hbar}$) or the $5^2 P_{1/2}, F' = 1$ state (where $\alpha_F = -\frac{1}{6} \frac{\mu_B}{\hbar}$)

$\frac{\hat{H}_I}{\hbar \alpha_F} =$	$m'_F = +1$	$m'_F = 0$	$m'_F = -1$
$m_F = +1$	B_Z	$\frac{1}{\sqrt{2}}(B_X - iB_Y)$	0
$m_F = 0$	$\frac{1}{\sqrt{2}}(B_X + iB_Y)$	0	$\frac{1}{\sqrt{2}}(B_X - iB_Y)$
$m_F = -1$	0	$\frac{1}{\sqrt{2}}(B_X + iB_Y)$	$-B_Z$

(C.21)

For the coupling between Zeeman sublevels of the $5^2 S_{1/2}, F = 2$ state (where $\alpha_F = +\frac{1}{2} \frac{\mu_B}{\hbar}$) or the

$5^2 P_{1/2}, F' = 2$ state (where $\alpha_F = +\frac{1}{6} \frac{\mu_B}{\hbar}$)

$\frac{\hat{H}_I}{\hbar\alpha_F} =$	$m'_F = +2$	$m'_F = +1$	$m'_F = 0$	$m'_F = -1$	$m'_F = -2$
$m_F = +2$	$2B_Z$	$B_X - iB_Y$	0	0	0
$m_F = +1$	$B_X + iB_Y$	B_Z	$\sqrt{\frac{3}{2}}(B_X - iB_Y)$	0	0
$m_F = 0$	0	$\sqrt{\frac{3}{2}}(B_X + iB_Y)$	0	$\sqrt{\frac{3}{2}}(B_X - iB_Y)$	0
$m_F = -1$	0	0	$\sqrt{\frac{3}{2}}(B_X + iB_Y)$	$-B_Z$	$B_X - iB_Y$
$m_F = -2$	0	0	0	$B_X + iB_Y$	$-2B_Z$

(C.22)

APPENDIX D: ENERGY LEVEL SHIFT CALCULATION USING BREIT-RABI EQUATION

Breit-Rabi equation describes the energy shift of Zeeman sublevels in an axial magnetic field for single valence electron atoms. For D1 line in ^{87}Rb , the following values and definitions are used in applying the Breit-Rabi formula. The electron spin is $J = 1/2$, the nuclear spin is $I = 3/2$. The upper & lower ground states are then $F = |J \pm I|$. The ground state frequency splitting between hyperfine states in the absence of B is $\Delta w = 6834.6826$ MHz. Three g-factors are defined: $g_J(5S^{1/2}) = 2.00233113$, $g_J(5P^{1/2}) = 0.666$, and g_I (nuclear) = -0.0009951414. Constants of nature are also defined: Planck's constant, $h = 6.626 \times 10^{-34}$ J s, Bohr magneton, $\mu_B = h \cdot 1.3996$ MHz/G, and nuclear magneton, $\mu_N = 5.05 \times 10^{-27}$ J/T. The energy shift is defined as

$$\Delta E_{F=I\pm 1/2} = \mu_B g_I m_F B_Z \pm \frac{h \Delta w}{2(2I + 1)} \sqrt{1 + \frac{2 m_F}{I + 1/2} x + x^2} \quad (\text{D.1})$$

where

$$x = \mu_B \frac{g_J - g_I}{h \Delta w} B_Z \quad (\text{D.2})$$

To account for the second order shifts with axial magnetic field, take the series expansion of ΔE around x for $F = 1$ and 2 to the second order:

$$\Delta E_{F=2, F=1} = \pm \frac{h \Delta w}{2} + g_I m_F \mu_B B_Z \pm \frac{h \Delta w m_F}{4} x \mp \frac{h \Delta w (m_F^2 - 4)}{16} x^2 \quad (\text{D.3})$$

$F = 2$ and $I = 3/2$

Plug in x:

$$\Delta E_{F=2} = \frac{h \Delta w}{2} + \frac{(3g_I + g_J)\mu_B m_F}{4} B_Z - \frac{(g_I - g_J)^2 (m_F^2 - 4)\mu_B^2}{16 h \Delta w} B_Z^2 \quad (\text{D.4})$$

F = 1 and I = 3/2

Plug in x:

$$\Delta E_{F=1} = -\frac{h\Delta w}{2} + \frac{(5g_I - g_J)\mu_B m_F}{4} B_z - \frac{(g_I - g_J)^2 (m_F^2 - 4)\mu_B^2}{16 h\Delta w} B_z^2 \quad (\text{D.5})$$

Examples in CPT

For the 0-0 clock transition, $m_F = 0$ for both $|F = 1\rangle$ and $|F = 2\rangle$ states, which results in 0 linear shift from the B_z term. Each ground state energy level contributing to CPT shifts in frequency relative to half the hyperfine frequency ($h\Delta w/2$) by

$$\frac{\Delta E_{2,1} \mp \frac{h\Delta w}{2}}{h} = \Delta f_{2,1} = \pm \frac{(g_J - g_I)^2 \mu_B^2}{4 h^2 \Delta w} B_z^2 \quad (\text{D.6})$$

This corresponds to a calculated value of $\Delta f_{clock} = \Delta f_2 - \Delta f_1 = 575.15 \text{ Hz}/G^2$.

Zeeman CPT resonances have both linear and quadratic shifts. For $m_F = \pm 1, \pm 1$ resonances, the total shift is:

$$\frac{\Delta E_2 - \Delta E_1 - h\Delta w}{h} = \Delta f_{\pm 1, \pm 1} = \pm \frac{(g_J - g_I)\mu_B}{2h} B_z + \frac{3}{8} \frac{(g_J - g_I)^2 \mu_B^2}{h^2 \Delta w} B_z^2 \quad (\text{D.7})$$

which results in $\Delta f_{\pm 1, \pm 1} = \pm 1.402 \text{ MHz}/G + 431.36 \text{ Hz}/G^2$ shifts in CPT.

For $lin||lin$ CPT transitions, the shifts for $m_F = -1, +1$ and $m_F = +1, -1$ are:

$$\frac{\Delta E_2 - \Delta E_1 - h\Delta w}{h} = \Delta f_{-,+} = \pm \frac{2 g_I \mu_B}{h} B + \frac{3}{8} \frac{(g_J - g_I)^2 \mu_B^2}{h^2 \Delta w} B_z^2 \quad (\text{D.8})$$

where the calculated values are $\Delta f_{-,+} = \mp 2785.65 \text{ kHz}/G + 431.36 \text{ Hz}/G^2$.

APPENDIX E: PUSH-PULL AND LIN \perp LIN EQUIVALENCE

The polarization states of the optical fields in the PPOP scheme are shown to be equivalent to those used in the $lin \perp lin$ scheme here. First, consider the two electromagnetic waves that make up the left circularly polarized (LCP) CPT beam:

$$\begin{aligned} \vec{E}_{CPT}^{(1)} = E_0 \{ & [\hat{x} \cos(k_1 z_1 - \omega_1 t) + \hat{y} \sin(k_1 z_1 - \omega_1 t)] \\ & + [\hat{x} \cos(k_2 z_1 - \omega_2 t) + \hat{y} \sin(k_2 z_1 - \omega_2 t)] \} \end{aligned} \quad (E.1)$$

where z_1 is the distance travelled by the LCP CPT beam. This can be expressed as:

$$\begin{aligned} \vec{E}_{CPT}^{(1)} = E_0 \left[2\hat{x} \cos\left(\frac{(k_1 + k_2)}{2} z_1 - \frac{(\omega_1 + \omega_2)}{2} t\right) \cos\left(\frac{(k_1 - k_2)}{2} z_1 - \frac{(\omega_1 - \omega_2)}{2} t\right) \right. \\ \left. + 2\hat{y} \sin\left(\frac{(k_1 + k_2)}{2} z_1 - \frac{(\omega_1 + \omega_2)}{2} t\right) \cos\left(\frac{(k_1 - k_2)}{2} z_1 - \frac{(\omega_1 - \omega_2)}{2} t\right) \right] \end{aligned} \quad (E.2)$$

combining terms:

$$\begin{aligned} \vec{E}_{CPT}^{(1)} = 2E_0 \cos\left(\frac{(k_1 - k_2)}{2} z_1 - \frac{(\omega_1 - \omega_2)}{2} t\right) \left[\hat{x} \cos\left(\frac{(k_1 + k_2)}{2} z_1 - \frac{(\omega_1 + \omega_2)}{2} t\right) \right. \\ \left. + \hat{y} \sin\left(\frac{(k_1 + k_2)}{2} z_1 - \frac{(\omega_1 + \omega_2)}{2} t\right) \right] \end{aligned} \quad (E.3)$$

$$= 2E_0 \cos\left(\frac{(k_1 - k_2)}{2} z_1 - \frac{(\omega_1 - \omega_2)}{2} t\right) [\hat{x} \cos(\bar{k} z_1 - \bar{\omega} t) + \hat{y} \sin(\bar{k} z_1 - \bar{\omega} t)] \quad (E.4)$$

where $k_1 \approx \bar{k} = (k_1 + k_2)/2$ and $\omega_1 \approx \bar{\omega} = (\omega_1 + \omega_2)/2$ are average values of the propagation constant and angular frequency of the CPT beam, respectively.

Similarly, for the right circularly polarized (RCP) CPT beams,

$$\begin{aligned} \vec{E}_{CPT}^{(2)} = E_0 \{ & [\hat{x} \cos(k_1 z_2 - \omega_1 t) - \hat{y} \sin(k_1 z_2 - \omega_1 t)] \\ & + [\hat{x} \cos(k_2 z_2 - \omega_2 t) - \hat{y} \sin(k_2 z_2 - \omega_2 t)] \} \end{aligned} \quad (E.5)$$

where z_2 is the distance travelled by the other CPT beam. This is also simplified to:

$$\vec{E}_{CPT}^{(2)} = 2E_0 \cos\left(\frac{(k_1 - k_2)}{2}z_2 - \frac{(\omega_1 - \omega_2)}{2}t\right) [\hat{x} \cos(\bar{k}z_2 - \bar{\omega}t) - \hat{y} \sin(\bar{k}z_2 - \bar{\omega}t)] \quad (E.6)$$

The difference between z_1 and z_2 in the interferometer is set to $\lambda_{hf}/2$, so

$$z_2 = z_1 + \Delta z = z_1 + \frac{\lambda_{hf}}{2} \quad (E.7)$$

Assuming $\omega_2 > \omega_1$ and $k_2 - k_1 = \frac{2\pi}{\lambda_{hf}} \Rightarrow \frac{\omega_2 - \omega_1}{c} = \frac{2\pi}{\lambda_{hf}}$, and so $k_{hf} = \frac{2\pi}{\lambda_{hf}}$. Subsequently, a phase

difference of $\pi/2$ is calculated:

$$\frac{(k_1 - k_2)}{2}z_2 = \frac{(k_1 - k_2)}{2}\left(z_1 + \frac{\lambda_{hf}}{2}\right) \quad (E.8)$$

$$\frac{(k_1 - k_2)}{2}z_1 - \frac{2\pi}{2\lambda_{hf}} \frac{\lambda_{hf}}{2} = \frac{(k_1 - k_2)}{2}z_1 - \frac{\pi}{2} \quad (E.9)$$

Thus,

$$\begin{aligned} \vec{E}_{CPT}^{(2)} &= 2E_0 \cos\left(\frac{(k_1 - k_2)}{2}z_1 - \frac{(\omega_1 - \omega_2)}{2}t - \frac{\pi}{2}\right) [\hat{x} \cos(\bar{k}z_2 - \bar{\omega}t) \\ &\quad - \hat{y} \sin(\bar{k}z_2 - \bar{\omega}t)] \end{aligned} \quad (E.10)$$

$$\begin{aligned} \Rightarrow \vec{E}_{CPT}^{(2)} &= 2E_0 \sin\left(\frac{(k_1 - k_2)}{2}z_1 - \frac{(\omega_1 - \omega_2)}{2}t\right) [\hat{x} \cos(\bar{k}z_2 - \bar{\omega}t) \\ &\quad - \hat{y} \sin(\bar{k}z_2 - \bar{\omega}t)] \end{aligned} \quad (E.11)$$

Therefore the amplitudes of $\vec{E}_{CPT}^{(1)}$ and $\vec{E}_{CPT}^{(2)}$ are 90° out of phase, i.e. when one reaches maximum (or minimum, the other is zero). Consequently, when the intensity of $\vec{E}_{CPT}^{(1)}(\sigma^+)$ reaches maximum, the intensity of $\vec{E}_{CPT}^{(2)}(\sigma^-)$ is zero and vice versa.

To check if these fields can be expressed as orthogonal linear polarizations, superpose all the CPT fields in eqn. (E.1) and (E.5):

$$\begin{aligned}
\vec{E}_T &= \vec{E}_{CPT}^{(1)} + \vec{E}_{CPT}^{(2)} \\
&= E_0 \{ [\hat{x} \cos(k_1 z_1 - \omega_1 t) + \hat{y} \sin(k_1 z_1 - \omega_1 t)] \\
&\quad + [\hat{x} \cos(k_2 z_1 - \omega_2 t) + \hat{y} \sin(k_2 z_1 - \omega_2 t)] \\
&\quad + [\hat{x} \cos(k_1 z_2 - \omega_1 t) - \hat{y} \sin(k_1 z_2 - \omega_1 t)] \\
&\quad + [\hat{x} \cos(k_2 z_2 - \omega_2 t) - \hat{y} \sin(k_2 z_2 - \omega_2 t)] \} \\
&= 2E_0 \left\{ \left[\hat{x} \cos \left[k_1 \frac{(z_1 + z_2)}{2} - \omega_1 t \right] \cos \left[k_1 \frac{(z_1 - z_2)}{2} \right] \right. \right. \\
&\quad \left. \left. + \hat{y} \cos \left[k_1 \frac{(z_1 + z_2)}{2} - \omega_1 t \right] \sin \left[k_1 \frac{(z_1 - z_2)}{2} \right] \right] \right. \\
&\quad \left. + \left[\hat{x} \cos \left[k_2 \frac{(z_1 + z_2)}{2} - \omega_2 t \right] \cos \left[k_2 \frac{(z_1 - z_2)}{2} \right] \right. \right. \\
&\quad \left. \left. + \hat{y} \cos \left[k_2 \frac{(z_1 + z_2)}{2} - \omega_2 t \right] \sin \left[k_2 \frac{(z_1 - z_2)}{2} \right] \right] \right\} \tag{E.12}
\end{aligned}$$

Eqn. (E.12) is composed of linearly polarized fields at ω_1 with angle $\theta_1 = k_1 \frac{z_1 - z_2}{2}$ and ω_2 with angle $\theta_2 = k_2 \frac{z_1 - z_2}{2}$. The following can now be defined:

$$\theta_1 - \theta_2 = \frac{k_1 - k_2}{2} (z_1 - z_2) = \frac{k_2 - k_1}{2} (z_2 - z_1) \tag{E.13}$$

Given eqn. (E.7),

$$\theta_1 - \theta_2 = \frac{k_1 - k_2}{2} \frac{\lambda_{hf}}{2} = \frac{\pi}{\lambda_{hf}} \frac{\lambda_{hf}}{2} = \frac{\pi}{2} \tag{E.14}$$

Therefore the two linear polarizations are orthogonal, i.e. $lin \perp lin$.

The superposition of the fields can then be written as:

$$\begin{aligned}
\vec{E}_T &= 2E_0 \{ \{ \hat{x} \cos(k_1 z' - \omega_1 t) \cos \theta + \hat{y} \cos(k_1 z' - \omega_1 t) \sin \theta \} \\
&\quad + \{ \hat{x} \cos(k_2 z' - \omega_2 t) \sin \theta - \hat{y} \cos(k_2 z' - \omega_2 t) \cos \theta \} \} \tag{E.15}
\end{aligned}$$

Combining terms,

$$\begin{aligned}\vec{E}_T = 2E_0[& \{\hat{x} \cos \theta + \hat{y} \sin \theta\} \cos(k_1 z' - \omega_1 t) \\ & + \{\hat{x} \sin \theta - \hat{y} \cos \theta\} \cos(k_2 z' - \omega_2 t)]\end{aligned}\tag{E.16}$$

where $z' = (z_1 + z_2)/2$ is the average distance and $\theta = k_1(z_1 - z_2)/2$ corresponds to the angle of the linear polarization state of the electric field at frequency ω_1 . The terms $\{\hat{x} \cos \theta \pm \hat{y} \sin \theta\}$ represent the orthogonal linear polarization CPT fields (i.e. $lin \perp lin$) at frequencies ω_1 and ω_2 , respectively.

APPENDIX F: COMSOL HELMHOLTZ COIL SIMULATION

In designing a physics package with a homogeneous axial magnetic field, a pair of Helmholtz coils were employed. The magnetic field across the length of the cell must be uniform ('flat') to ensure that the atoms do not see a gradient, which can produce unwanted shifts in the clock as the atoms move. If the coils are spaced apart the same distance as the radius of the coils,

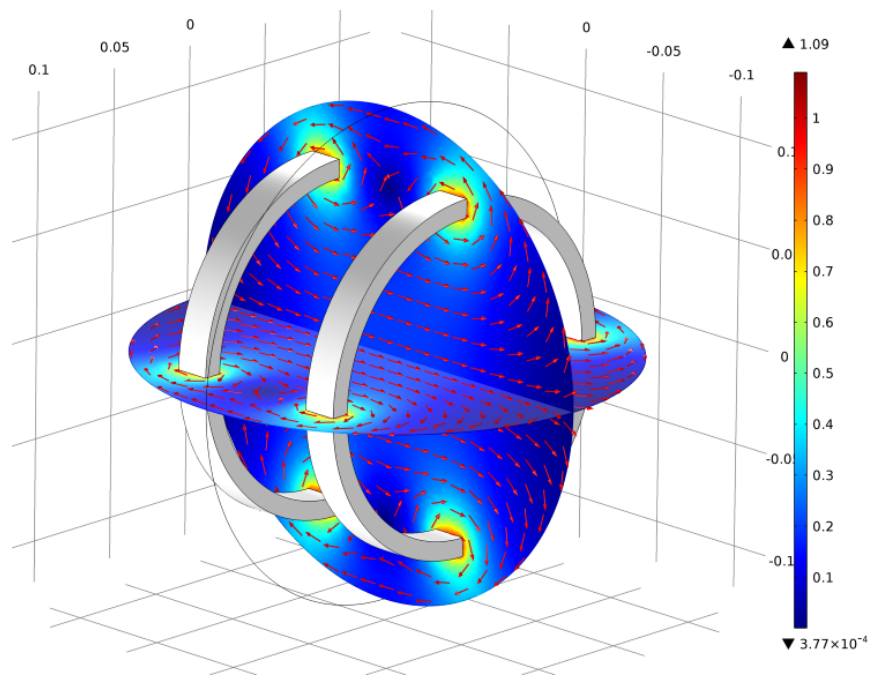


Figure F.1: Model of Helmholtz coils with two slices showing magnetic field strength in mG, and arrows showing the vector direction.

and the current flows in the same direction for each, a uniform magnetic field is formed. COMSOL simulation verified the correct dimensions needed for fabrication of the coils to produce a homogenous field. The simulation calculates the magnetic flux density in a volume surrounding two modeled coils. A current density of 20 A/m^2 (for visualization purposes) is applied to the coils and used in the calculation of the magnetic vector potential. Figure F.1 shows a model of

Helmholtz coils with realistic spatial dimensions indicating the field vectors and strength around the coils. Figure F.2 shows the region of mostly unchanging magnetic field between the two coils along ‘y’ in this simulation (axial, which is ‘z’ elsewhere in this document). This simulation was calculated to design a set of Helmholtz coils for a 7.5 cm long cell, and the variation in magnetic flux over that length at the center ($0 \text{ cm} \pm 3.75 \text{ cm}$) was found to be less than 1%. Similar results were found for simulations of coils for a smaller cell as well.

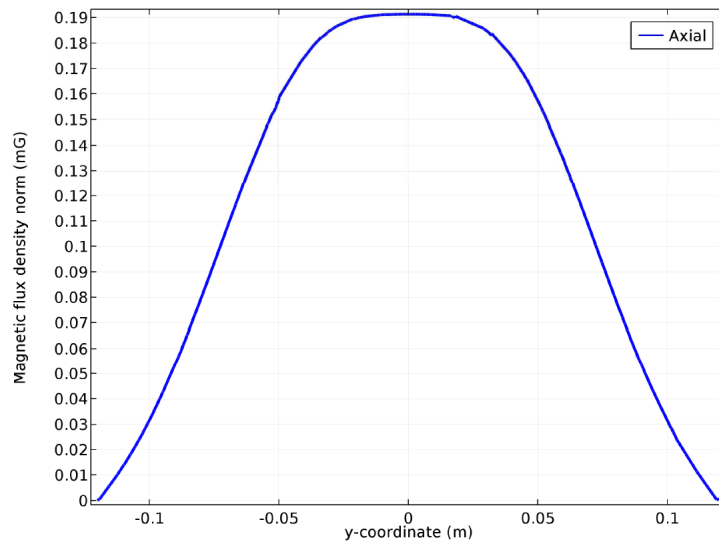


Figure F.2: Magnetic flux density through the center of the Helmholtz coils

APPENDIX G: LABVIEW CODE

To measure Ramsey interference fringes without a boxcar integrator, a PC digitizer card (National Instruments, PCI-5152) was used to collect both the trigger signal (query pulse trigger) and the corresponding optical pulse after the vapor cell. For a single query pulse Ramsey interference scheme, the input trigger defined the data collection gate, as shown in the lower plot of figure G.1. Because of line delays and rise times, the post-collection data window can be adjusted in both width and delay to ensure all of the input signal is used in the calculation.

Instead of the optical pulse, the unaveraged boxcar integrator output can be used, which provides a fixed DC level for each trigger. This can simplify the process of properly selecting a window around the data, as the sample-and-hold circuit of the boxcar maintains the level of the output until the next trigger.

For the repeated query pulse technique discussed in chapter 5, the option for calculating Ramsey fringes for up to 15 query pulses was added. In the case of $N > 1$, only the first gate trigger in the train of query pulse triggers is used. The digitizer collects a continuous signal until the next trigger. This signal includes all of the optical pulses as well as the low DC signal where no light is on the detector. Given a time separation between pulses (“query separation” on the front panel) and the “query width”, the code selects windows to gather the collected data only at the locations where a pulse exists. If the boxcar integrator is used, the time separation can occur anywhere between pulses and thus the window does not have to be precisely over the pulses. As shown in figure G.2, the full collected signal is divided up to 15 times per pulse cycle and summed to produce the Ramsey fringe signal as the two-photon detuning is swept around the $\Delta = 0$ point as described in the text.

The code presented here can be improved dramatically with an algorithm for an arbitrary number of query pulses, as well as a trigger counter to simplify both the hardware setup and the calculation. A sweep trigger would also improve this data collection scheme.

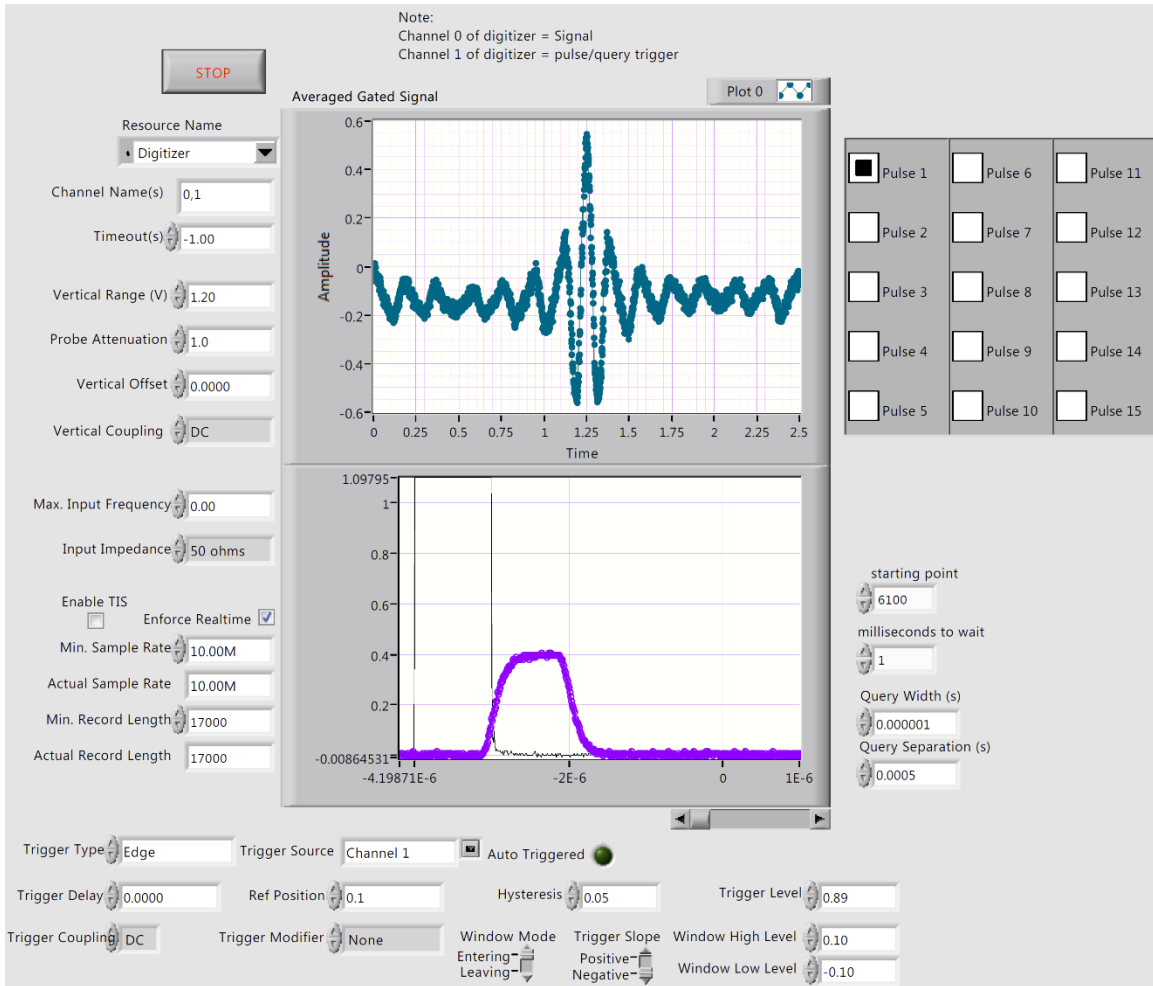


Figure G.1: LabVIEW front panel. Radio buttons provide selection of N query pulses up to N=15. The top plot displays the integrated Ramsey signal, and the bottom plot displays the optical query pulse signal or the unaveraged boxcar output signal. Controls allow modification of the gate size to optimize input signal usage in the calculation of fringes.

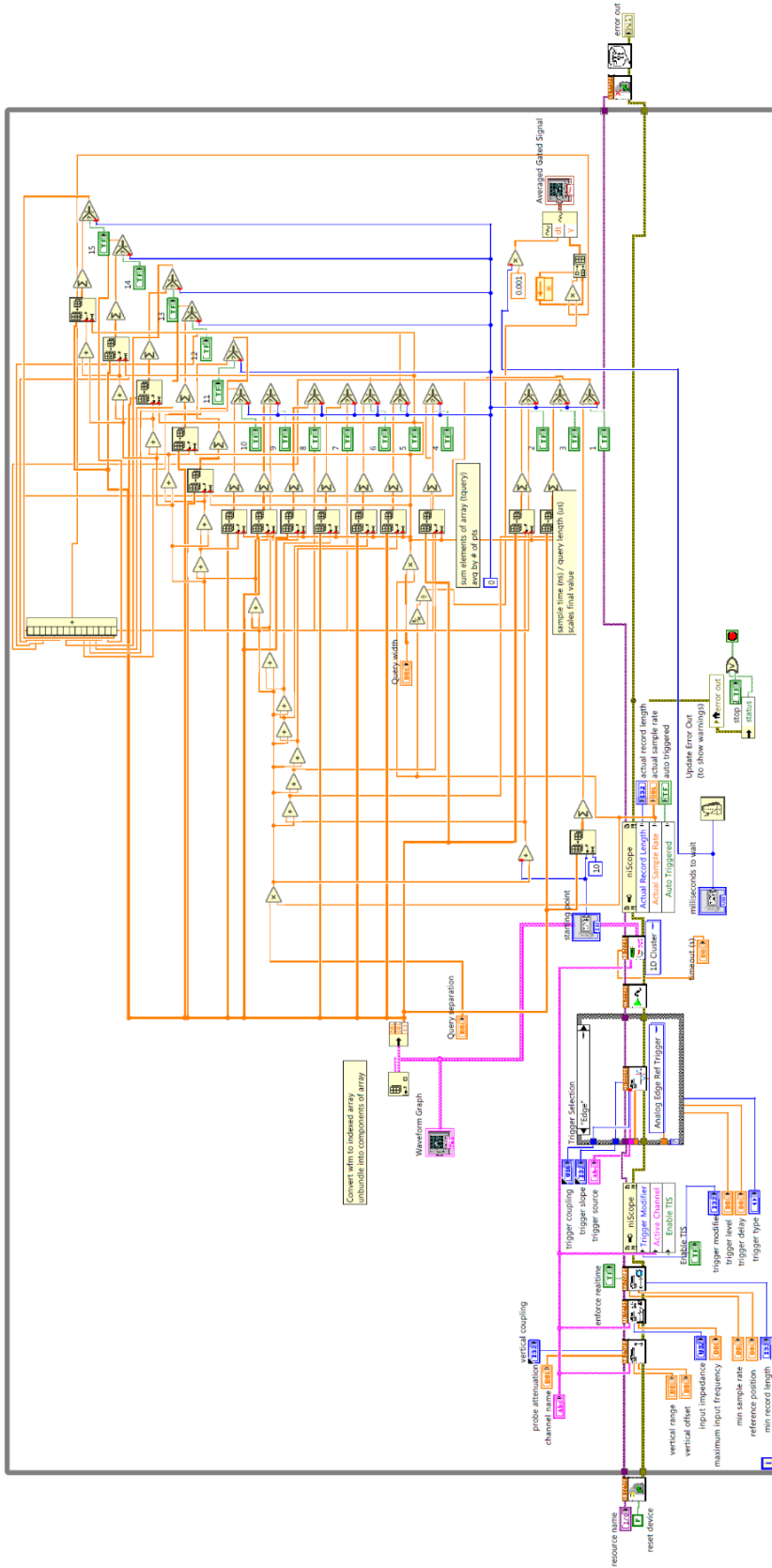


Figure G.2: Block diagram showing the digitizer data collection algorithm and calculation of Ramsey fringes for N query pulses.

PUBLICATIONS

Journal publications:

G. S. Pati, Z. Warren, N. Yu, and M. S. Shahriar, “Computational studies of light shift in a Raman–Ramsey interference-based atomic clock,” *J. Opt. Soc. Am. B* 32, 388-394 (2015)

Z. Warren, R. Tripathi, S. Shahriar, G. S. Pati, “Experimental and theoretical comparison of different optical excitation schemes for a compact coherent population trapping Rb vapor clock” (Accepted April 2017, *Metrologia*)

Z. Warren, R. Tripathi, S. Shahriar, G. S. Pati, “Repeated query Ramsey interference for enhanced atomic clock stability” (to be submitted 2017)

Conference presentations:

Zachary Warren, Renu Tripathi, Gour Pati. Two-photon Resonant Ramsey Interference using a Repeated-Query Scheme for Atomic Clock Development. 2016 Annual Meeting of the American Physical Society Mid-Atlantic Section. (2016)

Z. Warren, G.S. Pati, R. Tripathi, and S.M. Shahriar. Measurements and characterization of a Rb-based vapor cell atomic clock. SPIE Photonics West: Slow Light, Fast Light, and Opto-Atomic Precision Metrology VIII. (2015)

G.S. Pati, Z. Warren, and S.M. Shahriar. Investigations of AC Stark Shift in Pulsed Raman-Ramsey Interaction for Vapor Cell Clock Development (invited paper). SPIE Photonics West: Advances in Fast and Slow Light. (2014)

G.S. Pati, Z. Warren, and S.M. Shahriar. A comprehensive study of light shift in optical Ramsey interference for estimating the performance of a rubidium vapor cell atomic clock (Invited Paper). SPIE Photonics West: Advances in Fast and Slow Light. (2013)

Z. Warren, D. Riser, R. Tripathi, G.S. Pati. Comparative Studies of Coherent Population Trapping and Ramsey Interference in Rubidium Vapor for the Development of an Atomic Clock. Emerging Researchers National. (2013)